Deaeration in Rotating Packed Beds

Zur Erlangung des akademischen Grades eines

Dr.-Ing.

von der Fakultät Bio- und Chemieingenieurwesen
der Technischen Universität Dortmund
genehmigte Dissertation

vorgelegt von

M. Sc. Kai Michael Groß

aus

Haltern am See

Tag der mündlichen Prüfung: 02.03.2021

1. Gutachter/-in: Prof. Dr.-Ing. Andrzej Górak
2. Gutachter/-in: Prof. Dr.-Ing. Norbert Kockmann

Dortmund 2021

"Everything should be made as simple as possible, but no simpler." [1]

---

[1] Based on the original "It can scarcely be denied that the supreme goal of all theory is to make the irreducible basic elements as simple and as few as possible without having to surrender the adequate representation of a single datum of experience." Albert Einstein 'On the Method of Theoretical Physics', lecture delivered at Oxford, 10 June 1933

Abstract

Rotating packed beds (RPBs) overcome gravitational limitations as found in distillation or absorption columns by means of centrifugal force. The concept enables an intensified mass and heat transfer that leads to lower equipment volumes or increased performance. To impose centrifugal forces on gases or liquids the RPB consist of a motor-driven and packing equipped rotor in a static casing. An additional degree of freedom is offered due to the dependency of mass transfer performance and capacity on the rotational speed. Based on the equipment volume RPBs provide a very efficient mass transfer, enable large capacities and offer a high degree of flexibility. However, despite the high potential of the RPBs, their application in industry is limited. To facilitate the design process, a hydraulic and a mass transfer study was conducted. In the first step, a new prototype was designed and constructed together with an engineering partner to enable new investigation technologies and large-scale experiments.

Changing geometries and an increasing centrifugal force along the radius of the rotor require a thorough understanding of the internal processes within the packing of an RPB. In the framework of the hydraulic study, the key characteristics were elucidated. For different packing types and packing geometries pressure drop and operating limits were investigated. For the first time, the liquid hold-up in the rotating packing was measured using the angle-resolved gamma-ray tomography. The information derived from the experimental studies was combined into design guidelines and a pressure drop model.

The mass transfer of the RPB for liquid-side limited systems was investigated by the deaeration of water employing nitrogen as stripping gas. Lab-scale and pilot-scale equipment were investigated to generate a deeper understanding of the scaling effects. Co- and counter-current operations were evaluated for different packing-types and distributors. A model including literature correlations was developed and validated. Finally, cost models were included in a graphical user interface to quickly evaluate the costs of existing or potential RPB processes.

Zusammenfassung

Rotating packed beds (RPBs) sind in der Lage mittels Zentrifugalkraft die schwerkraftbedingten Grenzen klassischer Rektifikations- oder Absorptionskolonnen zu überwinden. Das Konzept ermöglicht einen intensiven Stoff- und Energieaustausch, welcher zu kompakten Apparatedimensionen oder effizienteren Prozessen führt. Um Gase oder Flüssigkeiten mittels Zentrifugalkraft zu beschleunigen, bestehen RPBs aus einem motorbetriebenem, mit einer Packung bestücktem Rotor in einem statischen Gehäuse. Die Rotationsgeschwindigkeit ermöglicht einen zusätzlichen Freiheitsgrad, da Stofftransport und Kapazität von ihr abhängen. RPBs stellen bezogen auf ihr Apparatevolumen einen hoch effiziente Stofftransportleistung bereit, ermöglichen hohe Kapazitäten und sind sehr flexibel. Obgleich des hohen Potentials dieser Technologie werden RPBs nur relativ selten in der Industrie verwendet. Die in dieser Arbeit durchgeführten hydraulischen Experimente und Strofftransportuntersuchungen sollen den Einsatz der RPBs erleichtern. In einem ersten Schritt wurde ein neuer Prototyp entwickelt und mithilfe eines Technikpartners gefertigt. Dieser Prototyp ermöglicht die Anwendung neuer Untersuchungsverfahren und auch Experimente im Pilotmaßstab.

Ein grundlegendes Verständnis der Prozesse innerhalb der RPB-Packung ist notwendig, da sich sowohl geometrische Dimensionen als auch die Zentrifugalkraft entlang des Rotorradius verändern. Im Rahmen des hydraulischen Teils dieser Arbeit wurden daher die wichtigsten Charakteristiken herausgearbeitet. Für verschiedene Packungs-Typen und Packungsabmessungen wurde der Druckverlust und das Betriebsfenster untersucht. Erstmalig kam auch die winkelaufgelöste Gammastrahlen-Tomographie zum Einsatz, um den Flüssigkeitsanteil innerhalb der rotierenden Packung zu bestimmen. Die gewonnenen Informationen wurden für die Erstellung eines Druckverlustmodels und Auslegungsrichtlinien verwendet.

Die Stofftransportleistung flüssigseitig limitierter Stoffsysteme wurde anhand der Entgasung von Wasser mithilfe von Stickstoff untersucht. Verschiedene Untersuchungen in RPBs im Labor- und Pilotmaßstab lieferten Ergebnisse zum besseren Verständnis des Skalierens der RPBs. Gleich- und Gegenstromfahrweise wurde zudem für verschiedenen Packungstypen und Flüssigkeitsverteiler untersucht. Ein Modell basierend auf Literaturkorrelationen wurde entwickelt und mithilfe der experimentellen Daten validiert. Schlussendlich wurde eine graphische Benutzeroberfläche geschaffen, welche unter anderem auch Kostenschätzungen für den RPB ermöglicht. Auf ihrer Basis können bestehende oder potenzielle RPB-Prozesse schnell und einfach evaluiert werden.

Table of contents

Abstract I

Zusammenfassung II

Table of contents III

Notation VI

1 **Introduction** 1

2 **State of the art** 3

2.1 Historical development of centrifugal force utilization 4

2.2 Fundamentals and concepts of RPB 6

2.2.1 Hydrodynamic operation and axial dispersion 9

2.2.2 Large surface area 12

2.2.3 Intensive gas-liquid contact 13

2.3 Process intensification 14

2.4 Gas-liquid contacting in RPBs 15

2.4.1 Pressure drop 15

2.4.2 Liquid hold-up 17

2.4.3 Operating ranges 21

2.4.4 Deaeration 22

3 **Hydrodynamic investigations** 27

3.1 Materials and methods 28

3.2 Pressure drop 30

3.2.1 Dry pressure drop 31

3.2.2 Wet pressure drop 34

3.2.3 Prediction of wet pressure drop 37

3.2.4 Pressure drop in co-current operation 39

3.3 Liquid hold-up 41

3.3.1 Materials and methods 41

3.3.2 Dry scans / reference scans 45

3.3.3 Liquid hold-up measurements 46

3.3.4 Comparison with literature correlations 52

3.3.5 Comparison with wet pressure drop model 55

3.4 Operating limits 56

3.5 Power consumption 61

4 Mass transfer 64

4.1 Theory 64

4.2 Materials and methods 66

4.2.1 Experimental setup 67

4.2.2 Experimental procedure 70

4.3 Co-current 70

4.3.1 Theoretical boundary 70

4.3.2 Influence of the radial packing length 71

4.3.3 Comparison of foam and mesh packing types for the pilot-scale RPB 76

4.3.4 Summary and conclusion 77

4.4 Counter-current 78

4.4.1 Theoretical improvement due to counter-current contact 78

4.4.2 Liquid flow rate 79

4.4.3 Distributors 80

4.4.4 Gas flow rate 81

4.4.5 Packing type 82

4.4.6 Comparison to column packings 83

4.4.7 Summary 84

5 Modeling 85

5.1 Radial k_La modeling 85

5.1.1 Co-current 86

5.1.2 Counter-current 89

5.2 Cost estimation 90

5.2.1 Capital expenditures 90
5.2.2 Operational expenditures 94
5.3 Software assisted process design 94
5.4 Cost estimation for existing industrial size equipment 97
6 Design recommendations 100
6.1 Guidelines: Hydraulic operation and design of RPBs 101
6.2 Guidelines: Deaeration and gas-liquid contacting in RPBs 106
7 Conclusion 111
8 Future work 113
9 References 114
10 Appendix 124
11 Declaration 162
12 Publications 164
13 Supervised theses 165

Notation

Latin letters		
a_c	centrifugal acceleration	$m\, s^{-2}$
A_{CH}	centrifugal head fitting parameter	$-$
a, a_{eff}	interfacial area, effective interfacial area	$m^2\, m^{-3}$
A_{geo}	absolute geometric surface area	m^2
a_p	geometric surface area of the packing	$m^2\, m^{-3}$
a_{ref}	geometric surface area of the reference	$m^2\, m^{-3}$
A_C	cross-sectional area	m^2
c	concentration	$mol\, m^{-3}$
CF	complexity cost factor	$-$
D	diffusion coefficient	$m^2\, s^{-1}$
d	diameter	m
d_p	pore size	m
$d_{packing}$	packing diameter	m
$d_{spherical}$	spherical equivalent diameter of the packing $\frac{6(1-\varepsilon)}{a_p\psi}$	m
E	radiation attenuation	$-$
f	frequency	s^{-1}
F_G	F-Factor = $u_g\sqrt{\rho_G}$	$Pa^{0.5}$
FM	material cost factor	$-$
g	gravitational acceleration	$m\, s^{-2}$
H	column height	m
h	height	m
$H_{O_2}^{CC}$	Henry solubility coefficient oxygen in water	$mol\, m^{-3}$ $mol^{-1}\, m^3$
I_0, I_x, I_{dry}	radiation intensity initial (0), behind object (x), dry reference (dry)	$-$
k_L, k_G	overall liquid/gas side mass transfer coefficient	$mol\, m^{-2} s^{-1}$
$k_L a$	volumetric liquid-side mass transfer coefficient	s^{-1}
K	wall effect constant	$-$
$K_H^{p,x}$	Henry volatility coefficient = $\frac{p_i}{x}$	mol bar mol^{-1}

$L_{packing}$	radial packing length	m
LL	liquid load	$m^3\ m^{-2}\ h^{-1}$
$\dot{m}_L$	liquid mass flow rate	$kg\ s^{-1}$
N	amount	$-$
$\dot{N}$	molar flow	$mol\ s^{-1}$
$\dot{n}$	molar flow per area	$mol\ m^{-2}\ s^{-1}$
n	rotational speed	s^{-1}
n_{th}	number of theoretical equilibrium stages	$-$
p, p_i	total pressure, partial pressure	Pa
p_R	pressure in the RPB	Pa
p_{xy}	fitting constants	$variable$
P_C, P	power consumption	W
r	radius	m
T	temperature	K
T_R	temperature within the RPB	K
t	time	s
t_a	annual operating hours	$h\ a^{-1}$
u	velocity	$m\ s^{-1}$
V	volume	m^3
V_P	packing volume	m^3
$\dot{V}_G$	gas flow rate	$m^3\ s^{-1}$
$\dot{V}_L$	liquid flow rate	$m^3\ s^{-1}$
x	molar fraction of liquid	$-$
y	molar fraction of gas	$-$
Z_0, Z_1	fitting constants for power consumption corr.	$variable$
Greek letters		
α	angular position of the RPB	deg
Ψ_0	resistance coefficient for single-phase flow	$-$
ε	porosity	$-$
η	efficiency	$-$
μ	dynamic viscosity	$Pa\ s$
κ	isentropic exponent	$-$

κ_{energy}	energy cost per kWh	€ kWh^{-1}
Δ	difference	$-$
ξ_{CH}	centrifugal head	Pa
ω	angular velocity	s^{-1}
σ	surface tension	$kg\ s^{-2}$
ρ	density	$kg\ m^{-3}$
φ	form factor of the dry packing	$-$
ψ	sphericity of the packing	$-$
ν	kinematic viscosity	$m^2 s^{-1}$
ω	angular velocity	$rad\ s^{-1}$
Subscripts		
avg	average	
$acceleration$	based on or occurring from acceleration forces	
C	celsius	
c	critical	
$casing$	based on the inner casing diameter	
$column$	related to the column dimensions	
dry	measured on dry packing	
$empty$	occurring from the empty rotor plates	
exp	experimental value	
f	frictional	
$friction$	occurring from frictional forces	
G	gas	
$gravitation$	based on or occurring from gravitational forces	
i	inner	
$ideal$	based on assumptions (e.g. ideal gas or frictionless)	
in	position e.g. inlet concentration	
int	integral	
K	Kelvin	
L	liquid	
max	maximal or based on the smalles cross-sectional area	
min	minimum or minimal	

n	nozzle
o	outer
out	position e.g. outlet concentration
$p, packing$	based on the packing dimensions
r	revolution
$real$	actual (e.g real power consumption)
ref	pointing at an closer to define reference state
rot	occuring from gas body rotation
$rotor$	based on the rotor dimension
RPB	related to the dimensions of the RPB
$samp$	sampling
sim	simulated value
$stat$	static
$total$	total amount (e.g total volume)
w	water
$wire$	based on wire dimensions
0	reference
Superscripts	
$*$	at equilibrium state
RPB	base on the RPB
$samp$	sampling fre
Abbreviations	
ANN	artificial neural network
BM	bare module
CAPEX	capital expenditures
CEPCI	Chemical Engineering Plant Cost Index
CF	complexity cost factor
CFD	computational fluid dynamics
C_{geo}	empirical correction factor based on geometric dimensions = $\frac{D\,a_p}{d_{spherical}\left(1-0.94\frac{V_o}{V_{total}} - 1.13\frac{V_i}{V_{total}}\right)}$
CMC	carboxymethyl cellulose
CT	computed tomography

*conv*CT	conventional CT
FF	full foam
FI	flow indicator
FM	material cost factor
FOB	free-on-board
Ga	Galileo number $= \frac{g d_p^3}{\nu^2}$
GL	guideline
Gr	Grashof number $= \frac{d_{spherical}^3 \, a_c \, \rho_L^2}{\mu_L^2}$
HOCL	hypochlorous acid
Ka	Kapitza number $= \frac{\mu^4 g}{\sigma^3 \rho}$
KM	knitted mesh
L+M*	labor and material cost, without labor and material for instrumentation
MFI	mass flow indicator
MFC	mass flow controller
OPEX	operational expenditures
pchip	Piecewise Cubic Hermite Interpolating Polynomial
PTFE	polytetrafluoroethylene
PVC	polyvinylchloride
REACH	European regulations concerning registration, evaluation, authorization and restriction of chemicals
RPB	Rotating Packed Bed
RCF	relative centrifugal force$= \frac{\omega^2 r}{g}$
Re	Reynolds number $= \frac{\frac{\dot{m}_L}{2\pi \, r \, h}}{a_p \, \mu_L}$
RMSE, NRMSE	(normalized) root mean square error
Sc	Schmidt number $= \frac{\mu_L}{\rho_L \, D}$
*tar*CT	time-averaged angle-resolved CT
We	Weber number $= \frac{\left(\frac{\dot{m}_L}{2\pi \, r \, h}\right)^2}{\rho_L \, a_p \, \sigma_w}$
WPD	wet pressure drop

1 Introduction

The chemical industry will face multiple challenges in the upcoming centuries. The mitigation of climate change might be one of the most important ones. To limit the average global temperature increase to values below 1.5 °C compared to the pre-industrial levels, strong measures are necessary, leading to a transformation of the primary energy sector towards renewable energy generation and eventually to net-zero global emissions [*1*]. Furthermore, the chemical industry will not be unaffected by these ambitious goals and pursue itself the objective of an emission-free and circular economy [*2*]. The transition to a renewable energy powered syntheses of chemical products and the utilization of bio-based feedstocks require a high grade of flexibility and facilitate the implementation of modular, multipurpose or high efficient apparatuses. This kind of equipment provides the user with a broad application range and the possibility to react to fluctuations occurring on the market.

Besides climate challenges, the world's population is estimated to increase by 34 %, based on 2010 levels, to 9 billion people in 2050 inducing significant growth in the chemical and pharmaceutical sectors to meet the needs of the growing society. [*3*, p. 307] Furthermore, modernization and harmonization of European regulations concerning registration, evaluation, authorization and restriction of chemicals (REACH) in 2007 is a giant step towards globally standardized regulation and procedures to provide the highest safety, environmental and toxicological standards for all chemicals used in industrial processes [*4*]. Moreover, worldwide tighter emission limits require large investments to meet new standards (e.g. sulphur-dioxide emissions of cargo chips [*5*]).

Emission limits, fluctuating markets, and feedstock transitions necessitate retrofitting existing plants or to incorporate flexibility margins into new process designs. Rotating packed beds (RPB) have been in the literature for more than 60 years [*6*]. They provide excellent contact between gas and liquid and have proven to be very effective devices even on an industrial scale [*7*]. The rotational speed as an additional degree of freedom offers new opportunities for adjusting the machine's capacity and separation performance. The large mass transfer rate at a conveniently small equipment volume makes it especially beneficial for space-limited environments (e.g. for debottlenecking of existing plants). With RPBs being broadly advertised for all kinds of fluid separations, the question arises why a comprehensive implementation into the chemical industry is still missing.

A potential answer is the barely available fundamental guidance for decision-makers to evaluate the RPB against other potential technologies. Advantages and more importantly drawbacks of the technology are not easily accessible. This work and the developed tools should enable an easy introduction to the topic of RPB for fluid separations. The work incorporates a wide range of investigated parameters to perform the hydraulic design of an RPB. It is focused on the hydraulic operating range and pressure drop evaluation. Correlations to estimate the pressure drop and an automated routine to evaluate the operating range are provided within chapters 3.2 and 3.4. Furthermore, the proof of feasibility for an innovative approach to determine the liquid hold-up within the rotating packing with the gamma-ray tomography is illustrated in chapter 3.3. Finally, the publicly available correlations for power consumption of RPBs are validated and extended in chapter 3.5.

The evaluation of the mass transfer performance focuses on stripping applications where the mass transfer is liquid-side limited. The deaeration of water utilizing nitrogen as a stripping gas is examined thoroughly for co- and counter-current operation, evaluating different packing types and presenting scale-up investigations. The mass transfer performance is compared to the performance of separation columns. Furthermore, the estimation of the mass transfer coefficient with available model equations is evaluated (cf. chapter 4).

Chapter 5.2 focusses on costs taking into account the additional energy costs for the rotation and supports the estimation of the annualized costs based on investment and operating costs for an RPB process.

In summary, this work wants to answer the most fundamental questions potential users encounter when reflecting on the implantation of RPB technology for gas-liquid contacting:

- *Do I need to expect additional pressure drop compared to columns? (Chapter 3)*
- *In which range can I operate the RPB? (Chapter 3)*
- *How can I estimate the mass transfer performance? (Chapter 4)*
- *Which additional costs do I have to consider when applying the RPB technology? (Chapter 5)*

2 State of the art

After a brief look back on historical developments and RPB related patents, the concept of RPB is derived from the fundamentals of gas-liquid contacting in conventional equipment. Based on hydrodynamic operation range, surface areas and mass transfer rates the abilities of the conventional separation technologies are assessed. Finally, the current research on RPBs is further evaluated focusing on pressure drop, liquid hold-up, operating ranges, and the deaeration case study.

Parts of chapter 2 are published in:

Groß, K.; Neumann, K.; Skiborowski, M.; Górak, A.: Analysing the Operating Limits in High Gravity Equipment, Chem. Eng. Trans., 2018, 69, 661-666, http://doi.org/10.3303/CET1869111

Neumann, K.; Gladyszewski, K.; Groß, K.; Qammar, H.; Wenzel, D.; Górak, A.; Skiborowski, M.: A guide on the industrial application of rotating packed beds, ChERD, 2018, 134, 443-462, http://doi.org/10.1016/j.cherd.2018.04.024

Groß, K.; Bieberle, A.; Gladyszewski, K.; Schubert, M.; Skiborowski, M.; Hampel, U.; Górak, A.: Evaluation of Liquid Hold-up in a Rotating Packed Bed for High Gravity Fluid Separation using Process-Synchronized Gamma-Ray Computed Tomography, Proceedings of the 9th World Congress on Industrial Process Tomography (2018), pp. 831–838

Groß, K.; Bieberle, A.; Gladyszewski, K.; Schubert, M.; Hampel, U.; Skiborowski, M.; Górak, A.: Analysis of Flow Patterns in High-Gravity Equipment Using Gamma-Ray Computed Tomography, CIT, 2019,136(6), 1032-1040, http://doi.org/10.1002/cite.201800085

Groß, K.; Beer, M. de; Dohrn, S.; Skiborowski, M.; Scale-Up of the Radial Packing Length in Rotating Packed Beds for Deaeration Processes, Ind. Eng. Chem. Res., 2020, 59(23), 11042-11053, DOI: http://doi.org/10.1021/acs.iecr.0c00868

A detailed overview including student contributions can be found in chapter 11. Scientific advice was given by A. Górak, M. Skiborowski and the corresponding co-authors

2.1 Historical development of centrifugal force utilization

Earth’s gravity is ubiquitous. Challenges in the chemical industry occur when forces acting on fluid or solid elements are either too small or too large: gravitation-driven liquid flow and separation of dispersions (i.e., sedimentation of small solid particles or breaking of unwanted emulsions) are just two examples where the gravitational force on its own can be too low for a feasible process.

Centrifugal pumps and centrifuges are triumphant examples from the past that illustrate how a rotary motion can be used to overcome gravitational limitations. The industry commonly uses pumps and especially centrifugal pumps. Early prototypes of centrifugal pumps by *di Giorgio Martini* [*8*, p. 290] can be dated back to approximately 1475 and more developed versions by *Papin* [*9*] to approximately 1695, 65-95 years before the start of the industrial revolution [*10, 11*].

Centrifugation efficiently realizes the separation of emulsions and other dispersions. The first centrifuges were introduced in 1875 at the world exhibition in Frankfurt am Main by *Prandtl,* the inventor of the first continuously operated milk centrifuge for cream separation [*12*].

Considering the early versions by *di Giorgio Martini,* the application of centrifugal forces for single-phase flow operation is more than 500 years old and 140 years for multiphase liquid-liquid or solid/liquid separation.

The concept of applying centrifugal forces to gas-liquid separations is not new. In 1897, *Eduard Theisen* stated in his patent “Process and Apparatus for Absorbing, Extracting, Distilling, or Evaporating Liquids and Gases or Vapours” that his invention “…differs from these known processes in that the gas or vapor to be treated is subject to centrifugal action...”[*13*]. Numerous patents followed and some important ones will be mentioned here to give a short overview of different developments for gas-liquid contact introduced in the early stages of centrifugal gas-liquid contactors. *Podbielniak,* famous for his centrifugal extractor [*14*, p. 68], proposed in 1930 a conveying channel in a spirally coiled form on a rotating conical body to establish intense contact between gas and liquid streams and therefore reduce the space requirement of distillation equipment [*15*]. Later in 1936, he refined his idea by removing the conical body and replaced it with multiple metal sheets in a spiral arrangement. The direction of gas and liquid flow is therefore switched from along the rotational axis to the radial direction when traveling from the outer to the inner radius [*16*]. This concept is similar to the currently proposed spiral packing design [*17*]. In 1937, *Placek* sketched a similar device, but instead of forcing the flow of the gas and liquid along a spiral path, he equipped the device with separate rings which contain holes in different amounts and sizes. A sieve-tray-like flow is established [*18*]. Moreover, the axial height is reduced from the inner to the outer diameter to keep the gas velocity constant.

In 1959, *Pilo et al.* [*19*] suggested the application of filler bodies or corrugated sheets for the distribution of the liquid and providing a large surface area for contacting liquid and gas. Due to the application of the packing material, the device is later classified by the review of *Rao* as the first version of RPB [*6*, p. 289]. Namely, a device that consists of a rotating shaft attached to a rotor plate which contains an annular packing or different packing fillings. The name “rotating packed bed” took several more years to gain acceptance in the literature. Figure 2.1 visualizes the number of publications in English literature according to a Scifinder® literature survey based on keywords. A period of approximately 80-90 years lays between the first appearance of centrifuges and centrifugal contactors. The establishment of the RPB has been fundamentally promoted by *Ramshaw,* including his patent in 1978 together with *Imperial Chemical Industries Ltd. Ramshaw* and *Mallinson* were among the first to publish actual mass transfer data in their patents and therefore enabled a quantitative performance comparison of RPBs and columns [*20*]. Currently, numerous design concepts applied in modern RPB technology can be traced back to the inventions from 1890 to 1980 presented in this chapter. For further information on early development, the reader is referred to *Rao's* “The story of HIGEE” [*6*]. The following chapter gives an overview of the current RPB concepts and their nomenclature.

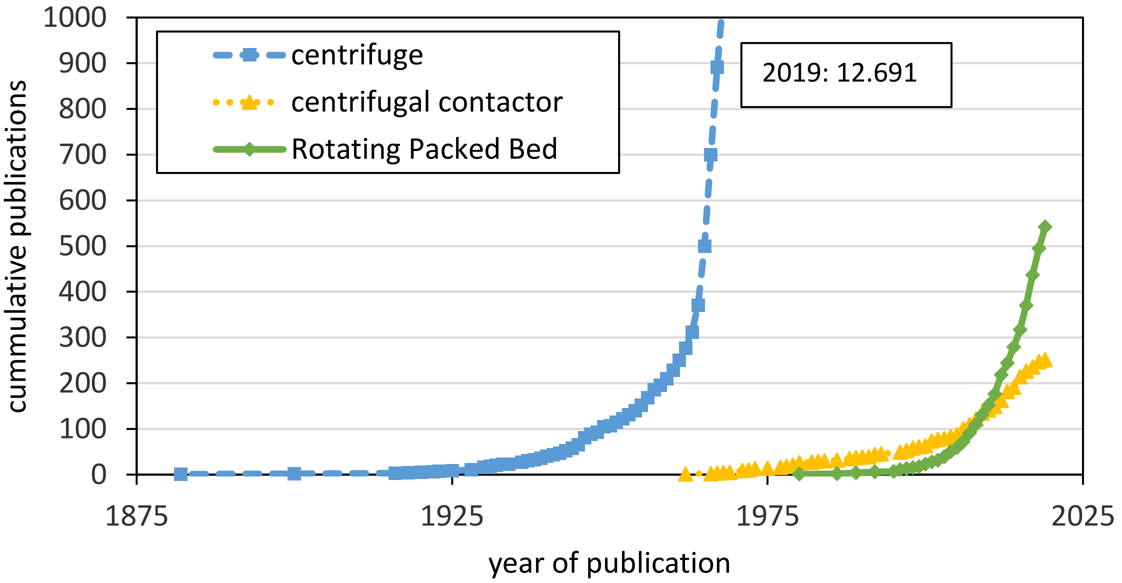

Figure 2.1: SciFinder® survey is based on different keywords and English-language literature.

2.2 Fundamentals and concepts of RPB

The performance of mass transfer equipment for a given component *i* can be described in a very general form by [*21*, p. 202ff.]

$$\dot{N}_i = \dot{n}_i\ a = k_G\ a\ (y_i - y_i^*) = k_L\ a\ (x_i^* - x_i) \tag{1}$$

where $\dot{N}_i$ corresponds to the molar mass transfer rate in mol s^{-1}, $k_{L/G}$ is the mass transfer coefficient in m s^{-1}, a is the interfacial area in m^2 m^{-3} and y_i is the molar fraction in the gas, where y_i^* denotes the equilibrium molar fraction. Analogously the molar fraction in the liquid (x_i) is described. The mass transfer coefficients describe the interaction of the gas and liquid. The coefficient can be a function of turbulence, film thickness, contact time, diffusion coefficient or other aspects. The interfacial area (a) is usually generated by internals in the contacting equipment; in many cases, the mass transfer rate is directly proportional to the interfacial area. The driving force $(y_i - y_i^*)$ or $(x_i^* - x_i)$ reflects the system's distance from the equilibrium. The countercurrent operation of the equipment realizes a high driving force [*22*, p. 456].

To introduce the concept of RPBs, it is reasonable to start with the fundamentals of already well-established conventional gas-liquid mass transfer equipment and then extend it to the RPB concept. Separation columns perform a significant amount of industrial gas-liquid separation processes. Distillation alone accounts for approximately 25 % of the total energy consumption in the US-industrial sector in 2005 [*23*]. With approximately 40,000 distillation columns in operation (1992), distillation columns perform 95 % of all technical separations [*24*, p. 689]. Other industrial processes include absorption and reactive absorption. In particular, exhaust gas cleaning and environmental technology have shown increased growth in recent years [*25*, p. 799].

Similar types of processing equipment perform distillation and absorption. These columns, constructed as cylindrical pressure vessels, are filled with different internals to reach the following objectives:

1. Countercurrent flow with little backmixing
2. Large surface area to generate a large gas-liquid-interface
3. Intensive gas-liquid contact

To achieve these objectives, columns are equipped with different internals. The contacting internals are trays, random or structured packings. They provide a surface to generate an interface between the gas and liquid in the form of thin films or droplets. Additionally, they generate an efficient surface renewal and effective cross- or countercurrent flow by guiding the fluids. Figure 2.2 shows the common types of column internals.

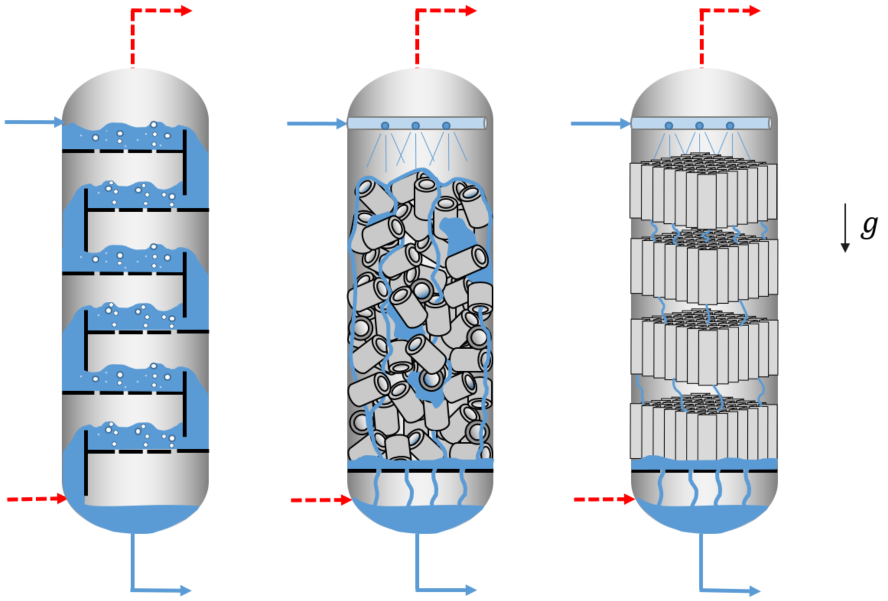

Figure 2.2: Different types of column internals trays, random and structured packings.

Even though exceptions exist [*26*, p. 251f.], in most configurations the gas is flowing upwards through the contacting equipment while it must overcome the pressure loss due to internals. Generally, the pressure drop of trays is much higher than in random or structured packings [*27*, p. 7]. In contrast, the liquid flows downwards through the equipment driven only by gravitation. Even when no gas/vapor is present, the throughput of liquid is limited. Capillary forces limit the packing structure to a certain pore size. Moreover, when gas/vapor is applied, the frictional forces between the gas and liquid decrease the maximum capacity further. Forces can become so large that a stable contacting of the two phases is not possible. In counter-currently operated distillation and absorption columns, the frictional forces of the gas can become so intense that they drag the liquid upward in the column. The backmixing leads to a reduced mass transfer performance [*24*, p. 760]. Consequently, designers are forced to limit the gas velocity and therefore the capacity. The superposition of gravitational force by centrifugal forces in RPBs extends the operational window far beyond gravitational capabilities. RPBs consist of a rotor and a casing. The rotor is equipped with packing. Common packings are stainless steel meshes, foams or beads. More recently, new structures have gained increasing interest (e.g. Zick-Zack packing [*28*]). A motor accelerates rotor and packing to a rotational speed between 10 and 1000 times gravity [*29*, p. 1152]. At the center of the rotor liquid is sprayed onto the rotating packing. The liquid is first decelerated strongly in the radial direction when it hits the packing due to flow deflection, then the rotor accelerates the liquid to the rotor's rotational speed in the direction of rotation which consequently drives the liquid through the packing by centrifugal force. While the liquid flows from the inner diameter to the outer diameter of the rotor, a gaseous phase can flow either co-currently or counter-currently through the rotor.

As illustrated in Figure 2.3, there are two main differences between RPBs and columns. In counter-currently operated columns, the flow path of the liquid is top to bottom, even though partial cross-flow is possible (e.g. in tray columns), the resulting overall flow direction remains unchanged. The separation of components occurs along the flow path due to the counter-current contact. Hence, the separation performance can be related to a specific length of the equipment.

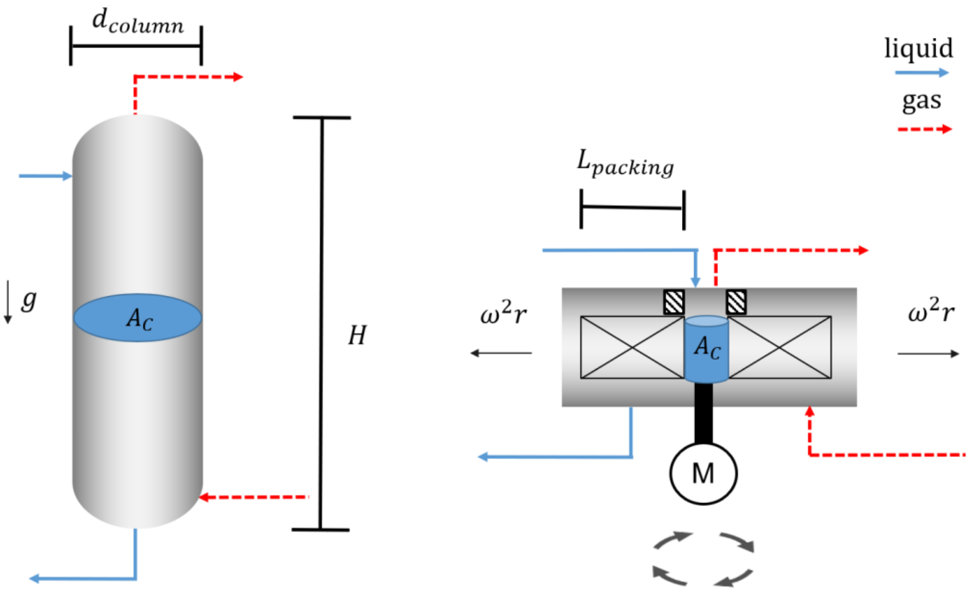

Figure 2.3: Schematic of the different cross-sectional areas in a conventional column and a RPB.

For columns, the specific length is the column height (H). In RPBs, the additional rotation creates a centrifugal field and therefore adds the centrifugal force to the force balance. Even though gravity is still acting, centrifugal acceleration is superimposing it by one or two orders of magnitude. Within the rotor, the flow direction of the liquid points from the inner radius to the outer radius and the gas-liquid contact is realized parallel to the upper and lower rotor plate. The separation performance for RPBs relates to the radial packing length ($L_{packing}$). While in columns the free cross-sectional area ($A_{C,column}$) remains constant and is proportional to the column diameter (d_{column}) (2), in RPBs the free cross-sectional area ($A_{C,RPB}$) is a function of the radius and the distance between the rotor plates ($h_{packing}$). This can lead to a significant variation of the cross-sectional area in a rotor with a long radial packing length (3).

$$A_{C,column} = \frac{\pi d_{column}^2}{4} \tag{2}$$

$$A_{C,RPB}(r) = 2\,\pi\,h_{packing} r \tag{3}$$

For a convenient comparison, it is reasonable to relate the gas and liquid flow rates to the free cross-sectional area of the equipment.

The liquid load is defined as

$$LL = u_L = \frac{\dot{V}_L}{A_C} \tag{4}$$

where u_L is the superficial liquid velocity and $\dot{V}_L$ is the applied liquid flow rate. For RPBs in most cases, flow rates are related to the inner diameter of the equipment because the rotor provides at the inner radius (r_i) the smallest cross-sectional area and therefore the highest load. The F-factor defines the gas load and incorporates density changes

$$F_G = u_G \sqrt{\rho_G} = \frac{\dot{V}_G \sqrt{\rho_G}}{A_C} \tag{5}$$

with the superficial gas velocity u_G and the gas density ρ_G. For a larger radial packing length, the average of LL and F_G is usually used by integrating the velocities along the radius to incorporate the changes in packing geometry.

$$\bar{F}_{G,int} = \frac{\sqrt{\rho_G}}{r_o - r_i} \int_{r_i}^{r_o} u_G(r)\ dr \tag{6}$$

For a constant packing height and incompressibility of the gas phase, (6) transforms to (7).

$$\bar{F}_{G,int} = \frac{V_G \sqrt{\rho_G}}{2\,\pi\, h_P\, (r_o - r_i)} \ln\left(\frac{r_o}{r_i}\right) \tag{7}$$

For a direct comparison between gravitational and centrifugal accelerated equipment, the relative centrifugal force (RCF) is used [*30*], in which r is the radius and ω is the angular velocity of the centrifugal equipment, while g is the gravity of earth.

$$RCF = \frac{\omega^2 r}{g} \tag{8}$$

The following section discusses objectives for an efficient gas-liquid contacting device (cf. 2.2).

2.2.1 Hydrodynamic operation and axial dispersion

The operation boundaries of columns and RPB are similar. A low volume of entrained liquid and a minimal axial dispersion are important for efficient operation. The avoidance of axial dispersion along the flow direction of the fluids is necessary to prevent partial equilibration of concentration differences which would reduce the separation efficiency [*21*, p. 231]. The boundary for the maximal hydraulic operating capacity in columns is called the flooding limit. In tray columns, the flooding limit is accompanied by a high pressure drop, a large amount of liquid leaving the top of the column and unstable levels and indicators [*27*, p. 51]. In structured packings, a similar behavior can be observed; at the flooding point, the frictional forces of the gas on the liquid become so high that a stable operation, without entrainment and axial dispersion, is no longer possible [*27*, p. 152].

The "maximal hydraulic operating capacity", where the highest hydraulic throughput can be achieved and the "maximum useful capacity", where the highest mass transfer efficiency can be observed, are not always equal. Usually, close to the maximal hydraulic operating capacity, the mass transfer efficiency decreases. Approximately 0-20 % below the maximal hydraulic operating capacity, the maximal mass transfer efficiency is reached [*31*, p. 58].

Evaluating the hydraulic potential for structured packings in columns, as shown in Figure 2.4 based on data by *Yildirim et al.* [*32*], it is evident that there is always a trade-off between high gas loads and high liquid loads. With increasing liquid loads, the allowable F-Factor F_G decreases significantly. The number of column packings that enable high liquid loads above 150 $m^3 m^2 h^{-1}$ is limited. A larger geometric surface area a_{geo} for example as in "Montz B1-750" with 750 $m^2 m^3$ or "Mellapak 500-Y" with 500 $m^2 m^3$ substantially limits the maximal allowable gas throughput. Only very low surface packings (e.g. "Mellapack 125-X") allow for a LL above 100 $m^3 m^2 h^{-1}$ and an F_G above 4 $Pa^{0.5}$ simultaneously.

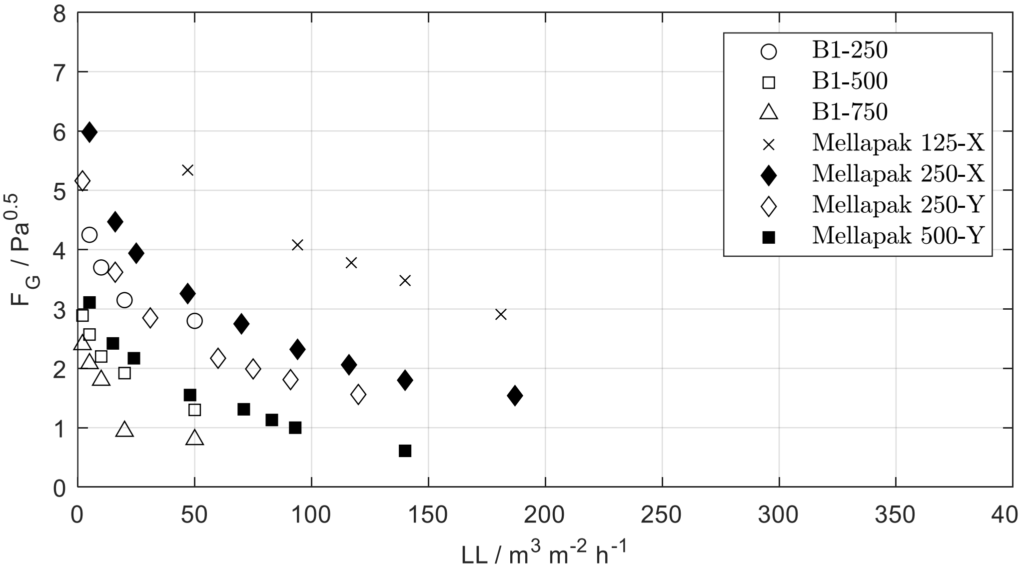

Figure 2.4: Comparison of hydraulic flooding data from *Yildirim et al.* [*32*] for structured packings with different specific surface areas. Flooding criterion was based on a pressure drop >12 mbar m^{-1} (Reuse with permission of John Wiley and Sons).

Sherwood et al. show that the flooding velocity depended on the gas and liquid ratios as well as on the gravitational force [*33*]. A comprehensive overview of correlations for column packings is provided by *Mackowiak* [*34*, p. 36ff.]. The vast majority of the correlations include the gravitational force as a parameter. The dependency of gravitational force on the pressure drop derives in many cases from a force balance between frictional and gravitational forces on liquid elements, as in

Mackowiak's suspended bed of droplets(SBD)-model [*34*, p. 41ff.], where flooding starts when the gas velocity is higher than the effective downflow velocity of droplets.

Due to the experience with already implemented technologies in separation equipment, the gravitational force appears as the hydraulic bottleneck. As described earlier, high gravity technology tackles the problem by superimposing the gravitational force with a centrifugal force.

There are numerous definitions for the maximal hydraulic operating capacity in conventional columns [*35*, p. 1672]. The same applies to RPBs. In addition to visual determination and hold-up studies, many definitions are based on pressure drop analysis [*36*]. The pressure drop increases steeply when the operating limit is approached. *Rajan et al. [37]*, *Singh et al. [38]*, and *Lockett [39]* provide the most common definitions for the maximal hydraulic operating capacity based on pressure drop analysis. Figure 2.5 illustrates a schematic pressure drop curve. Empirical observations show that high rotational speeds increase the stability of the system and avoid entrainment of droplets; at lower rotational speeds extensive entrainment of droplets increases, which ultimately leads to an inoperability of the machine. Consequently, there is a minimal rotational speed (n_{min}) and lower rotational speeds should be avoided. Chapter 2.4.1 provides further information on the shape of the pressure drop curve.

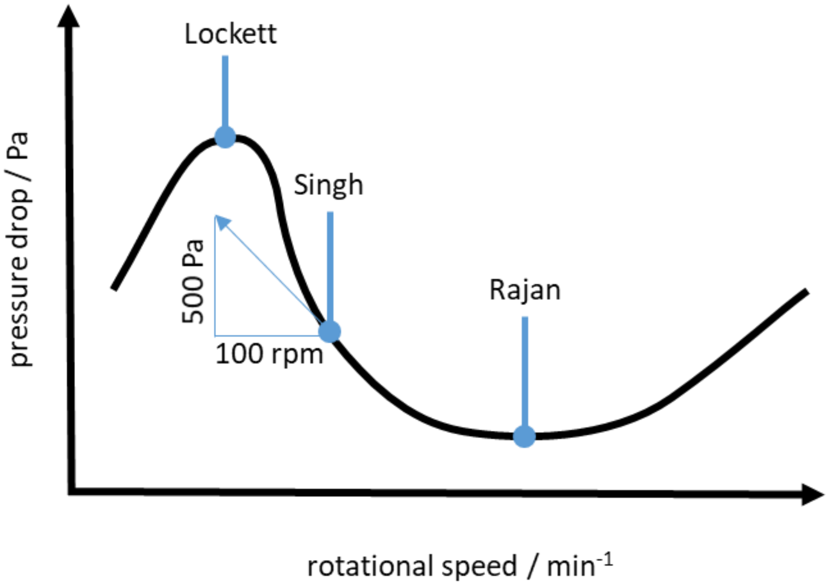

Figure 2.5: Characteristic pressure drop curve for an RPB with marked points for minimal rotational speed according to *Lockett, Singh, and Rajan.*

Rajan defines n_{min}, at the smallest pressure drop (see Figure 2.5) [*37*, p. 988]. Of the different approaches, *Rajan's* approach is the most conservative because it creates the largest distance to the real maximal hydraulic operating capacity. However, of the three different definitions, it is the easiest to determine n_{min} because a stable pressure drop and limited entrainment is expected. S*ingh* defines the position of n_{min} where the slope of the pressure drop curve increases above

500 Pa/100 rpm [*38*, p. 577]. This definition usually leads to a lower $n_{\min}$ compared to Rajan. 500 Pa/rpm is an empirical value and has no physical meaning. The universal applicability is therefore questionable. When the rotational speed is gradually reduced, the pressure drop will first decrease, then increase to a maximum and then decrease again. The pressure drop maximum is accompanied by entrainment of liquid through the gas outlet of the machine. This highly unstable condition is defined by *Lockett* [*39*, p. 380] as the maximal hydraulic operating capacity and therefore as $n_{\min}$. His visual observations support this definition. The approach of *Lockett* requires an experimental setup suitable for operating under unstable conditions. Especially in larger-scale equipment, this can be impractical to measure.

In summary, for a given capacity based on volumetric flow rates, a minimal rotational speed exists due to hydrodynamic reasons. The operation close to the minimal rotational speed is preferred due to decreased power consumption.

2.2.2 Large surface area

The mass transfer rate is proportional to the interface between gas and liquid in the equipment. It must be distinguished between the specific geometrical surface area (a_{geo}) provided by trays/packings and the specific effective interfacial area (a_{eff}) created by the equipment. In columns, standard structured packings provide an a_{geo} from 100 to 750 $m^2\,m^{-3}$ [*27*, p. 14]. Increasing the geometrical surface area reduces the maximal hydraulic operating capacity of the equipment (cf. Figure 2.4) and designers need to lower the gas velocities by adjusting the equipment diameter. The application of rigid foams in columns has been investigated by *Große* [*40*]. It was found that foams with 20 and 30 pores per inch were mostly inoperable in columns. Less and bigger pores (10 pores per inch) could be operated but showed a small operating window compared to conventional column packings. However, the highest operating load was approx. 25 $m^3\,m^{-2}\,h^{-1}$ LL and F_G 2 $Pa^{0.5}$, which is comparable to a Montz B1-750 packing at a comparable geometric surface area (cf. Figure 2.4) . Centrifugal forces in RPBs enable smaller pore sizes and finer structures. Meshes and foams are commonly used in RPBs with an a_{geo} between 750 and 2800 $m^2\,m^{-3}$ [*36*, p. 246]. Packings for columns with an a_{geo} > 750 $m^2\,m^{-3}$ are seldom found on the market. If the wetting behavior can be assumed to be similar compared to columns and the mass transfer to be proportional to the geometric surface area provided, the mass transfer in RPBs could be between three and four times higher than that of columns; thus, the potential performance increase is significant.

2.2.3 Intensive gas-liquid contact

Gas-liquid contactors aim at efficient and intense contact between phases. The product of the overall liquid/gas side volumetric mass transfer coefficient (k_L, k_G) and the effective interfacial area (*a*) is a quantitative measure to evaluate the equipment performance. Large values for k_La lead to compact equipment size. Figure 2.6 illustrates that the spread of k_La includes several orders of magnitude. Co-currently operated equipment types reach the highest mass transfer coefficients due to virtual unlimited throughput. While flooding or entrainment does not exist in co-current operation (e.g. horizontal pipes, static mixers, venturi ejectors or co-current packed beds), gas and liquid velocities can be increased to highest values increasing turbulence and reducing film resistance. Mechanically agitated equipment types (e.g. stirred tanks) also reach high values due to the induced mixing and dispersion by the agitator. However, stirred tanks usually suffer from backmixing and would therefore only be appropriate for reactive systems. Moreover, other co-currently operated equipment types are facilitating the driving force less efficient compared to counter-currently operated equipment.

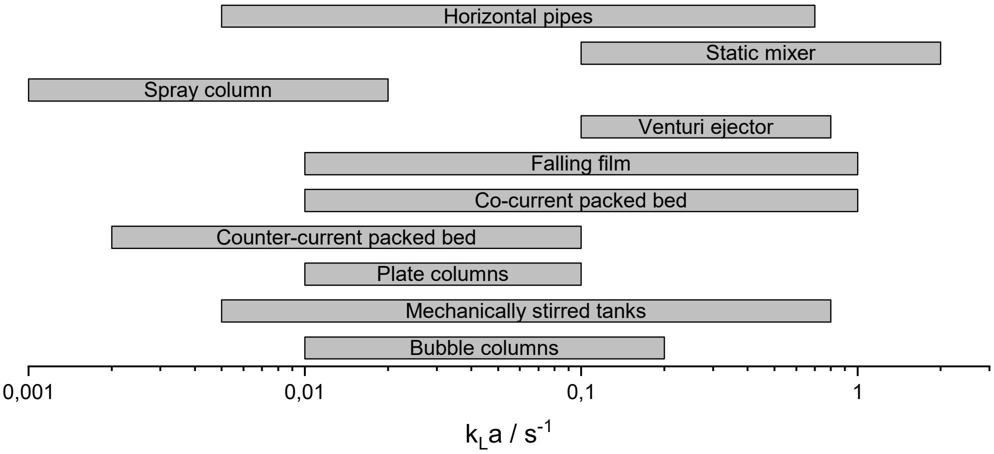

Figure 2.6: Overview on k_La values for gas-liquid contactors according to *Trambouze et al. [26]*.

Counter-currently operated packed beds are the state of the art deaeration equipment when a stripping gas is used, the process is thoroughly described in chapter 2.4.4. *McCabe et al.* [*41*, p. 715] and *Laso et al.* [*42*, p. 255] have examined commercially available packings for the stripping application. The results of *McCabe* are for Raschig rings for the stripping of oxygen with a stripping gas. The liquid load ranged from 2.5 to 141 $m^3 m^{-2} h^{-1}$ and the gas load between 407 and 936 $m^3 m^{-2} h^{-1}$. While *Laso* presents data for stripping of oxygen saturated water with air for liquid loads between 13 and 73 $m^3 m^{-2} h^{-1}$ the F-factor was varied between 0.8 and 3.1 $Pa^{0.5}$. Mellapak packings of the Y-type with specific geometrical surface areas of 125, 250 and 500 $m^2 m^{-3}$ were investigated. The observed k_La-values with highest values observed of approximately 0.05 to 0.06 s^{-1} fall within the range 0.002 to 0.1 s^{-1} mentioned by *Trambouze et al. [26]*. Experimental results with gas and liquid loads in a comparable range to this work are illustrated in Figure 2.7. A linear dependency between liquid load and the k_La-value is observed. The literature results for packed columns are compared with the RPB in chapter 4.4.6.

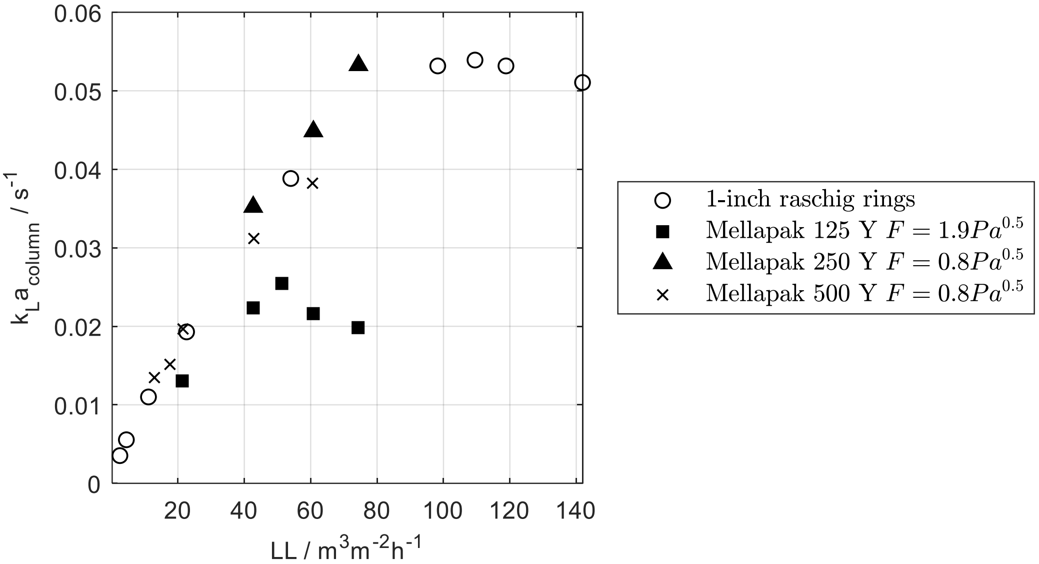

Figure 2.7: Selected k_La-values for packed columns with different internals. Data from *McCabe et al.* [*41*, p. 715] and *Laso et al.* [*42*, p. 255]. Data extracted from original graphs with Origin plot digitizer.

2.3 Process intensification

The part of chemical engineering discipline that deals holistically with an improvement of performance and efficiency is called process intensification. There are numerous definitions of process intensification, each one focusing on different areas, being less or more specific in its definition [*43*, p. 6]. However, process intensification is characterized by its integral approach from the molecular level up to the consideration of complete plants. It is open-minded towards new and innovative technology and considers these technologies already at an early stage as a potential alternative to conventional technologies. A very general form is given by *Costello* [*44*] who describes process intensification as "any engineering development that leads to a substantially smaller, cleaner, safer and more energy-efficient technology" [*43*]. *Van Gerven and Stankiewicz* [*45*] created a more structural approach with introducing the four principles of process intensification and the four domains where these principles are applied.

From a small scale to a large scale these principles are [*43, 45*]:

1. maximize the effectiveness of intra- and intermolecular events (Spatial domain)
2. give each molecule the same processing experience (Thermodynamic domain)

3. optimize the driving forces and resistances at every scale and maximize the specific surface areas to which theses forces or resistances apply (Functional domain)
4. maximize the synergistic effects from partial processes (Temporal domain)

RPBs are addressing the third and fourth principle, by creating thin films and providing large surface areas (cf. 2.2.2). Furthermore, the rotational speed offers an additional degree of freedom which supports the utilization of synergies (4th principle) within the whole plant (e.g. capacity adjustment based on available heating or cooling utilities). RPBs are a perfect example of how size reduction can be realized by intensifying the mass transfer within the equipment. Further information will be given in chapter 2.4.4.

2.4 Gas-liquid contacting in RPBs

After assessing the state of the art for conventional equipment, this chapter performs an extensive analysis of the existing RPB research works. The focus is set by the author on deaeration relevant contents, addressing hydraulic features (e.g. pressure drop, liquid hold-up and operating range). The deaeration (stripping of oxygen from a liquid) is considered as a model system for liquid-side limited mass transfer processes.

2.4.1 Pressure drop

The total pressure loss over the contacting equipment can be a crucial design parameter. Especially in low pressure or high throughput applications, it can have a significant influence on the cost. A general equation for pressure drop calculations of multiphase flow in pipes is found in (9) [*46*, p. 510]. It is common to relate the different fractions of the pressure drop to certain effects. The $\left(\frac{dp}{dz}\right)_{friction}$ describes the pressure losses created by the interaction of the fluids with pipes, walls or other internals, while the $\left(\frac{dp}{dz}\right)_{acceleration}$ is attributed to losses by changes in the cross-sectional area that happens in valves or at changing pipe diameters and gravitational losses $\left(\frac{dp}{dz}\right)_{gravitation}$ [*46*, p. 510].

$$\left(\frac{dp}{dz}\right)_{total} = \left(\frac{dp}{dz}\right)_{friction} + \left(\frac{dp}{dz}\right)_{acceleration} + \left(\frac{dp}{dz}\right)_{gravitation} \tag{9}$$

Pressure drop calculations for RPB follow a similar approach; the majority of pressure drop correlations are based on a summation of the different contributing effects which are assumed to be independent of each other. The correlations divide into dry pressure drop and wet pressure drop correlations. The dry pressure drop correlations incorporate influences of the rotational speed and frictional forces of the gas flowing through the RPB but are limited to single-phase flow. An overview of correlations can be found in [*47*, p. 51]. However, 4 of the 7 mentioned correlations originate from Chinese literature and are therefore not easily accessible.

Neumann et al. proposed a straightforward correlation to model the dry pressure drop [*48*]. This correlation uses the extended channel model for column packings [*49*, p. 133]. Two main contributions describe the pressure drop:

- Centrifugal head (ξ_{CH}) can be understood as blower or compressor behavior of the rotor and packing counteracting the gas flow
- The friction pressure drop of the gas ($\Delta p_{f,stat}$) should be similar to the frictional pressure losses of gas flowing through a static packed bed. The parameters A_{CH} and φ are deduced by experimental data.
- Additional contributions ($\Delta p_{f,rotor} + \Delta p_{f,empty} + \Delta p_{rot}$) are usually small and can be neglected. If a significant influence is expected, they are described by a pipe analogy [*48*].

$$\Delta p_{total,dry} = \left(\xi_{CH} + \Delta p_{f,stat} + \Delta p_{f,rotor} + \Delta p_{f,empty} + \Delta p_{rot}\right) \tag{10}$$

Tab. 1: Additional equations for the pressure drop model from *Neumann et al.* for the dry, unirrigated packing [*48*].

With: Centrifugal head $\xi_{CH} = A_{CH} \dfrac{\rho_G \cdot \omega^2}{2} \left({r_O}^2 - {r_i}^2\right)$	(11)
Static packing frictional pressure drop $\Delta p_{f,stat} = \Psi_0 \cdot (1 - \varphi) \dfrac{(1-\varepsilon)}{\varepsilon^3} \cdot \dfrac{{\bar{\mathrm{F}}_{\mathrm{G,int}}}^2}{d_p} \cdot \dfrac{(r_o - r_i)}{K}$	(12)
$\Psi_0 = \dfrac{725.6}{\overline{\mathrm{Re}}_{\mathrm{G,int}}} + 3.203$	(13)
$\overline{\mathrm{Re}}_{\mathrm{G,int}} = \dfrac{d_p}{(1-\varepsilon)\nu_G} \cdot \dfrac{\bar{\mathrm{F}}_{\mathrm{G,int}}}{\sqrt{\rho_G}}$	(14)
$d_p = 6 \cdot \dfrac{(1-\varepsilon)}{a_p}$	(15)
Additional experimental determined contributions: $\Delta p_{f,rotor} + \Delta p_{f,empty} + \Delta p_{rot} \approx 0$	(16)

The correlations of the wet pressure drop, which include the influence of liquid, are scarce. Possible reasons are the more complex behavior of the pressure drop curve which cannot easily be approximated and the not yet thoroughly understood liquid flow behavior. Often, the wet pressure drop behavior is imagined as an additional liquid film that reduces the free area of the packing and therefore increases the frictional pressure losses [*50*, p. 3855].

There is a pressure drop phenomenon within RPBs which is discussed controversially. Some authors have explored that when liquid is wetting a dry packing at a constant gas flow rate, the pressure drop decreases [*51*, p. 50][*52*, p. 831]. This behavior is not observed in packed columns and different authors could not confirm the results presented in the literature for RPBs [*39*, p. 380, *50*, p. 3855, *53*, p. 387]. Chapter 3.2.2 presents our own experiments that do not support the above observations. The information on co-current pressure drop investigations is very scarce. Recently, *Hendry et al.* [*54*] have published data on the co-current pressure drop behavior for a limited parameter range. LL_{max} up to 57.3 $m^3 m^{-2} h^{-1}$ and a constant $F_{G,max}$ 3.8 $Pa^{0.5}$ and a rotational speed of 240 min^{-1} was investigated. The rotor inner diameter is similar to the RPB design investigated in this work (di, do, hp / 0.2 m, 1 m, 0.1 m), while height and outer diameter are significantly increased. An expanded metal mesh sheet packing was used (a_P = 663 $m^2 m^{-3}$, ε = 0.801). The new investigations present pressure measurements from the inside of the rotor and a one dimensional pressure drop contribution model for co- and counter-current operation. The pressure measurements within the rotating packing are very important to gain further insights in the flow behavior of the gas within the packing. They might be an excellent way for packing design optimization to combine a high mass transfer performance with a reduced pressure drop.

2.4.2 Liquid hold-up

Flow characteristics in the packing relate strongly to the performance of RPBs. Flow behavior determines capacity, mass transfer performance, residence time and pressure drop. Hence, the correct choice of design parameters(e.g. pore size, material, and structures) for packing internals is crucial. Multiple researchers have developed new and tailored existing technology to enable liquid flow measurements within rotating packing. The concept ranges from visual studies [*55*] over to conductance measurements [*56, 57*] and to computer tomographic evaluations [*58, 59*].

White emulsion paint was used by *Burns and Ramshaw* [*55*] to visualize the liquid behavior within a black PVC foam packing. An acrylic rotor plate was used to enable photographs by a strobe light and a camera (cf. Figure 2.8a). Their observation showed a heterogeneous flow behavior, grouped into a droplet, pore and film flow (cf. Figure 2.8b).

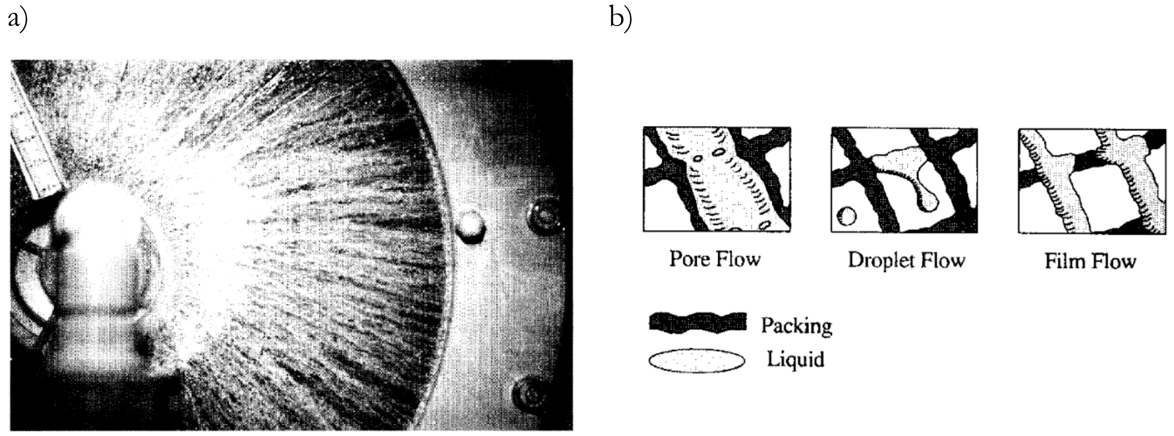

Figure 2.8: Liquid flow behavior as observed by *Burns et al.* [*55*] a) Declon PVC foam packing at 750 min^{-1} with a single point distributor b) flow regimes as defined by *Burns et al.* [*55*] (Reuse with permission from Elsevier).

Although the existence of film flow could not be confirmed unambiguously, there were some indications for film flow (e.g. color change due to wetting). To enable quantitative liquid hold-up measurements *Basic and Dudukovic* [*56*] implemented conductivity measurements within the rotor. The method required a nonconductive packing material. Therefore, glass beads were used. Electrodes at the inner and outer diameters measured the radial liquid distribution while additional electrodes on the upper and lower rotor plate were conducting transverse hold-up measurements. The accuracy of the transverse measurement was low but showed a significant difference between radial and transverse liquid distribution. The data confirmed the existence of different flow regimes and an anisotropic distribution within the packing.

Burns et al. [*57*] generated further improvement with four electrodes in the radial direction while one pair was at the inner diameter and another pair was close to the outer diameter of the rigidized PVC packing. According to their findings, the liquid hold-up was inversely linear proportional to the packing radius. The gas flow had a small influence on the liquid hold-up close to the entrainment region. Tracer response experiments showed a short liquid residence time of approximately 1 to 1.5 s. The study of the liquid flow behavior within a rotating system is a complex task. Most RPB configurations require materials with strong mechanical strength (e.g. stainless steel) which obstruct insight into the equipment. Methods involving probes require some sort of telemetry or data logging to transfer the measurement online or after the experiment is run for evaluation.

A very elegant method is the application of noninvasive measurement technology. *Yang et al.* [*58*] conducted the first application in the area of RPB technology. The application of X-ray computed tomography enabled a quantitative liquid hold-up determination inside the RPB. Measurements for wire mesh packing and metal foam packing revealed an increasing liquid hold-up with an increasing liquid flow rate and liquid viscosity. Elevated rotational speeds decreased the liquid hold-up. The study was restricted to a single liquid phase flow and relatively small radial packing length of several centimeters which is small compared to the scale of pilot or industrial applications.

To further develop the liquid hold-up measurement technology and generate a more fundamental understanding of the liquid flow behavior within the RPB in this work, we conducted further measurements with a high-energetic gamma-ray computed tomography on an RPB with pilot-scale dimensions (cf. chapter 3.3). Tab. 2 shows additional information on liquid hold-up technologies developed and the RPBs investigated in the past and this work.

Tab. 2: Overview of different studies addressing liquid flow observations and liquid hold-up determination in RPBs ($F_{G,i}$ air at p = 1.013 bar and T = 20°C assumed).

	Packing							Operation						
Author	d_i	d_o	h_{rotor}	$L_{packing}$	ε	a_P	Material	n	$\dot{V}_{G,i}$	$\dot{V}_{L,i}$	$F_{G,i}$*	LL_i	Measurement	
	m	m	m	m	-	$m^2\,m^{-3}$		s^{-1}	$m^3\,h^{-1}$	$m^3\,h^{-1}$	$Pa^{0.5}$	$m^3\,m^{-2}\,h^{-1}$	System	comment
Burns, 1996 [55]	0.07	0.32	0.1	0.125	0.95	1500	PVC foam	5 - 20	0	0.659	0	29.96	35 mm camera, strobe light	visual observation
Basic, 1995 [56]	0.062	0.171	0.025	0.054	NN	NN	glass beads	5 - 27	NN	0.873	NN	175.33	conductivity measurements	electrodes top/bottom inner/outer
Burns, 2000 [57]	0.07	0.32	0.01	0.125	0.95	786	PVC foam	4 - 27	46.8	0.684	5.4	311.03	conductivity measurements	electrode pairs inner outer
Yang, 2015 [58]	0.035	0.078	0.02	0.022	0.8	1098	metal foam	8 - 20	0	0.155	0	70.48	X-ray CT	conventional CT
Yang, 2015 [58]	0.042	0.082	0.02	0.020	0.95	497	wire mesh	8 - 20	0	0.155	0	58.74	X-ray CT	conventional CT
This work	0.146	0.45	0.01	0.152	0.92	1000	metal foam	5 - 20	60	0.378	3.32	82.41	gamma-ray CT	angle resolved CT

2.4.3 Operating ranges

From the hydraulic point of view, centrifugal acceleration enables a significant increase in the gas and liquid flow rates. In the field of centrifugation technology, diameters of 3 m and circumferential velocities of 100 m s^{-1} are well established and are already commercially available on the industrial scale [*60*, p. 91]. The given dimensions reach a relative centrifugal force (RCF) of approximately 680. For RPBs the RCFs between 10 and 1000 can be found [*29*, p. 1152]. However, this is not a sharp boundary, and increasing to higher mechanical levels than that found in common centrifuges is imaginable. It can be assumed that for a wide range, the available knowledge from commercial centrifuges is transferable to the construction of RPBs.

The rotational speed, as an additional degree of freedom, determines the allowable throughputs. Based on visual or pressure drop analysis, different authors [*38, 39, 61, 62*] defined minimal rotational speeds as explained in chapter 2.2.1. The complete data, including the determination method and the minimal rotational speeds, can be found in A1.

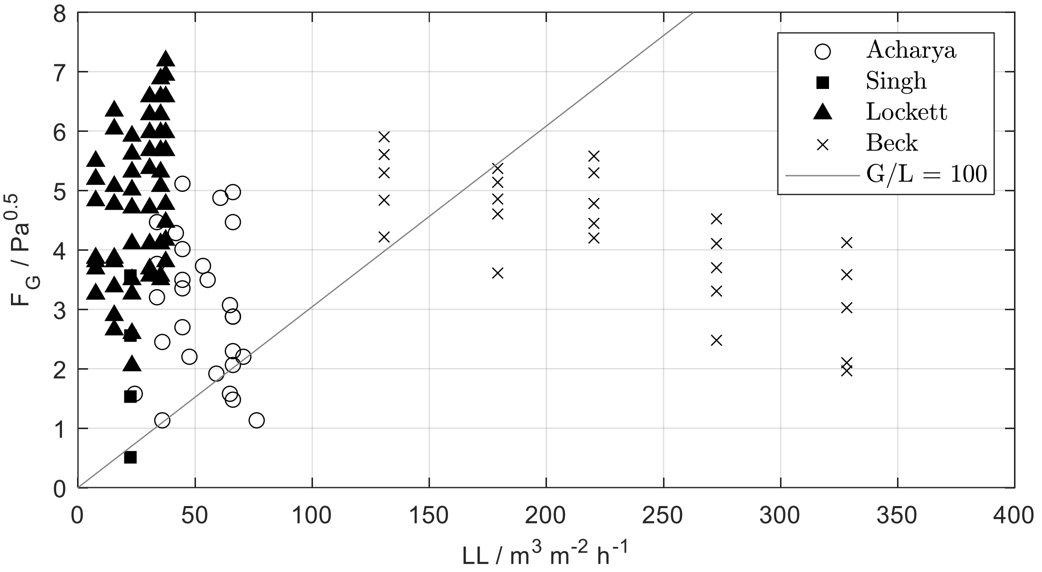

Figure 2.9: Overview of hydrodynamic operating ranges within RPBs [*38, 39, 61, 62*].

From the data, it can be concluded that the majority of the experiments were conducted in a liquid load between 0 and 100 m^3 m^{-2} h^{-1} and an F-factor at an inner diameter below 7 Pa$^{0.5}$. The gas and liquid loads investigated are similar to conventional columns (cf. Figure 2.4). Most of the data was measured for a G/L ratio above 100 m^3 m^{-3}, which is more relevant for distillation and absorption processes. Especially for distillation experiments at $F_{G,i}$ > 7 Pa$^{0.5}$, the data would be of high interest because high gas-flow Reynolds numbers could reduce the gas-side mass transfer limitations. Consequently, knowledge of the minimal rotational speed (n_{min}) is important because operation close to n_{min} allows for high mass transfer efficiency and lower energy costs for rotation.

Data typical for stripping and desorption applications for a wide range of liquid loads and smaller gas loads is limited to *Beck* [*61*], who investigated packing with a_{geo} of 850 m^2m^{-3}. Compared to that of conventional packings (e.g. Mellapack 125 or 250-X) this is a specific surface area that is three to seven times higher. Further information in this operating range would be beneficial for comparison and additional selected experiments at higher gas loads are of interest.

Multiple terms can describe the maximal operating limit in the RPB. Following the conventional notation, it is commonly named the flooding limit [*39*]. Others distinguish between nozzle-induced entrainment, due to liquid outlet velocities from the nozzle that are too low, and gas-induced entrainment by means of frictional forces [*36*, p. 242] and yet others describe the repelling of liquid from the inner support ring as splashing, where no gas is involved and ejection from the packing by gas flow [*29*, p. 1156].

In this work, we assume that the maximal hydraulic operating conditions are determined by liquid entrainment. It is a combination of splashing, ejecting and/or other gas, liquid and packing interactions. To prevent confusion with the flooding phenomena in columns, the term flooding is avoided, and the maximum hydraulic operating limit or entrainment is used.

2.4.4 Deaeration

The following chapter divides into the literature dealing with the industrial scale operation of RPBs for deaeration purposes and into the design investigations, which are usually performed on smaller scale equipment.

Industrial-scale deaeration

Deaeration has shown some promising advantages and multiple industrial-scale applications are known in the literature [*7*]. The stripping process covers a broad field of applications. The most common application is corrosion prevention in boiler or piping systems [*63*]. Others are the extension of shelf life in the food processing industry due a low in-product oxygen concentration [*64*]. Moreover, deaerated water is used for reinjection in oil fields where both aspects, bacteria growth and corrosion, are of major importance [*65*, p. 585]. Tab. 3 gives an overview of the reported industrial-scale case studies. The following paragraphs provide further information.

The deaeration of liquids utilizes two main effects. First, flash degassing employs the temperature dependence of the oxygen solubility. When a superheated liquid is sprayed and partially evaporated, the oxygen solubility is greatly diminished in the boiling liquid and therefore, the oxygen concentration decreases. Other concepts reduce the oxygen partial pressure in the gas phase. This is usually accomplished by additional stripping gases (e.g. N_2 and CO_2) or the reduction of the total pressure by a vacuum pump. The generation of a large interfacial area between the gas and liquid is beneficial for the overall process. Usually, an oxygen content between 0.02 - 0.50 mg L^{-1} (20 to 500 ppb) is considered sufficiently low to prevent bacterial growth and equipment corrosion. The method of choice is process dependent; when heat is readily available hot deaeration is the method of choice, while heat sensitive products require low-temperature and vacuum deaeration. [*7*]

Tab. 3: Overview of the different case studies in the industrial or semi-industrial state [*64–66*].

	Oil industry		Beverage Industry
Authors	Peel [*65*]	Zheng [*66*]	Harbold [*64*]
Rotor			
d_i/m	0.11	0.3	-
d_o/m	0.89	0.6	-
h_{rotor}/m	0.01	0.25	-
V_{rotor}/m^3	0.006	0.053	
Casing			
d_{casing}/m	1	-	-
h_{casing}/m	0.14	-	-
Operation			
Rotation/min^{-1}	200-500	700-1500	-
V_G /$m^3 h^{-1}$	4	100	-
V_L /$m^3 h^{-1}$	1.80	50	34
$F_{G,i}/Pa^{0.5}$	0.35^1	0.13^1	-
$F_{G,int}/Pa^{0.5}$	0.10^1	0.09^1	-
$LL_i/m^3 m^{-2} h^{-1}$	520.9	212.2	-
$LL_{int}/m^3 m^{-2} h^{-1}$	153.6	147.1	-
Concentrations			
$c(O_2)_{in}$/mg L^{-1}	8-12	6-14	-
$c(O_2)_{out}$/mg L^{-1}	0,05 - 0,2	<0,05	<0,5

[1] $F_{G,}$ air at $p = 1.013$ bar and $T = 20$ °C assumed and estimated from drawings

Peel et al. [*65*] investigated the deaeration in an RPB for liquid flow rates up to 1.8 $m^3 h^{-1}$ and gas flow rates up to 4 $m^3 h^{-1}$ in a single stage countercurrent RPB. Nitrogen was used as the stripping gas. The rotor had an outer diameter of 1 m and an axial packing height of 0.01 m. As in the studies of *Burns* and *Ramshaw* [*55*], a rigidized PVC packing (Declon 20/30) was used. From inlet liquid concentrations of 8 to 12 mg L^{-1}, a decrease down to 0.2 mg L^{-1}(200 ppb) was reported. For certain operating parameters, an outlet concentration below 0.05 mg L^{-1} (50 ppb) was achieved. Compared to that of a conventional packed column, a size and weight reduction of 85 % is estimated (38.4 t to 5.5 t). [*67*]

Zheng et al. [*66*] have shown the application of RPBs with a liquid capacity of 10 t h^{-1}, 50 t h^{-1} and 300 t h^{-1}. Natural gas or steam was used as a stripping agent to reduce the residual oxygen content below 0.05 mg L^{-1} (50 ppb). Detailed information for an RPB with liquid flow rates of 50 m^{3} h^{-1} and gas flow rates of 100 m^{3} h^{-1} was given. In a beverage application, *Harbold and Park* [*64*] realized successful commercial implementation. The RPBs manufactured by the company GasTran realized at a vacuum level of 1-2 kPa a residual oxygen concentration between 0.3 mg L^{-1} and 0.5 mg L^{-1} (300-500 ppb) at a reported liquid flow rate of 34 t h^{-1}. In the production line, the removal of oxygen increased the bottling speed through an improved filling level and carbonation control [*64*].

In summary, it can be concluded that based on the evaluation of the literature data, deaeration has been conducted in gas stripping and vacuum applications. The feasibility even on larger scales has been shown. Compared to other gas/liquid processes (e.g. absorption/distillation), the gas load with $F_{G,i} < 1$ Pa$^{0.5}$ is significantly lower. The liquid loads range up to 500 m^{3} m^{-2} h^{-1} (cf. Tab. 3), which is higher than that in columns (cf. Figure 2.4).

Design investigations for deaeration

Multiple researchers have investigated the deaeration of oxygen with stripping gas. Studies on the deaeration of oxygen provide valuable information for the process itself. Moreover, the stripping of oxygen from water is completely limited by the resistance on the liquid side hence results are likely to apply to general gas-liquid contacting processes limited by the liquid-side resistance. *Guo et al.* [*68*] investigated the stripping of oxygen with nitrogen and found that the mass transfer rate increases sharply with increasing rotational speed up to 800 min^{-1} (RCF at the inner diameter: ~75). Additionally, they found a positive effect on the mass transfer rate for packing support rings at the inner diameter with a large free area.

Chen Yu-Shao et al. [*69*] performed a large quantity of research on the stripping of oxygen in RPBs. A viscosity dependent correlation for volumetric mass transfer coefficient (k_La) derived from experimental data with glycerol, and a carboxymethyl cellulose (CMC) solution was proposed and later extended based on an RPB with adjustable inner and outer radius equipped with stainless steel wire mesh. Chen divided the mass transfer contributions into three zones/volumes: the volume of the packing ($V_P = \pi(r_o^2 - r_i^2)h_{packing}$), the volume from the center of the rotor to the inner radius of the packing ($V_i = \pi\, r_i^2\, h_{packing}$) and the volume from the outer radius of the rotor to the casing ($V_o = \pi\left(r_{casing}^2 - r_o^2\right) h_{packing}$) [*70*]. Contributions other than the packing volume are called end effects and need to be considered to avoid an overestimation of the mass transfer coefficients [*70*]. Rotors with a varying inner diameter between 0.02 and 0.10 m and an outer diameter between 0.04 and 0.12 m have been investigated in a stationary casing of 0.15 m. Finally, *Chen et al.* [*71*] derived a second extension for different packing types (e.g. beads, meshes, foams, and random packings). Equation (17) provides the final correlation [*71*].

$$\frac{k_L a\, d_{spherical}}{D\, a_p}\left(1-0.93\frac{V_o}{V_{total}}-1.13\frac{V_i}{V_{total}}\right) = 0.35\, Sc^{0.5}\, Re^{0.17}\, Gr^{0.3}\, We^{0.3}\left(\frac{a_p}{a_{ref}}\right)^{-0.5}\left(\frac{\sigma_c}{\sigma_w}\right)^{0.14} \tag{17}$$

De Beer et al. [*72*] proved the applicability of the correlation from *Chen* for the flash degassing of water without any additional stripping gas within a reasonable error of around 30 %. They investigated a liquid flow rate between $0.8\cdot10^{-4}$ m^3 s^{-1} and $2.8\cdot10^{-4}$ m^3 s^{-1} in a machine with an inner diameter of 0.100 m and 0.130 m and an outer diameter of 0.152 m and 0.154 m and a bed height of 0.050 m. Experimental k_La-values up to 4 s^{-1} have been found, after subtracting an initial flash of the liquid. Recently, *Mello et al.* [*73*] have filed together with Chevron U.S.A Inc. a patent for the deaeration of seawater using a rotating packed bed. They provided data which shows that the RPB reaches a residual oxygen content below 0.05 mg L^{-1} in processes applying stripping gas or vacuum. The deaerated seawater is then injected into a hydrocarbon producing reservoir for enhanced oil recovery purposes. To further increase the performance of the RPB *Chen Qiu-Yun et al.* [*74*] investigated PTFE-packings for high corrosive applications but found no superiority in the mass transfer results compared to conventional stainless steel mesh.

To overcome the limitations of single block packings, split-packings are used, which consist of multiple foam rings that are alternately connected to two independently rotatable rotating plates. *Shivhare et al.* [*75*] compare a single block packing and a split-packing including co- and counter-rotation of the up to four alternating rings. The inner diameter was for all experiments 0.090 m, and the outer diameter was varied up to 0.180 m. For low rotational speed, the split-packing shows a better performance. This performance advance vanishes at a higher rotational speed of 1200 min^{-1} (RCFat the inner diameter: ~145).

The literature survey shows that the industrial-scale application of RPBs is very limited. As a possible reason, the lack of scale-up investigations is identified by reviewing the deaeration literature dealing with the design of RPBs (cf. Tab. 4). As the industrial scale feasibility of RPB technology for deaeration purposes has already been shown, deaeration is a good choice for further design investigations. Moreover, researchers have derived correlations based on small-scale equipment to predict the k_La-value. Chapter 4 thoroughly evaluates the deaeration process in the RPB by investigating co- and counter-current deaeration for multiple internals and at different equipment scales.

Tab. 4: Overview of the deaeration design investigations in RPB.

	Packing						Operation			
Authors	d_i	d_o	$h_{packing}$	ε	a_p	Packing Type	Rotation	$\dot{V}_G$	$\dot{V}_L$	content
	m	m	m	-	$m^2\,m^{-3}$		min^{-1}	$m^3\,h^{-1}$	$m^3\,h^{-1}$	
Guo[68] 2001	0.210	0.350	0.1	0.97	526	stainless steel wire mesh	0 - 1200	1-5	0.5-2	cc[1], influence of packing support ring
Chen Y.-S.[69] 2005	0.020	0.120	0.02	0.95	829	stainless steel wire mesh	600-1500	0.06	0.006-0.054	cc[1], viscous fluids, glycerol solution and CMC[2]-solution
Chen Y.-S.[70] 2005	0.020	0.120	0.02	0.95	829	stainless steel wire mesh	600 - 1500	0.06	0.015-0.049	cc[1], varying radii 0.01 m steps investigated inner outer diameter
Chen Y.-S.[71] 2006	0.020	0.120	0.02	0.31 -0.95	677 - 2074	various	600 - 1800	0.12	0.018-0.061	cc[1], packing size and shape, material and surface properties
Chen Q.Y.[74] 2016	0.080	0.164	0.015	-	1300-4690	PTFE wire mesh	800 - 2400	0.05-0.250	0.018-0.030	cc[1], PTFE packing
Shivare[75] 2013	0.090	0.180	0.028	0.90	1700	metal foam	750 - 1800	0.06	0.360-0.880	cc[1], split packings, single block packings
De Beer[72]	0.100	0.154	0.05	0.92	2975	wire mesh gauze	0 - 5000	-	0.288-1.008	co[3], flash degassing two packing sizes
This work (selection)	0.146	0.200-0.450	0.01	0.92	1000	metal foam	350 - 1500	6.00	0.360-0.961	co[3], variation of packing length lab- and pilot-RPB

[1] counter-current; [2] carboxymethyl cellulose; [3] co-current

3 Hydrodynamic investigations

The following chapters address pressure drop, liquid hold-up, operating limits and power requirements. Correlations for the prediction of the dry pressure drop are provided. Furthermore, an artificial neural network is used to provide estimates for the complex behavior of the wet pressure drop in the entrainment region. The investigations of the local liquid hold-up within the rotating packing by gamma-ray tomography reveal conditions at which maldistribution becomes significant. Operating maps are generated from the pressure drop data for different packing types. Finally, the power requirements based on liquid flow rate and rotational speed are evaluated.

Parts of chapter 3 are published in:

Groß, K.; Neumann, K.; Skiborowski, M.; Górak, A.: Analysing the Operating Limits in High Gravity Equipment, Chem. Eng. Trans., 2018, 69, 661-666, http://doi.org/10.3303/CET1869111

Groß, K.; Bieberle, A.; Gladyszewski, K.; Schubert, M.; Hampel, U.; Skiborowski, M.; Górak, A.: Analysis of Flow Patterns in High-Gravity Equipment Using Gamma-Ray Computed Tomography, CIT, 2019,136(6), 1032-1040, http://doi.org/10.1002/cite.201800085

Groß, K.; Bieberle, A.; Gladyszewski, K.; Schubert, M.; Skiborowski, M.; Hampel, U.; Górak, A.: Evaluation of Liquid Hold-up in a Rotating Packed Bed for High Gravity Fluid Separation using Process-Synchronized Gamma-Ray Computed Tomography, Proceedings of the 9th World Congress on Industrial Process Tomography (2018), pp. 831–838

Neumann, K.; Gladyszewski, K.; Groß, K.; Qammar, H.; Wenzel, D.; Górak, A.; Skiborowski, M.: A guide on the industrial application of rotating packed beds, ChERD, 2018, 134, 443-462, http://doi.org/10.1016/j.cherd.2018.04.024

A detailed overview including student contributions can be found in chapter 11. Scientific advice was given by A. Górak, M. Skiborowski and the corresponding co-authors

3.1 Materials and methods

The RPB used has an inner casing diameter of 0.650 m, the outer rotor diameter corresponds to 0.500 m. Due to spacers that enable an exact distance between the upper and lower rotor plate the maximal outer packing diameter is restricted to 0.460 m. The dimensions were restricted by the maximal casing diameter that could be implemented into the gamma-ray computer tomography scanner. All packings used provide an inner packing diameter of 0.146 m. At the inner packing surface, a packing support ring is installed (cf. Figure 3.1a). This ring enables the exact spacing of rotor plates and secures the position of the packing. It consists of wide rectangular windows and provides a porosity of 90 % which is comparable to the porosity of the packings used. Within the casing, stream breakers are installed to avoid the rotation and to enable a fast draining of the liquid in the casing.

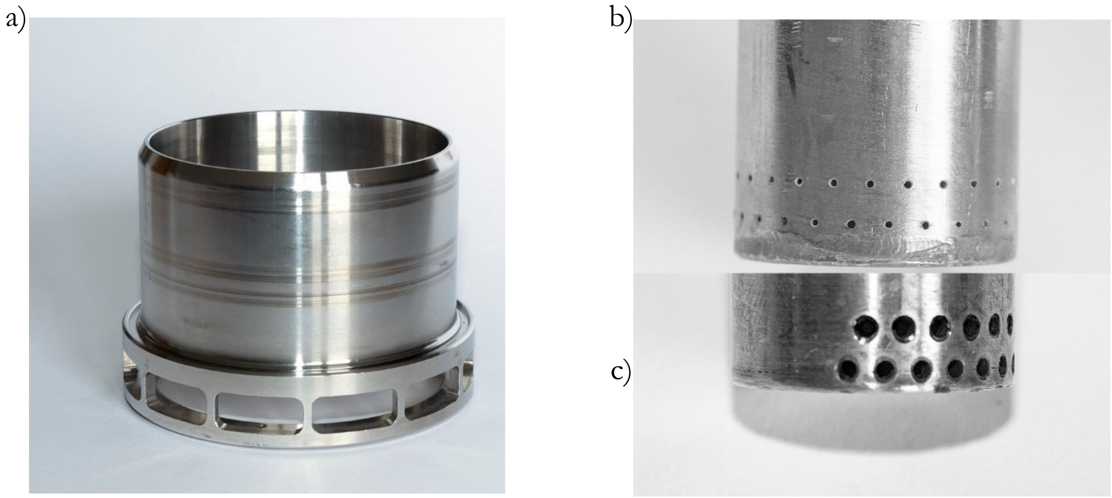

Figure 3.1: a) Packing support ring placed in the center of the rotor b) distributor 360° spraying angle 0.8 mm boreholes 24 holes per row (15°-hole circle division) c) distributor 90° spraying angle 1.6 mm boreholes 13 holes total in two rows (15°-hole circle division). Outer distributor diameter 25 mm.

A pipe-distributor with 0.8 mm boreholes was used to distribute the liquid to the packing surface. The distributor for a 10 mm packing height consisted of two rows with 24 holes each (cf. Figure 3.1b). For 20 mm packings one row of 24 holes was added. To reduce the wetting area a distributor with only 90° spraying angle was used (cf. Figure 3.1c) . The diameter of the holes was adjusted to 1.6 mm to provide the same outlet velocity as the 360° distributor at given flow rate. The packing height was selected based on the envisioned high gas and liquid loads and was restricted by the capacity of the peripheral equipment. Special attention was paid to the correct positioning of the distributor. Poor alignment led to liquid jets hitting the bottom or top rotor plate. Spraying liquid directly at the upper part of the support ring generated significant entrainment. Moreover, the liquid flow rate was always set high enough to avoid the disintegration of liquid jets into droplets before reaching the packing surface. Two types of different packings are used for the hydrodynamic study a dense knitted mesh with a very high specific surface area of 2957 $m^2 m^{-3}$ (cf. Figure 3.2a) and a metal foam packing from RECEMAT® with a specific packing surface area of 1000 $m^2 m^{-3}$ (cf. Figure 3.2b). Further details of the packing are listed in Tab. 5.

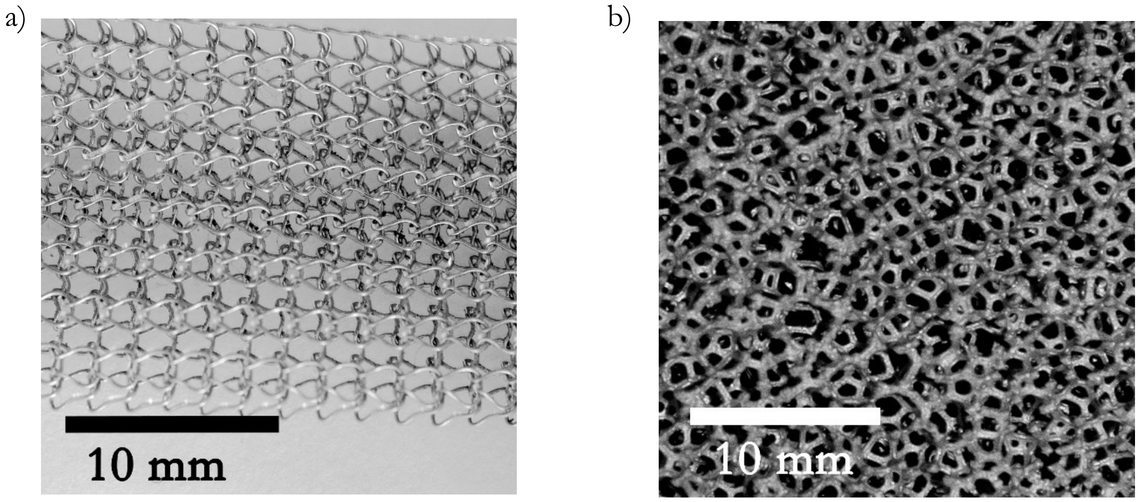

Figure 3.2: Packings used within the hydraulic study a) knitted mesh (KM) b) RECEMAT® NCX 1116 metal foam packing (FF).

Tab. 5: Overview of the packings used for the hydrodynamic study.

Type	RECEMAT® NCX 1116 (FF)	Knitted mesh (KM)
a_p /m^2m^{-3}	1000	2957
ε / -	0.92	0.83
$d_{packing,i}$ /m	0.146	0.146
$d_{packing,o}$ /m	0.450	0.460
$h_{packing}$ /m	0.010-0.020	0.010

The hydraulic experiments were conducted with tap water from the university network. The liquid flow rate was adjusted with a ball valve and measured with a turbine wheel flow meter (DRS-9159I4L4420, Kobold) with a measurement range from 2 to 40 L min^{-1} and an error of ±1.5 % of the end of scale. Compressed air from the university network up to 60 $m^3 h^{-1}$ or ambient air compressed by a radial high pressure blower (Type: HRD 2 T FU-95/1,5, Elektror) was used. The blower is capable of compressing 462 $m^3 h^{-1}$ to up to 8500 Pa. The flow rate was measured with a thermal mass flow meter (KMT-114R10L1NQ4, Kobold) covering a range from 0.32 to 63 $Nm^3 h^{-1}$ with an error of ±1.5 % of the measured value plus ±0.5 % of the end of scale. Higher flow rates were measured by an orifice flow meter provided by Envimac engineering GmbH with an approximated error of ±10 %. An overview of the used equipment can be found in chapter A8.

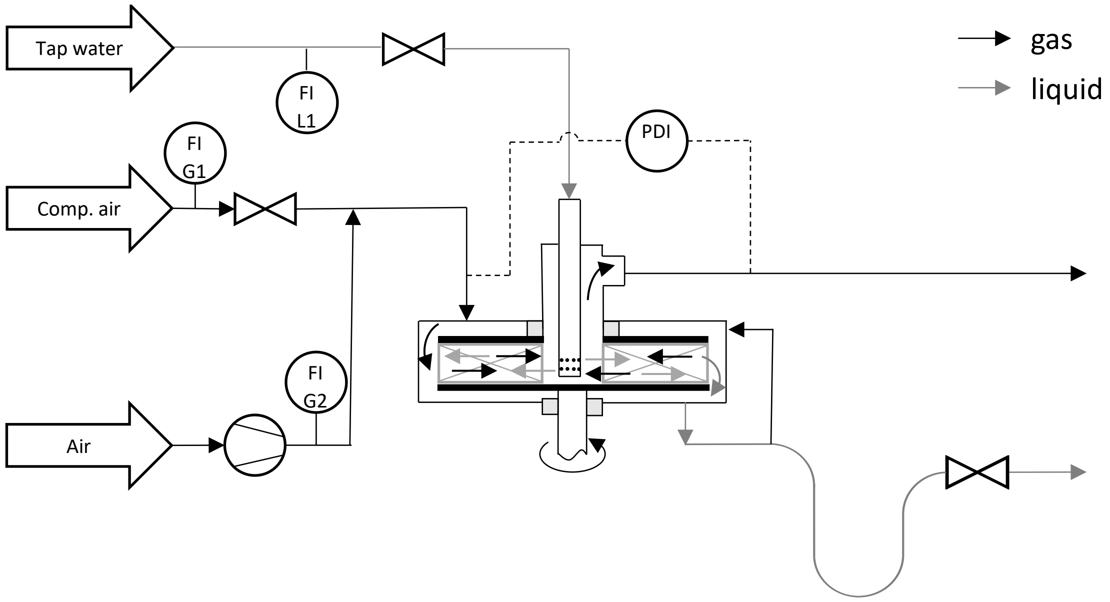

Figure 3.3: RPB setup for hydraulic experiments.

The differential pressure between the gas inlet and outlet was measured with a water-filled U-tube manometer (PDI) connected by PVC hoses. Depending on the height difference in the U-tube the differential pressure could be backcalculated. To avoid entrainment of gas through the liquid outlet, a siphon was installed. The siphon enabled the separation of gas and liquid. The entrained gas in the liquid outlet was fed back to the RPB casing, while the liquid left to the drain. It is important to note that especially close to the maximal hydraulic operating capacity of the RPB, the pressure drop in the machine could reach values above the hydraulic pressure provided by the siphon. This led to an extensive breakthrough of gas in the liquid outlet. Therefore, a valve was installed which allowed adjusting the outflow resistance and liquid level in the outlet. When measuring the pressure drop, the rotational speed was adjusted first. After the rotational speed and pressure drop reached a constant value the liquid flow was increased. The gas flow was started last, to avoid entrainment of droplets onto the sight window at the RPB gas outlet.

3.2 Pressure drop

The pressure drop studies are divided into dry measurements without liquid presence and wet measurements with liquid presence. The prediction of the dry pressure drop is based on a set of equations presented by *Neumann et al.* [*48*]. In this work, the model is extended to wet pressure drop by the application of an artificial neural network which estimates the porosity in the irrigated packing.

3.2.1 Dry pressure drop

As described in 2.4.1, the procedure of *Neumann et al.* [*48*] is based on two fitting parameters, one for the centrifugal head (A_{CH}) and one as a form factor for the dry packing (φ). The parameter A_{CH} was determined from experimental runs without gas and liquid flow. All machine openings were closed, except for the gas outlet. Figure 3.4 illustrates the fitting process, which was performed for KM and FF packing solving a least-square problem. Figure 3.4a shows that the influence of packing height and packing type is relatively small. The KM packing shows a slightly higher centrifugal pressure drop than the FF packing. The quadratic trend proposed by equation (11) is very accurately followed by both packings with deviations of less than 10 %. For lower rotational speeds the relative deviations increase when values close to the accuracy of the pressure drop measurement are reached (20 Pa). Both packings behave similarly to the ideal behavior were the no-slip condition between the gas phase and packing is valid. Therefore, a high centrifugal head constant (A_{CH}) of 0.95 and 0.88 resulted for KM and FF packing, respectively.

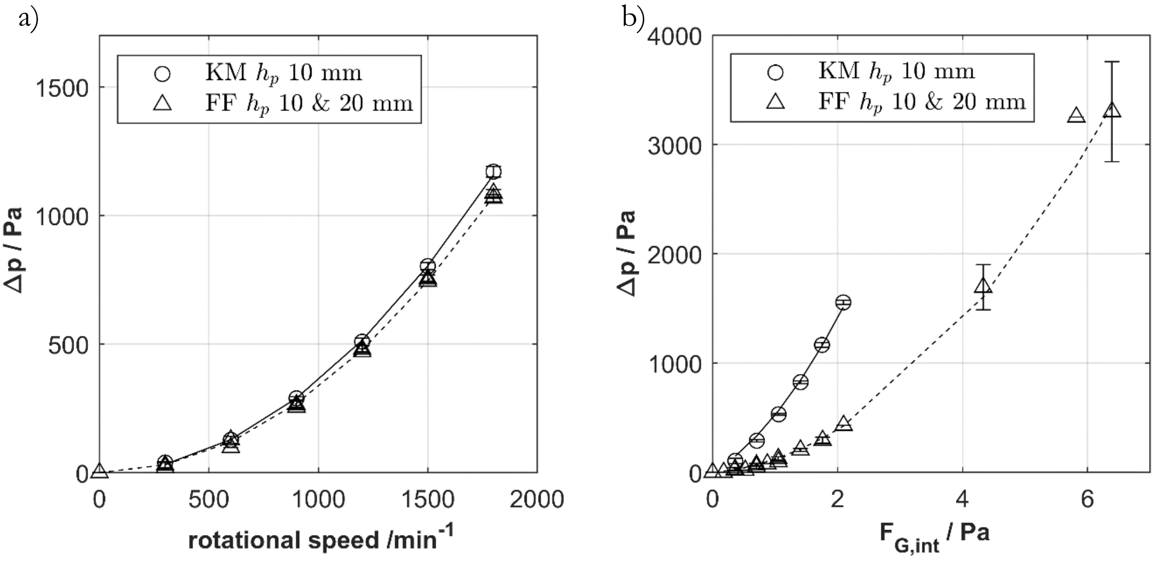

Figure 3.4: Determination of fitting parameters for the dry pressure drop calculations for knitted mesh (KM) and full foam (FF) a) centrifugal head constant (A_{CH}) fitting (KM = 0.95; FF= 0.88), b) fitting of the packing form factor (φ) (KM = 0. 60; FF=0.30), due to a lower data accuracy at higher $\bar{F}_{G,int}$, fitting data was restricted to $\bar{F}_{G,int} < 2.1$. (-) and (--) are corresponding model results. Error bars depict the standard deviation.

Figure 3.4b) illustrates the differences between knitted mesh and metal foam for the gas flow-dependent parameter φ. Equation (12) relates the frictional pressure drop of the packing ($\Delta p_{f,stat}$) and the form factor with the proportionality factor (1-φ). Figuratively speaking, the model assumes parallel channels in the packing. The flow through these channels leads to frictional losses. However, the path length is critical for the pressure drop. If the channels are interconnected as in perforated packings, one can imagine that φ symbolizes the interconnectivity of the channels and consequently a path shortening factor [*49*]. The measured pressure drop for experiments without rotation shows a quadratic dependency for both packing types. Moreover, the KM packing shows that $\bar{F}_{G,int}$ has a stronger influence on the pressure drop, which was expected due to the higher packing surface area and smaller packing porosity. (Tab. 5). The determined constant for the FF packing shows a -6 % deviation compared to the literature data of *Neumann et al.* [*48*] and can even be extrapolated for higher gas flow rates 2.1 $\mathrm{Pa}^{0.5} < \bar{F}_{G,int} < 6.5\ \mathrm{Pa}^{0.5}$.

Certainly, the knitted mesh form factor φ shows larger deviations of 30 %, but this can be accounted to the smaller packing porosity compared to *Neumann et al.* [*48*]. Moreover, the packing surface (a_p) is estimated by calculations from *Blass* [*76*]

$$a_p = \frac{4\,(1-\varepsilon_p)}{d_{wire}} \tag{18}$$

solely based on the wire diameter of the mesh (d_{wire}) and the porosity of the packing (ε_p). Errors and uncertainties in the estimation of a_p (e.g. packing deformation and irregularities of the wire), propagate to the calculation of the spherical diameter of the packing (d_p) and the gas phase Reynolds number $\overline{Re}_{G,int}$ (cf. EQ (14)).

$$d_p = \frac{6\,(1-\varepsilon_p)}{a_p} = \frac{3}{2} d_{wire} \tag{19}$$

Nevertheless, uncertainties in the calculation of a_p can be compensated by the fitting parameter φ if regressed by experimental results as performed in this work (cf. Figure 3.4). After fitting the constants A_{CH} and φ to the experimental results, varying either gas flow or rotation, without the other one being set to zero, the dry-pressure drop model can be used to span an imaginary surface with combinations of varying gas flow rates and rotational speeds. From Figure 3.5a it can be concluded that the model satisfactorily predicts the experimental pressure drop within an error of ±30 %. This is in good agreement with the results from *Neumann et al.* [*48*]. However, Figure 3.5b) shows for the FF packing with h_p of 10 mm that the relative error rises when the rotational speed is increased. The other packings (KM and FF with h_p 20 mm) show a similar behavior which is displayed in appendix A2.

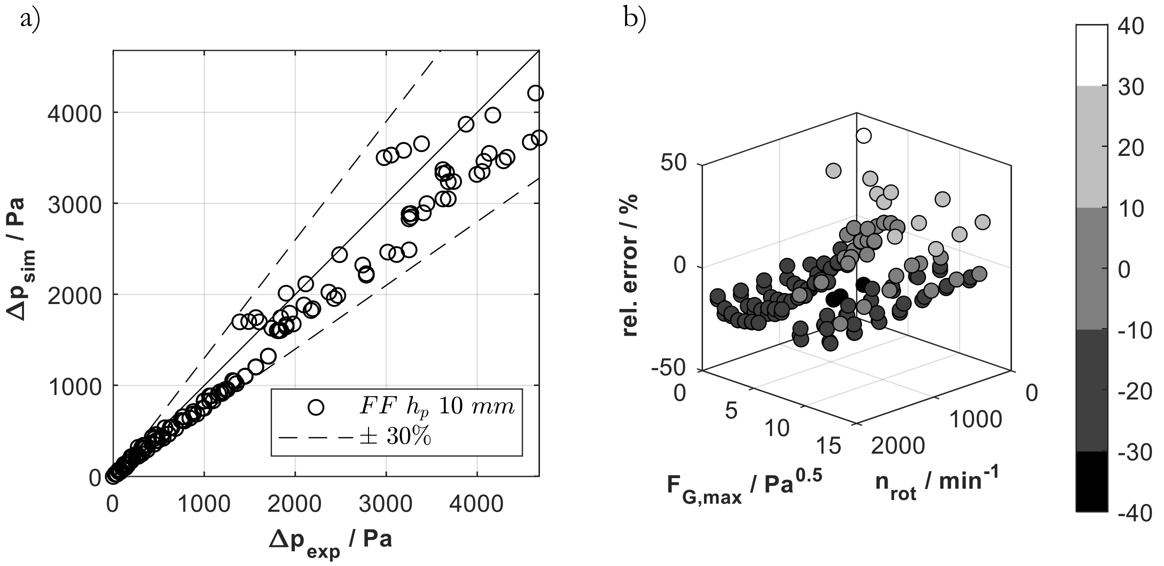

Figure 3.5: a) parity plot for the simulated and the experimental dry pressure drop b) overview of the full foam (FF) data with h_p = 10 mm. (A_{CH} = 0.88; φ=0.30).

To further improve the accuracy of the correlation, the data generated for the knitted mesh and the FF packings were combined. The centrifugal head parameter (A_{CH}) was regressed with the genetic algorithm implemented in MATLAB®R2018a optimization toolbox. The initial population range for the parameter was set between -10 and +10. With a uniformly distributed start generation of 100 individuals an after 100 generations the optimized solution A_{CH}=1.19 was reached. It is emphasized that A_{CH} is usually less than unity, when estimated based on data without gas flow. However, when rotational speed experiments are used where additionally a gas flow was introduced A_{CH} is estimated bigger than unity. This clearly shows that the combination of rotation and gas flow leads to a higher pressure drop than either of the two. It is imaginable that the rotation is causing increased turbulence in the gas phase. In literature values for A_{CH} between 0.5 and 2 have been observed [*53*, p. 388]. Figure 3.6 illustrates the fit of A_{CH} which improves prediction results especially for pressure drops in the range between 500 and 2000 Pa. The underestimation of the correlated pressure drop can be reduced. Approximately 70 % of the results are well predicted between ±10 %. However, larger deviations appear for very low rotational speeds (300 min^{-1}) and low $F_{G,max}$ (< 2 $Pa^{0.5}$). This is reasonable because when fitting the correlation to experimental data that has two dependencies (gas flow, rotational speed) the interaction effects between both get promoted. It is assumed that for low rotational speed and low gas flow rates interdependencies as vortex/eddy formation, which additionally dissipate kinetic energy, are reduced. Consequently, the correlation is overestimating these effects in the mentioned range.

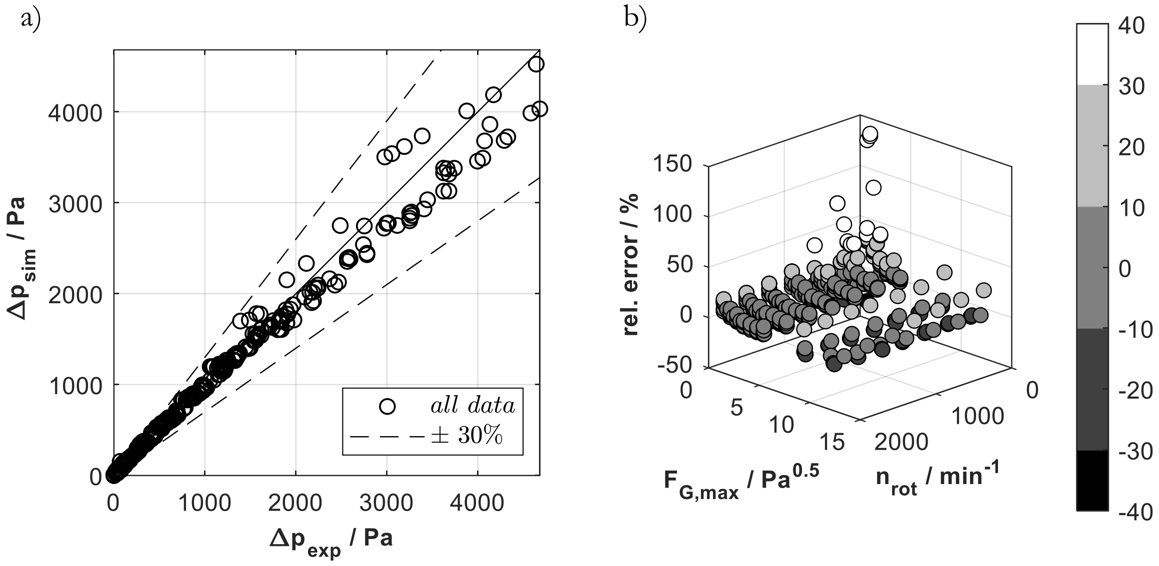

Figure 3.6: a) parity plot for the simulated and the experimental dry pressure drop b) Overview of the FF and KM data with h_p = 10-20 mm. (A_{CH} = 1.19; φ_{FF}= 0.30; φ_{KM} = 0.60).

Finally, the following can be concluded from the dry pressure drop investigations. The dry pressure drop in an RPB can be described by two main effects, the centrifugal head, depending on the rotation, and the frictional pressure drop, depending on the gas flow rate. Both effects can be satisfactorily predicted by the method of *Neumann et al.* [*48*] within an error of ±30 % if two empirical constants are determined. A_{CH} is derived by varying the rotational speed without any gas flow. φ can be obtained from static experiments and the Ergun equation. Experiments with rotational speeds in the range from 300 to 2000 min^{-1} and $F_{G,max}$ between 0 and 12 Pa$^{0.5}$ were evaluated on knitted mesh and FF packings to extend the currently available data significantly. To further increase the estimation accuracy, data originating from combined gas flow/rotational speed-experiments can be used to estimate most of the results with an accuracy of ±10 %, as has been shown in this work.

3.2.2 Wet pressure drop

As described in chapter 2.2.1, the difference between wet and dry pressure drop is small at a high rotational speed. At moderate F-factors ($F_{G,max}$= 2 Pa$^{0.5}$) and liquid loads (LL_{max}) between 80 and 240 m^3 m^{-2} h^{-1} this trend is followed until approximately 600 min^{-1}(cf. Figure 3.7a). Below 600 min^{-1} the FF-packing shows a significant difference between the wet and the dry pressure drop. While the dry pressure drop further decreases with the rotational speed, the wet pressure drop shows a sudden increase. At increased gas loads ($F_{G,max}$= 8 Pa$^{0.5}$) the dry pressure drop is still significant when the rotor is static due to significant frictional losses. The rotational speed at which dry and wet pressure drop deviate shifts to higher rotational speeds and the pressure drop shows an increased dependency on the liquid load.

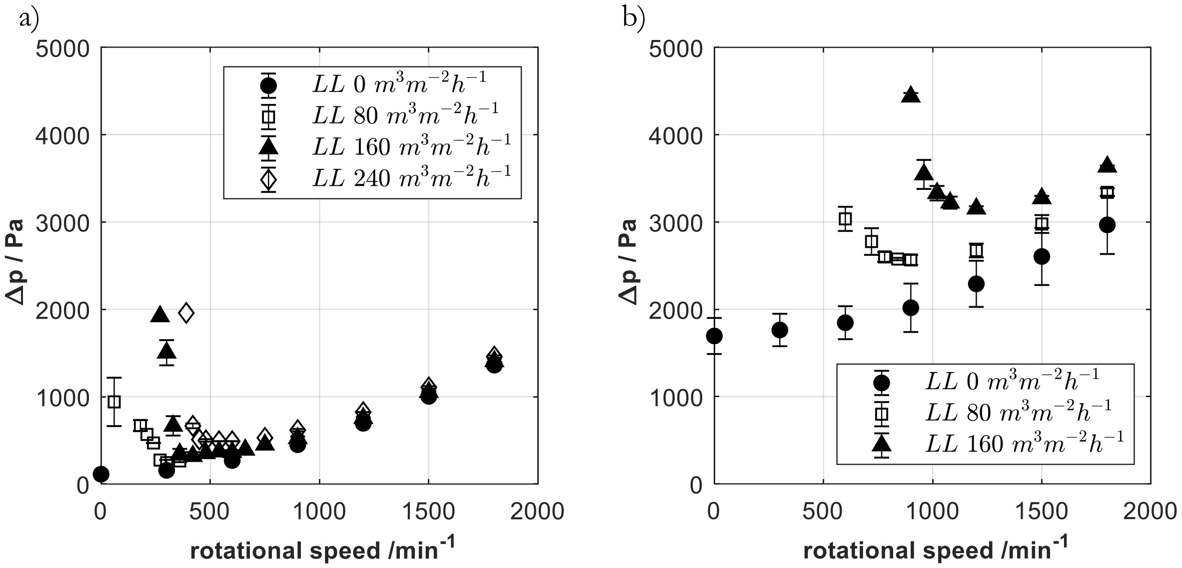

Figure 3.7: Influence of the liquid load on the pressure drop for the full foam (FF) packing $h_p = 10$ and 20 mm. a) $F_{G,max}$ 2 Pa$^{0.5}$ b) $F_{G,max}$ 8 Pa$^{0.5}$. Error bars depict the standard deviation.

The data is further qualitatively analyzed in Figure 3.8. Firstly, it is illustrated that the wet pressure drop is always higher than the dry pressure drop. This is contradictory to some of the findings in the literature [*51*, p. 50][*52*, p. 831], but supports the hypothesis that the liquid increases the resistance for the gas to flow through the packing as described by other authors as *Guo, Lockett* and *Sandilya* [*39*, p. 380, *50*, p. 3855, *53*, p. 387]. Based on the large amount of pressure drop data generated for various packing materials and geometries in this work it is reasonable to assume that the liquid is generally increasing the pressure drop in RPBs with packed internals. Observations other than that might be related to uncharacterized sealing bypass or other structural differences (e.g. gas entrainment through the liquid outlet) and should be handled with caution. However, recently *Neumann* presented that the pressure drop in an unpacked rotor is reduced when liquid is added [*77*, p. 62]. He suspects the reduction through the breaking of vortices in the gas phase by liquid jets, which is reasonable when comparing packed and empty rotors. Secondly, for different gas loads a varying dependency of the liquid flow rate on the pressure drop is observed. At moderate gas loads ($F_{G,max}$= 2 Pa$^{0.5}$), liquid loads between 80 and 240 m^3 m^{-2} h^{-1} and high rotational speed of 1800 min^{-1} the pressure drop difference of the dry and wet measurement is less than 10 % and can be neglected. When the rotational speed is reduced further to 900 min^{-1}, the maximal deviation rises to up to 40 % at a liquid load of 240 m^3 m^{-2} h^{-1}. While at 600 min^{-1} is even higher with 80 % at a liquid load of 240 m^3 m^{-2} h^{-1}.

To avoid underprediction of the pressure drop, the influence of the liquid should be accounted for liquid loads of 240 m^3 m^{-2} h^{-1} and higher, at rotational speeds lower or equal to 900 min^{-1}. For liquid loads of 160 m^3 m^{-2} h^{-1}, at rotational speeds lower or equal to 600 min^1. At low liquid loads of 80 m^3 m^{-2} h^{-1} the pressure drop can be estimated without considering the liquid with a maximal deviation of +15 % in the range between 600 and 1800 min^{-1}.

For high gas loads ($F_{G,max}$= 8 Pa$^{0.5}$) and liquid loads (LL_{max}) between 0 and 160 m^3 m^{-2} h^{-1} the corresponding pressure drop is illustrated in Figure 3.8b. For all measurements, a significant influence of the liquid load on the pressure drop can be observed. At a rotational speed of 1800 min^{-1} the deviation between wet and dry pressure drop is approximately 20 %. Furthermore, the pressure drop is increasing extremely fast if the rotational speed decreases. For a rotational speed of 900 min^{-1} at a liquid load of 160 m^3 m^{-2} h^{-1} the pressure drop is more than twice as high as for the dry pressure drop at an equivalent rotational speed. It is not possible to reduce the rotational speed further because 600 min^{-1} is to close to the operating limit of the machine.

The following guidelines can be concluded from wet pressure drop data. The RPB is capable of operating at liquid loads (LL_{max}) of up to 240 m^3 m^{-2} h^{-1}. The gas load ($F_{G,max}$) can simultaneously be increased to up to 8 Pa$^{0.5}$. However, the liquid is heavily influencing the measured pressure drop. The increase of the pressure drop by the liquid can be compensated by an increased rotational speed. At the maximal investigated liquid load the wet pressure drop is approximately 20 % higher than the dry pressure drop which was 3000 Pa at a radial packing length of 0.157 m and a rotational speed of 1800 min^{-1}.

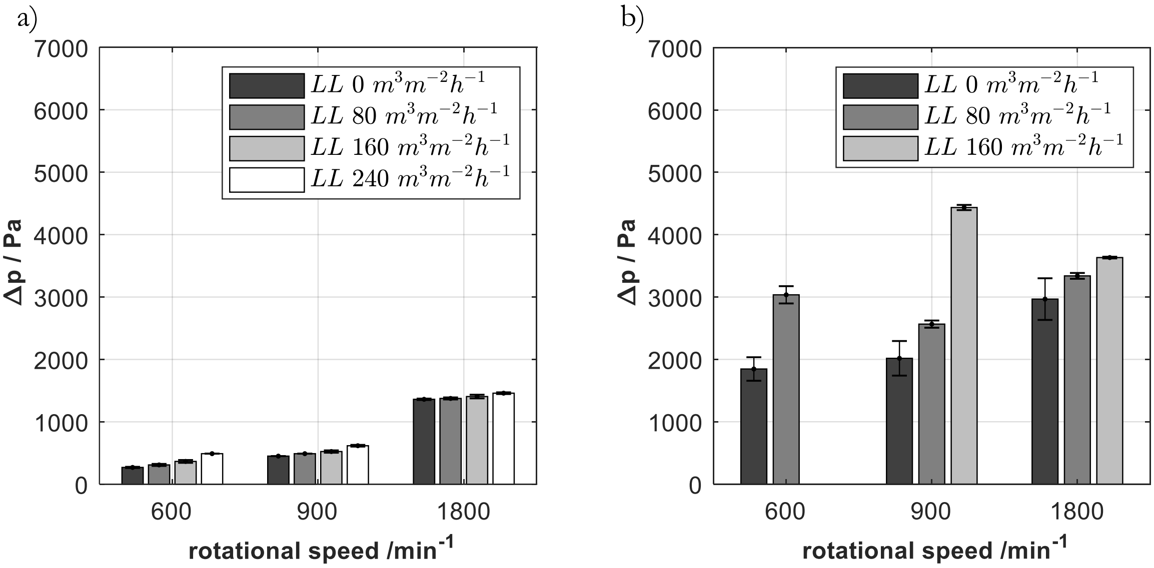

Figure 3.8: Influence of the liquid load on the pressure drop for the full foam (FF) packing h_p = 10 mm and 20 mm. a) $F_{G,max}$ 2 Pa$^{0.5}$ b) $F_{G,max}$ 8 Pa$^{0.5}$.

3.2.3 Prediction of wet pressure drop

As shown in chapter 3.2.2 for many process parameters and high rotational speeds (1800 min^{-1}) wet and dry pressure drop do not significantly differ. If the accuracy of ±20 % is sufficient liquid influences can be neglected. However, at high gas loads, high liquid loads or low rotational speeds close to the maximal hydraulic operating capacity, the pressure drop predictions need to be corrected for the liquid influence (cf. Figure 3.8). Based on the data presented in 3.2.1 and the model assumptions in 2.4.1 it was shown that the dry pressure drop depends on two main contributions, the centrifugal head pressure drop (ξ_{CH}) arising from rotor rotation and the frictional pressure drop ($\Delta p_{f,stat}$) resulting from the gas flow through the porous packing (20).

$$\Delta p_{total,dry} = \xi_{CH} + \Delta p_{f,stat} \tag{20}$$

To extend the model to wet pressure drop a liquid load independent centrifugal head is assumed. Figure 3.9 illustrates that for the experimental data this is a good assumption. The pressure drop is increasing slightly with the liquid load by approximately 0.29 Pa per $m^3\,m^{-2}\,h^{-1}$ liquid.

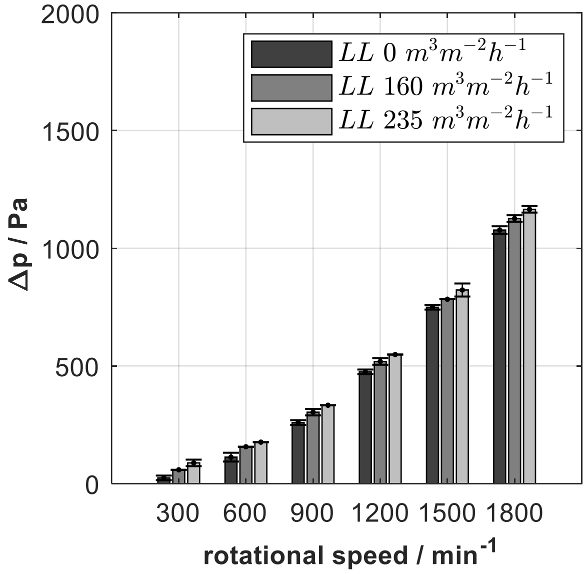

Figure 3.9: Dependency of liquid load on the centrifugal head (ξ_{CH}), $F_{G,max}$= 0 $\text{Pa}^{0.5}$. Error bars depict the standard deviation.

By assuming that the liquid load is changing the porosity, the influence of the liquid load on the pressure drop is incorporated in equation (12). When the liquid is distributed in the porous metal foam packing it is closing some of the pores and decreases the free volume by forming a liquid film on the packing. This leads to a smaller cross-sectional area for the gas to pass through.

$$\Delta p_{total,wet} = \xi_{CH} + \Delta p_{f,stat}\ (\varepsilon) \tag{21}$$

$$\text{with } \varepsilon = \varepsilon_{packing} - \varepsilon_{L,sim}$$

The estimated wet pressure drop was fitted to the experimental pressure drop data by varying ε with the *fsolve* algorithm from MATLAB®. All other model parameters were taken from the previously presented pressure drop model (cf. 3.2.1). The liquid distribution and its influence on the pressure drop are of complex nature. The data on hydraulic interactions within the packing is limited. There are no physical models that accurately describe the two-phase behavior within the RPB. To compensate the lack of physical models an artificial neural network (ANN) was used to predict the variation of ε. It is based on an existing framework developed by *Kruber* and *Miroschnitschenko* at the Laboratory of Fluid Separations for the MATLAB® Deep Learning Toolbox. ANNs provide a fast and straight forward function approximation. They do not require detailed knowledge of the hydraulic processes. This is a great advantage because knowledge about gas-liquid interaction in RPBs is currently very limited. Besides experimental efforts on the characterization of liquid flow and liquid hold-up (cf. 2.4.2) [*58, 59*] or pressure measurements within the rotating packing [*54*], recently computational fluid dynamics (CFD) get further implemented to investigate RPBs [*78, 79*]. However, the validation of such CFD-models is challenging and calculations can be very time-consuming. Additionally, at the current stage, neither of these methods provides sufficient data and accuracy, especially in the region close to the maximal hydraulic operating capacity, where the liquid hold-up rises significantly and entrainment occurs. The ANN provides an experimentally validated base for pressure drop approximation and can be used in process optimizations and cost evaluations. For the training phase the number of hidden neurons was varied between 1 and 20. For each run the training of the network was performed 30 times to reduce stochastical variations. As inputs the liquid load, the F-factor and the rotational speed were selected. The data was divided into a training set (80 %) and a test set (20 %). The data set was reduced to FF data with increased gas flow rate to provide a high enough accuracy. Data with predicted centrifugal head bigger than the total pressure drop was removed because it would produce unreasonable high porosities bigger than 1. This deviation occurs at small process parameters for (LL, F_G and n). Moreover, data with a pressure drop < 50 Pa was removed because it is close to the accuracy of the pressure drop measurement (~20 Pa). Bayesian regularization backpropagation was used. The normalized root mean square error (NRMSE) was selected as the cost function to evaluate the performance of the network (22). NRMSE relates the root mean square error with the observed range of the calculated targets corresponding to the pressure drop range.

$$NRMSE = \frac{RMSE}{y_{max} - y_{min}} \tag{22}$$

The network with 16 neurons performed best based on the NRMSE (cf. Figure 3.10a). The resulting network was used to estimate the porosity of the packing (ε) when liquid was present. The adjusted porosity was transferred to the pressure drop model (cf. Figure 3.10b). The estimated pressure drop fits well with a deviation of ±30 %. The developed and validated model can further be used for the calculation of pressure drop in simulations or the evaluation of operating boundaries based on strong pressure increase close to the maximal hydraulic operating capacity.

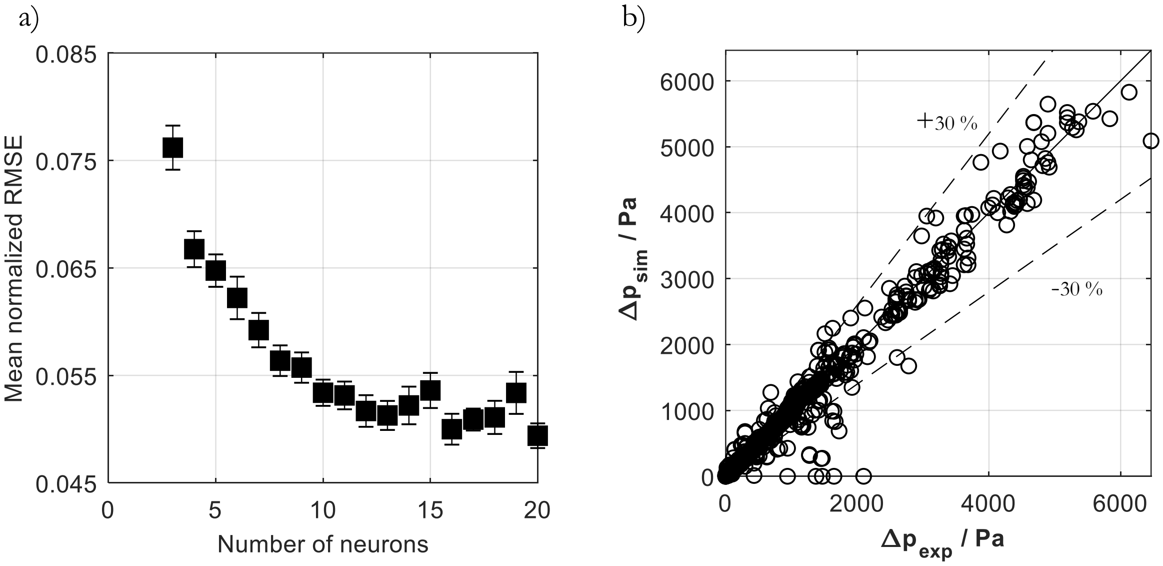

Figure 3.10: a) Development of the normalized root mean square error for a different amount of neurons b) Parity plot estimated pressure drop for the full foam (FF) data. Error bars depict the standard deviation.

3.2.4 Pressure drop in co-current operation

The co-current pressure drop is generally of smaller importance. The reason is that flow and the centrifugal force point in the same direction. The centrifugal head created by the rotation reduces the pressure drop. This circumstance makes pressure drop control easy because the rotational speed can be increased to reduce the pressure drop in co-current operation. Figure 3.11. illustrates this behavior. The pressure drop without any gas flow starts at zero when increasing the rotational speed a negative pressure drop (pressure gain) is found from the inner to the outer diameter. When no gas flow is present the liquid flow rate has no additional impact on the pressure drop for LL_{max} up to 235 $m^3 m^{-2} h^{-1}$. At an $F_{G,max}$ of 4 $Pa^{0.5}$ the dependency of rotational speed and pressure drop becomes evident. The moderate rotational speed of 600 min^{-1} allows reducing the pressure drop below 1000 Pa. The pressure drop vanishes at rotational speeds of 1500 min^{-1}. For the co-current deaeration case study (cf. 4.3) the pressure drop has no significance because only pressure gains are observed for a low $F_{G,max}$ of 0.4 Pa. However, if in other cases stripping gas is available only at low pressure levels, the co-current operation of an RPB can eliminate the additional blower if a pressure gain of around 1000 Pa is sufficient.

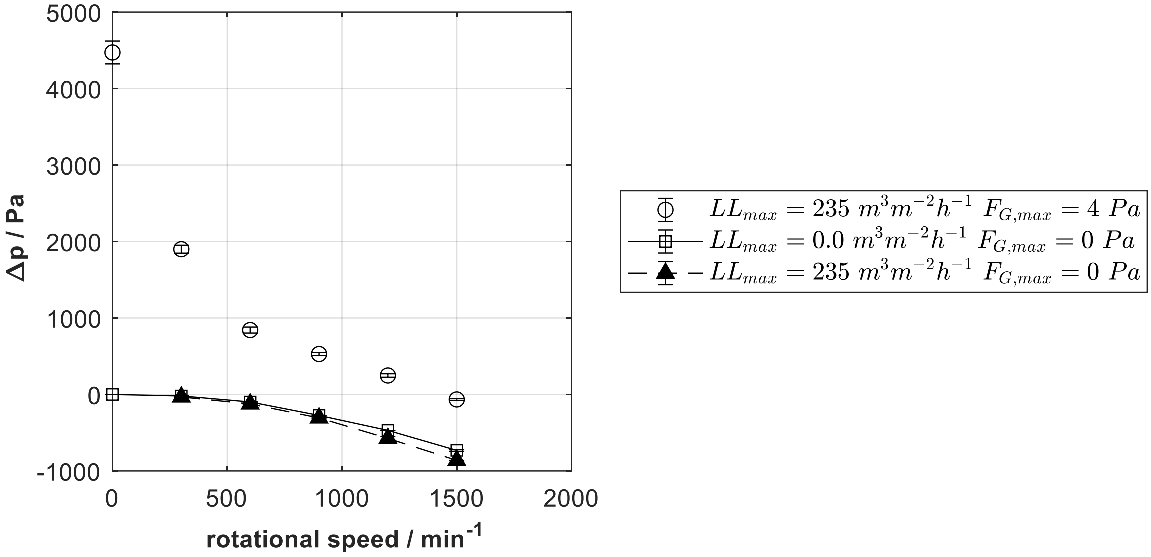

Figure 3.11: Influence of liquid and gas flow rate on the co-current pressure drop for a metal foam packing (d_i, d_o, h_p / 0.146 m, 0.450m, 0.01 m) a_p = 1000 $m^2 m^{-3}$. Error bars depict the standard deviation.

3.3 Liquid hold-up

As introduced in chapter 2.4.2 a variety of methods has been applied to investigate the liquid hold-up in rotating packed beds. Until today, computed tomography is the most advanced technology applied. The non-intrusive technology allows investigating the liquid hold-up without making any changes to the RPB itself. The resolution (approximately 0.5 mm) of the experimental results is much more detailed than probes in the packing could provide. However, the energy of the radiation source is determining the allowable material type and thickness. In case of dense materials (e.g. stainless steel) high-energetic gamma radiation is superior compared to X-ray radiation. This chapter presents for the first time liquid hold-up measurements in RPBs applying gamma-ray CT. The new application of the angle-resolved scanning method enables specific insights into the liquid behavior within the rotating packing.

Parts of chapter 3.3 are published in:

Groß, K.; Bieberle, A.; Gladyszewski, K.; Schubert, M.; Hampel, U.; Skiborowski, M.; Górak, A.: Analysis of Flow Patterns in High-Gravity Equipment Using Gamma-Ray Computed Tomography, CIT, 2019,136(6), 1032-1040, http://doi.org/10.1002/cite.201800085

The section Gamma-ray CT setup in chapter 3.3.1 results from the main contribution of the CT-experts A. Bieberle and M. Schubert. This part was drafted by the named experts and then reviewed and revised by all authors of the above-named publication.

3.3.1 Materials and methods

The following section provides details for the RPB-system and the CT-system. The experimental procedure is described and additional information on the CT-procedures is supplied.

RPB setup

The RPB consists of a rotor with an outer diameter of 500 mm, which was operated at rotational speeds up to 20 s^{-1}. The inner casing diameter is 650 mm. A RECEMAT® B.V. nickel-chromium foam NCX1116 was used as ring-shaped packing with an inner diameter of 146 mm, an outer diameter of 450 mm and a height of 10 mm (cf. Figure 3.12a). Due to the installed spacers at the outer diameter the packing cannot be extended further to the outer rim of the rotor. Porosity and specific surface area are 92 % and 1000 $m^2 m^{-3}$, respectively, provided by the manufacturer. Additionally, the same foam type was used as a segmented version consisting of 5 nestable rings with increasing radii (cf. Figure 3.12b). The free space between the rings was less than 1 mm, hence the influence on the liquid distribution was expected to be small. A single point injector with one 3.2 mm diameter hole was used to generate a single full jet wetting of the packing at a small dedicated area at the inner diameter. In addition, a multi-point distributor consisting of two rows, each equipped with 24 equidistantly distributed holes of 0.8 mm, was used to ensure a homogeneous liquid distribution and wetting of the inner front face of the rotating packing. [*59*]

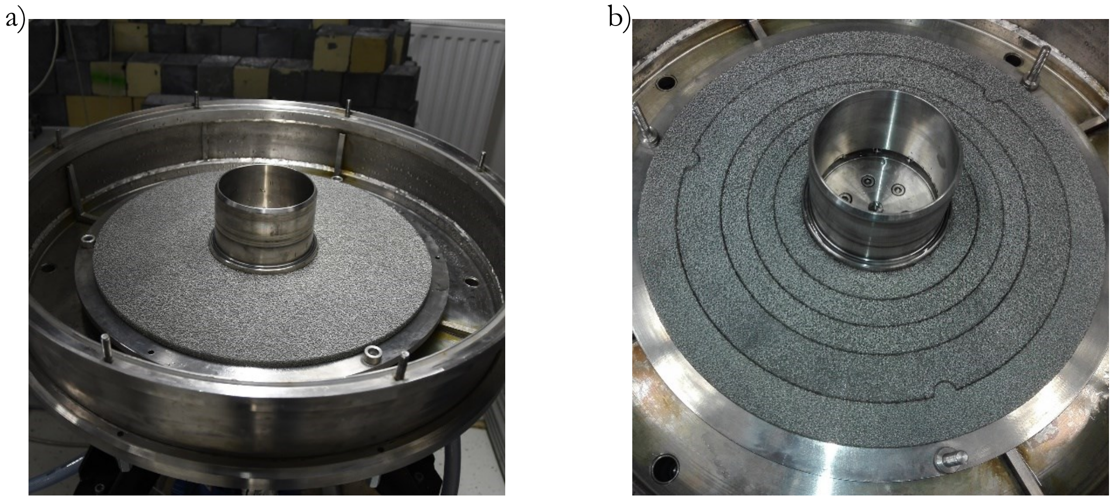

Figure 3.12: a) Full foam packing (FF) b) Segmented ring foam packing consisting of five nestable rings (d_{rotor} 500 mm, $d_{packing}$ 450 mm)

For the hydrodynamic experiments tap water was used. The liquid flow rate was adjusted manually via a ball valve and measured with a turbine wheel flow meter (DRS-9159I4L4420, Kobold) with a measurement range from 2 to 40 L min^{-1} and an error of ±1.5 % of the full scale. Compressed air was used as the gas phase and adjusted manually via a needle valve. The gas flow rate was measured with a thermal mass flowmeter (KMT-114R10L1NQ4, Kobold) covering a range from 0.32 to 63 $Nm^3\,h^{-1}$ with an error of ±1.5 % of the measured value plus ±0.5 % of the full scale. The differential pressure between gas inlet and outlet was measured with a water-filled U-tube manometer. All experiments were conducted at ambient operating conditions. The experimental runs were started by increasing the rotational speed to the desired set point followed by successively adjusting the liquid and gas flow rates to the targeted values. After several minutes (many times longer than the short liquid residence time) steady state was assumed [*51*]. Between each experimental run, the packing was drained at a high rotational speed of 20 s^{-1} for 10 min to avoid liquid accumulation by the transition from high to low rotational speed or vice versa. [*59*]

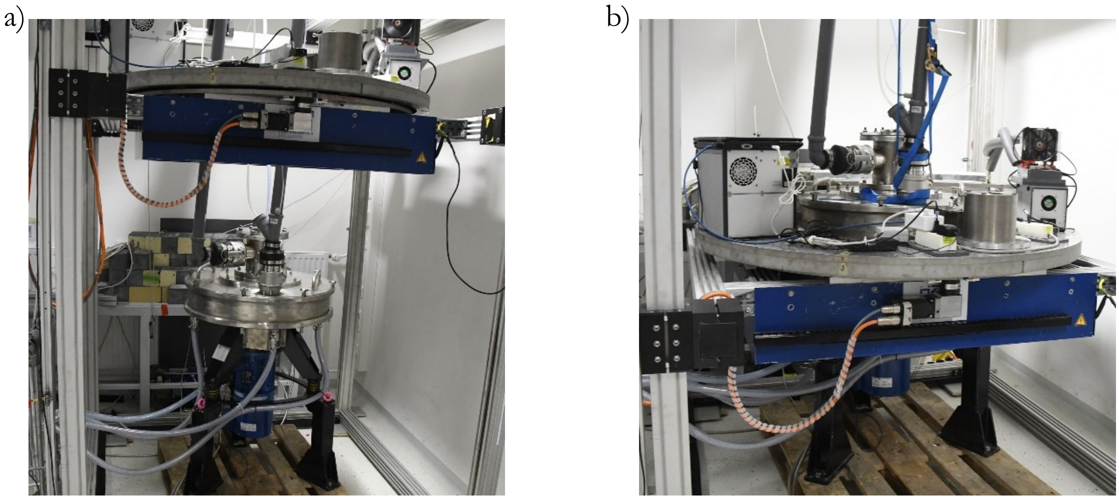

Figure 3.13: a) Installation position: CT unit lifted, RPB accessible b) Measurement position, CT unit aligned with the packing height of the RPB, CT rotates around the RPB.

Gamma-ray CT setup

A rotary lifting unit enables an angular and height change of the movable source-detector assembly (cf. Figure 3.13). Figure 3.14a displays the arrangement of RPB and gamma-ray CT setup. The CT setup consists of a radiation source directed at the RPB and a radiation detector on the opposite side of the RPB. The detectors measure the residual radiation penetrating the object. For a complete CT-scan the projection data must be required from different angular positions of the RPB. The gamma-ray CT comprises a Cs^{137} isotopic source and a radiation detector arc which contains 320 scintillation detector pixels. Both radiation fan and detector arc are collimated to 1 mm height. For more detailed technical information refer to *Hampel et al.* [*80*] and *Bieberle et al.* [*81*]. Based on the Beer-Lamberts law the radiation attenuation

$$E = \ln\left(\frac{I_0}{I_x}\right) \tag{23}$$

is calculated for each ray between source and detector using the radiation intensity behind the object (I_x) and the initial radiation intensity (I_0). The raw data consists of a data matrix with one attenuation value per detector element and angular position of the scanner. Reconstruction algorithms process the data for the calculation of the cross-sectional images of the RPB. The CT scanner enables two different scanning modes namely conventional CT (*conv*CT) and time-averaged angle-resolved CT (*tarCT)* as firstly introduced by *Prasser et al.* [*82*]. In the *conv*CT mode the scanner rotates slowly around the RPB with a frequency of $f^{scanner}$= 0.04 min^{-1} (corresponding to a measuring duration of 25 min) and acquires integral projections i from N_i= 1000 equidistantly distributed positions. Reconstructed images of *Conv*CT raw data represent displays static objects sharp (e.g. RPB housing, flow breakers (10) and stationary located liquid phases, while all rotating parts of the RPB appear motion-blurred (cf. Figure 3.14.b).

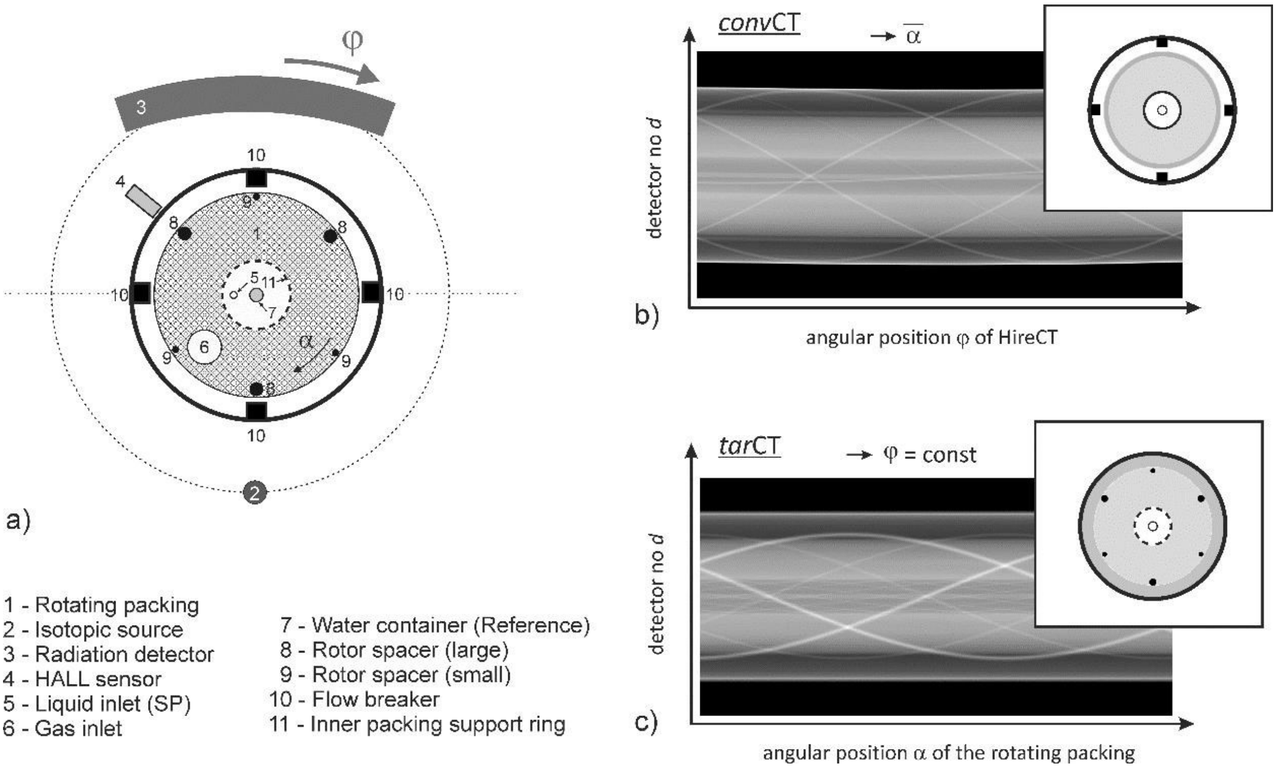

Figure 3.14: a) Principle of CT and RPB setup and sketch of b) conventional and c) time-averaged angle-resolved CT scanning mode with illustrations of the reconstructed images [*59*]. (Reuse with permission of John Wiley and Sons).

The *tar*CT method enables a sharp reconstruction of moving parts. In the imaging process the CT system is over-sampled with a frequency of f^{samp} = 22 kHz [*83*]. At each projection i of the CT scanner,

$$N_j = \frac{f^{samp}}{f^{RPB}} \tag{24}$$

projections per revolution of the RPB are acquired for approximately

$$N_r = \frac{f^{RPB}}{f^{scanner} \cdot N_i} \tag{25}$$

revolutions. For the synchronization of rotations of packed bed and CT system, a Hall effect sensor (Geartooth Speed Sensor, GS100701) with short response time (installed close to the driving shaft on which a small protruding screw is installed as a signal inducer) is used providing a zero-crossing signal. As the photon statistic for a single revolution is not sufficient to reconstruct a tomographic image, all N_r projection data matrices from every CT position i are summed. All rotating parts, such as the rotor spacers, inner packing support ring, the rotating packed bed as well as the liquid phase that rotates with the same rotational speed as the packed bed, are sharply visualized, while static parts appear smeared as shown in Figure 3.14c. [*59*]

To reconstruct corresponding slice images the simultaneous iterative reconstruction technique (SIRT) is applied with 50 iteration steps using the open-source CT reconstruction tool ASTRA v1.8 [*84–86*] in GNU Octave v4.2.1. The reconstruction grid contains 1440 ·1440 pixels (x·y) with a pixel size of 0.5 mm. The obtained projection matrix is interpolated to a parallel beam sinogram with 1840 virtual detector elements and 1600 virtual projections for a 180° rotation. While slice images containing of all materials contributions (packed bed, housing, fluid phases, shaft, etc.) are reconstructed with a reference scan $I_0(d)$ without object, the liquid phase fraction distribution is obtained using an additional reference scan $I_{dry}(d)$ of the dry RPB (no liquid content in the packed bed). To quantify the liquid phase fraction, a liquid-filled reference body (water container) placed in the center of the packed bed (7), provides the reference value for the 100 % liquid fraction. [*59*]

3.3.2 Dry scans / reference scans

Dry scans without any liquid present in the rotor display the solid material distribution in the machine. Hence, they are useful for packing porosity is determination. The determined porosity data lies between 88 % and 89 % percent, this is in reasonable agreement with the porosity value provided by the manufacturer (92 %). [*59*]

As illustrated in Figure 3.14, *conv*CT and *tar*CT are providing different insights. Figure 3.15a) shows that the c*onv*CT is providing data for a sharp reconstruction of static objects (e.g. flow breakers or liquid distributor). The *conv*CT is not suitable to sharply visualize the rotating parts within the machine. While due to the additional information from the Hall-effect sensor in the *tar*CT measurements the reconstruction algorithm can be adjusted. The *tar*CT enables to analyze the rotating elements of the RPB in more detail. Rotor spacers and the geometry of the inner support ring are clearly identifiable. The advantage of sharp rotating internals is more relevant in the liquid hold-up analysis. However, the evaluation of the *tar*CT result in the dry state can be used for validation purposes, since the geometry of the rotor and its internals are known. Both methods provide the same averaged porosity for the packing and Figure 10.4 shows that the radially averaged porosity is additionally just fluctuating by mere percents. If packings not as rigid as metal foam packings would be used, an asymmetric deformation in certain areas of the rotor could only be visualized in the *tar*CT mode. Further advantages of the *tar*CT will be explained in the following chapters.

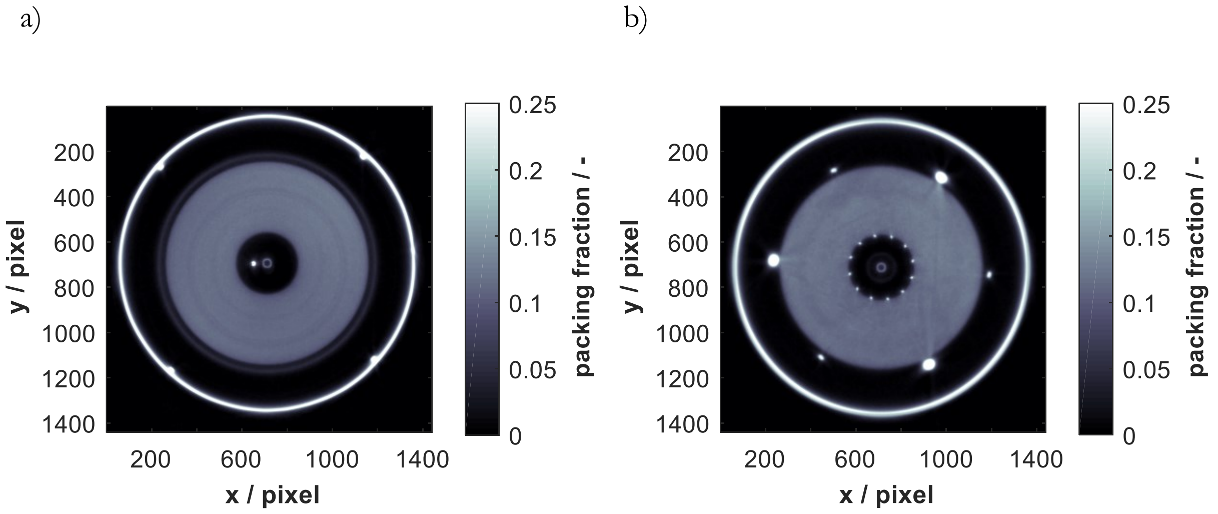

Figure 3.15: Dry reference scan: 1200 min^{-1} full foam (FF) a) *conv*CT b) *tar*CT for the FF packing, the single-point distributor and centered water container.

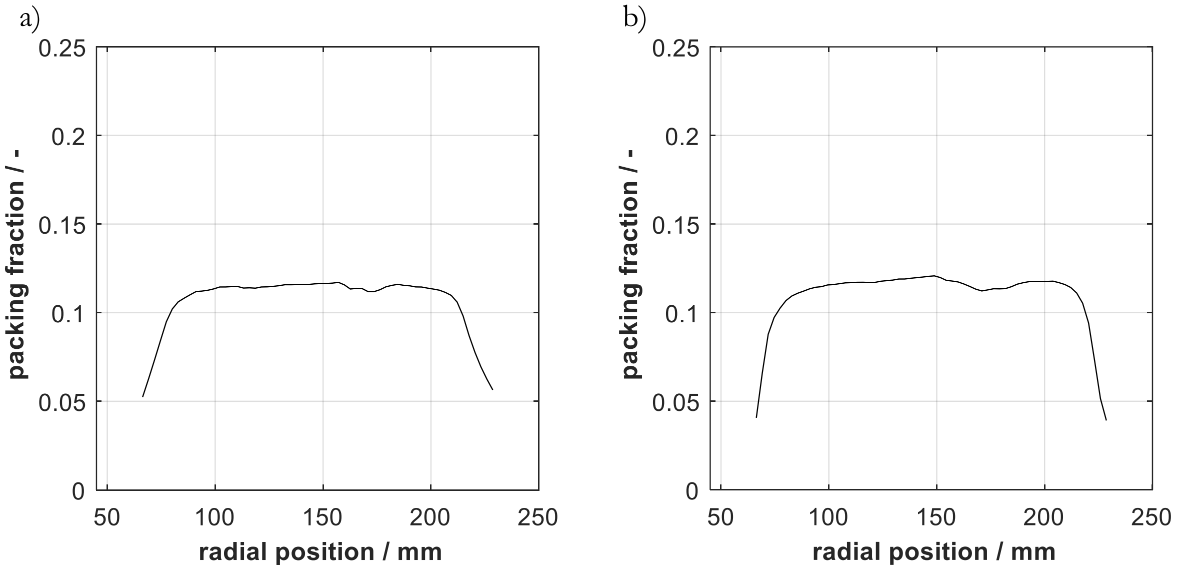

Figure 3.16: Dry reference scan: 1200 min^{-1} full foam (FF) a) *conv*CT b) *tar*CT.

3.3.3 Liquid hold-up measurements

In industrial practice, the liquid distribution within RPBs is extremely relevant. The distribution dictates the available interfacial area for gas-liquid or liquid-liquid mass transfer, leading to high efficiencies. Moreover, the generation of thin films reduces the mass transfer resistance, increasing the mass transfer coefficient (k_La). An initial inhomogeneous distribution or a developing maldistribution along the radial packing direction will inevitably reduce the performance of the equipment. In the following chapters the influence of several process parameters on the liquid hold-up will be investigated. Furthermore, the advantages of each, the *conv*CT and *tar*CT method, will be further elucidated.

Effect of the initial liquid distribution

To analyze the effect of the initial liquid distribution on the evolving flow pattern, a single point (1x3.2 mm hole) distributor and a multi-point distributor (48x0.8 mm holes) were applied. The nozzle diameters were selected to ensure a full liquid jet and to avoid break up before reaching the inner packing surface. This results in a different outlet velocity of the liquid jet for both nozzles. Applying the continuity equation, the liquid velocity through the holes of the multi-point distributor is approx. 4.5 m s^{-1}, while it is three times higher for the single nozzle. However, it is expected that the jet spreads more within the packing at higher liquid velocity due to the high loss of momentum when impacting on the rotating packing. As a consequence, the higher the liquid velocity the better the performance of the single point distributor. Figure 3.17 shows the flow patterns reconstructed for the configuration with a single point and multi-point distributor. The *conv*CT scanning mode was used to visualize the different static liquid impinging areas sharply. For the single point distributor, the liquid jet is dragged on a spiral trajectory following the rotational path of the packing. The flow pattern evolving from the multi-point distributor is a superposition of 48 overlapping single jets, which accordingly homogenize the liquid distribution. The average liquid hold-up in the packing increases slightly from 15.5 % to 16.8 %. [*59*]

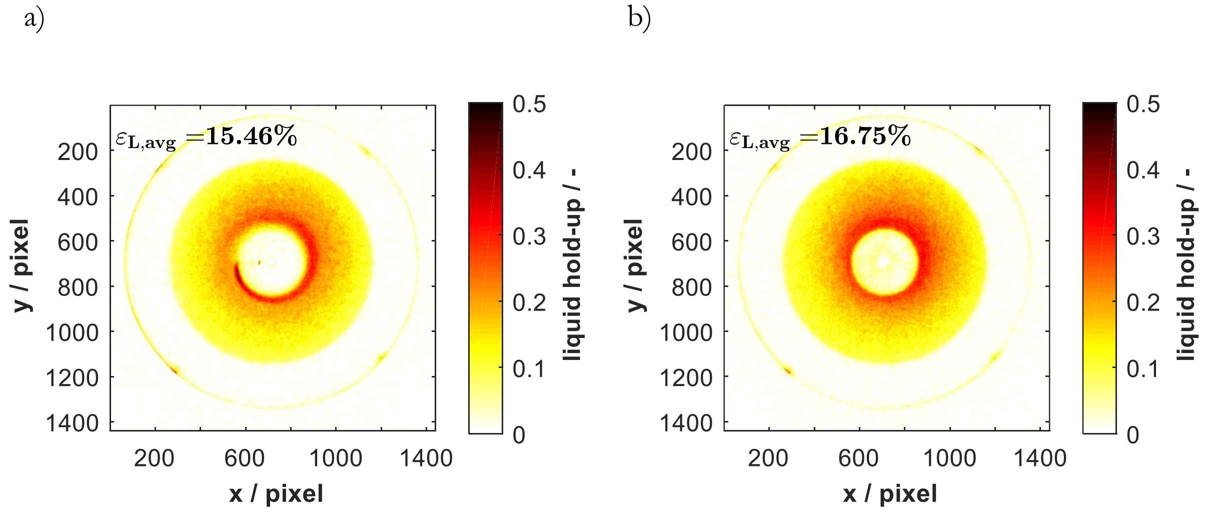

Figure 3.17: Comparison of flow patterns evolving from a) single-point and b) multi-point distributor at a rotational speed of 600 min^{-1}, $\dot{V}_L$ = 0.378 m^3 h^{-1} and $\dot{V}_G$=60 m^3 h^{-1}for the FF packing obtained from *conv*CT scanning mode [*59*](Reuse with permission of John Wiley and Sons).

Influence of rotational speed

The gamma-ray CT measurements indicate that the rotational speed has a direct influence on the average liquid hold-up in the packing ($\varepsilon_{L,avg}$) between rotational speeds of 1200 to 600 min^{-1} and a gas flow rate of 60 $\text{m}^3\,\text{h}^{-1}$ the average liquid hold-up varies between 9 and 16.75 %, respectively. This is in a similar range in which columns equipped with structured packings can be operated [*87*]. However, the high surface foam packings would not be able to be operated in columns at these high loads as was shown by *Große* [*40*] for ceramic foam packings. When the rotational speed is decreased to 300 min^{-1} the gas flow rate has to be reduced to avoid entrainment. The local liquid hold-up results from the *conv*CT-scanning mode show an even distribution. Furthermore, the liquid hold-up decreases from the inner to the outer diameter as expected due to the increase in the cross-sectional area. When the rotational speed is reduced close to the rotational speed where entrainment occurs, the liquid strongly builds up in the center of the rotor (cf. Figure 3.19b). [*59*]

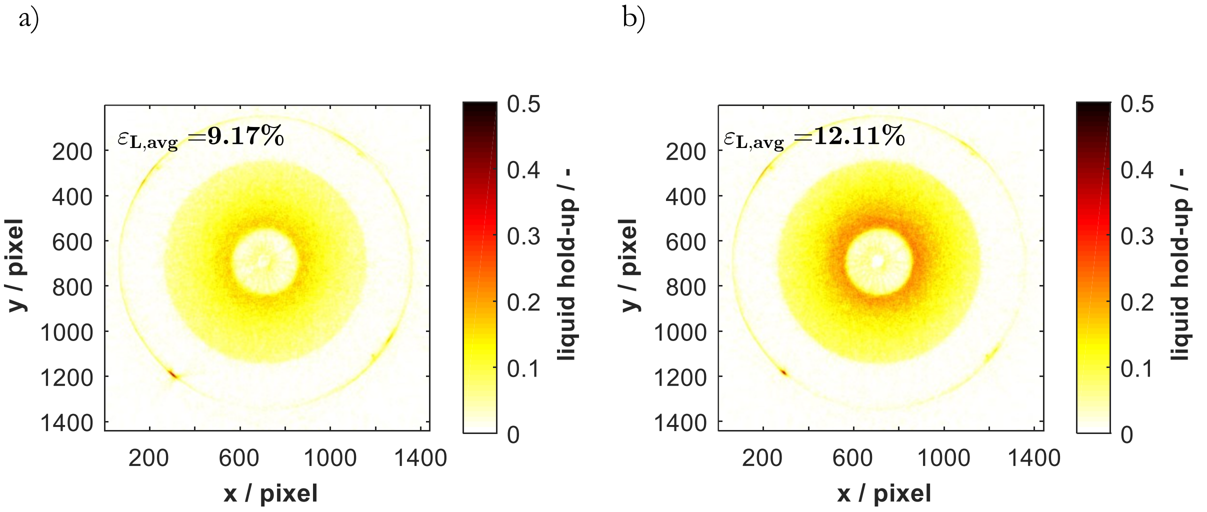

Figure 3.18: Comparison of flow patterns a) 1200 min^{-1} and b) 900 min^{-1}; multi-point distributor at, $\dot{V}_L$ = 0.378 $\text{m}^3\,\text{h}^{-1}$ and $\dot{V}_G$=60 $\text{m}^3\,\text{h}^{-1}$ for the full foam (FF) packing obtained from *conv*CT scanning mode.

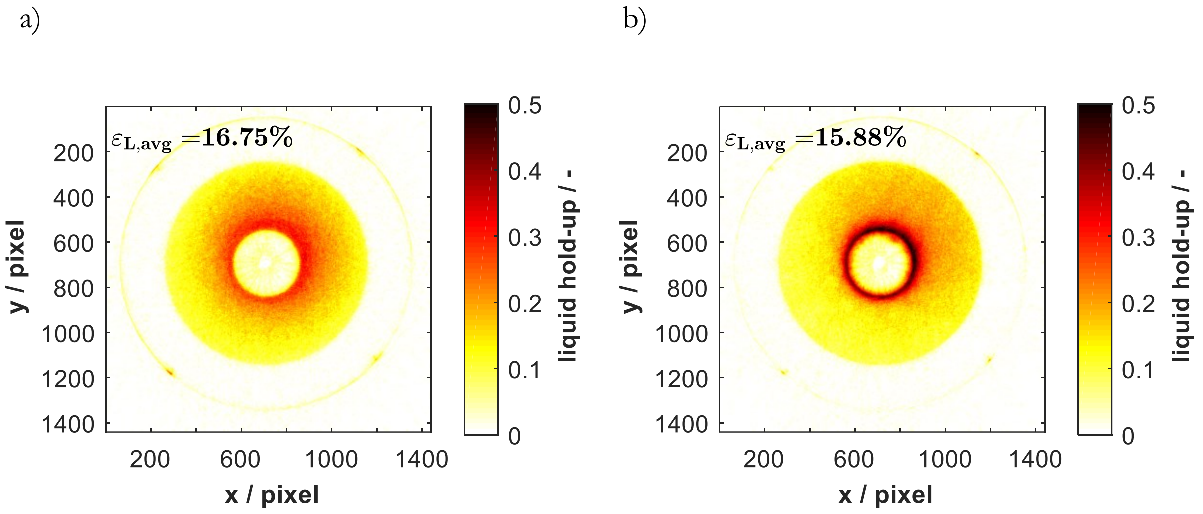

Figure 3.19: Comparison of flow patterns a) 600 min^{-1} and $\dot{V}_G = 60 m^3\ h^{-1}$or b) 300 min^{-1} and $\dot{V}_G$=45 m^3 h^{-1}; multi-point distributor at $\dot{V}_L$ = 0.378 m^3 h^{-1} for the full foam (FF) packing obtained from *conv*CT scanning mode.

Increasing the rotational speed is a potential way to increase mass transfer efficiency and the capacity of the machine [*36*]. Some authors identified a plateau or an optimum varying the rotational speed in their studies [*88, 89*] which can be explained by the results obtained through the *tar*CT scans illustrated in Figure 3.20 and Figure 3.21. At low rotational speeds of 300 min^{-1}, the centrifugal force from the packing acting on the liquid is not sufficiently high to ensure a sufficient liquid distribution. Moreover, friction forces from gas acting on the liquid can push the liquid back to the inner periphery of the rotor. Figure 3.21b shows a ring-shaped liquid accumulation at the inner diameter of the packing. At a higher rotational speed of 600 min^{-1}, a more homogeneous liquid distribution is achieved, while the average total hold-up is still almost the same. Increasing the rotational speed further to 1200 min^{-1}, the average liquid hold-up decreases rapidly. Applying the tarCTscanning mode, severe maldistribution induced by the support ring in the eye of the rotor is revealed (cf. Figure 3.20). It can be concluded that the spatial redistribution of the flow is rather negligible. Consequently, small disturbances of the initial wetting of the packing can already cause severe maldistribution at the outer radii of the packing. This observation is remarkable since a certain slip velocity between liquid and packing would easily counterbalance initial maldistribution. Accordingly, the low redistribution capability has to be considered when designing packing and support materials of RPBs. While this was also suggested based on visual investigations by Burns [*55*], the quantitative results, which are shown in Figure 3.20, clearly proof this effect. [*59*]

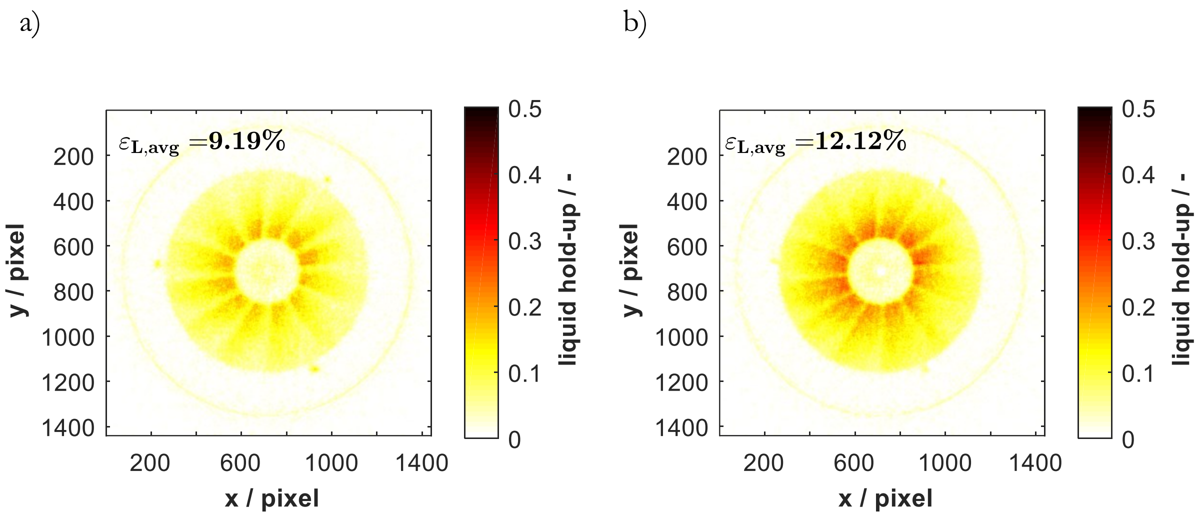

Figure 3.20: Comparison of flow patterns a) 1200 min^{-1} and b) 900 min^{-1}; multi-point distributor at, $\dot{V}_L$ = 0.378 m^3 h^{-1} and $\dot{V}_G$ = 60 m^3 h^{-1}for the full foam (FF) packing obtained from *tar*CT scanning mode [*59*] (Reuse with permission of John Wiley and Sons).

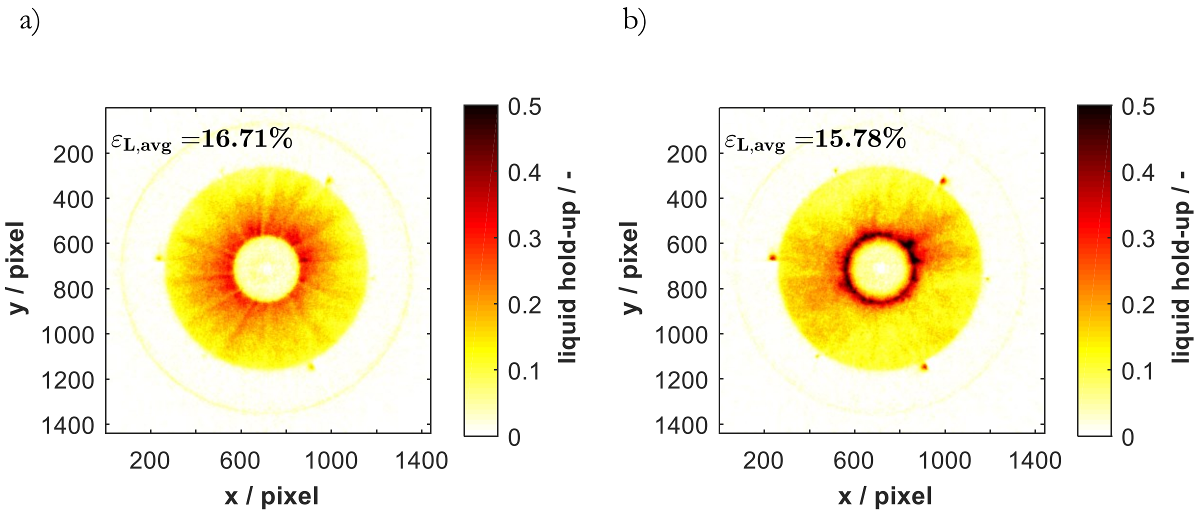

Figure 3.21: Comparison of flow patterns a) 600 min^{-1} and $\dot{V}_G$ = 60 m^3 h^{-1}or b) 300 min^{-1} and $\dot{V}_G$ = 45 m^3 h^{-1}; multi-point distributor at $\dot{V}_L$ = 0.378 m^3 h^{-1}for the full foam (FF) packing obtained from *tar*CT scanning mode. [*59*] (Reuse with permission of John Wiley and Sons).

Figure 3.22 summarizes the results that were obtained, showing the radial profile of the liquid hold-up for varying rotational speed. The results are generated by averaging the liquid hold-up in 60 equidistant elements with a radial thickness of 2.3 mm. For rotational speeds between 600 to 1200 min^{-1}, a slight increase of the liquid hold-up is measured in the first few millimeters from the inner radius of the packing until a maximum is reached. A similar increase in liquid hold-up along the first millimeters of the radius was found by *Yang* [*58*] who explained this by the packing capturing the liquid. Moreover, the accumulation can be explained by the deceleration of the liquid interacting with the packing. Beyond the maximum value, the hold-up gradually decreases until the end of the packing is reached. Two factors explain this behavior – firstly, the packing provides larger packing volumes at larger radii to distribute the liquid, and secondly, the centrifugal acceleration increases with increasing radius hence the liquid is accelerated again, which reduces the hold-up. For a small rotational speed of 300 min^{-1}, a comparably strong increase in the liquid hold-up for the first 10 mm of the packing compared to higher rotational speeds can be observed as also shown in Figure 3.22. [*59*]

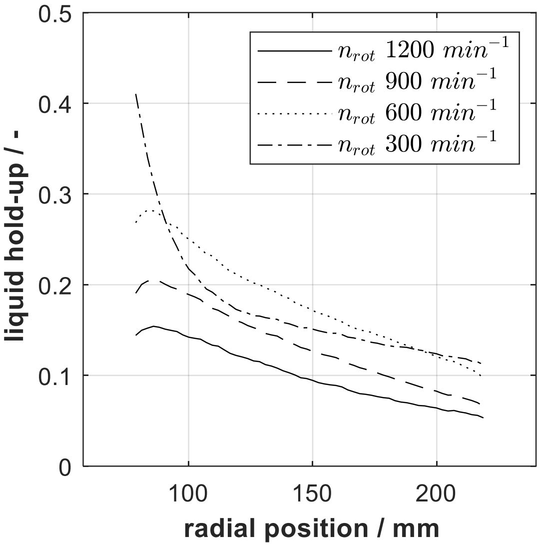

Figure 3.22: Comparison of radial liquid hold-up for 1200 min^{-1} to 600 min^{-1} at $\dot{V}_G = 60\ m^3\ h^{-1}$ and 300 min^{-1} at $\dot{V}_G = 45\ m^3\ h^{-1}$; multi-point distributor at $\dot{V}_L = 0.378\ m^3\ h^{-1}$ for the full foam (FF) packing obtained from *tar*CT scanning mode. [*59*] (Reuse with permission of John Wiley and Sons).

Influence of gas flow rate

Figure 3.23 shows the averaged radial liquid hold-up for different rotational speeds with and without gas flow. At a high rotational speed of 1200 min^{-1}, the difference in the liquid hold-up is negligible regardless of the gas flow rate. When reducing the rotational speed further, a steep increase in the hold-up is evident. This can be found in measurements with and without gas and can be related to the free flow through the packing. Here, the centrifugal force is not sufficient to prevent any liquid accumulation. For a gas flow of 60 m^3 h^{-1}, an additional increase of the liquid hold-up up to 40 % can be observed. [*59*]

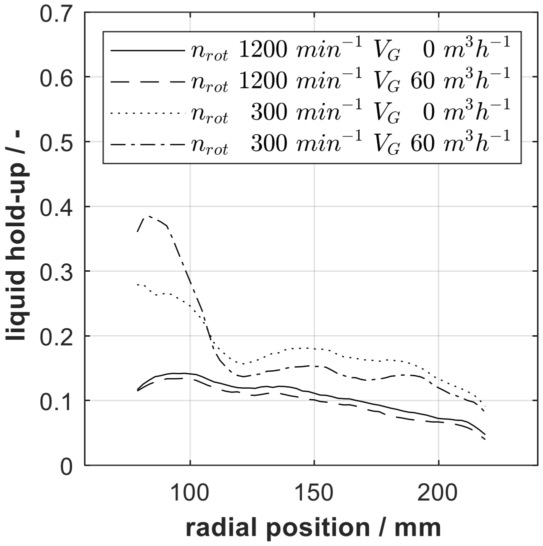

Figure 3.23: Comparison of radial liquid hold-up for 1200 min^{-1} and 300 min^{-1} at $\dot{V}_G$ = 60 m^3 h^{-1}; single-point distributor at $\dot{V}_L$ = 0.378 m^3 h^{-1} for the segmented foam packing obtained from *conv*CT scanning mode [*59*] (Reuse with permission of John Wiley and Sons).

3.3.4 Comparison with literature correlations

Based on a literature survey two correlations were selected for the comparison with the results of the gamma-ray tomography. The correlation from *Burns et al.* [*57*] is based on tracer response experiments and electrical resistance (cf. 2.4.2). The reticulated PVC packing is similar to the metal foam packing used in this work. The average void fraction (95 %) and the estimated specific surface area with 786 m^2 m^{-3} is similar to the metal foam packing used in this work (92 %, 1000 m^2 m^{-3}). However, the average pore size of the packing was approximately two times bigger than in this work, 2.54 mm to 1.4 mm in this work. For a better representation in the figures, the radial measurements were divided into 15 equidistant radial steps and then averaged. The comparison in reveals that the model of *Burns et al.* [*57*] is largely underestimating the liquid hold-up in the packing. A possible explanation is that the model does not account for the packing pore size, therefore capillary effects or the higher flow resistance due to ligament position and occurrence are not considered (26). On the other hand, the spatial resolution in the experiments of *Burns et al.* [*57*] was a lot lower than in our experiments. Assumptions of constant tortuosity and a continuous liquid film might have further affected the accuracy of the proposed correlation. Taking this into consideration, the difference observed might be seen as a first indicator that a significant amount of the liquid is traveling as a discontinuous film or as small droplets through the packing. Their empirical calculation is based on characteristic values of the centrifugal acceleration g_0 = 100 m s^{-2}

and the specific liquid load $LL_0 = 0.01$ m s^{-1} for rotating packed beds. The properties used for the calculation are listed in Tab. 6. [*59*]

Tab. 6: Properties for the calculation of the liquid hold-up.

density water (20 °C), ρ	998 kg m^{-3}
viscosity, µ	0.001 Pa s
surface tension, σ	0.07275 N m^{-1}
specific packing surface, a_p	1000 m^2 m^{-3}
collision distance/pore diameter, d_p	0.0014 m

$$\varepsilon_L = 0.034 \left(\frac{g}{g_0}\right)^{-0.38} \left(\frac{LL}{LL_0}\right)^{0.62} \; for\ water\ only \tag{26}$$

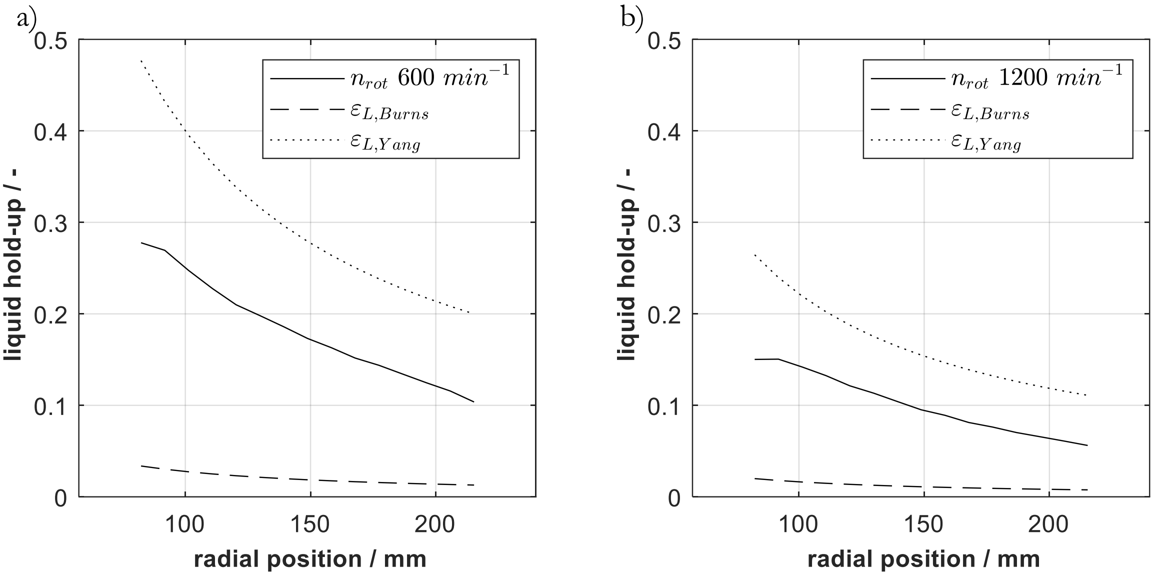

Figure 3.24: Comparison of radial liquid hold-up for a) 600 min^{-1} and b) 1200 min^{-1} at $\dot{V}_G$ = 60 m^{3}h^{-1}; multi-point distributor at $\dot{V}_L$ = 0.378 m^3 h^{-1} for the full foam (FF) packing obtained from *tar*CT scanning mode with the correlations of *Burns et al. [57]* and *Yang et al. [58]*. [*59*]

The correlation of *Yang et al.* [*58*] on the contrary is highly overestimating the liquid hold-up. The correlation is based on four empirical parameters and three dimensionless numbers Reynolds, Galileo and Kapitza number (28). [*59*]

$$\varepsilon_L = 12.159\ \mathrm{Re}^{0.479} Ga^{-0.392} Ka^{-0.033} \; for\ nickel\ foam\ packing \tag{27}$$

$$\text{with } Re = \frac{LL\rho}{a_p \mu} \qquad Ga = \frac{g d_p^3}{\nu^2} \qquad Ka = \frac{\mu^4 g}{\sigma^3 \rho} \tag{28}$$

In both experiments, metal foams with a similar specific surface area have been investigated. A certain difference in the experimental setup can be found in the radial packing length, *Yang et al.* [*58*] used a packing length of 22 mm while in this work a radial packing length of 152 mm has been used. As a consequence, the inner zone of the packing could have had a larger influence on the correlation proposed by *Yang et al.* [*58*]. However, the pore size diameter was not given and could not be compared. [*59*] As illustrated in the correlation of *Yang et al.* [42] is predicting the trend of the radial hold-up. A reduced liquid hold-up when the rotational speed is increased from 600 min^{-1} to 1200 min^{-1} is found in predicted values, but the correlation is overestimating the absolute value of the liquid hold-up. [*59*]

In summary, both of the proposed correlations are not suitable to estimate the liquid hold-up within an error tolerance of ±30 % without modifications (cf. Figure 3.25). Firstly, there is a need for additional experiments including different packings and liquid flow rates to evaluate its influence on prediction accuracy. Secondly, the adequate description of the packing morphologies is crucial, this makes more detailed investigations necessary to describe the morphology, e.g. the determination of spatially resolved porosities or pore diameter distributions. Finally, further studies on the modeling side to identify effects not yet taken into account by the correlations could extend the understanding of the packing influence. [*59*]

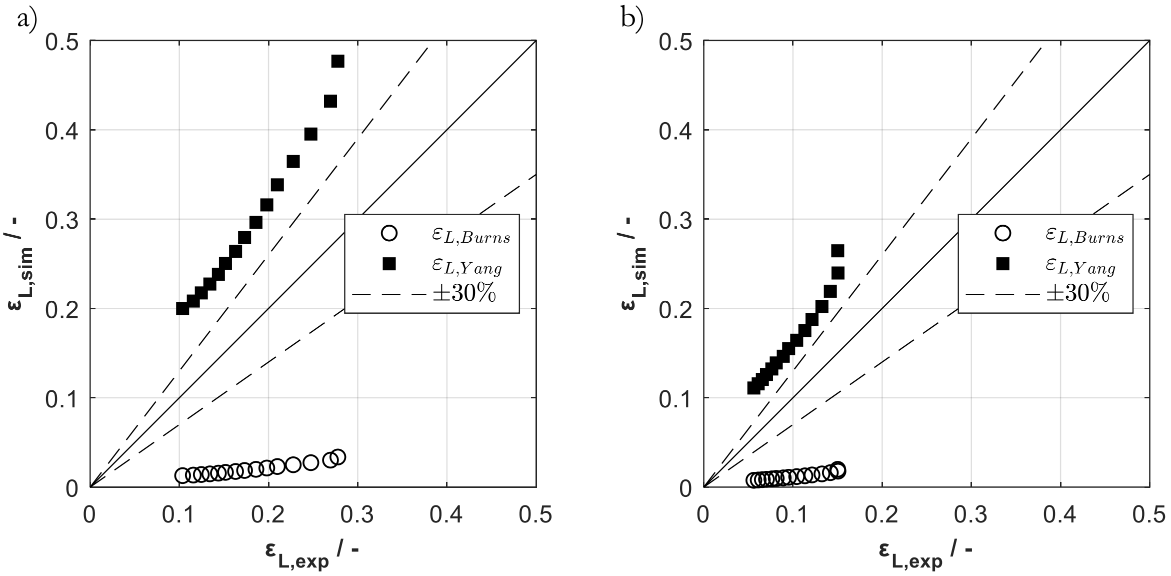

Figure 3.25: Comparison radial liquid hold-up for a) 600 min^{-1} and b) 1200 min^{-1} at $\dot{V}_G$ = 60 m^3 h^{-1}; multi-point distributor at $\dot{V}_L$ = 0.378 m^3 h^{-1}for the full foam (FF) packing obtained from *tar*CT scanning mode with the correlations of *Burns et al.* [*57*] and *Yang et al.* [*58*]. [*59*]

3.3.5 Comparison with wet pressure drop model

The developed ANN-model (cf. 3.2.3) reflects the wet pressure drop by adjusting a porosity constant within the packing. This constant can be considered as liquid hold-up and influences, by narrowing the free space for the gas, the calculation of the frictional pressure drop (cf. (20)). The estimated liquid hold-up was evaluated against the result of the gamma-ray tomography. Tab. 7 shows the difference between liquid hold-up measurements and the estimated hold-up based on pressure drop measurements. It can be concluded that for high rotational speed (900 – 1200 min^{-1}) the liquid hold-up is estimated with sufficient accuracy of ±30 %. For lower rotational speed, the deviation strongly fluctuates. A possible reason is that the low rotational speed in combination with high gas flow rates leads to a strong non-uniform liquid distribution as illustrated in the reconstructions of the liquid hold-up by the gamma-ray measurements for near entrainment measurements (cf. Figure 3.21). The assumption of a relatively homogeneous liquid distribution and hence a constant liquid hold-up is not justified. Direct estimation of the liquid hold-up by overall pressure drop measurements seems therefore impractical. The results may improve by the implementation of local pressure drop measurements. Furthermore, the data basis consisting of one liquid flow rate with and without gas flow per packing configuration for the CT measurements is very limited. Especially, an investigation at different liquid loads could significantly contribute to the understanding of liquid flow-dependent effects.

Tab. 7: Comparison of the average liquid hold-up from the gamma-ray CT measurements with the wet pressure drop model (WPD) based on $\varepsilon_{packing}$ 92 %, for 1200 min^{-1} to 600 min^{-1} at $\dot{V}_G$ = 60 m^3 h^{-1} and 300 min^{-1} at $\dot{V}_G$ = 45 m^3 h^{-1}; multi-point distributor at $\dot{V}_L$ = 0.378 m^3 h^{-1} for the full foam (FF) packing obtained from *tar*CT scanning mode.

Rotational speed / min^{-1}	$\dot{V}_L$ /m^3 h^{-1}	$\dot{V}_G$ /m^3 h^{-1}	ε_L Gamma-ray CT (*tar*)	ε_L WPD model (ANN)	Relative deviation / %
1200	0.378	60	9.19 %	10.20 %	+11 %
900	0.378	60	12.12 %	9.04 %	-25 %
600	0.378	60	16.71 %	9.76 %	-42 %
300	0.378	45	15.78 %	25.87 %	+64 %

3.4 Operating limits

Three different methods are available to determine the operating limit. Visual observation, liquid hold-up measurements and pressure drop analysis. The visual method is biased by the observation of the operator, who identifies the operating state when liquid starts to accumulate in the eye of the rotor or significant entrainment of liquid through the gas outlet occurs. The visual observation can be supported by the quantitative analysis of the entrained liquid. The liquid hold-up measurements, as described in chapter 2.4.2, are not trivial and it requires an advanced measurement setup. Lastly, pressure drop analysis is simple, reliable and enables an easy evaluation of experimental results. Figure 3.26 illustrates that the pressure drop is directly correlated with visual observations. In counter-current operation, entrainment occurs when the pressure drop curve is reaching its maximum. For ease of use and reliability, pressure drop analysis is used in the following to determine the maximal hydraulic operating capacity.

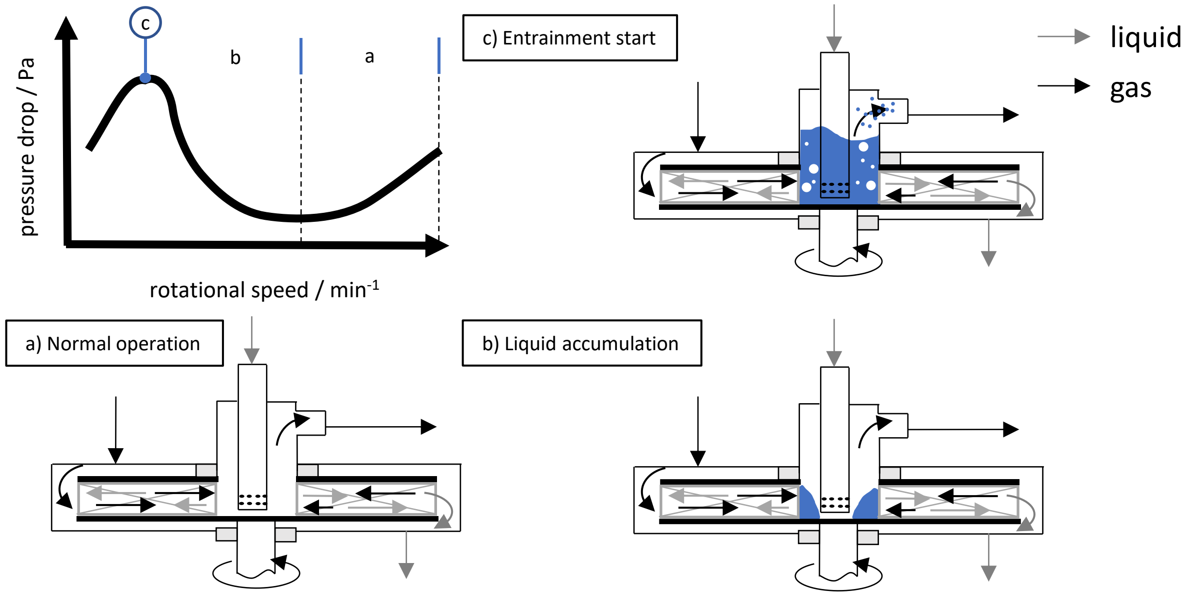

Figure 3.26: Illustration of the pressure drop behavior. a) Normal operation: no liquid accumulation in the eye of the rotor b) Liquid accumulation starts in the eye of the rotor, the pressure drop rises after passing a minimum c) Entrainment through the gas outlet occurs at the maximum of the pressure drop curve

When entrainment occurred at the pressure drop maximum, larger fluctuations in the pressure drop measurement were observed. This circumstance makes it difficult to measure the pressure drop at this point. However, the pressure drop minimum can be accurately and reproducibly determined hence it is used to define the minimal rotational speed according to the definition of *Rajan et al.* [*37*, p. 988]. The experimental data consisted of 907 data points for the metal foam and 748 data points for the knitted mesh packing. The data was evaluated in an automatic routine as illustrated in Figure 3.27. First, it was imported from the database, sorted according to liquid load and gas load (F-factor) at the inner cross-sectional area. A histogram was generated to evaluate if data for similar loads could be combined into one group. 70 data bins proved to be sufficient for the data resolution in this work. All data with less than 10 experimental points were discarded to improve the automatic recognitions in the pressure drop analysis. The processed data can be analyzed in manual or auto mode. In the manual mode, the maximal hydraulic operating capacity is determined by the user in the visual representation of the pressure drop and rotational speed diagram. In the automatic procedure, the user can optionally remove inconsistent data points from the automatic evaluation. Experimental points that were measured at the same rotational speed are averaged. A polynomial curve is then fitted to the pressure drop curve. Piecewise Cubic Hermite Interpolating Polynomial (pchip) method is used, which is available in MATLAB R2018a®. The method is chosen because of its shape-preserving characteristics, which follows monotonicity and therefore does not introduce new local extrema not represented by the experimental data [*90*].

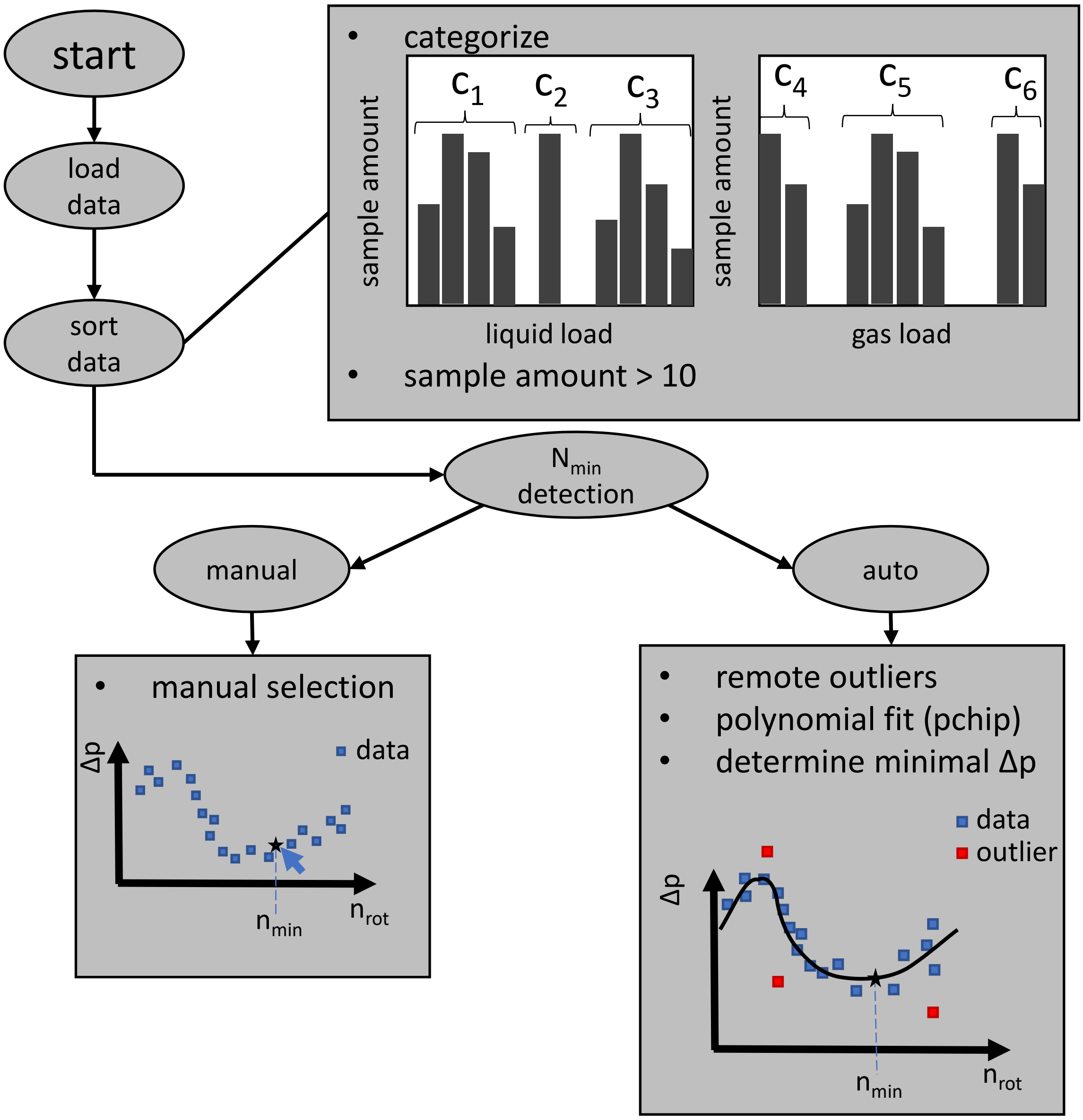

Figure 3.27: Automatic and manual determination of the minimal rotational speed.

Figure 3.28 and Figure 3.29 illustrate the results for the automated procedure and a variety of gas and liquid loads. For a moderate gas load of approximately $F_{G,max} = 1\ \text{Pa}^{0.5}$ knitted mesh and foam perform similar. The approximation of the pressure drop curve by the interpolating polynomial shows only minor deviations from the experimental data. The automatic detection of the minimal rotational speed is close to the steep increase of the pressure drop curve. It should be mentioned that the pressure drop data sometimes ends abruptly at low rotational speeds. The reason is that at those low rotational speeds strong entrainment through the gas outlet was experienced and the experiment was stopped. Fortunately, this data for lower rotational speeds has no relevance for the RPB process, because the counter-current gas and liquid contact within the packing is strongly diminished at entrainment conditions.

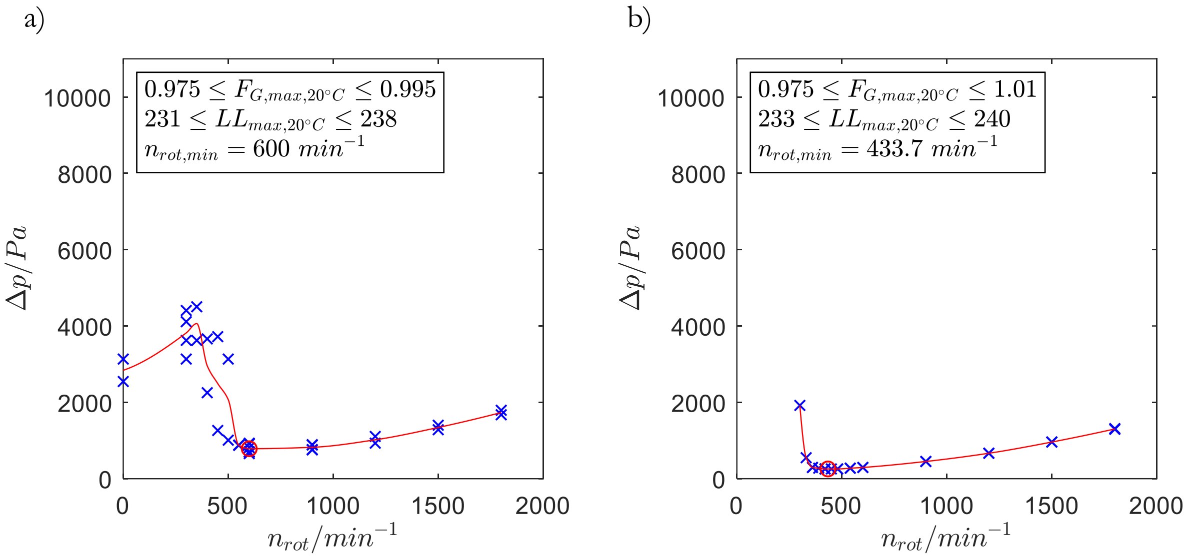

Figure 3.28: Pressure drop curve, and detection of the minimal operational speed ($n_{rot,min}$,○) for a) knitted mesh packing (KM) and b) metal foam packing.

Figure 3.29 compares the operational behavior for a liquid load of approximately 158 $m^3\,m^{-2}\,h^{-1}$ for knitted mesh and metal foam packing. The same minimal rotational speed is determined for both packings. However, the gas load can be doubled for the foam packing before a rotational speed of 1200 min^{-1} is reached. This elucidates that the pressure drop behavior can have a significant influence on the minimal rotational speed. $n_{rot,min}$ should be considered for the design, which considers energy consumption and capacity boundaries. The complete evaluation of the data can be found in A4 and A5.

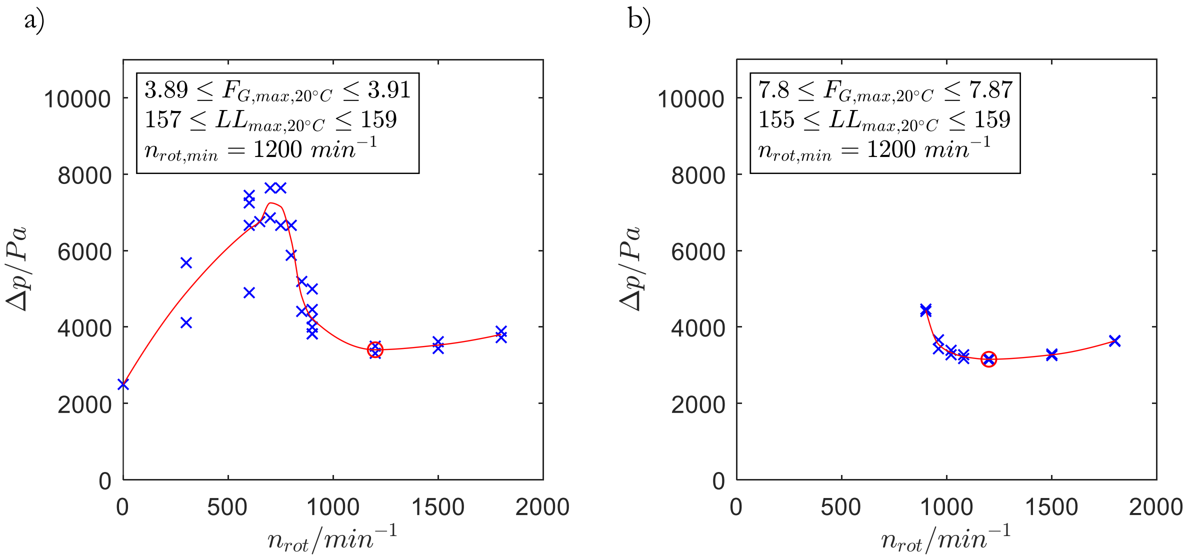

Figure 3.29: Pressure drop curve, and detection of the minimal operational speed ($n_{rot,min}$,○) for a) knitted mesh packing and b) metal foam packing.

The estimated minimal rotational speed data was compiled into a three dimensional grid. $LL_{max,20°C}$ and $F_{G,max,20°C}$ served as X-axis and Y-axis, respectively. While the minimal rotational speed is used as Z-axis. After fitting a polynomial of the form

$$n_{rot,min} = p_{00} + p_{10} \cdot x + p_{01} \cdot y + p_{20} \cdot x^2 + p_{11} \cdot x \cdot y + p_{02} \cdot y^2 + p_{30} \cdot x^3 + p_{21} \cdot x^2 y + p_{12} \cdot x y^2 \tag{29}$$

to the data, where p_{xy} are fitting coefficients of the polynomial. The data is visualized in a contour plot. From the contour lines the minimal rotational speed for a certain flow configuration can easily be accessed. For the metal foam packing, 28 pressure drop curves and the respective minimal rotational speed were compiled into Figure 3.30a). The major influence of the minimal rotational speed is the gas load ($F_{G,max,20°C}$), the liquid load ($LL_{max,20°C}$) is having a minor influence in the investigated range. The histogram (Figure 3.30b) illustrates that the minimal rotational speed is well met by the polynomial fit. The maximal deviation is ±100 min^{-1}, while 75 % of the data is met within a deviation of ±50 min^{-1}. The contour lines not neighbored by experimental data should be handled with caution due to the extrapolation of the data.

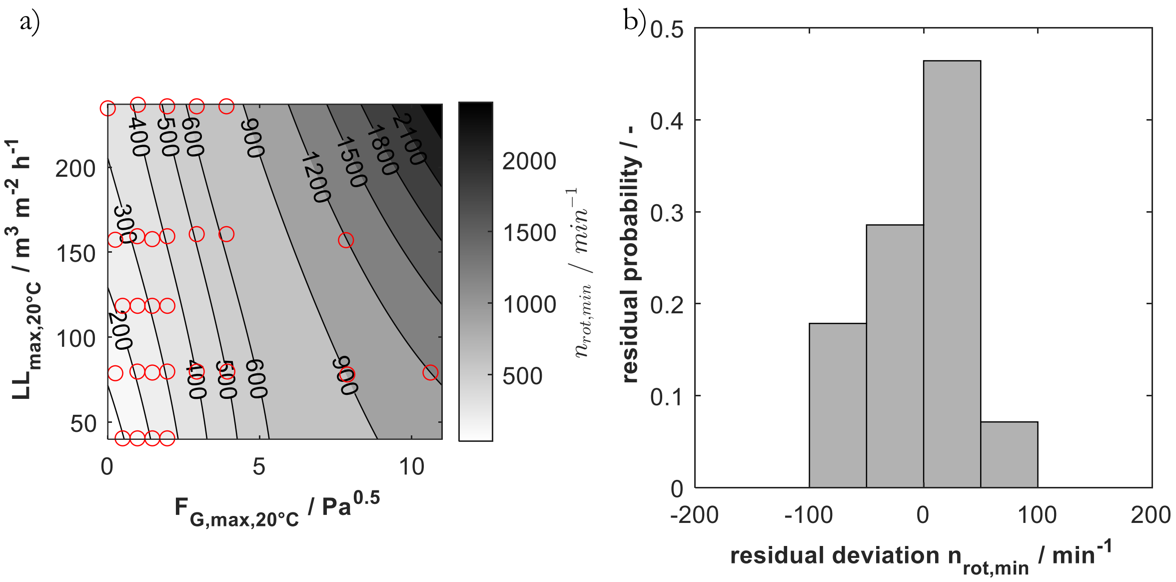

Figure 3.30: Overview surface fitted data of the metal foam packing a) contour plot of the minimal operational speed ($n_{rot,min}$) (○ =data points) and b) histogram of the residual deviation.

Figure 3.31a illustrates the results for the knitted mesh. The main trend, the major influence of gas load, is met for the knitted mesh as well. However, especially in the lower range of liquid loads some strong curvatures of the contour lines are evident. The histogram (Figure 3.31b) shows that the polynomial fit is not meeting the residuals as well as for the metal foam packing. The minimal rotational speed data meets the residuals in the range of ±150 min^{-1}. Compared to the metal foam, the residual deviation has broadened and only 56 % of the data lies within the deviation of

±50 min^{-1}. This can be explained by the lower resolution of the data points. Only 16 pressure drop curves have been used. A narrower distribution would improve the result of the fit. As summarized in chapter 2.2.1 columns equipped with structured packings are seldomly operated above liquid loads of 100 m^3 m^{-2} h^{-1} and F-factors of 4 Pa$^{0.5}$. High loads are also limiting the applicable geometric surface area of the packing. Standardized column packings are limited to a geometrical surface area between 250 and 750 m^2 m^{-3} (cf. 2.2.2.). This chapter concludes that two packings with a specific surface area of 1000 m^2 m^{-3} and approximately 3000 m^2 m^{-3} can readily be operated with an RPB. The geometrical surface area can be increased by a factor of 3 compared to standardized column packings. Furthermore, the hydraulic capacity can be significantly increased. Simultaneous operation of liquid loads between 200 and 300 m^3 m^{-2} h^{-1} and a gas load ($F_{G,max,20^\circ C}$) of 4 Pa$^{0.5}$ is feasible. For the metal foam packing highest loads of 236 m^3 m^{-2} h^{-1} at an $F_{G,max,20^\circ C}$ of approximately 4 Pa$^{0.5}$ or a liquid load of 80 m^3 m^{-2} h^{-1} at an $F_{G,max,20^\circ C}$ of approximately 11 Pa$^{0.5}$ could be achieved.

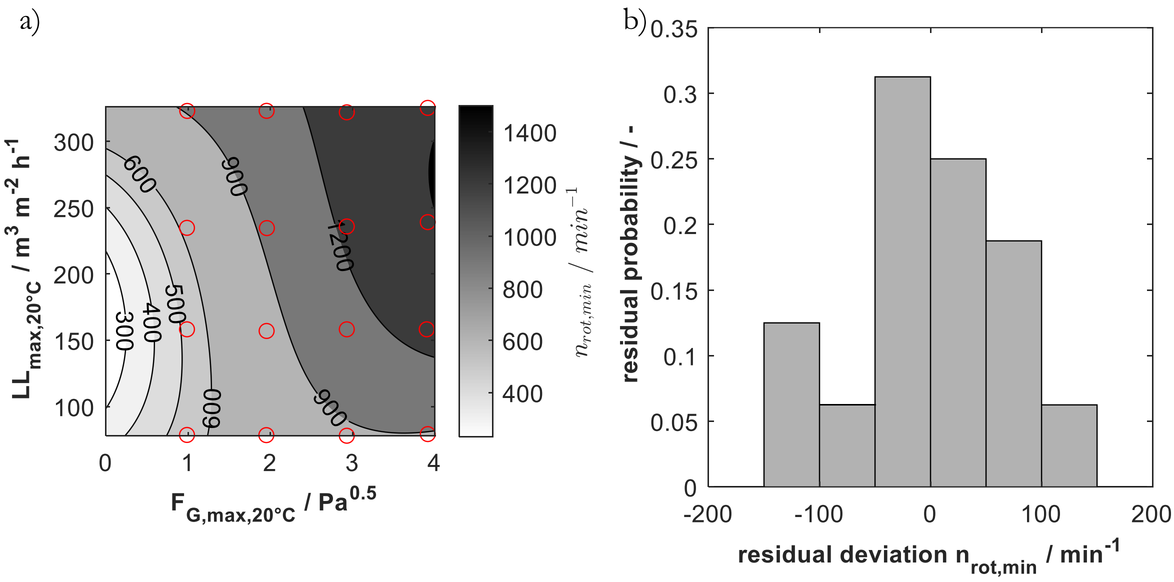

Figure 3.31: Overview surface fitted data of the knitted mesh a) contour plot of the minimal operational speed ($n_{rot,min}$) (○ =data points) and b) histogram of the residual deviation.

3.5 Power consumption

The power consumption in RPBs is crucial when operational costs of columns and RPBs are compared. The additional power input due to the rotation needs to be considered. To estimate the power requirements for a gas-liquid contacting RPB process, three main contributions should be considered, the power requirements for the RPB, for the pump to spray the liquid and for the blower/van to overcome the pressure drop of the gas. *Singh* [*91*, p. 141] provides a correlation based on experimental evaluations to estimate the power consumption of the RPB. The major contribution is the acceleration of the liquid to the speed of the rotor. The correlation

$$P_C = Z_0 + Z_1\, \rho_L r_o^2 \omega^2 \dot{V}_L \tag{30}$$

defines two fitting constants, Z_0 accounts for frictional losses and Z_1 is a multiplicator for the ideal energy which would be required to accelerate the liquid stream to the tip speed of the outer rotor circumference. The constant Z_1 considers slip losses during the acceleration of the liquid [*38*, p. 579]. The final correlation to calculate the power consumption (P_C) of the RPB in W equals

$$P_{C,Singh} = 1222\, W + 1.1\, \rho_L r_o^2 \omega^2 \dot{V}_L \tag{31}$$

The correlation was derived for three different rotor dimensions, consisting of an inner diameter and a packing height of 0.254 m. The outer diameter varied with 0.457, 0.610 and 0.762 m. For liquid flow rates between 2.3-11.3 $m^3\,h^{-1}$ and a Sumitomo metal foam packing with a specific surface area of 2500 $m^2\,m^{-3}$ and void fraction of 0.95. Based on hydraulic results in this work the constants were regressed to

$$P_{C,Groß} = 744.4\, W + 1.43\, \rho_L r_o^2 \omega^2 \dot{V}_L \tag{32}$$

for rotor dimensions d_i = 0.146 m, d_o = 0.500 m, h_p = 0.01 m and 0.02 m. The liquid flow rate varied between 0 and 1.4 $m^3\,h^{-1}$ for a RECEMAT® metal foam packing with a specific surface area of 1000 $m^2\,m^{-3}$ and a void fraction of approximately 0.92. Comparing the results for both machines some conclusions can be made. The constant factor for frictional losses is not proportional to liquid flowrate or equipment size. Even though the height of the rotor was 25 times larger and the liquid flow rates were approximately one order of magnitude higher in Singh's experiments the bearing and friction losses increase by 64 %. A direct comparison is however difficult since no detailed information on the sealing type is available. The liquid flow rate dependency is comparable for both machines. For the smaller machine in this work used it is approximately 30 % higher, which is possibly originating from the different packing used. The packing of *Singh* with a higher specific surface area could more efficiently counteract the slippage between liquid and packing due to smaller pore sizes. However, both correlations are in good agreement and will therefore later be used to calculate the energy requirements of the RPB in chapter 5.2. The experimental results for the power consumption exhibit a diverging trend (cf. Figure 3.32). Further investigations reveal that this trend is related to the liquid hold-up within the casing. With increased liquid flow rate the liquid cannot be drained fast enough from the casing and the casing starts to fill with liquid. This phenomenon is related to the equipment design and is avoidable if larger outlets are used. For the operation of the equipment in this work, the influence is negligible because the motor delivers enough power to overcome the additional frictional losses. For the approximation of the power consumption of the RPB the experimental data must be cleaned from unfavorable process conditions, to avoid an overestimation of the power consumption. The complete figures can be found in A6. The investigations for an increasing liquid hold-up in the casing can be found in A7.

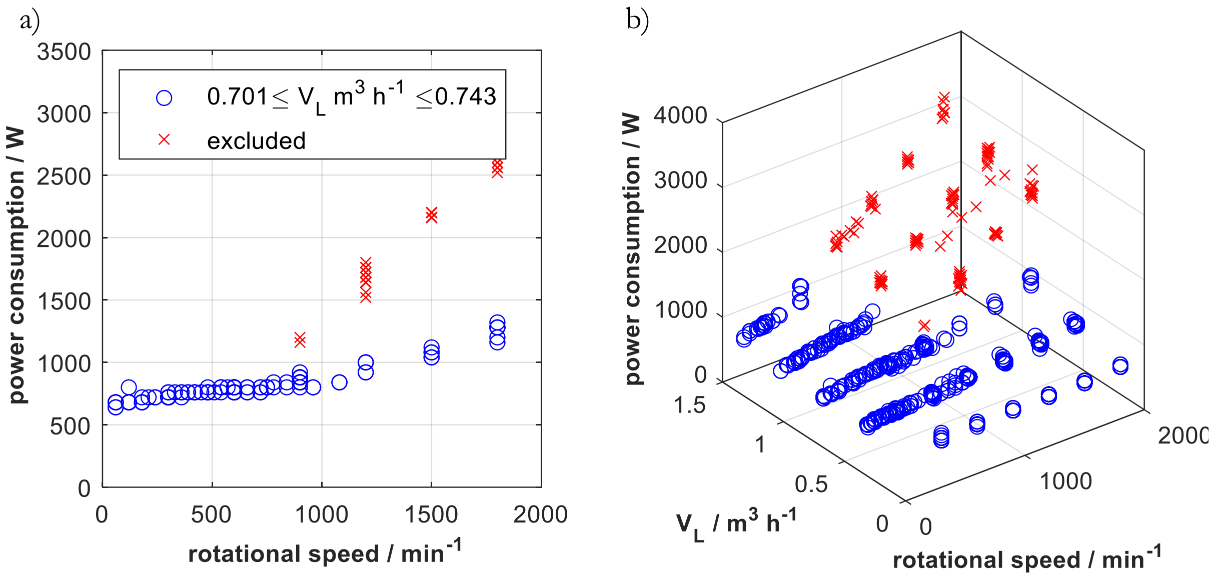

Figure 3.32: Power consumption data of the full foam (FF) with $\dot{V}_G$=0-330 m^3 h^{-1} a) Excluded data for $\dot{V}_L$ of approx. 0.72 m^3 h^{-1} b) Overview of the complete data for correlation (32) (x =excluded data points).

To determine the coefficients of (32) nonlinear least square fitting was applied. The coefficients Z_0 and Z_1 were determined with 95 % confidence bounds to 744.4±3.8 and 1.43±0.054, respectively. Figure 3.33 shows the fitted surface a) and the residuals b). The maximal relative deviation is 23 %.

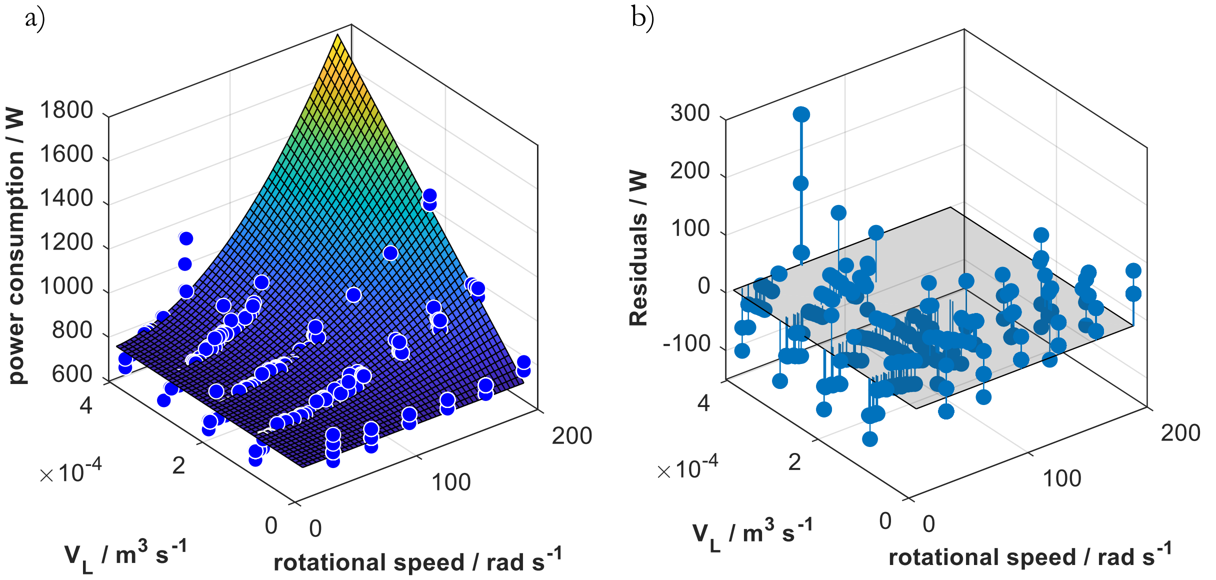

Figure 3.33: Power consumption a) surface fit of the full foam (FF) with $\dot{V}_G$=0-330 m^3 h^{-1} correlation (32) b) residuals for the corresponding surface fit.

4 Mass transfer

As described in the previous chapter on gas-liquid contacting in RPBs (cf. 2.4), there are several differences when the RPB is compared to a column. The difference in the centrifugal acceleration compared to the gravitational acceleration and the changing cross-sectional area requires additional attention when designing RPB equipment. The following chapters introduce the main definitions, materials and methods before leading to the experimental results of the co-current and counter-current deaeration experiments. They address the change of the mass transfer coefficient depending on operational or equipment parameters.

Parts of chapter 4 are published in:

Groß, K.; Beer, M. de; Dohrn, S.; Skiborowski, M.; Scale-Up of the Radial Packing Length in Rotating Packed Beds for Deaeration Processes, Ind. Eng. Chem. Res., 2020, 59(23), 11042-11053, DOI: http://doi.org/10.1021/acs.iecr.0c00868

The experimental data of the lab-scale RPB (cf. sections 4.2, 4.3) was generated by Michiel de Beer and his team at Nouryon in the framework of the ImPaCCt project. The corresponding sections and evaluations were drafted by Kai Groß and then reviewed and revised by all authors of the above-named publication.

A detailed overview including student contributions can be found in chapter 11. Scientific advice was given by A. Górak, M. Skiborowski and the corresponding co-authors

---

4.1 Theory

Within RPBs, different zones contribute to the mass transfer rates. *Munjal et al.* [*92*] name four main contributions based on the differences in the interfacial area:

- Interfacial area inside the packed bed (a_1)
- Interfacial area of the spray between the inside edge of the packed bed and the inside packing support (a_2)
- Interfacial area of the spray between the outside packing support and the liquid weir (a_3)
- The exposed surface area of the liquid held against the rotor wall (a_4)

Munjal et al. [*92*] distinguish between contributions from the packing surface (a_1) and other effects, which they term as so-called end effects (a_{2-4}). Other authors as *Luo et al.* [*93*] utilize a rotor structure that does not collect the liquid within the rotor. The liquid leaves the packing as droplets at the outer diameter and collides after a short distance with the static casing wall. These rotor designs, which do not incorporate a liquid weir at the outer packing diameter, generate additional surface area in the casing (a_5).

It is important to note that the definition of the mass transfer zones according to *Munjal et al.* [*92*], *Keyvani et al.* [*51*, p. 51], *Peel* [*67*], *Beck* [*61*, p. 50], and *Chen et al.* [*70*, p. 7868] is significantly different from the ones used in many recent publications. Especially the terminology end effect zone is frequently used in reference to an inner zone of the packing that is providing the main contribution to mass transfer, as e.g. described by *Yang et al.* [*94*] and *Luo et al.* [*93*, p. 9164]. Despite this conflict in the terminology, we will pursue with the terminology introduced by *Munjal et al.* [*92*] and call all contributions other than the packing end effects, in order to further analyze the different mass transfer contributions inside the RPB, apart from the packing itself.

Mass transfer inside the equipment is regularly described by experimentally derived mass transfer coefficients. A detailed derivation of the calculation of the liquid-side volumetric mass transfer coefficient (k_La) for counter-current stripping is provided by *Chen et al.* [*70*] and for co-current stripping by *de Beer et al.* [*72*] The final equation to calculate a single radial independent k_La-value for co-current degassing can be written as

Co-current:

$$k_L a = \frac{\dot{V}_L}{\left(1 + H_{O_2}^{CC} \cdot \frac{\dot{V}_L}{\dot{V}_G}\right)(r_o^2 - r_i^2)\pi z} \ln\left(\frac{c_{L,i} - H_{O_2}^{CC} \cdot c_{G,i}}{\left(1 + H_{O_2}^{CC} \cdot \frac{\dot{V}_L}{\dot{V}_G}\right) c_{L,o} - H_{O_2}^{CC} \cdot \frac{\dot{V}_L}{\dot{V}_G} c_{L,i} - H_{O_2}^{CC} \cdot c_{G,i}}\right) \tag{33}$$

Counter-current:

$$k_L a = \frac{\dot{V}_L}{\left(1 - H_{O_2}^{CC} \cdot \frac{\dot{V}_L}{\dot{V}_G}\right)(r_o^2 - r_i^2)\pi z} \ln\left(\left(1 - H_{O_2}^{CC} \cdot \frac{\dot{V}_L}{\dot{V}_G}\right)\left(\frac{c_{L,i}}{c_{L,o}}\right) + H_{O_2}^{CC} \cdot \frac{\dot{V}_L}{\dot{V}_G}\right) \tag{34}$$

with Henry's law solubility constant ($H_{O_2}^{CC}$) of oxygen in water, the volumetric gas and liquid flow rates ($\dot{V}_G, \dot{V}_L$) and the inlet and outlet concentrations of gas and liquid ($c_{L/G,i}$, $c_{L/G,o}$). Further information for the calculation of Henry's law constant can be found in the appendix B1.

It is common practice to evaluate this equation for the radial dimensions (r_i,r_o) of the packing ($k_La_{packing}$), while in the case of an empty rotor the k_La-value relates to the total volume of the rotor (k_La_{rotor}). In most publications the volumetric total mass transfer coefficient of the packing is determined on the experimentally determined concentration difference for the inlet and outlet of the whole RPB, therefore assuming that other contributions to the mass transfer are negligible. However, if the concentrations are measured in the ingoing and outgoing streams of the RPB, one needs to consider the validity of this assumption. In this work, optical oxygen sensors are used for the evaluation of the O_2 concentrations. Since these sensors need to be fully immersed in the liquid, measurements of the liquid oxygen concentration are only possible after the liquid collects at the bottom of the casing and leaves through the liquid outlet. Consequently, there exists the possibility of additional mass transfer happening in the casing. This additional effect should be limited due to the large flow rates, which would create low residence time, the limited available surface area in the casing and the small casing diameter in the lab-scale RPB. This assumption is later validated, by the comparison of mass transfer for different casing volumes in the lab- and pilot-scale RPB at the same packing length and similar loads (cf. Figure 4.5). Finally, for the analysis of the performance the degassing efficiency (η) for co-current stripping is defined, where $c_{L,o}^{*}$ denotes the thermodynamically lowest oxygen concentration feasible, when the outgoing liquid and gas phase are in equilibrium.

co-current:

$$\eta = \frac{c_{L,i} - c_{L,o}}{c_{L,i} - c_{L,o}^{*}} \tag{35}$$

$$c_{L,o}^{*} = \frac{c_{G,o}}{H_{O_2}^{CC}} \tag{36}$$

For counter-current operation, the Kremser equation can be used to determine the number of theoretical equilibrium stages necessary for the separation. Assuming constant molar flow rates ($\dot{n}_G, \dot{n}_L$), constant pressure and the validity of Henry's law [*95*].

counter-current:

$$n_{th} = \frac{\ln\left(\frac{x_{in} - \frac{y_{in}\,p}{K^{PX}}}{x_{out} - \frac{y_{in}\,p}{K^{PX}}}\left(1 - \frac{\dot{n}_L\,p}{\dot{n}_G\,K^{PX}}\right) + \frac{\dot{n}_L\,p}{\dot{n}_G\,K^{PX}}\right)}{\ln\left(\frac{\dot{n}_G\,K^{PX}}{\dot{n}_L\,p}\right)} \tag{37}$$

$$K^{px} = \frac{p_i}{x_i} \tag{38}$$

4.2 Materials and methods

In order to outline the performed experimental investigations, an overview of the experimental setup, analytics, and geometries of the different machine types is presented. Furthermore, the experimental procedure including the sealing test and start-up is described.

4.2.1 Experimental setup

In this work, a lab-scale and a pilot-scale RPB were used. Tab. 8 provides detailed information on the specific geometries and packing types that were investigated. It is important to note that the terms lab and pilot are referring to the outer equipment dimensions. The lab-scale RPB is suited for the lab environment (e.g. on a lab bench), while the pilot-scale RPB dimensions prohibit such an implementation. However, the hydraulic capacity of both machines is similar, based on the sizing of outlets. The main difference is the larger outer rotor diameter (lab: 0.160 m, pilot: 0.500 m). The pilot-RPB accommodates a roughly six times larger radial packing length ($L_{packing}$) (lab: 0.026 m, pilot: 0.152 m).

Tab. 8: Overview of the RPB-types used in this work.

		lab-scale RPB (Andritz, VZP 16/0.03)	pilot-scale RPB		
Rotor	d_i /m	0.100	0.146		
	d_o /m	0.160	0.500		
	h_{rotor} /m	0.050	0.010		
	d_{casing} /m	0.240	0.650		
Packing	Type	wire mesh	RECEMAT® NCX 1116		knitted mesh
	a_p /$m^2 m^{-3}$	2975	1000	1000	2957
	ε / -	0.915	0.92	0.92	0.83
	$d_{packing,i}$ /m	0.100	0.146	0.146	0.146
	$d_{packing,o}$ /m	0.152	0.450	0.200	0.460
	$h_{packing}$ /m	0.050	0.010-0.020	0.010	0.010
Distributor	d_n /m	0.080	0.025	0.025	0.025
	details	35 x 1.3 mm (7x 3 rows 7x 2 rows alternating)	2 x 24holes x 0.8 mm (360 ° spray) 2 x 6 x 1.6 mm (90° spray)		

The lab-RPB

The lab-RPB consists of a rotating packing support structure, on which a wire mesh packing was wound, enclosed by a cylindrical housing (diameter: 0.240 m). A wire mesh packing with a length ($L_{packing} = r_o - r_i$) of $26 \cdot 10^{-3}$ m and a height of $50 \cdot 10^{-3}$ m was used. The liquid (demineralized water) was fed from a 2.1 m^3 feed vessel, which contains a gas sparger to saturate the liquid with air, through the inner tube of the concentric central shaft of the RPB to the liquid distributor. The liquid flow rate was measured with a Krone Optiflux 4300C flowmeter (up to $278 \cdot 10^{-6}$ m^3 s^{-1}, accuracy: 0.2 %) and controlled with a manual needle valve. The gas-phase (nitrogen, supplied from a central nitrogen tank) was fed through the outer tube of the concentric shaft, resulting in co-current gas-liquid flow through the packing. The gas flow rate was controlled by a Bronkhorst EL mass flow controller ($33.33 \cdot 10^{-6}$ to $1667 \cdot 10^{-6}$ m^3 s^{-1} at normal conditions). The accuracy is 0.5 % of reading plus 0.1 % of full scale. The liquid phase was withdrawn from the bottom of the RPB and recycled to the feed vessel; the gas phase was vented from the top of the RPB. Figure 4.1 displays the schematic setup for a counter-current deaeration. For counter-current deaeration, a detailed plant setup of lab- and pilot-RPB can be found in the appendix B2.

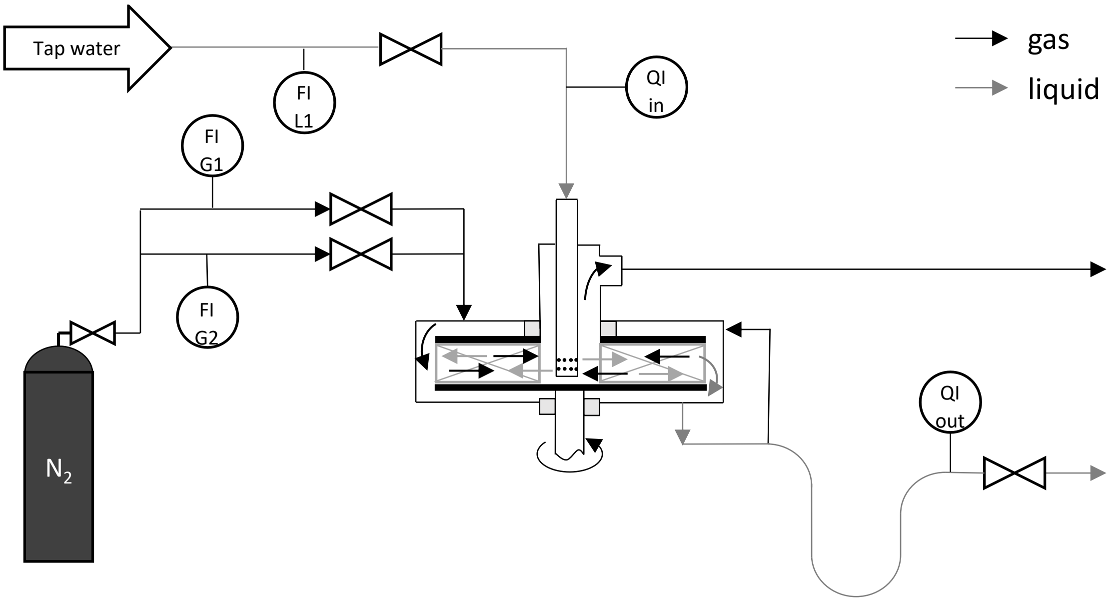

Figure 4.1: RPB setup for deaeration experiments for co-current deaeration gas inlet and outlet are exchanged.

The rotor of the lab-RPB was driven by a Helmke DOR112M-2-157 motor, up to rotational speeds of 4000 min^{-1}. The oxygen concentrations were measured in the liquid inlet and outlet of the machine using a Mettler Toledo Inpro 6860i (accuracy: 1 % of reading + 8 ppb) and a Mettler Toledo Inpro 6970i dissolved oxygen sensor (accuracy: 1 % of reading + 2 ppb), respectively. Temperatures (PT-100 type A) and pressures (ABB 2600T) were measured in the liquid inlet and outlet. All process data was continuously collected in a HiTec Zang process computer.

The pilot-RPB setup

The pilot-RPB was equipped with three kinds of packing in the scope of the investigations. At first a knitted mesh similar to the one used in the lab-scale RPB with ε of 0.83 and a_p of 2953 m^2 m^{-3} estimated according to *Blass* [*76*] was applied. Furthermore, a RECEMAT® B.V. nickel-chromium foam NCX1116 (ε of 0.92 and a_p of 1000 m^2 m^{-3}), which was cut into rings and that allowed for a variation between an outer diameter of 0.200 m and 0.450 m was applied. Note that for large radial packing length, the mesh showed significant handling disadvantages. Being wound on the rotor inner support ring the potential for increased nonuniformities increases significantly with increasing radius/increasing number of revolutions due to small inaccuracies in the winding process or the manufactured width of the mesh. Additionally, the winding force influences the packing porosity. Therefore, it was decided to use the cutted foam rings instead for greater reproducibility. As will be shown in the subsequent sections, mesh and foam show a similar mass transfer behavior (cf. 4.3.3).

For the introduction of the liquid phase, a liquid distributor with 48 holes with a diameter of $0.8\cdot10^{-3}$ m and an outer diameter of $25\cdot10^{-3}$ m was used. The liquid flow rate was measured with a turbine wheel flow meter (DRS-9159I4L4420, Kobold) with a measurement range from $33.3\cdot10^{-6}$ to $666.6\cdot10^{-6}$ m^3 s^{-1} and an error of ±1.5 % of the full scale and manually adjusted via a ball valve. The nitrogen stream was fed by a pressure cylinder and measured for all co-current experiments and counter-current experiments of the knitted mesh by a thermal mass flow meter (KMT-114R10L1NQ4, Kobold) for the measuring range from $8.8\cdot10^{-5}$ to $1.75\cdot10^{-2}$ m^3 s^{-1} with an accuracy of ±1.5 % of the full scale + 0.5 % of the measurement value. For counter-current measurements of other packings, the nitrogen flow rate was measured with ball flow meters with an error of ±3 % of full scale ($\dot{V}_G$ 0.1-1 NL min^{-1}: UK-040GML0100, Honsberg and $\dot{V}_G$ 10-100 NL min^{-1}: UKV-040GML0001, Honsberg). The dissolved oxygen concentration was measured in the liquid inlet with a Mettler Toledo optical probe (InPro 6860i) for oxygen-saturated liquids with an error of ±1 % + 8 ppb and at the outlet with a Mettler Toledo/Thornton Pure Water Optical DO Sensor for lowest oxygen concentrations with an accuracy of ±1 % of the reading or at least 2 ppb. Tap water was used for the liquid stream, which already contained sufficient amounts of oxygen. 5.0-graded nitrogen from cylinders was used with a purity of 99.999 % to avoid smallest oxygen concentrations in the stripping gas. The outflowing gas was led trough an additional washing tank, to avoid backflow of oxygen into the RPB through the gas outlet. The washing liquid (H_2O) prevented the backflow of air/oxygen in case of under pressure in the machine, which could occur during the shift of rotational speed. An overview of the used equipment can be found in chapter A8.

4.2.2 Experimental procedure

Prior to the experimental investigation, the lab setup was tested for leakage of air using a pressure test, for which a maximum increase of $3.1 \cdot 10^2$ Pa h^{-1} was observed, indicating no significant leak in the setup. The airtightness of the pilot machine was verified by flushing the dry RPB with the smallest gas flow used in the experimental run and at the highest rotational speed used. The gas-phase concentration was measured at the liquid outlet, which did not contain any liquid at this time. At these conditions, there was a small vacuum induced in the machine, which would have revealed even a small air leakage. A very low oxygen concentration in the range of the measurement error of the sensor was reached (2 to 3 ppb) while flushing the RPB. After the tightness of the experimental setup was validated, the liquid was introduced into the machine, and the gas flow rate and rotational speed were adjusted. The inlet and outlet oxygen concentrations and temperatures were monitored. When both temperature and concentration were stable, steady-state was assumed. To avoid large errors in the estimation of the k_La-value, data close to the equilibrium were excluded. This was done, when the difference between outlet concentration and equilibrium concentration was less than three times the accuracy of the sensor ($[c_{L,o} - c_L^*]$ < 3 sensor accuracy). This was especially the case for a packing length ($L_{packing}$) of 0.152 m and a relative centrifugal force (RCF) above 100 (cf. Figure 4.5 and Figure 4.6). The gas phase concentration was calculated from mass balance, which assumes that the liquid inflow is the only source of oxygen and no other sources of oxygen are present. The validity of this assumption was guaranteed by pressure and leak tests and the application of high graded nitrogen with a purity of 99.999 %.

4.3 Co-current

The co-current operation can be used as a model system for stripping or flash evaporation. When stripping gas is available at low cost (e.g. air) it can be a promising alternative for counter-current operation. The maximal separation is limited to a single equilibrium stage. However, in a co-current operation, the pressure drop plays a minor role because the centrifugal head reduces the pressure losses.

4.3.1 Theoretical boundary

For the co-current deaeration at fixed temperature and pressure the theoretical oxygen concentration at the outlet depends solely on the gas-to-liquid ratio. Assuming equilibrium between the leaving streams is equivalent to a 100 % thermodynamic efficiency (cf. (35)). Figure 4.2 shows that gas-to-liquid ratios > 5 lead to a sufficiently low oxygen concentration below 50 μg L^{-1}.

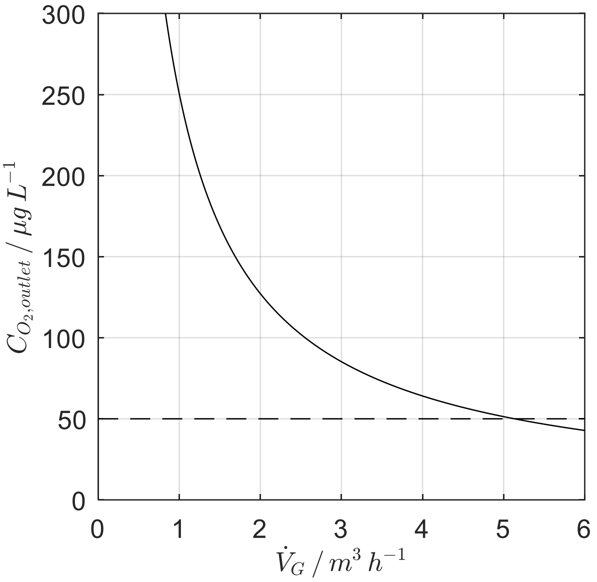

Figure 4.2: Theoretical liquid outlet oxygen concentration (cf. (35)) at equilibrium for oxygen saturated liquid $\dot{V}_L$ = 1 m^3 h^{-1} (p = 1.01325 bar, T = 25°C).

Based on the performed series of experiments an investigation of the mass transfer performance based on different radial packing length was performed, including a comparison of the lab-scale and pilot-scale RPB. Furthermore, a comparison between the different packing materials was conducted. Finally, the applicability of correlations for the estimation of the mass transfer coefficient is discussed with regards to the different scales of equipment.

4.3.2 Influence of the radial packing length

To provide insight on the benefit of adding packing to the mass transfer a set of experiments was performed in the pilot-RPB, with an empty rotor without packing (d_i: 0.146 m, d_o: 0.500 m, h_{rotor}: 0.010 m), with a foam packing of a short packing length of 0.027 m (d_i: 0.146 m, d_o: 0.200 m, $h_{packing}$: 0.010 m) and an extended packing length of 0.152 m (d_i: 0.146 m, d_o: 0.450 m, $h_{packing}$: 0.010 m). The rotor dimensions were kept constant for all experiments.

Deaeration efficiency

In the co-current operation, efficiency is defined according to equation (35). An efficiency value of one denotes the thermodynamic maximal potential. The efficiency, a key figure to evaluate the feasibility of reaching the process requirements, enables a simple comparison of different equipment configurations. Figure 4.3 illustrates the performance of foam packings for different liquid flow rates. For the packed rotor, no variation of efficiency is found when the flow rate is changed. However, the efficiency decreases for the empty rotor if the flow rate is increased. All three rotor configurations reach high efficiencies close to one. The use of longer radial packing length enables high efficiencies at a lower rotational speed.

The use of efficiencies is especially suitable for more general evaluations or thermodynamic feasibility. Although efficiencies are used to predict the mass transfer performance in many separators, they also have drawbacks. The concept of efficiencies is purely relying on thermodynamic data. The design and especially the scaling of apparatuses, with complex geometrical and hydrodynamic conditions, requires to consider the equipment specific features in addition to the thermodynamic boundaries. The rate-based approach, in which the mass transfer of each component can be calculated as a combination of mass transfer coefficient and driving force is more suitable. It incorporates packing geometry, hydraulics or surface area, into the calculation of the mass transfer coefficients. It will be used in the following section to describe the mass transfer in the RPB more adequately.

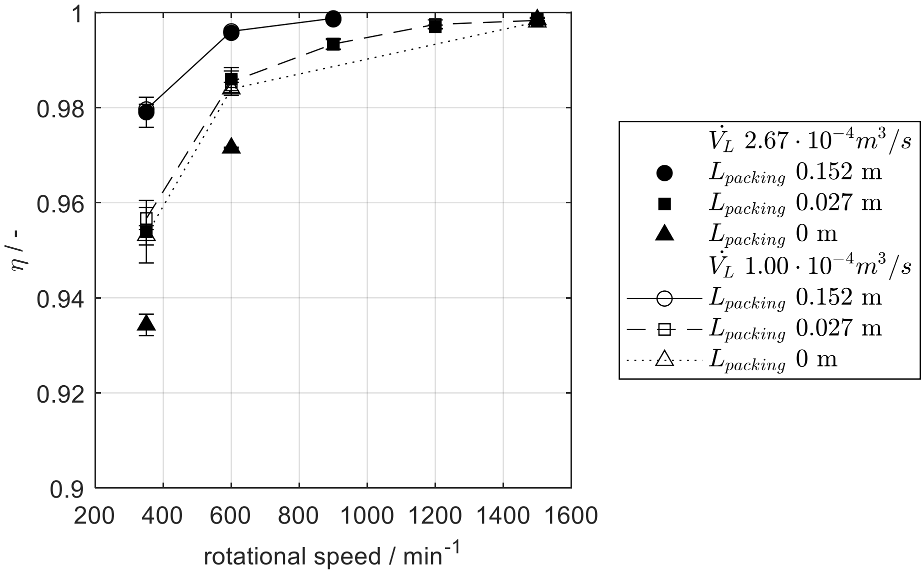

Figure 4.3: Packing effect on the efficiency (η) for different liquid flow rates at constant rotor dimensions (d_i: 0.146 m, d_o: 0.500 m, h_{rotor}: 0.010 m) with and without foam packing and $\dot{V}_G$ $=1.67 \cdot 10^{-3}$ m^3 s^{-1} in the pilot-RPB. Error bars depict the standard deviation (Reprinted (adapted) with permission from [*96*]. Copyright 2020 American Chemical Society).

Mass transfer coefficient based on rotor or packing volume

To calculate the k_La-value for packed and empty rotors, the rotor volume was chosen as a common reference volume (k_La_{rotor}). Figure 4.4 illustrates the estimated volumetric mass transfer coefficients for the different packings at two different liquid loads and varying rotational speeds. Obviously, the difference in k_La_{rotor} -values between a packed and an empty rotor is more prominent for higher liquid flow rates, while the difference becomes negligible with increasing rotational speed. At flow rates of $2.67 \cdot 10^{-4}$ m^3 s^{-1}, a clear contribution of the packing can be noted for rotational speeds between 350 and 600 min^{-1}. The packing increases the k_La_{rotor}-value by approximately 42-54 % compared to an empty rotor. The improvement by the packing reduces to roughly 24-31 % with a lower liquid flow rate of $1.00 \cdot 10^{-4}$ m^3 s^{-1}.

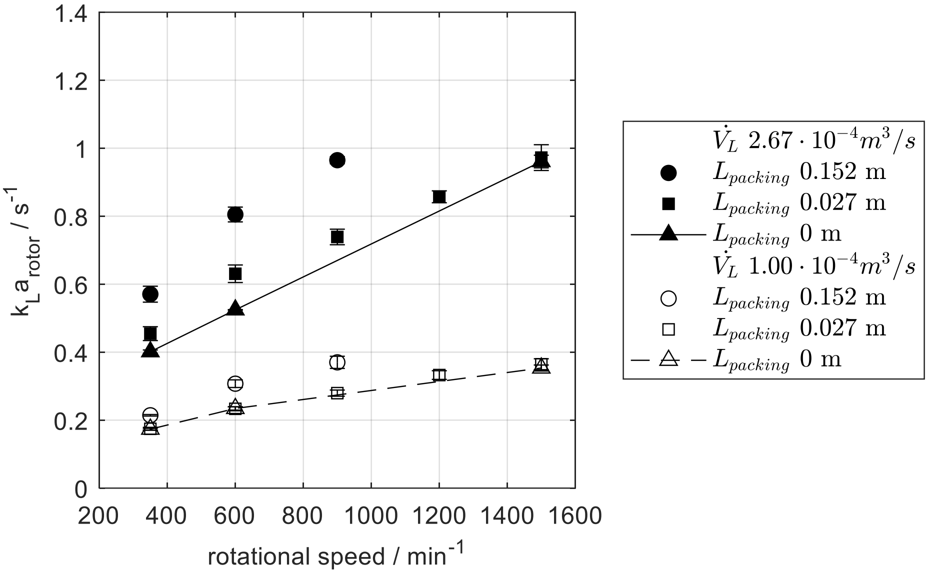

Figure 4.4: Packing effect on the k_La_{rotor} for different liquid flow rates at constant rotor dimensions (d_i: 0.146 m, d_o: 0.500 m, h_r: 0.010 m) with and without foam packing and $\dot{V}_G = 1.67 \cdot 10^{-3}$ m^3 s^{-1} in the pilot-RPB. Error bars depict the standard deviation (Reprinted (adapted) with permission from [*96*]. Copyright 2020 American Chemical Society).

Tab. 9 further lists the geometric surface area for the different internals. The casing is assumed to have a cylindrical body. Assuming a constant k_La-value along the radial direction of the rotor, a proportional relationship between k_La-value and geometrical area is expected. A potential k_La_{rotor}-value improvement of 80 % is estimated from the geometrical surface area when packing is added and either the empty rotor (casing and rotor plates) or the packed rotor (casing and packing) is contributing to the mass transfer. The difference between the theoretical and experimental contributions shows that an additional performance increase due to the packing design seems possible. The atomization of the liquid jets into tiny droplets by the inner support ring will additionally increase the surface area. This atomization cannot be estimated easily. However, it is reasonable to believe that the influence will be stronger when no packing is present due to the long free path length. If packing is used, the droplets will accumulate to films at the packing surface. Consequently, atomization can be a reason why the RPB without any packing works better than expected.

Tab. 9: The geometrical surface area of the pilot-scale rotating packed bed with $L_{packing}$= 0.152 m.

	Casing	Rotor	Packing
	$= 2\,\pi \frac{d_{casing}^2}{4} + \pi\, d_{casing}\, h_{casing}$	$= 2\,\pi \frac{d_o^2}{4}$	$= \pi \frac{d_{packing,o}^2 - d_{packing,i}^2}{4}\, h_P\, a_p$
A_{geo} / m^2	0.89	0.39	1.42
	Casing + Rotor	Casing + Packing	
A_{geo} / m^2	1.28	2.31	

The short radial packing length ($L_{packing}$= 0.027 m) exhibits only a small improvement in the mass transfer coefficient compared to the empty rotor. For a liquid flow rate of around $1.00 \cdot 10^{-4}$ $m^3\,s^{-1}$ there is no observable difference between the k_La_{rotor}-value of the empty and the packed rotor. When the difference in the k_La_{rotor}-value between empty and packed rotor is small it indicates that packing is not superior to plain rotor plates. From a practical point of view, the benefit of using packing is then questionable. However, a more severe cause can be the presence of end effects as defined in chapter 4.1. Non-packing related mass transfer contributions can lead to a large overestimation of the mass transfer coefficient when the total mass transfer contribution is accounted for the packing volume in the mass transfer coefficient ($k_La_{packing}$). In Figure 4.5, the overestimation due to the selection of the packing volume is illustrated. Considering the short packing length in the pilot-RPB, the comparison between pilot-RPB and lab-RPB illustrates that similar results for the measured mass transfer are obtained at the same relative centrifugal force and a comparable liquid load at the inner diameter (pilot: 80 $m^3\,m^{-2}\,h^{-1}$ lab: 56 $m^3\,m^{-2}\,h^{-1}$). Despite the increased mass transfer, the larger radial packing size results in a significantly lower $k_La_{packing}$-value, which fosters the conclusion that the mass transfer coefficient is variable and not constant along the radius for different packing length. We assume two possible reasons. Firstly, the relative contributions of the end effects (i.e., the mass transfer rate contributions other than that by the packing volume), are more prominent when only a small packing volume is used. Secondly, the geometrical changes along the radius, especially the increasing cross-sectional area, as well as the increasing centrifugal acceleration to the outside of the rotor have a direct and considerable influence on the gas- and liquid velocities and liquid distribution. Eventually, these changing conditions lead to variable mass transfer behavior. Considering the approximately 10-fold increase in the reference volume for the foam packing with a radial length of 0.152 m compared to the foam packing with a radial length of 0.027 m, the increased mass transfer inside the RPB results in an estimated $k_La_{packing}$-value of only 13 % of the one resulting for the radial packing length of 0.027 m. Therefore, mass transfer correlations originating from small scale RPB experiments should be cautiously used when extrapolating the results to large scale units without correcting for the specific dimensional and flow characteristics of the RPB. The decreasing $k_La_{packing}$ is also supported by data presented by *Groß et al.* [*59*] based on tomographic evaluations, which illustrate that high rotational speeds of about 1200 min^{-1} lead to significant maldistribution and a reduced overall liquid hold-up within the packing. When the results for the short packings in the lab and pilot-scale RPB are compared, it can be seen as an indicator that the end effect related to the surface area generated in the casing is smaller than in the eye of the rotor. The lab-scale RPB provides one-fourth of the geometrical casing surface area (0.22 m^2) compared to the pilot-scale RPB (0.89 m^2), yet shows a comparable mass transfer rate at equivalent loads.

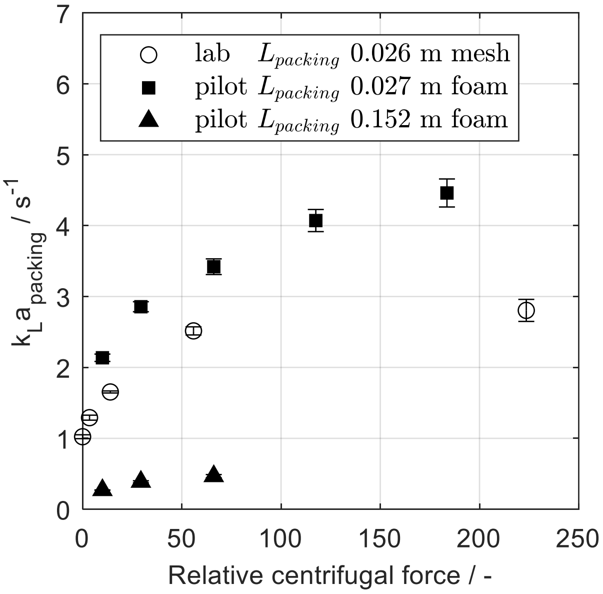

Figure 4.5: Evaluation of liquid-side mass transfer coefficient (k_La) for the pilot-RPB and the lab-RPB at comparable liquid loads (pilot 80 $m^3 m^{-2} h^{-1}$ lab: 56 $m^3 m^{-2} h^{-1}$) and $\dot{V}_G = 1.67\cdot10^{-3}$ m^3 s^{-1}. Error bars depict the standard deviation (Reprinted (adapted) with permission from [*96*]. Copyright 2020 American Chemical Society).

Finally, Figure 4.6 relates the overall degassing efficiency according to (35) to the mass transfer coefficient. The extended packing length shows at relative centrifugal forces < 100 a superior degassing efficiency compared to the results with the shorter packing length, while the results of the $k_La_{packing}$-value show opposite results. The $k_La_{packing}$-value is significantly smaller for the larger packing size. These diverging trends may look counter-intuitive at first glance, but they are a sign that the added packing volume at a higher radius is used less efficiently, while still contributing to the overall mass transfer. The combination of a larger packing radius and additional packing volume leads in total to an increased mass transfer efficiency. Even though the increase is in the range of mere percent, it enables the product quality of less than 50 ppb at a rotational speed of 600 min^{-1} (RCF_i: 63) while with the short packing length it would need 1200 min^{-1} (RCF_i: 118) to achieve comparable quality. Due to the reduction of the rotational speed by 50 % the power consumption reduces by 20 % for LL_i of 80 m^3 m^{-2} h^{-1}.

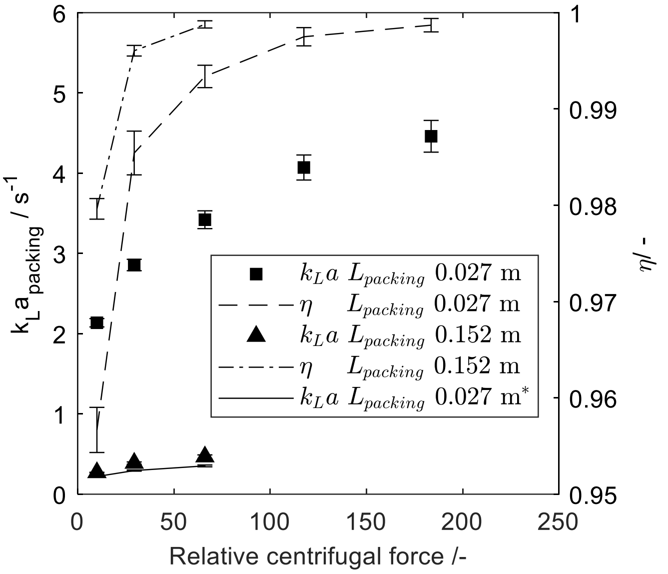

Figure 4.6: Degassing efficiency and k$_L$a-values of the pilot-RPB for equivalent liquid loads LL_i = 80 m^3 m^{-2} h^{-1} at a gas flow rate of $\dot{V}_G$ = 1.67·10^{-3} m^3 s^{-1}, *denotes the theoretical k_La-value when the reference volume is changed to the volume of $L_{packing}$ =0.152 m. Error bars depict the standard deviation (Reprinted (adapted) with permission from [*96*]. Copyright 2020 American Chemical Society).

4.3.3 Comparison of foam and mesh packing types for the pilot-scale RPB

Two different packing types (foam and mesh) were compared in the co-current operating mode in the pilot-RPB based on their estimated mass transfer coefficient, calculated according to equation (33). As apparent from the illustration of the volumetric mass transfer coefficients at different rotational speed depicted in Figure 4.7, the k$_L$a$_{packing}$ of both packing types is in a similar range, with a maximum reduction of the k$_L$a-value by 15 % for $\dot{V}_L$=2.67·10^{-4} m^3 s^{-1} compared foam to mesh. For all rotational speeds, the k$_L$a-value increases with an increasing liquid flowrate and an increasing rotational speed. This increase is qualitatively in agreement with the publications of *Chen et al.* [*71*] and *Beer et al.* [*72*], who performed counter-current deaeration and co-current flash degassing, respectively.

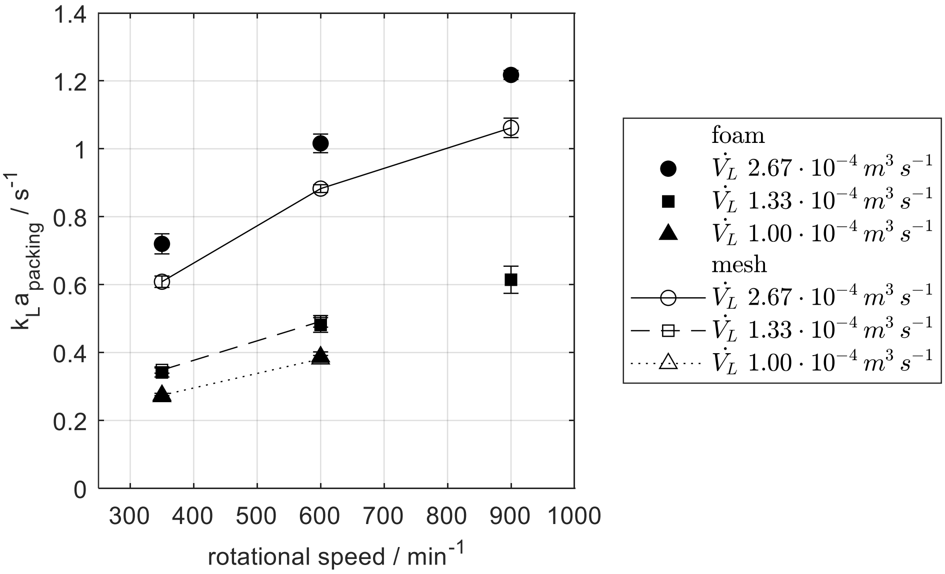

Figure 4.7: Comparison of the different k_La-values based on the packing volume for the pilot-RPB equipped with stainless steel mesh and foam and $\dot{V}_G = 1.67 \cdot 10^{-3}$ m^3 s^{-1} packing dimensions (d_i, d_o, $h_{packing}$): mesh (0.146 m, 0.460 m, 0.01 m), foam (0.146 m, 0.450 m, 0.01 m). Error bars depict the standard deviation (Reprinted (adapted) with permission from [*96*]. Copyright 2020 American Chemical Society).

4.3.4 Summary and conclusion

The co-current investigation presents a dedicated analysis of different packing types for the deaeration with nitrogen as stripping gas. It is shown that knitted mesh and metal foam packings provide approximately similar performance, judging from the derived $k_La_{packing}$-values. However, the metal foam packings provide superior handling compared to knitted mesh due to the rigid form. Furthermore, it is shown that liquid dispersion inside a rotating empty rotor can have a significant contribution to the mass transfer rate. However, additional surface added by the metal foam packing increases the k_La_{rotor}-value further. The scale-up of an RPB was evaluated by comparison of mass transfer experiments inside a lab-scale and a pilot-scale RPB. Under similar liquid loads, radial packing length and comparable relative centrifugal accelerations (RCF) similar $k_La_{packing}$-values were determined. The scale-up in terms of an increased mass transfer performance has further been evaluated based on the investigation of two radial packing lengths (0.027 m, 0.152 m). It was shown that the increased packing volume for the larger radial packing length improves the overall mass transfer to an extent that enables a sufficient degassing at a 50 % lower rotational speed. Yet, the volumetric mass transfer coefficient reduces to a considerably lower $k_La_{packing}$-value for the larger radial packing length compared to the shorter packing length, indicating the importance of non-constant k_La-values for scale-up computations.

Future works should address the radial dependence of the k_La-value to increase the efficiency of a larger radial packing length. Maldistribution in the tangential and radial direction should be avoided by the design of the packing. Directly addressing the variations in the cross-sectional area seems to be a promising direction. A well-designed RPB balances the dependencies of the mass transfer rate on packing length and rotational speed to save costs and energy. For such investigations on the design of the packing, an online measurement along the radius would be beneficial to understand how the concentration changes alongside the rotor. The characterization of the residence time distribution would furthermore allow for a more detailed insight into the flow behavior and axial dispersion of the fluids. At these small scales, backmixing will also have a significant influence on the separation efficiency, especially for counter-currently operated processes.

4.4 Counter-current

The following chapter focuses on the counter-current deaeration process. Nitrogen is used as a stripping gas to remove the oxygen from the liquid phase at atmospheric conditions. Results based on process parameters (gas, liquid flow rate and rotational speed) and machine parameters (distributor, packing type, packing height) are presented.

4.4.1 Theoretical improvement due to counter-current contact

The counter-current deaeration is a promising alternative to the co-current deaeration. Co-current deaeration is limited to one equilibrium stage. If the RPB could facilitate approximately 1.5 theoretical stages through counter-current contact, the corresponding outlet concentration reduces significantly compared to co-current contact due to the improved utilization of the driving force. Figure 4.8 illustrates that a broad range of gas flows between 1 and 6 $m^3 h^{-1}$ enables a liquid oxygen outlet concentration below 50 $\mu g\ L^{-1}$. In contrast to the counter-current configuration, the co-current process depends strongly on the applied gas flow rate.

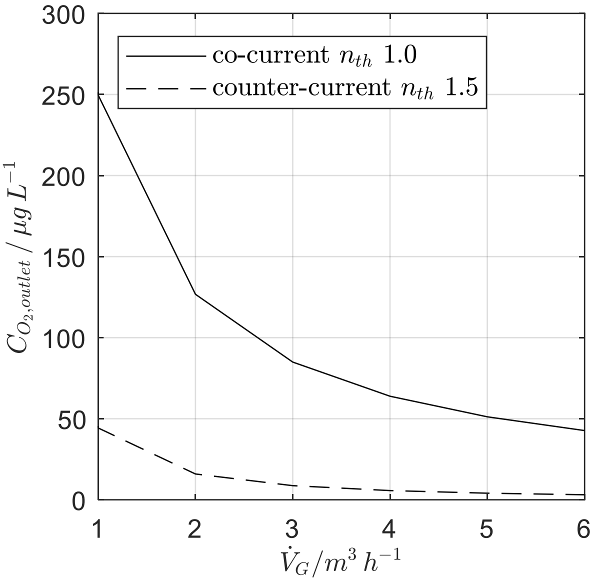

Figure 4.8: Theoretical liquid outlet oxygen concentration for co- and counter-current operation for saturated liquid $\dot{V}_L$ = 1 m^3 h^{-1}, $C_{O_2,inlet}$ = 8200 µg L^{-1} (p = 1.01325 bar T = 25°C).

4.4.2 Liquid flow rate

The knitted mesh packing (KM) shows increased performance at higher liquid flow rates. Liquid flow rates of 0.960 m^3 h^{-1} lead to the biggest $k_La_{packing}$-value. The $k_La_{packing}$-value is proporational to the rotational speed. Figure 4.9 shows in dotted and solid lines the calculated boundaries for outlet concentrations of 6 µg L^{-1} and 1 µg L^{-1}. It is evident that for a rotational speed above 1000 min^{-1} in most cases the measured values are in the range of 6 µg L^{-1} and 1 µg L^{-1}. Even though, the sensor accuracy is 2 µg L^{-1} as specified by the manufacturer the results should be handled with caution because small inaccuracies in the measurement have a considerable influence on the k_La-value. In all following chapters the 6 µg L^{-1} and 1 µg L^{-1} boundaries will be marked if relevant for interpretation.

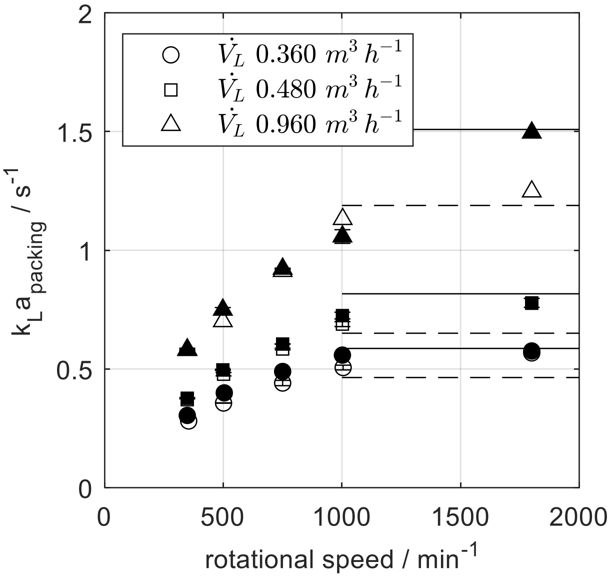

Figure 4.9: Variation of the k_La-value with increasing rotational speed and different liquid flow rates for the knitted mesh packing. $\dot{V}_G = 6$ m^3 h^{-1}; ○ 360° distributor; ● 90° distributor; Solid line(-) denotes the theoretical maximum (<1 µg L^{-1}). Dashed line(--) denotes low outlet concentrations (<6 µg L^{-1}). Error bars depict the standard deviation.

4.4.3 Distributors

As described in section 4.2.1, two distributor types have been investigated with the KM packing for counter-current deaeration. Both distributors, one with a 360° spraying angle the otherone with a 90° spraying angle, were designed to give an equivalent liquid jet outlet velocity. The results show no significant difference between both distributors (cf. Figure 4.9). It has been expected that the radically lower spraying angle of the 90°-distributor would lead to significantly increased maldistribution. However, it is imaginable that the high rotational speed leads to a frequent wetting of the packing. For the lowest rotational speed (350 min^{-1}) the non-wetted time interval for the 90° spraying angle translates to around 130 ms according to (39). Based on the results from gamma-ray tomography an average hold-up of about 15 % is assumed (cf. Figure 3.23). The estimated mean residence time of the liquid is in the range of 2 s. It is shown that a non-wetting interval of approximately 130 ms is not having a negative influence on the mass transfer results for the counter-current deaeration in the investigated range.

$$t_{non-wetting} = \frac{2\pi\, r}{\omega\, r}\frac{3}{4} = 129\ ms \tag{39}$$

$$t_{mean,residence} = \frac{V_{packing}\,\varepsilon_L}{\dot{V}_L} = \frac{1.42\ L\ 0.15}{6.3\ L\,\mathrm{min}^{-1}} = 2\ s \qquad (40)$$

4.4.4 Gas flow rate

The gas flow rate has no significant influence on the mass transfer coefficient in the range between 3 and 6 $m^3 h^{-1}$ and a rotational speed of 900 min^{-1} (Figure 4.10a). If $\dot{V}_G$ is decreased by two orders of magnitude, an approximately 70 % reduction of k_La-value can be observed. This is of technical importance. Lower amounts of stripping gas lead to lower operational costs. However, if at very low gas flow rates the deaeration task cannot be fulfilled anymore a compensation, e.g. by enlarging the radial packing length, is needed. As shown in the co-current investigations (cf. 4.3) and tomography measurements(cf. 3.3.3), radial scaling of the packing is complex and requires detailed knowledge about liquid behavior inside the packing. The variation of the gas flow rate should aim at small gas flow rates with a reasonable efficiency loss. In both cases the same number of theoretical stages is reached (cf. Figure 4.10b). However, due to the different gas loads less oxygen is removed from the liquid phase for the lower gas flow rate. For rising liquid flow rates an increasing trend of the $k_La_{packing}$-value is observed.

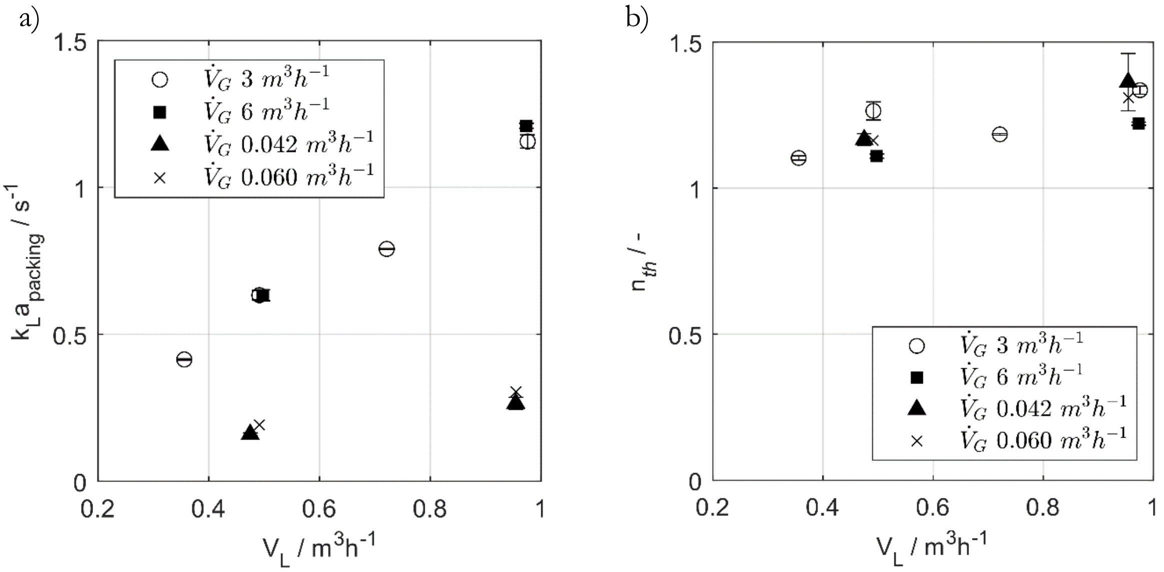

Figure 4.10: Variation of the k_La-value a) or the number of theroretical stages b) with increasing liquid flow rate and different gas flow rates for the full foam (FF) packing n_{rot} = 900 min^{-1}. Error bars depict the standard deviation.

4.4.5 Packing type

Identical to the co-current experiments, two types of packing were investigated. Knitted mesh and FF packing showed very similar behavior (cf. 4.3.3). Experiments in counter-current operation validate these results. At a flow rate of 0.480 $m^3 h^{-1}$ the performance of mesh and foam is equivalent. When the flow rate is doubled to 0.960 $m^3 h^{-1}$ the foam performs approximately 16 % better than the mesh.

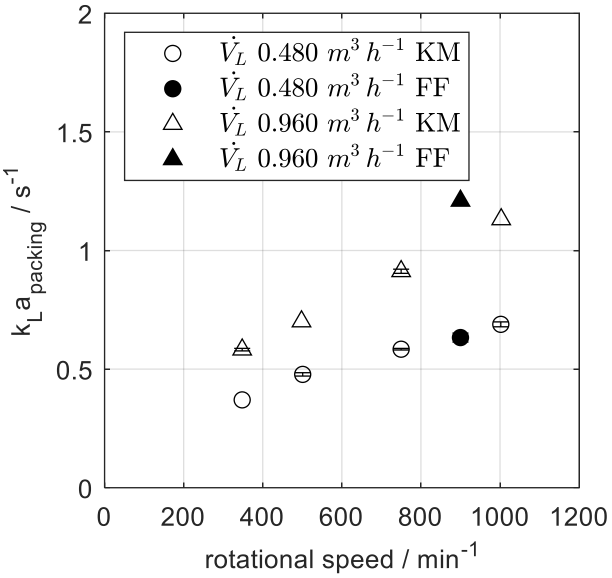

Figure 4.11: Variation of the k_La-value with increasing rotational speed and different liquid flow rates for the knitted mesh(KM) and full foam (FF) packing $\dot{V}_G = 6$ $m^3 h^{-1}$. Error bars depict the standard deviation.

To validate the scale-up criteria of a constant load at the inner surface area of the packing, experimental runs have been conducted with two different packing heights (0.01, 0.02 m) for the FF packing. Figure 4.12a illustrates that there is no variation in the k_La-value when equivalent gas- and liquid loads at the inner packing diameter are considered. As in previous investigations (cf. 4.4.2) an increasing liquid load results in an increased k_La-value. Moreover, there is only little variation in the k_La-value with the rotational speed observed. Figure 4.12b shows the parity-plot for both packing heights, both packings show a variation smaller than 30 % the maximal relative deviation is 14 %.

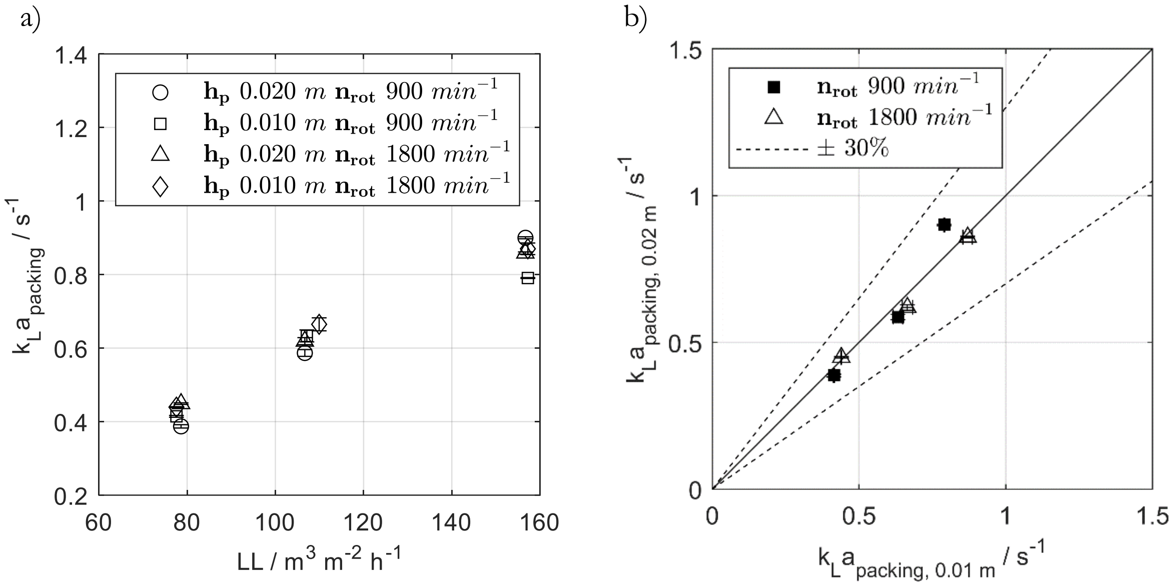

Figure 4.12: a) Variation of the k_La-value with liquid load and different rotational speeds b) Parity-plot: for packing heights (h_p) 0.01; 0.02 m; full foam (FF) packing; F_G= 0.197 $Pa^{0.5}$. Error bars depict the standard deviation.

4.4.6 Comparison to column packings

In Figure 4.13 the deaeration data for the RPB is evaluated against the packing data for 1-inch Raschig rings available in the literature and published for comparable gas and liquid loads(cf. 2.2.3). The k_La-values are significantly larger for the RPB than for the column. The difference lies within the range of one order magnitude for comparable liquid loads. A linear increase with the liquid load is found for the RPB, the same trend is observed for the column packing but at lower liquid loads (cf. Figure 2.7). For liquid loads above 100 $m^3 m^{-2} h^{-1}$ a significant flattening of the k_La-value is observed for the Raschig ring packing in the column. There are two possible explanations for this behavior, the accuracy of the oxygen measurement is too low to show a further decrease in the oxygen concentration or the packing performance is decreasing because it reaches its capacity limit. The high liquid loads will generate thicker films and increase the liquid hold-up, which hinders intensive contact between gas and liquid. The RPB does not show the mentioned behavior in the investigated range, high centrifugal forces support the distribution of the liquid on the high surface packing as thin films and droplets. The results recommend the application of the RPB with a high surface metal foam packing (1000 $m^2 m^{-3}$) in the deaeration, especially for high liquid loads.

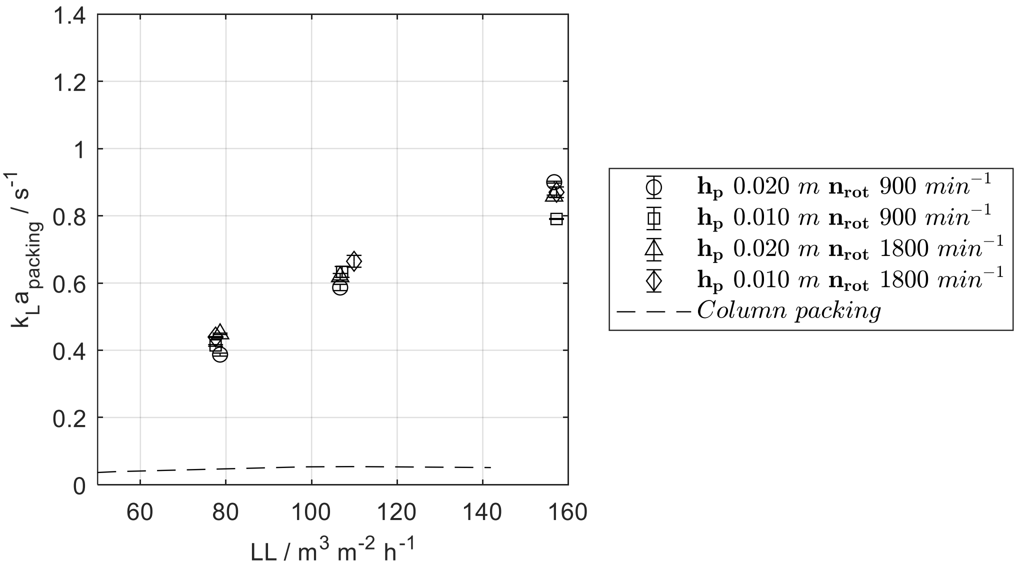

Figure 4.13: Variation of the k_La -value with liquid load and different rotational speeds for the RPB packing heights (h_p) 0.01; 0.02 m; full foam (FF) packing; F_G= 0.197 $Pa^{0.5}$ was applied. The column data for 1-inch Raschig rings are taken from [*41*, p. 715] and are described in 2.2.3. Error bars depict the standard deviation.

4.4.7 Summary

As in co-current operation, the liquid flow rate increases the k_La-value of the packing. When the rotational speed is increased the k_La-value increases further until a plateau is reached. It should be considered that the plateau could not be verified due to the accuracy error of the sensors. No influence of the gas flow rate was found for the range of 3 to 6 m^3 h^{-1}. A drastic reduction of the gas flow rate to 0.042 to 0.060 m^3 h^{-1} led to a strong decrease in the k_La-value. The investigated distributors with a 360° spraying angle and a 90° spraying angle showed no significant difference. Metal foam packing and knitted mesh showed a comparable performance which is in line with the findings of the co-current investigation (cf. 4.3.3). The axial scaling of the packing height was successful for a 0.01 m and 0.02 mm packing which showed less than 30 % deviation. Compared to column packings an around 8 times higher k_La-value was found.

5 Modeling

The modeling section addresses the radial change in the $k_L a$-value and the solution of the boundary value problem for co- and counter-current operation. Literature correlations are used to predict the experimental data. Furthermore, operational and investment costs are estimated. Finally, the results are used to estimate the costs of an industrial deaeration process applying the RPB.

Parts of chapter 5 are published in:

Groß, K.; Beer, M. de; Dohrn, S.; Skiborowski, M.; Scale-Up of the Radial Packing Length in Rotating Packed Beds for Deaeration Processes, Ind. Eng. Chem. Res., 2020, 59(23), 11042-11053, DOI: http://doi.org/10.1021/acs.iecr.0c00868

Lukin, I.; Pietzka, L.; Groß, K.; Górak, A.; Schembecker, G.; Economic evaluation of rotating packed bed use for aroma absorption from bioreactor off-gas; Chem. Eng. Process., 2020, 154, 108011, DOI: https://doi.org/10.1016/j.cep.2020.108011

A detailed overview including student contributions can be found in chapter 11. Scientific advice was given by A. Górak, M. Skiborowski and the corresponding co-authors

---

5.1 Radial $k_L a$ modeling

Experimental data can easily be used to calculate an average mass transfer coefficient based on the inlet and outlet concentrations of the gas and liquid streams. However, as explained in chapter 4.3 there is a strong indication for a non-linear behavior of the $k_L a$-value with a change in the radial position of the rotor. It is mandatory to account for this radial change in the $k_L a$-value for an accurate estimation of the mass transfer performance. To create a flexible framework a model was implemented in the MATLAB R2020a®-environment. The core of the model is the mass balance

$$\frac{dc_L}{dr} = -\frac{k_L a}{\dot{V}_L}\left(c_L - H_{O_2}^{CC}\, c_G\right) 2\,\pi\, z\, r \tag{41}$$

co-current

$$\frac{dc_G}{dr} = \frac{k_L a}{\dot{V}_G}\left(c_L - H_{O_2}^{CC}\, c_G\right) 2\,\pi\, z\, r \tag{42}$$

counter-current

$$\frac{dc_G}{dr} = -\frac{k_L a}{\dot{V}_G}\left(c_L - H_{O_2}^{CC}\, c_G\right) 2\,\pi\, z\, r \tag{43}$$

It should be noted that the differential equation for the gas phase mass balance and boundary conditions change depending on co- or counter-current process configuration. Moreover, the k_La-value can be a function of radius, hydraulic characteristics and packing morphology. Plug flow of gas and liquid phase is assumed.

Boundary conditions:

co-current:

$$c_L(r_i) = c_{L,in} \tag{44}$$

$$c_G(r_i) = c_{G,in} \tag{45}$$

counter-current:

$$c_L(r_i) = c_{L,in} \tag{46}$$

$$c_G(r_o) = c_{G,in} \tag{47}$$

To solve the set of differential equations the bvp5c-solver from MATLAB® is used. The finite difference implicit Runge-Kutta implementation uses the four-stage Lobatto IIIa formula. [*97*] Further information on the model can be found in the appendix B3.

5.1.1 Co-current

The potential to predict the volumetric mass transfer coefficients based on the correlation of *Chen et al.* [*71*] (cf. equation (17)) is evaluated for the specific experimental results. As illustrated by Figure 5.1 the prediction of the k_La-value with the correlation of *Chen et al.* [*71*] for the different packing lengths is surprisingly accurate, considering that it was derived for packings with a maximal outer radius of 0.06 m [*70*]. It sufficiently reflects the curvature of the k_La-curve, only the predicted values at increased RCF-values show somewhat larger deviations. The detailed analysis of the different factors contributing to the k_La-value shows, that most of the contributions are not influenced by the change in the outer packing diameter (Figure 5.2), even though the geometric dimensions change, Reynolds-, Grashof- and Weber-contributions are almost constant. Moreover, while Reynolds- and Weber-contributions are diminished by the decreasing specific liquid load, this effect is compensated by an increasing centrifugal acceleration which positively influences the Grashof-contribution. The geometrical correction factor

$$C_{geo} = \frac{D\, a_p}{d_{spherical}\left(1-0.94\frac{V_o}{V_{total}} - 1.13\frac{V_i}{V_{total}}\right)} \tag{48}$$

introduces the most significant change, as it decreases by approximately 80 % with the increase in the outer packing diameter.

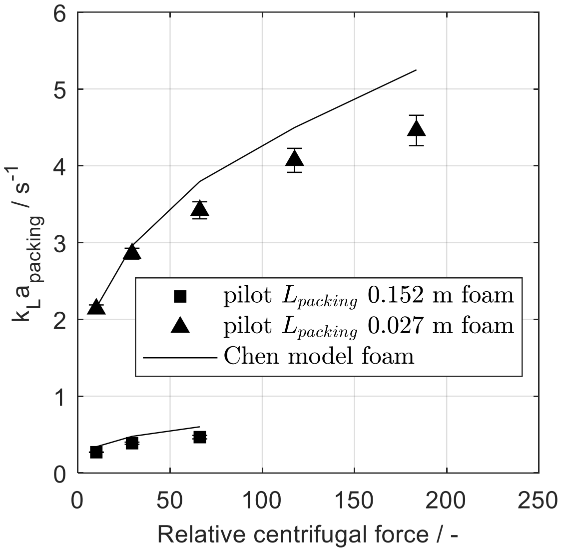

Figure 5.1: Comparison of experimental and model results according to *Chen et al. [71]* for the pilot-RPB at liquid loads of 80 $m^3 m^{-2} h^{-1}$ and $\dot{V}_G$=1.67·10^{-3} m^3 s^{-1}. Error bars depict the standard deviation. (Reprinted (adapted) with permission from [*96*]. Copyright 2020 American Chemical Society).

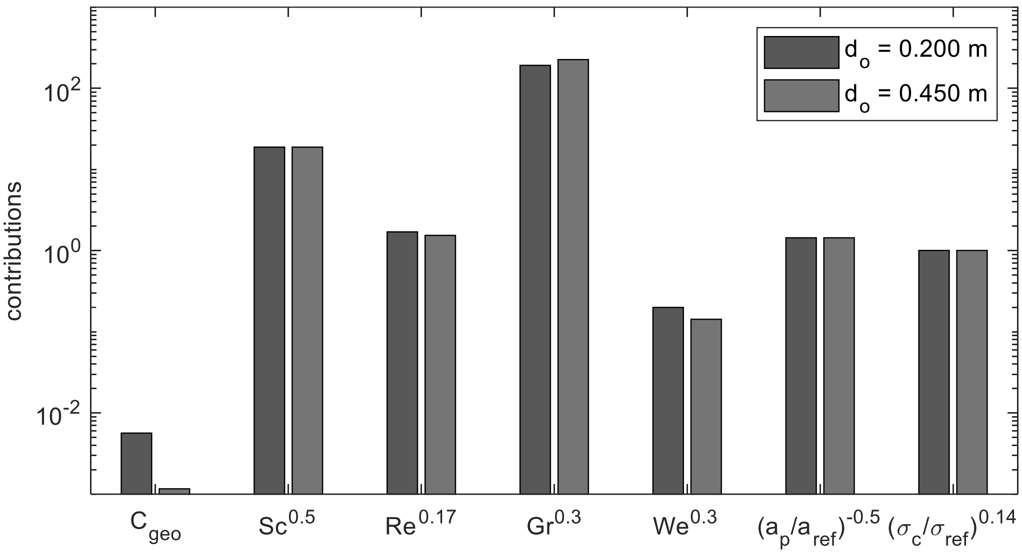

Figure 5.2: comparison of the different contributions on the k_La-value based on the Chen-correlation [*70*]. For $\dot{V}_L$= 1.00x10^{-4} $m^3\ s^{-1}$, $C_{geo} = \frac{D\ a_p}{d_{spherical}\left(1-0.94\frac{V_o}{V_{total}} - 1.13\frac{V_i}{V_{total}}\right)}$ (Reprinted (adapted) with permission from [*96*]. Copyright 2020 American Chemical Society).

In Figure 5.3 and visually enlarged in Figure 5.4 the parity plots of estimated and experimental data are displayed for varying liquid flow rates at a constant gas flow rate. These changes in the k_La-value are well reflected by the correlation of *Chen et al.* [*71*], for which an acceptable error of ±30 % was determined for the compilation of measurement data produced in the scope of the current study. It needs to be noted that the correlation seems to overpredict the k_La-value when the relative centrifugal force (RCF) becomes large.

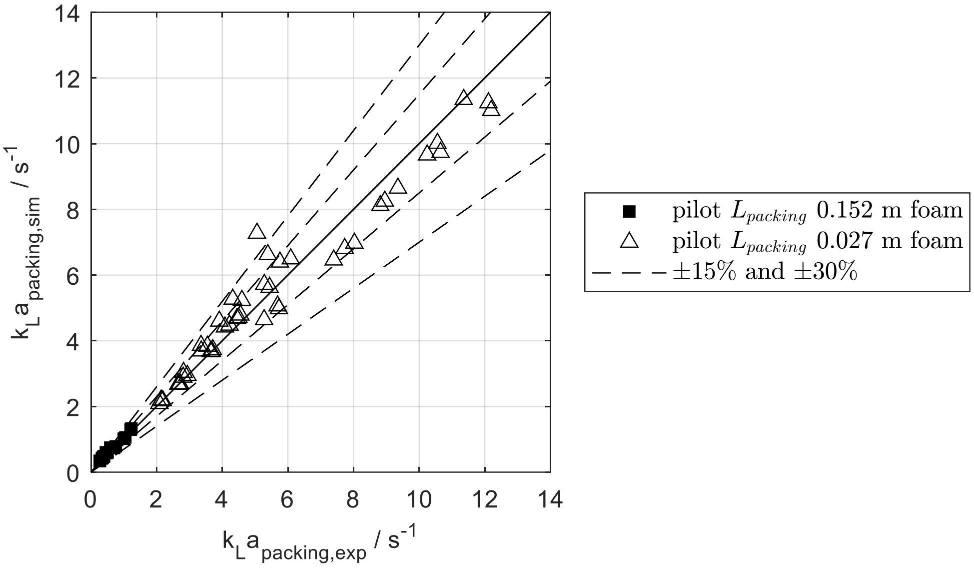

Figure 5.3: parity plot of experimental and model results according to *Chen et al. [71]* $\dot{V}_L$ =1x10^{-4}-2.67x10^{-4} m^3 s^{-1}; $\dot{V}_G$= 1.67·10^{-3} m^3 s^{-1} (Reprinted (adapted) with permission from [*96*]. Copyright 2020 American Chemical Society).

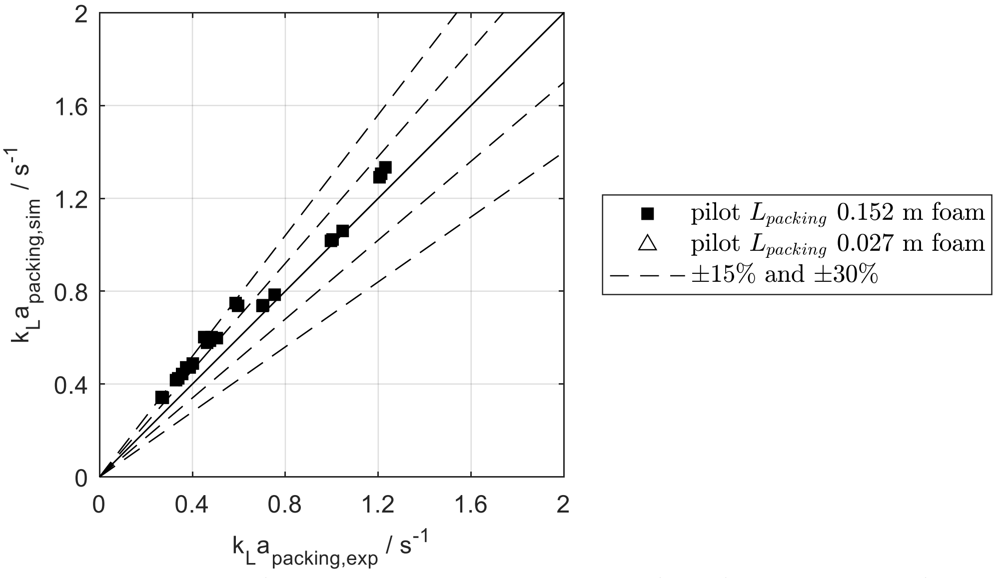

Figure 5.4: Visually enlarged parity plot of experimental and model results according to *Chen et al.* [*71*] $\dot{V}_L$= =1x10^{-4}-2.67x10^{-4} m^3 s^{-1}; $\dot{V}_G$= 1.67·10^{-3} m^3 s^{-1} (Reprinted (adapted) with permission from [*96*]. Copyright 2020 American Chemical Society).

5.1.2 Counter-current

The results for the counter-current deaeration show a moderate overprediction of the k_La-value for most cases. The average overprediction is 34 %±26 % based on standard deviation (cf. Figure 5.5a). The maximal deviation is 109 %. Deviations above 50 % are especially found for results above 1800 min^{-1}. A reasonable explanation is that the influence of the centrifugal force for the different radial packing length was investigated for an RCF_i of up to 126 by *Chen et al.* [*70*], whereas at the maximal rotational speed of 1800 min^{-1} investigated in this work an RCF_i of 264 was reached. Hence, it is shown that the results of the correlation cannot be extrapolated to higher centrifugal forces. This observation further fosters the assumption that the k_La-value is negatively influenced by maldistribution at high centrifugal forces as was seen in the results from the gamma-CT measurements (cf. 3.3). Excluding the results for the rotational speed of 1800 min^{-1} the average overprediction reduces to 22 %±12 % based on standard deviation, which is an acceptable result. The overprediction of the k_La-value results in a maximal underprediction of the oxygen outlet concentration of 91 μg L^{-1} (cf. Figure 5.5b)

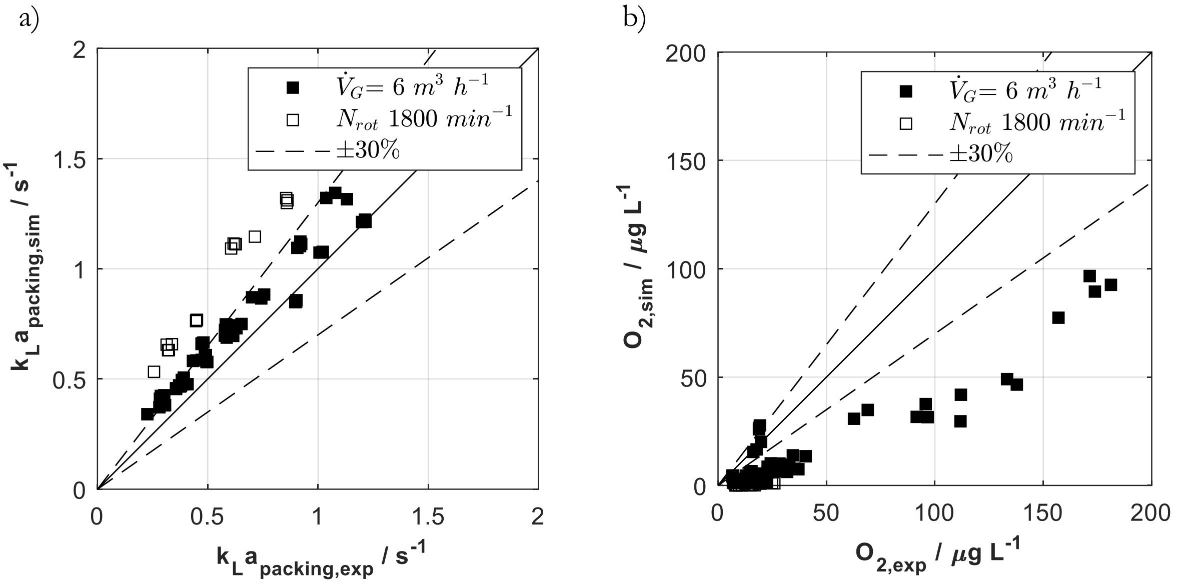

Figure 5.5: Parity plot of the estimated k_La-value and the experimental k_La-value for full foam (FF) (di/do/hp) 0.146/0.450/[0.01,0.02] m and knitted mesh packings. 0.146/0.460/0.01. LL_{max} varied between 40 and 213 m^3 m^2 h^{-1}.

Besides the mentioned extrapolation of the correlation, there are additional potential reasons for the overprediction of the k_La-value. The correlation relies on the exact specification of the packing characteristics. Some of the packing data must be estimated from literature correlations (e.g. the specific packing surface of the knitted mesh), others are delivered by the manufacture (e.g. specific surface area of the metal foam packing). The fact that these parameters may differ from the true value may increase the difference between correlation and result. Furthermore, the experiments were conducted in a pilot-scale machine that has a larger packing length than the original packing investigated by *Chen et al.* [*70*] and the influence of the casing or other end-effects could just be estimated indirectly from the overall-mass transfer rate. An increased casing contribution in the lab-scale RPB of *Chen et al.* [*70*] could facilitate the overestimation for larger RPBs. However, to eliminate uncertainties in end-effect contributions an online concentration measurement within the rotor would be extremely beneficial, which was unfortunately not available in this work or other publications known to the author.

5.2 Cost estimation

The cost estimation divides into operating expenditures (OPEX) and capital expenditures (CAPEX). In this chapter OPEX will be estimated from energy requirements, while CAPEX are calculated according to the equipment cost correlations from *Woods [98]*, which was especially suitable due to a large amount of quantitative cost data.

5.2.1 Capital expenditures

The capital costs for equipment are calculated from the modified free-on-board (FOB) costs. FOB costs do not account for installation or other indirect costs. The FOB costs are adjusted to the size of the equipment by the capacity method. The capacity method has the general form of

$$Cost_2 = Cost_{ref}\left(\frac{size_2}{size_{ref}}\right)^n \tag{49}$$

where the reference costs ($Cost_{ref}$) are scaled based on a characteristic size dimension (e.g. diameter, flow rate or power consumption) to the costs of an estimated equipment ($Cost_2$). To convert the FOB costs to total-module (TM) costs the cost factor method is used. The overview of the calculation process is given in Figure 5.6. Tab. 10 illustrates the different cost factors. The highest values for the cost factors A to E are assumed. The optional contributions (F-K) were not considered because they are strongly fluctuating based on plant location and industry sector. The amortization factor to convert the capital cost to a yearly basis was set to 33 %, consisting of 10 % annual capital depreciation, 10 % interest rate, 10 % profit margin and 3 % maintenance [*17*].

$$\mathrm{TM} = \underbrace{\underbrace{\underbrace{\underbrace{(\mathrm{FOB}\ (\mathrm{L+M}^{*} + (\mathrm{FM}-1))\ \mathrm{CF})}_{\text{L+M*-cost}} + \mathbf{A}\cdot\mathrm{FOB}}_{\text{Physical module cost (PM)}} + \mathbf{B}\cdot(\mathrm{L+M})}_{\text{Bare module cost (BM)}} + (\mathbf{C}+\mathbf{D}+\mathbf{E})\cdot\mathrm{BM}}_{\text{Total module cost (TM)}} + \text{optional factors}$$

Figure 5.6: Cost calculation based on Woods [*98*].

Tab. 10: Cost factors according to *Woods* [*98*] FOB= free-on-board; L+M = labour and material cost included, BM = bare module cost, TM = total module cost.

No.	Cost factors	Range
A	taxes, freight and insurance	15–25 % FOB cost
B	offsites, indirects for home office and field expenses	10–45 % of L+M
C	contractors fees	3–5 % BM
D	contingency for unexpected delays	10–15 % BM
E	design contingency for changes in scope during construction	10–30 % BM
	optional	
F	royalties and licenses	no guideline
G	land	1–2 % TM
H	spare parts	1–2 % TM
I	legal fees	1 % TM
J	working capital	For year-round commodities (15–20 % TM); For seasonal commodities (25–40 % TM). For specialties and pharmaceuticals (15–40 % of sales).
K	startup expenses	15–40 % TM

RPB equipment cost

The current publications on cost estimation and profitability analysis [*98–100*] do not offer correlations to estimate the equipment cost for an RPB. All of the above-mentioned offer correlations for centrifugal apparatuses as solid-liquid separating centrifuges or liquid-liquid extraction centrifuges. While correlations based on real RPB-data are missing in this work we will estimate the cost of RPBs by other related centrifugal equipment, assuming that sealings, bearings and mechanical stability are the main cost factors which are in both types of equipment comparable. Filtering centrifuges for solid-liquid separation consist of a basket on which the cake builds up. This cake can be continuously removed (continuous pusher) or in batch operation (peeler centrifuge), where the cake is removed by a peeler after it reaches a certain height. Different washing steps are used to remove impurities or solvents from the solid particles. However, a transformation of a filtering centrifuge into an RPB is imaginable, by replacing the cake with a high porous packing, removing solids from the suspension and adding a gas stream. Therefore, the filtering centrifuge correlation of *Woods et al.* [*98*, p. 411] is used. The specification for a vertical basket: under-driven with a batch top discharge is selected because it is very similar to the industrial design depicted by *Trent* [*14*, p. 75] for the HOCL production. The FOB costs can be calculated by

$$L + M^{*} - \ Cost = 60\,000\$ \left(\frac{d_o}{0.6\,m}\right)^{1.04} \left(\mathrm{L{+}M}^{*} + (FM - 1)\right) \cdot \mathrm{CF} \tag{50}$$

where $\mathrm{L{+}M}^*$ denotes the additional labor and material costs excluding additional labor and material costs for instrumentation. FM denotes the material cost factor and CF the complexity cost factor to define certain configurations of the equipment e.g. including motor etc. The height of the basket is only indirectly incorporated in the correlation. Based on commercially available filtering centrifuges a height to diameter ratio between is found between 0.25 and 0.70. [*101*, p. 11, *102*, p. 9].

Tab. 11: Sizing parameter, material factors and other factors according to *Woods* [*98*, p. 165] for a vertical basket filtering centrifuge.

Sizing parameter		**Complexity Factor (CF)**	
0.3 m ≤ d_o ≤ 1.25 m		Including motor drive	1.35
Material Factors (FM)		**Other Factors**	
carbon steel	1.0	L+M*	3
stainless steel 1.4401	1.5	$\mathrm{CEPCI}_{\mathrm{ref}}$	1000
rubber lined	1.2		

Pump equipment cost

The pump equipment costs are calculated according to the costs of a gear pump [*98*, p. 385]. The correlation is not specified for a certain range to avoid large estimation errors a maximal shift in the order of a factor of 10 is allowed. For lower or higher values equipment costs are calculated at the boundary.

$$L + M^{*} - \ Cost = 6\,000\$ \left(\frac{V_L}{0.01\, m^3\, s^{-1}}\right)^{0.43} \left(\mathrm{L{+}M}^{*} + (FM - 1)\right) \cdot \mathrm{CF} \tag{51}$$

Tab. 12: Sizing parameter, material factors and other factors according to *Woods* [*98*, p. 385] for a gear pump.

Sizing parameter		**Complexity Factor (CF)**		
$0.001\ m^3 s^{-1} \leq V_L \leq 0.1\ m^3 s^{-1}$		base plate, open drip-proof motor		1.00
Material Factors (FM)		**Other Factors**		
cast iron	1.0	L+M*	2.3	
stainless steel 1.4401	2.4	CEPCI_{ref}	1000	
glass-lined	3.6			
bronze	1.4			

Blower/fan equipment cost

Due to low pressure drop a fan delivers a sufficient pressure increase for a wide range of applications. The costs are calculated for a radial bladed centrifugal fan including TEFC motor, starter and gearing [*98*, p. 380].

$$L + M^{*} - \ Cost = 27\,750\$ \left(\frac{V_{G,in}}{10\, Nm^3 s^{-1}}\right)^{0.93} \left(\mathrm{L{+}M}^{*} + (FM - 1)\right) \cdot \mathrm{CF} \tag{52}$$

Tab. 13: Sizing parameter, material factors and other factors according to *Woods [98, p. 380]* for a centrifugal radial bladed fan.

Sizing parameter		**Complexity Factor (CF)**		
$2\ Nm^3 s^{-1} \leq V_{G,inlet} \leq 50\ Nm^3 s^{-1}$		TEFC motor, starter, gearing		1.00
Material Factors (FM)		**Other Factors**		
carbon steel	1.0	L+M*	1.7	
fiberglass	1.8	CEPCI_{ref}	1000	
stainless steel 1.4401	2.5	Δp_{max}	2500 Pa (g)	

5.2.2 Operational expenditures

The operational expenditures for RPB, pump and blower are based on power requirements.

$$OPEX\ Cost = t_a \cdot \kappa_{energy} \cdot P \tag{53}$$

The annual operating hours per year (t_a) are set to 8000 h a^{-1}, the specific energy costs are set to 0.1 € kWh^{-1}. The power consumption for the RPB is calculated according to the empirical correlation of this work (cf. 3.5). The ideal pump power requirement is calculated by

$$P_{pump,ideal} = \dot{V}_L \cdot \Delta p_{nozzle} \tag{54}$$

$$\Delta p_{nozzle} = \frac{\rho}{2}\left(\frac{\dot{V}_L}{A}\right)^2 \tag{55}$$

where Δp_{nozzle} is the ideal pressure drop for spraying the liquid through the nozzles at the liquid distributor. Due to the small height differences in RPB application, the height contribution on the power consumption is neglected.

The ideal fan power requirement is calculated by assuming ideal gas behavior by

$$P_{fan,ideal} = \frac{\kappa}{\kappa-1} \cdot V_{G,in} \cdot p_{in} \cdot \left[\left(\frac{p_{out}}{p_{in}}\right)^{\frac{\kappa-1}{\kappa}} - 1\right]. \tag{56}$$

The ideal pump or fan power requirement can be translated to the real power requirement with the pump efficiency (η) by

$$P_{real} = \frac{P_{ideal}}{\eta} \tag{57}$$

the pump efficiency (η_{pump}) is the combined efficiency of the mechanical efficiency of the pump and the efficiency of the motor and needs to be adjusted for the specified pump. A general pump and fan efficiency of 0.6 is selected, both are conservative estimates.

5.3 Software assisted process design

The reluctant implementation of the RPB as a new equipment type in the chemical industry may have several reasons. Firstly, there are only limited and vague guidelines for the design and operation of the RPB available in the literature. Secondly, the identification of promising fields of application is hindered by a limited understanding and in particular the missing 'feel' for the working areas of the RPB (gas and liquid loadings, pressure drop, energy requirement etc.). Moreover, misconceptions e.g. that the additional rotation of the machine is a significant cost driver for the operating cost further foster the standing of separation columns as the optimal solution for all gas-liquid separations. To address this issue and to enable intuitive training on the RPB concept a software-assisted process design is implemented via the MATLAB® appdesigner environment.

The application guides the user through the hydraulic design of the equipment (cf. Figure 5.7). Process conditions e.g. gas and liquid flow rates are defined, based on the selected packing characteristics. The dry pressure drop is calculated by the experimentally validated model of *Neumann et al.* [*48*] (cf. 3.2.1). For the metal foam packing the wet pressure drop can be additionally estimated by the artificial neural network correlation (cf. 3.2.3). Furthermore, the minimal allowable rotational speed is calculated according to the automatic evaluation of the pressure drop data (cf. 3.4). The distributor design assumes ideal nozzles and estimates the pressure drop based on the Bernoulli equation (cf. (55)). The power consumption can be estimated by the correlation of *Singh* with the original constants or the updated empirical correlation for the machine types of this work (cf. 3.5). The data export allows for a convenient export of all parameters and data including cost evaluations to excel for further evaluation.

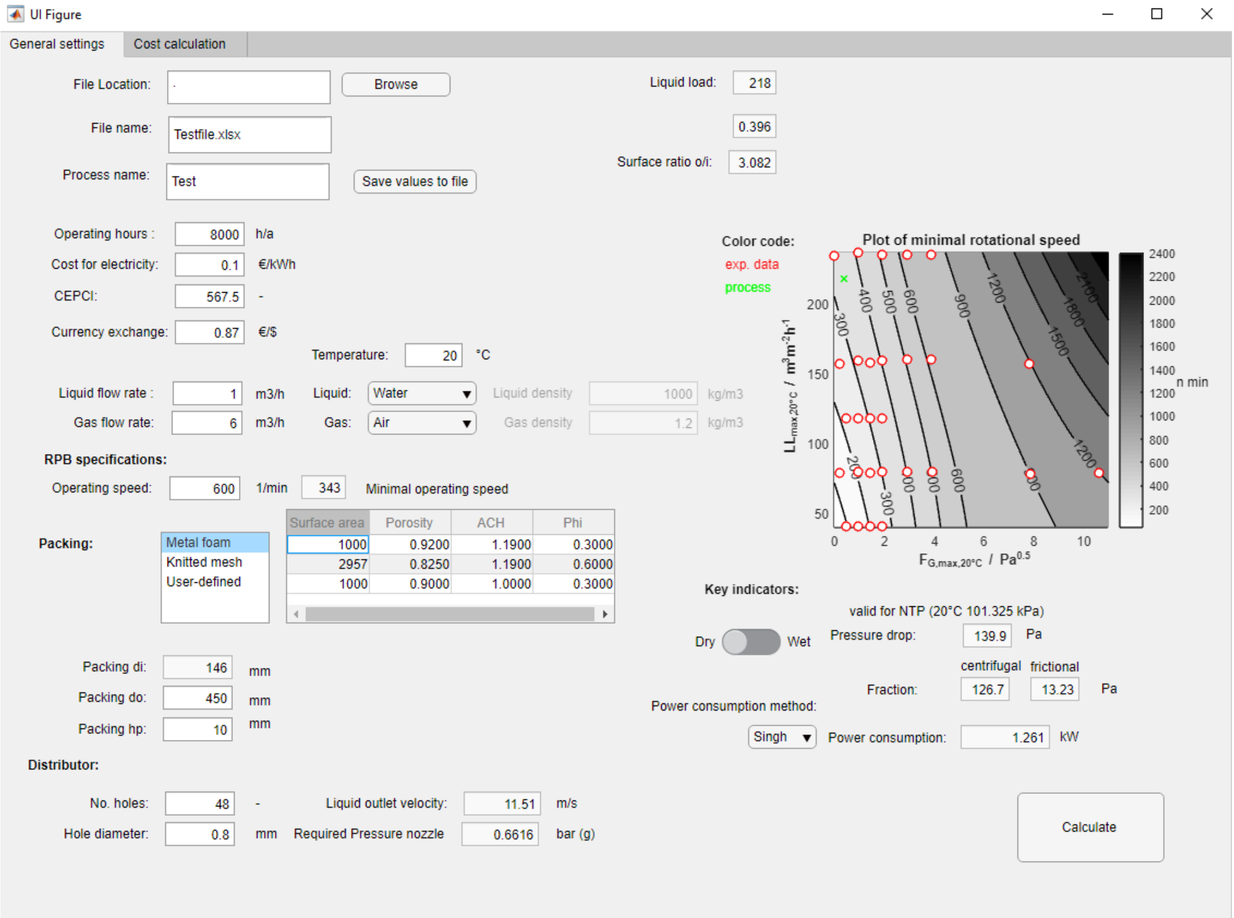

File Location: .

File name: Testfile.xlsx

Process name: Test

Liquid load: 218

0.396

Surface ratio o/i: 3.082

Operating hours : 8000 h/a

Cost for electricity: 0.1 €/kWh

CEPCI: 567.5 -

Currency exchange: 0.87 €/$

Temperature: 20 °C

Liquid flow rate : 1 m3/h Liquid: Water Liquid density 1000 kg/m3

Gas flow rate: 6 m3/h Gas: Air Gas density 1.2 kg/m3

RPB specifications:

Operating speed: 600 1/min 343 Minimal operating speed

Packing: Metal foam / Knitted mesh / User-defined

Surface area	Porosity	ACH	Phi
1000	0.9200	1.1900	0.3000
2957	0.8250	1.1900	0.6000
1000	0.9000	1.0000	0.3000

Packing di: 146 mm

Packing do: 450 mm

Packing hp: 10 mm

Distributor:

No. holes: 48 - Liquid outlet velocity: 11.51 m/s

Hole diameter: 0.8 mm Required Pressure nozzle 0.6616 bar (g)

Key indicators:

valid for NTP (20°C 101.325 kPa)

Dry ○ Wet Pressure drop: 139.9 Pa

Fraction: centrifugal 126.7 frictional 13.23 Pa

Power consumption method: Singh Power consumption: 1.261 kW

Figure 5.7: General setting for the hydraulic design of the RPB.

When the hydraulic design is completed, the operational costs are estimated according to the power requirements of RPB, pump and blower. The capital investment is calculated according to *Woods et al.* [*98*] (cf. 5.2). Different materials can be selected. Moreover, the cost factors can be adjusted to the recommendations of *Woods*. To give an overview both FOB cost or total module cost and the annualized investment cost are displayed. Finally, the annualized costs are visually represented in the bar diagram and categorized in operating expenditures and capital investments.

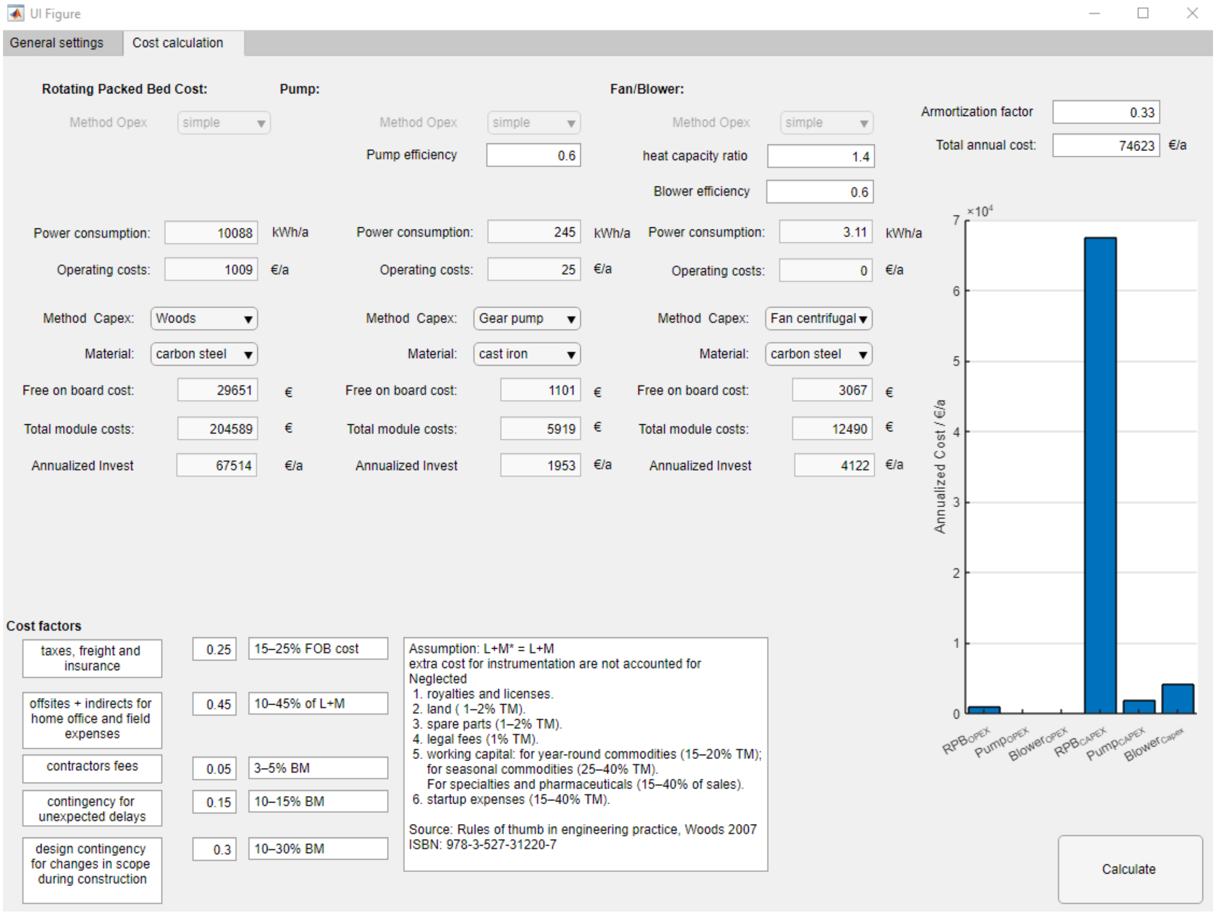

Rotating Packed Bed Cost:

Method Opex: simple

Power consumption: 10088 kWh/a

Operating costs: 1009 €/a

Method Capex: Woods

Material: carbon steel

Free on board cost: 29651 €

Total module costs: 204589 €

Annualized Invest 67514 €/a

Pump:

Method Opex: simple

Pump efficiency 0.6

Power consumption: 245 kWh/a

Operating costs: 25 €/a

Method Capex: Gear pump

Material: cast iron

Free on board cost: 1101 €

Total module costs: 5919 €

Annualized Invest 1953 €/a

Fan/Blower:

Method Opex: simple

heat capacity ratio 1.4

Blower efficiency 0.6

Power consumption: 3.11 kWh/a

Operating costs: 0 €/a

Method Capex: Fan centrifugal

Material: carbon steel

Free on board cost: 3067 €

Total module costs: 12490 €

Annualized Invest 4122 €/a

Amortization factor 0.33

Total annual cost: 74623 €/a

Cost factors

taxes, freight and insurance	0.25	15–25% FOB cost
offsites + indirects for home office and field expenses	0.45	10–45% of L+M
contractors fees	0.05	3–5% BM
contingency for unexpected delays	0.15	10–15% BM
design contingency for changes in scope during construction	0.3	10–30% BM

Assumption: L+M* = L+M
extra cost for instrumentation are not accounted for
Neglected
1. royalties and licenses.
2. land (1–2% TM).
3. spare parts (1–2% TM).
4. legal fees (1% TM).
5. working capital: for year-round commodities (15–20% TM);
   for seasonal commodities (25–40% TM).
   For specialties and pharmaceuticals (15–40% of sales).
6. startup expenses (15–40% TM).

Source: Rules of thumb in engineering practice, Woods 2007
ISBN: 978-3-527-31220-7

Figure 5.8 Cost calculation parametrization and evaluation for the RPB, blower and pump costs.

5.4 Cost estimation for existing industrial size equipment

The information on the cost of existing processes is limited. *Zheng et al.* [*66*] provide dimensions and power requirements for a stripping gas supported deaeration process at two different scales. The liquid flow rates investigated are 50 $m^3 h^{-1}$ and 250 $m^3 h^{-1}$. The gas to liquid ratio is varied between 1 and 3. For the estimation of the annual costs, a gas liquid ratio of 3 is assumed as worst case estimation which gives the highest pressure drop and highest fan cost. However, for all examples the flow rate of the fan was below the minimum range, therefore the lowest value within the range was assumed to calculate the blower cost.

Tab. 14: Data for the industrial-scale RPBs of *Zheng et al.* [*66*] estimated from publication graphs.

	50 $m^3 h^{-1}$	250 $m^3 h^{-1}$
Rotor		
d_i/m	0.300	0.600[2]
d_o/m	0.600	1.000[2]
h_R/m	0.250	0.700[2]
Operation		
Rotation/min^{-1}	700-1500	750[2]
$V_G/m^3 h^{-1}$	150	750
$V_L/m^3 h^{-1}$	50	250
$F_{G,i}*/Pa^{0.5}$	0.19	0.17
$LL_i/m^3 m^{-2} h^{-1}$	212.21	189.47
Power requirement[1] /kW		
1300/min^{-1}	37.5	-
750/min^{-1}	-	160
700/min^{-1}	16.0	-

[1]estimated from publication graphs

[2]assumed to be identical to the 300 $m^3 h^{-1}$ RPB mentioned in the publication

The pressure drop was calculated with the dry pressure drop correlation because the liquid will have a neglectable influence, which was validated by the experimental results in 3.2.2. Figure 3.7a) illustrated that for the whole range between 0 and 240 $m^3 m^2 h^{-1}$ and an F-Factor of 2 Pa, the liquid flow rate has only a small influence on the entrainment, when operated above the minimal possible rotational speed. Furthermore, the F-Factor varies between 0.17 and 0.19 which is very small compared to the experimental results we found. The influence of the liquid on the pressure drop may be much smaller.

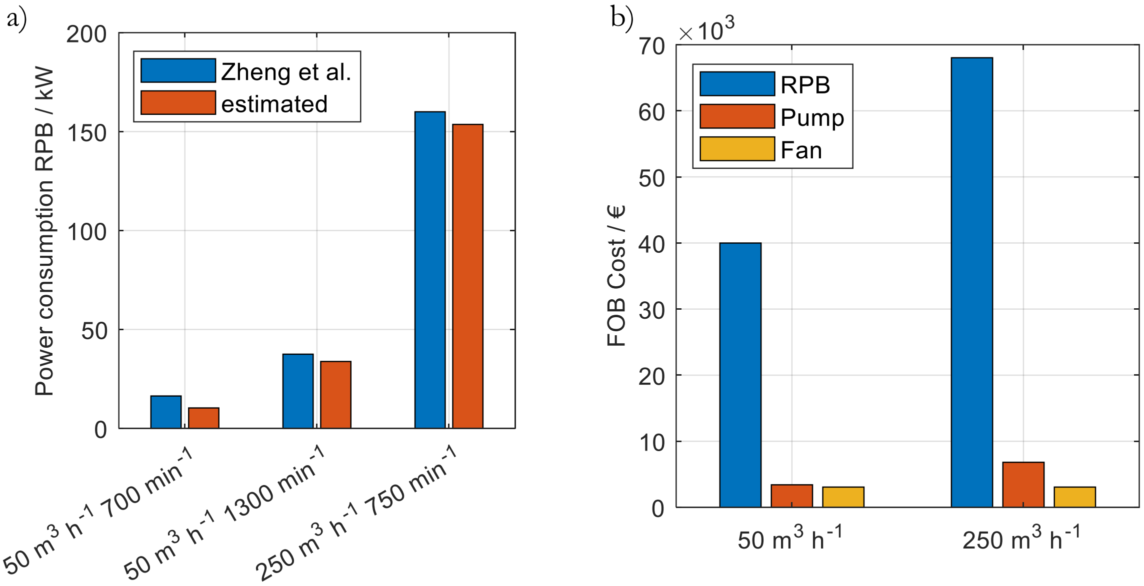

Figure 5.9: a) Power consumption of the RPB based on the reported values by *Zheng et al.* [*66*] and the estimated values with the power consumption equation (32) b) FOB cost for RPB, pump and fan, based on 5.2.1.

The estimated power consumption by the empirical correlation (32) is in good agreement with the reported power requirement from *Zheng et al.* [*66*] (cf. Figure 5.9a). For a first estimation of the investment costs, the FOB costs are compared (cf. Figure 5.9b). It can be seen that the investment costs for both processes (50 and 250 $m^3 h^{-1}$) are dominated by the RPB. The FOB of pump and blower accumulate to approximately 15 % of the RPB FOB cost. Figure 5.10 offers a more detailed overview while considering annualized investment as well as operating costs for the processes. Pump and fan neither increase investment, nor the operating expenditures. The pressure drop of 893 and 708 Pa for the 50 and 250 $m^3 h^{-1}$, respectively, seems in terms of energy requirements negligible. For 50 $m^3 h^{-1}$ process the operating cost of the RPB account for 18 % of the total annualized cost. It increases by a factor of two for the 250 $m^3 h^{-1}$ processes to 37 % hence it contributes significantly to the total annualized costs. However, the capital expenditures reduce from 70 % to 54 % from the 50 $m^3 h^{-1}$ to 250 $m^3 h^{-1}$, respectively. The proportionality of operating costs to liquid flow rate stands out for the different scales. The liquid flow rate increases by a factor of five, while the operating costs increase by a factor of 4.54. The investigated equipment sizes illustrate that the contribution of operating cost is very limited for smaller capacities below 50 $m^3 h^{-1}$.

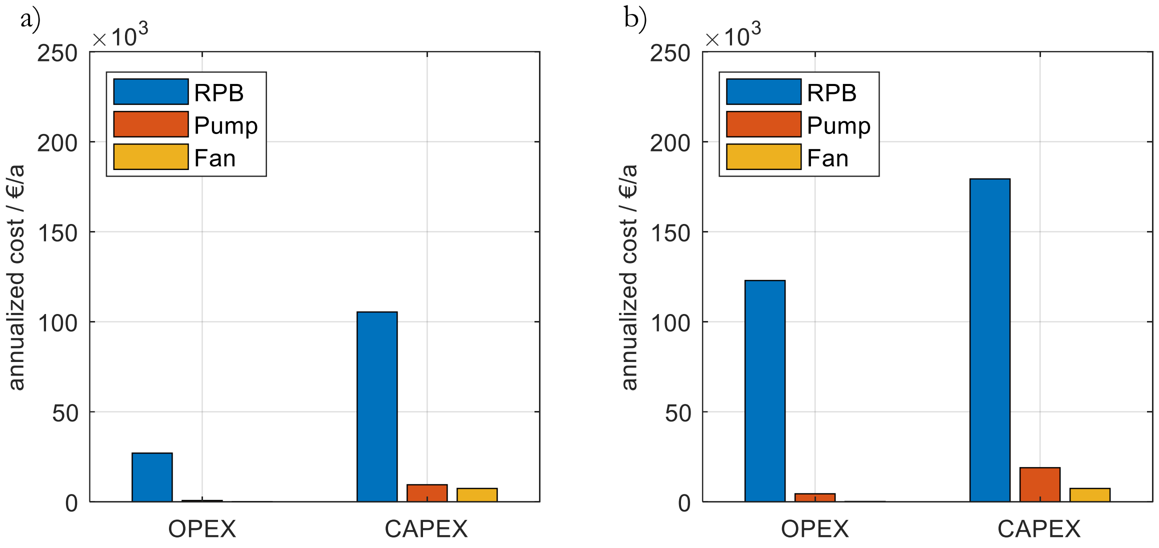

Figure 5.10: annualized cost of the deaeration process for operating expenditures and capital investment of RPB, pump and fan, based on 5.2.1 a) process for 50 $m^3 h^{-1}$ b) process for 250 $m^3 h^{-1}$.

The total annualized costs accumulate to 150,142 € a^{-1} and 333,232 € a^{-1} for the 50 and 250 $m^3 h^{-1}$ process, respectively. For a five-fold increased capacity, the costs increase by +120 %. This translates to a degression exponent of 0.50, favoring a higher capacity to reduce the overall annualized costs per m^3 deaerated water.

6 Design recommendations

The chapters on hydrodynamics (3), mass transfer (4) and modeling (5) can be used to design an RPB for the deaeration process. Figure 6.1 illustrates the procedure which guides through hydraulic design, mass transfer and cost estimation. Gas and liquid flow rates are the starting point for the design procedure. The flow diagram includes feedback loops to optimize the product quality or the total costs of the equipment.

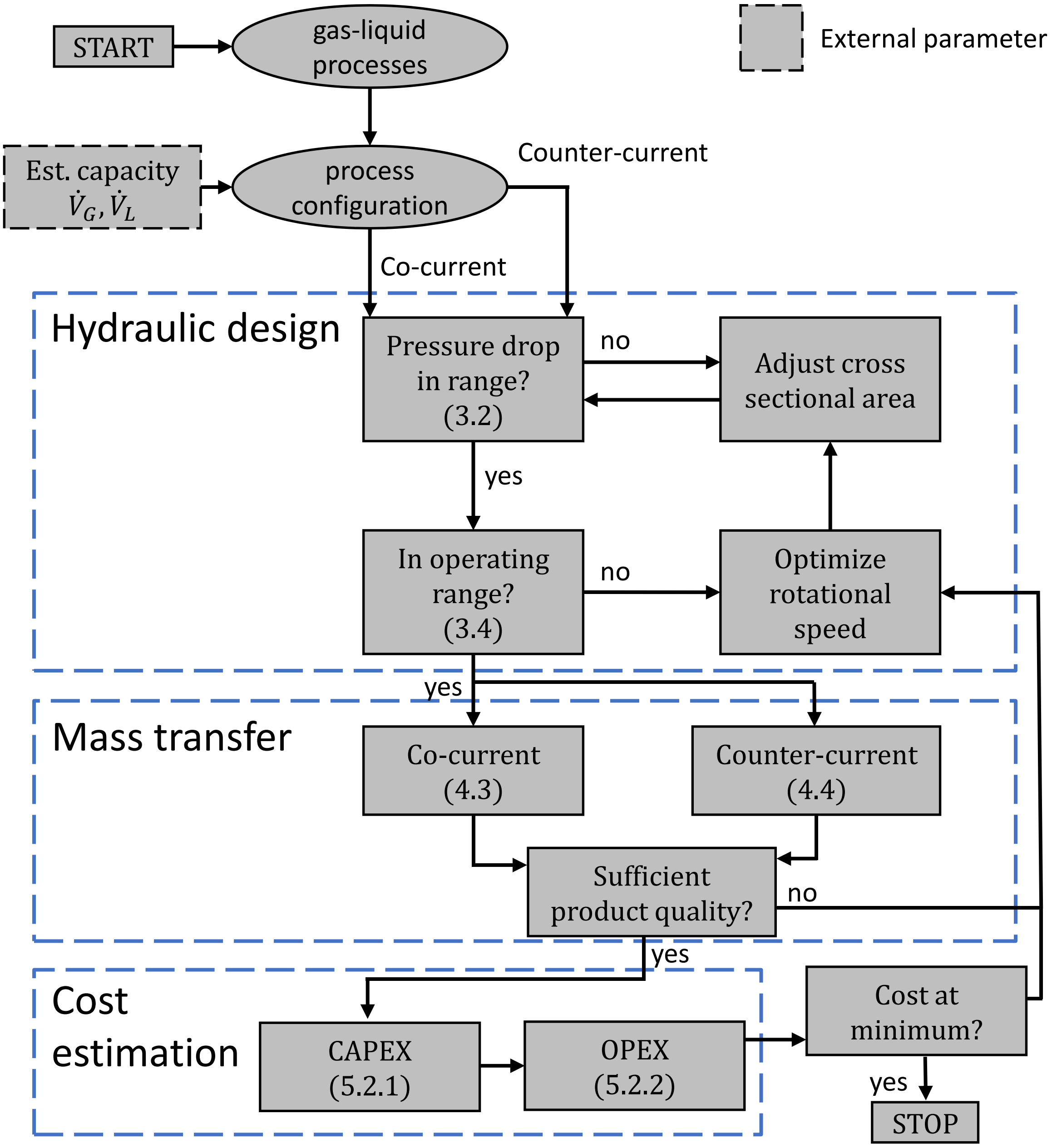

Figure 6.1: Schematic approach to design an RPB for the co- or counter-current deaeration. (x.x.x) refers to the corresponding chapters of this work.

Furthermore, a condensed form of design guidelines is given below for hydraulic operation and mass transfer design. The design guidelines were developed in the context of the ImPaCCt project (Improved Process Performance by Process Intensification in Centrifugal Contactors) they contain both academia and industrial input.

6.1 Guidelines: Hydraulic operation and design of RPBs

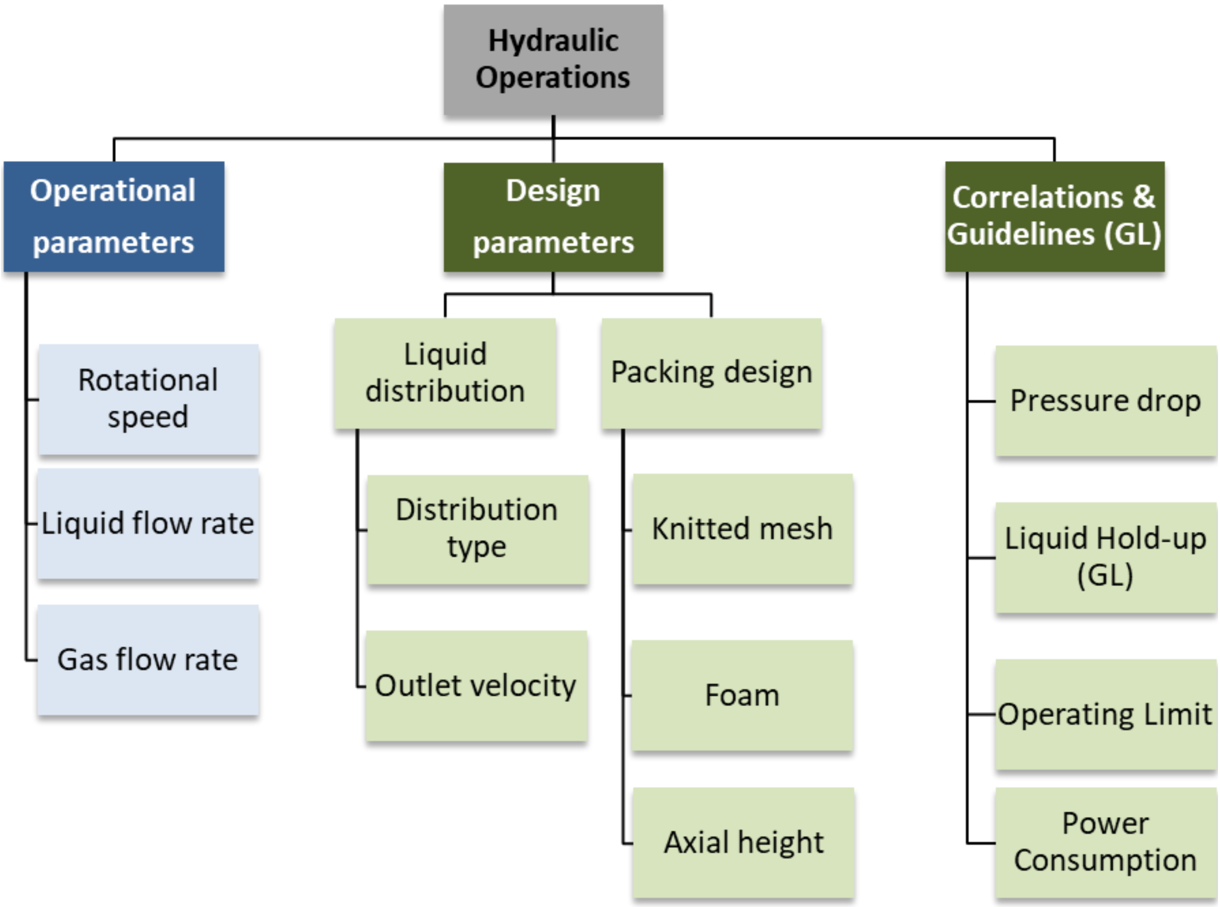

Figure 6.2: Overview of operational and design parameters investigated in the hydraulic study.

Tab. 15: Summary of the hydraulic study.

OPERATIONAL PARAMETERS	
Rotational speed	**Literature Results**[1,2] • The results report that an increasing rotational speed increases the capacity of the RPB regarding gas and liquid load. • From the data, it can be concluded that the majority of the experiments were conducted in a liquid load between 0 and 100 $m^3\,m^{-2}\,h^{-1}$ and an F-factor at an inner diameter below 7 $Pa^{0.5}$. • High specific surface packings find application in RPBs (e.g. 850 $m^2\,m^{-3}$) • Required energy amount for achieving a certain rotational speed is dependent on the rotational speed and the liquid flow rate. *Singh et al.* provide a two variable correlation. **Experimental Results**[1,2,3,7] • Experimental investigations revealed the significance of nozzle type on the operating limit. For liquid loads of up to 51 $m^3\,m^{-2}\,h^{-1}$ and F-factors of up to 3.4 $Pa^{0.5}$.[2] • The new design of a nozzle test facility (NTF)-RPB significantly enlarged the investigated range. The design is capable to reach liquid loads of up to 240 $m^3\,m^{-2}\,h^{-1}$ and F-factors of up to 12 $Pa^{0.5}$, by application of a maximal rotational speed of 1800 min^{-1}. Additionally, visual observation enables to differentiate between nozzle-induced entrainment and entrainment related to the packing. Full jet nozzles provide an easy handling. The liquid jets should not disintegrate into smaller droplets before reaching the packing because the gas easily entrains smaller droplets. A liquid outlet velocity of 5 $m\,s^{-1}$ or higher is usually sufficient. An exact positioning of the nozzle is mandatory. Flat fan nozzles can be used but have shown in some occasions an early entrainment.[1,3] • The minimal allowable rotational speed for knitted mesh and metal foam packings is correlated with the experimental results. [1,3] • The empirical correlation derived by *Singh et al.* was adjusted with own experimental results and compared to reported large-scale operations up to liquid flow rate of 250 $t\,h^{-1}$. At highest flow rates the difference between estimated and reported energy requirement was less than ±10 %, for 50 th^{-1} and a rotational speed of 700 min^{-1} the difference was less than ±40 %.[1] **Summary** ➢ RPBs provide a significant hydraulic capacity increase compared to columns. Nozzles need to be selected for the appropriate outlet velocity and positioning to avoid nozzle-induced entrainment. The rotating speed dictates the power consumption and should be selected as low as possible. The investigated minimal rotational speed maps give insight on the minimum allowable rotational speed. The power consumption correlations help to estimate the additional operating cost when RPBs are applied.

Liquid flow rate and Liquid hold-up	**Literature Results**[1,4] - Liquid hold-up investigations rely on visual, conductive or x-ray tomographic methods. - Film flow, droplet flow and rivulet flow have been identified as flow regimes. - Maldistribution and liquid hold-up reduction were found along the radial direction of the packing. **Experimental Results**[1,4,7] - The application of gamma-ray tomography overcomes limitations of the existing methods (e.g. RPB size restrictions, low resolutions, accuracy). - The rotational speed has a distinctive influence on the evolving flow pattern. The time-averaged angle-resolved CT visualizes maldistribution and flow patterns. This CT-method has never been applied to RPBs before. - Maldistribution is revealed for rotational speeds above 1200 min^{-1}. The flow patterns match the geometry of the inner packing support ring. Therefore, a support ring with highly porous open structure is recommended. - The radial liquid hold-up decreases with increasing rotational speed. A linear decrease along the radius is found, which matches the increase of the cross sectional area. A liquid hold-up between 5 % and 30 % is found for rotational speeds between 1200 and 600 min^{-1}. With a liquid load of 82 $m^3\,m^{-2}\,h^{-1}$ and an F-factor of 3.9 $Pa^{0.5}$ at the inner diameter for a metal foam packing. - Close to minimal allowable rotational speed, the liquid accumulates exponentially at the inner rotor diameter. This unambiguously proves that flooding starts at the inner diameter. **Summary** ➢ Gamma-ray tomography has proven to be an important tool when the liquid hold-up within the RPB packing is investigated. The technology enables the investigation of liquid hold-up for large radial diameters (object diameters up to 800 mm). Additionally, the height of the measurement plane can be varied which enables multiple planes per rotor. This is very beneficial for larger axial packing heights as high throughput investigations.
Gas flow rate and pressure drop	**Literature Results**[5] - Most of the dry pressure drop correlations are a summation of different independent effects on the gas pressure drop (e.g. frictional force, centrifugal force etc.). - The correlations incorporate empirical factors, some of the correlations are based in Chinese literature and therefore not easily accessible. **Experimental Results**[1,6,7] - The correlation for dry pressure drop from *Neumann et al.* was developed during the ImPaCCt project. The correlation is based on the extended channel model for column packings. - The main contributions are centrifugal head induced by the rotational speed and frictional pressure drop. Two fitting constants are to be determined in independent experimental runs. - The dry pressure drop can be predicted for knit mesh (F-Factor 0-4 $Pa^{0.5}$, rotational speed 0-1800 min^{-1}) and metal foam (F-Factor 0-12 $Pa^{0.5}$, rotational speed 0-1800 min^{-1}) within an error of ±30 %. The maximal measured pressure drop was 4680 Pa.

	• For many cases far from the entrainment region, the additional pressure drop by the liquid is negligible. Starting at a high rotational speed the wet pressure drop decreases with rotational speed to a minimum. When the rotational speed decreases further, in the near entrainment region, the pressure drop curve exhibits a strong increase. • The wet pressure drop was thoroughly examined for the metal foam packing with liquid loads between 0 and 240 $m^3\,m^{-2}\,h^{-1}$. An artificial neural network(ANN) was used to adjust the porosity in the dry pressure drop model to include porosity reduction through liquid accumulations. The accuracy of the model is within ±30 %, in the entrainment regions larger errors are possible. **Summary** ➢ The dry pressure drop can be reasonably well predicted in the investigated range. Furthermore, the influence of the liquid can be neglected at moderate F-factors below 2 $Pa^{0.5}$. For higher gas loads an artificial neural network can be used to predict the pressure drop of the metal foam packing.
DESIGN PARAMETERS	
Liquid distribution	**Literature Results**[2] • The amount of studies on liquid distribution are limited. Static or rotating pipes are common as well as multiple distribution arms with boreholes. • The angle between nozzle and packing should have an influence on the maximum operating limit. High tangential velocities of the injected liquid increase the operating limit. **Experimental Results**[1,2,7] • Full jet nozzles provide a more stable operation than flat fan nozzles because flat fan nozzles provide a finer spray fraction, which the gas entrains. Moreover, the positioning of the flat fan nozzles can be more demanding because of the larger spray area. If the spray area is not matching the packing area, this leads to nozzle induced entrainment. The right selection of the flow velocity is mandatory for flat fan nozzles, while full jet nozzles provide a better turn down ratio. **Summary** ➢ The handling advantages promote the use of full yet nozzles.
Packing design	**Literature Results**[1] • The most prominent packing types are knitted or wired mesh and metal foam packings. • Operating limits or pressure drop results are reported for those packing types. However, the specific loads for which the results were obtained are sometimes very low. • Moreover, many results are performed on small scale machines with only several millimeter of packing length. **Experimental Results**[1,6,7] • The influence of the packing type (knitted mesh, metal foam) on the centrifugal pressure drop is negligible. • The knitted mesh packing shows a strong influence on the pressure drop. The influence of the metal foam packing is smaller and can be related to the specific packing surface (KM: ~3000 $m^2\,m^{-3}$, FF: 1000 $m^2\,m^{-3}$). It is recommended to use the pressure drop model based on the extended channel model that was validated with experimental results to evaluate the influences of porosity, surface area etc.

- The knitted mesh requires higher rotational speeds for the same operating parameters (F-factor, Liquid load).
- For large radial packing lengths, the mesh showed significant handling disadvantages. Being wound on the rotors inner support ring the potential for increased nonuniformities increases significantly with increasing radius/increasing number of revolutions due to small inaccuracies in the winding process or the manufactured width of the mesh. Additionally, the winding force influences the packing porosity.
- The axial height between 10 and 20 mm has been investigated. At comparable F-factor and liquid load the packing shows equivalent performance (pressure drop, operating limit).

Summary

➢ The packing selection needs to balance the influence on pressure drop or operating range. Foams have shown handling advantages, while meshes in general provide larger surface areas. The mass transfer performance is the key parameter (cf. case study guidelines).

Supporting Information

(1) *Deaeration in rotating packed beds*, Ph.D. thesis
Groß, K.
(2) *Experimental investigations on the upper operating limit in rotating packed*
Neumann, K., Hunold S., Groß, K., Górak A. [*36*]

(3) *Analysing the Operating Limits in High Gravity Equipment*,
Groß, K., Neumann, K., Skiborowski, M., Górak, A. [*103*]

(4) *Analysis of Flow Patterns in High-Gravity Equipment Using Gamma-Ray Computed Tomography*,
Groß, K., Bieberle, A., Gladyszewski, K., Schubert, M. Hampel, U. Skiborowski, M, Górak, A. [*59*]

(5) *Process, performance and modeling of CO_2 capture by chemical absorption using high gravity: A review*,
Zhao, B. et al. [*47*]

(6) *Dry Pressure Drop in Rotating Packed Beds—Systematic Experimental Studies*
Neumann, K. et al. [*48*]

(7) *Deaeration and Hydraulic database V4.67*
Groß, K.

6.2 Guidelines: Deaeration and gas-liquid contacting in RPBs

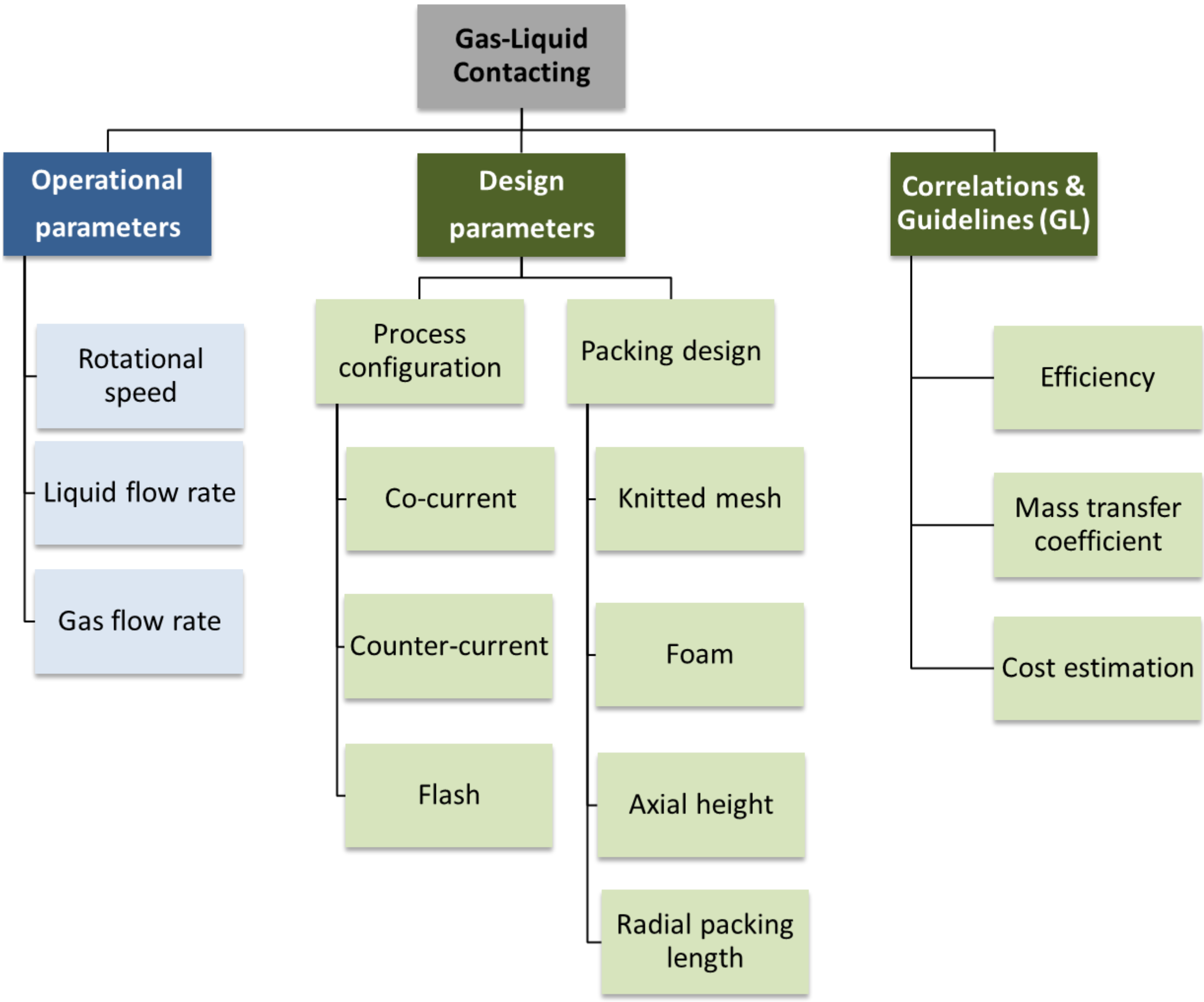

Figure 6.3: Overview of operational and design parameters investigated in the mass transfer study.

Tab. 16: Summary of the mass transfer study.

OPERATIONAL PARAMETERS	
Rotational speed	**Literature Results**[1] • Increasing rotational speed improves the mass transfer rate (e.g. number of theoretical stages, mass transfer coefficients). • Some authors describe a flattening trend for higher rotational speed (Relative centrifugal force at the inner diameter > 75). **Experimental Results**[1,2,4,5] • The deaeration efficiency is increasing for co-current, counter-current and flash processing with increasing rotational speed. • For the co-current degassing deaeration efficiency (fraction of one theoretical stage) reaches above 99 % for liquid flow rates between 0.360 and 0.960 $m^3 h^{-1}$ with 6 $m^3 h^{-1}$ nitrogen as stripping gas at rotational speeds between 900 and 1500 min^{-1}

	• Similar efficiency can be reached for the flash degassing without stripping gas but a liquid stream superheated by 0.4 K to 2.2 K and pressure of 6.2 to 11 kPa (a). • The counter-current operation provides a larger driving force. The results of the counter-current operation improve compared to the co-current operation in the same range of gas and liquid flow rates and rotational speeds. However, the number of theoretical stages is currently limited to approximately 1.5 theoretical stages for knitted mesh and foam packings. **Summary** ➢ The rotational speed is an additional degree of freedom to adjust the deaeration efficiency. Uncertainties in the design or additional purity constraints can be compensated by a higher rotational speed
Liquid flow rate	**Literature Results**[1,3] • Industrial-scale processes with liquid flow rates up to 250 m^3 h^{-1} are available in the literature. Compared to columns a 6 to 9 fold size reduction at equivalent product qualities is reached. • The reported results state that a sufficient low outlet concentration can be reached. **Experimental Results**[1,2,5] • High efficiencies can be reached independently of the liquid flow rate between 0.360 and 0.960 m^3 h^{-1}. The mass transfer coefficient increases with increasing liquid flow rate. • The correlation of *Chen et al.* can be used to predict the mass transfer coefficients for flash degassing and co-current stripping. **Summary** ➢ The RPB is capable to process high liquid capacities. Correlations for flash degassing and co-current deaeration are available and validated by experimental results.
Gas flow rate	**Literature Results**[1,3] • Volumetric gas to liquid ratios between 0.5 and 3 are commonly found. • An increased gas flow reduces the liquid outlet concentration. • Increasing efficiencies are reported for increasing gas flow rates **Experimental Results**[1,5] • The most trends reported in the literature are found in the experimental results. • For counter-current operation, the gas flow rate between 0.06 m^3 h^{-1} and 6 m^3 h^{-1} has a negligible influence on the number of theoretical stages at 900 min^{-1}. However, the outlet concentration is changed due to different equilibrium concentrations. • At low oxygen concentrations, the equipment sealing is mandatory. Small leaks will drastically change the observed results. The influence of leaks is more prominent at low gas velocities. A backflow of gas through the gas outlet, when the rotational speed is changed needs to be prevented (e.g. washing flask).

	Summary ➢ For co-current and counter-current operation, the volumetric gas to liquid ratio has a significant influence on the liquid outlet concentration. The gas to liquid ratio needs to be balanced with the necessary rotational speed, both should be minimized to save costs.
DESIGN PARAMETERS	
Process configuration	**Experimental Results**[1,2,4,5] • **Flash degassing:** The flash degassing occurs in two steps, initial flash and subsequently the gas-liquid contact. The initial flash efficiency increases with increasing the superheating of the liquid stream. It decreases with an increasing liquid stream. The gas-liquid contact, described by the mass transfer coefficient, increases with rotational speed and increasing liquid flow rate, it can be predicted with the empirical correlation by *Chen et al.* within ±30 %. Flash degassing is limited to one theoretical stage. Outlet liquid oxygen concentrations close to the equilibrium limit ($< 5\ \mu g\ kg^{-1}$) are obtained. The mass transfer coefficients are roughly one order of magnitude higher than in conventional columns, which leads to size reduction and enabling the selection of higher grade construction materials for corrosive process streams. • **Co-current contacting:** Similarly, to flash degassing the co-current contact in RPBs is limited to one equilibrium stage. For saturated liquid at ambient conditions, the volumetric gas to liquid ratio of six is sufficient to reach equilibrium concentrations below $50\ \mu g\ kg^{-1}$. The RPB reaches the required liquid outlet concentrations between 600 and 1200 min^{-1} depending on the radial packing length. • **Counter-current contacting:** The counter-current contact decreases the amount of stripping gas necessary for liquid outlet concentrations below $50\ \mu g\ kg^{-1}$ at ambient conditions by a factor of six, if 1.5 theoretical stages are assumed to be present within the RPB. Within the accuracy of the sensors for 3 and 6 $m^3\ h^{-1}$ gas flow rate at a liquid flow rate of 1 $m^3\ h^{-1}$ a maximum number of theoretical stages of approximately 1.4 has been realized. The result seems to be independent of the gas flow rate as the same result has been observed for low gas flow rates of 0.06 $m^3\ h^{-1}$. • It is important to note that very low oxygen concentrations can be reached during operation. The mass transfer coefficient levels off when the sensor's accuracy limit is reached. Excluding values closer to the equilibrium concentration than a factor three of the sensor accuracy has proven good practice. **Summary** ➢ All three process configurations reach sufficiently low liquid oxygen concentrations. Where a stripping gas is available at low costs the counter-current and co-current contacting are preferable. Where cheap thermal energy is available the flash degassing seems to be a good alternative. Moreover, low-grade heat can be utilized when a vacuum is applied. The equipment size reduction promotes the RPB for vacuum operation instead of columns.

Packing design, radial packing length and axial height	**Experimental Results**[1,2,4,5] • Knitted mesh and metal foam provide similar mass transfer coefficients for the co-current deaeration. • At co-current conditions, the radial packing length has a significant influence on the mass transfer coefficient. When the packing length is increased from 27 mm to 152 mm the mass transfer coefficient reduces by approximately 80 %. The metal foam provides mass transfer coefficients between 0.4 and 1.4 s^{-1} for a larger packing length of 152 mm and between 2 and 12 s^{-1} for a short packing length of 27 mm. The corresponding liquid flow rate was between 0.360 and 0.960 $m^3\,h^{-1}$ while the gas flow rate was kept constant at 6 $m^3\,h^{-1}$. The increased mass transfer coefficient for small packing length can be accounted to high relative velocities at the packing entrance. Moreover, it is an indicator that the mass transfer shows a nonlinear behavior. It should be noted calculations of mass transfer coefficients for small packing volumes are prone to errors due to other mass transfer contributions (e.g. casing, rotor plates, etc.). • It was found that already empty rotor plates incl. the packing support ring shows a high deaeration efficiency above 93 %. For a rotational speed of 1500 min^{-1} the empty rotor reaches a comparable efficiency compared to the packed rotor at 600 to 900 min^{-1}. • In the investigated range between 10 and 20 mm the axial height has no significant influence on the mass transfer performance if operated at equivalent F-factor and liquid loads the mass transfer coefficient variation is within ± 30%. **Summary** ➢ The mass transfer coefficient seems to be nonlinear with the radial packing length. One needs to be careful if very small packing volumes are used for the calculation of mass transfer coefficients. The axial height has a negligible influence. The correlation of *Chen et al.* was validated for flash degassing and co-current nitrogen stripping applications.
Cost estimation	**Literature Results**[1] • There are currently no cost correlations for RPBs available in the literature. • *Singh* provides a correlation to calculate the power consumption. **Experimental/Theoretical Results**[1] • Constants for the empirical correlation for RPB power consumption were adjusted with own experimental data. • The main contributions to the process cost are RPB, pump and blower cost. The RPB costs are estimated from cost correlations for filtering centrifuges. • For the 50 th^{-1} and 250 th^{-1} processes of *Zheng et al.* costs are estimated. For both capacities operating and investment costs blower and pump costs are negligible. The main cost driver is RPB costs. The estimated power consumption matches the report power consumption ±10 %. The free-on-board costs of the RPB are between 40 and 70 k€. Total annualized costs are in the range of 150,142 €a^{-1} to 333,232 €a^{-1} including pump and blower cost. **Summary** ➢ For the deaeration cost, capital expenditures of the RPB are the main cost driver. The power consumption has for a medium-scale process (e.g. 50 $t\,h^{-1}$) a minor influence.

Supporting Information

(8) *Deaeration in rotating packed beds*, Ph.D. thesis
Groß, K.

(9) *Intensified and Flexible Flash Degassing in a Rotating Packed Bed*
de Beer, M., Schmuhl, R. et al. [*72*]

(10) *A guide on the industrial application of rotating packed beds*
Neumann, K. et al. [*7*]

(11) *Scale-up of the radial packing length in rotating packed beds for deaeration processes*
Groß, K., de Beer, M., Dohrn, S., Skiborowski M. [*96*]

(12) *Deaeration and Hydraulic database V4.67*
Groß, K.

7 Conclusion

The structure of this work was formed by open questions regarding RPB technology. Addressing operating range, pressure drop, mass transfer performance and costs, experimental and theoretical studies were conducted and compared to the state of the art gas-liquid contactors to assess the potential of the RPB technology. Answers to the previously asked questions are summarized in the following paragraphs. Open questions and the future perspective of the RPB technology is addressed towards the end of this chapter.

In cooperation with an engineering partner, a tailor-made design of an RPB was developed and constructed. Own experimental data was used to extend the model of *Neumann et al.* [*48*] and successfully estimate the dry pressure drop with an error of less than ±30 %. Investigations with different liquid loads have proven that the influence of liquid is moderate at low gas loads ($F_{G,max}$= 2 $Pa^{0.5}$) up to a liquid load of LL_{max} 240 $m^3\,m^{-2}\,h^{-1}$. The rotational speed allows to compensate the frictional pressure drop at high liquid loads by the generation of a smaller film thickness. To further estimate the wet pressure drop, an artificial neural network (ANN) was used to estimate the porosity reduction due to the liquid hold-up in the packing. The ANN could successfully estimate the wet pressure drop for most experimental data points with an accuracy of ±30 %. Furthermore, an innovative non-invasive gamma-ray method was used to validate the results of the ANN. The gamma-ray scans enabled the quantitative local liquid hold-up measurement within the packing, but the experimental results gained could not validate the estimated liquid hold-up of the wet pressure drop model, the real liquid hold-up and the estimated liquid hold-up, based on the ANN, varied significantly for low rotational speed below 600 min^{-1}. Despite the correct estimation of the wet pressure drop by the model, the application of the ANN showed limitations when deducing physical relations on the liquid hold-up. Besides the validation attempt of the wet pressure drop model, gamma-ray measurements enable the detection of an increasing maldistribution when the rotational speed increases and reveals a small capability of the isotropic metal foam to redistribute the liquid when flowing through the packing. The gamma-ray measurements proved that entrainment starts at the inner packing parts, which allowed to identify the inner diameter and the corresponding maximal liquid and gas loads as important parameters for the determination of the operating range. A database with more than 1500 experimental data points for metal foam and KM was generated to aid the hydraulic design. Compared to column packings the geometrical surface area can be significantly increased up to approximately 3000 $m^2\,m^{-3}$. While for a 1000 $m^2\,m^{-3}$ geometric surface of the metal foam packing specific liquid loads of up to approximately 240 $m^3\,m^{-2}\,h^{-1}$ were investigated. The highest F-factor investigated was 11 $Pa^{0.5}$. This is considerably higher than the load range for column packings which provide a similar surface area. The deaeration of water with nitrogen, a model system for liquid-side limited mass transfer, was investigated in the mass transfer study. Both co-current and counter-current deaeration are of industrial relevance. Although the empty rotor already showed a high mass transfer performance, the application of KM or FF packing could significantly contribute to the mass transfer. Scale-up experiments with different packing length showed a non-linearity of the overall mass transfer coefficient (k_La). The non-idealities were satisfactorily reflected by the mass transfer correlation of *Chen et al.* [*71*] with an error range of approximately 30 % for co- and counter-current mass transfer. However, the error increases in the counter-current operation. The correlation tends to overpredict the k_La-value at higher rotational speeds or for low gas-flow rates. Deviations from ideal plug flow behavior and the disintegration of the liquid film into rivulets which are not yet considered within the correlation could be a possible explanation. To estimate the operating costs of the RPB the power consumption was closely examined. The investigation showed a direct dependence on the rotational speed and the liquid flow rate. The data generated was used to adjust the correlation of *Singh* [*91*, p. 141] to map machine-dependent characteristics. A rising liquid height within the casing had a significant influence on the power consumption as well as the frictional losses of bearings or sealings. The findings on the power consumption, hydraulic data and literature correlations were combined into a cost model and implemented in MATLAB® App designer to support the user in the design phase of the RPB and show potential costs. The investment costs were derived from centrifuges as comparable equipment type. The model was then used to calculate the costs of existing deaeration processes. The estimated power requirement was in good agreement with the literature. The main cost drivers of the total annualized cost were the investment costs of the RPB. The degression exponent of 0.5 favors deaeration processes for RPBs with an increased capacity.

8 Future work

The contents of this work substantially contribute to the fundamental understanding of the RPB technology. All findings were summarized in hydraulic and gas-liquid design recommendations. They support RPB equipment design, both for hydraulic operation and for mass transfer calculations. A first step towards cost evaluation was made with the costing framework at the end of this thesis. Nevertheless, there are still open topics that are promising to address in future studies.

The feasibility of measurements along the radial packing length was shown with liquid hold-up and porosity measurements by non-invasive gamma-ray tomography, but liquid hold-up and porosity are just two of many factors valuable for the packing evaluation. The availability of local measurements for other key parameters (e.g. pressure drop, temperature, concentration) would considerably improve the current development strategies for the packing design. Computational fluid dynamics (CFD) may support the development of new packings reducing pressure drop and improving the liquid distribution within the packing.

The non-idealities (e.g. packing wetting, effective interfacial area) and their influence on the k_La-value should be further investigated, especially for different packing structures. The consideration of liquid and gas phase back mixing may be helpful in this task. Furthermore, the multistage operation with different rotors may increase the performance of the RPB. Researchers need to take caution designing multistage operation, the introduction of changes into the equipment structure may create a necessity for an adjusted hydraulic operation. The design of gas and liquid separation between different stages will be a challenge. Especially when high pressure losses must be avoided.

Long-term and large-scale studies are necessary to assess maintenance or scale-up criteria not jet evaluated. The influence of fouling on the highly porous packings is not yet sufficiently evaluated. However, the influence of the centrifugal force may support cleaning the packing from residue. Eventually, the RPB and its model equations should be incorporated in global cost optimization studies to evaluate the potential of the RPB with respect to the entire process. Synergy effects between the RPB and other equipment types and especially the higher flexibility of the equipment have not yet been considered in many studies. Especially the influence of comparably small equipment dimensions and low hold-up must be considered in maintenance cost estimation or dynamic modeling. A large part of the advantages may not be visible due to the current structure of the models.

9 References

[1] Masson-Delmotte, V.; Zhai, P.; Pörtner, H.-O.; Roberts, D.; Skea, J.; Shukla, P.R.; Pirani, A.; Moufouma-Okia, W.; Péan, C.; Pidcock, R.; Connors, s.; Matthews, J.B.R.; Chen, Y.; Zhou, X.; Gomis, M.I.; Lonnoy, E.; Maycock, T.; Tignor, M.; Waterfield, T. *Global Warming of 1.5°C. An IPCC Special Report on the impacts of global warming of 1.5°C above pre-industrial levels and related global greenhouse gas emission pathways, in the context of strengthening the global response to the threat of climate change, sustainable development, and efforts to eradicate poverty*, 2018.

[2] Geres, R.; Kohn, A.; Lenz, S.; Ausfelder, F.; Bazzanella, A. M.; Möller, A. R*oadmap Chemie 2050. Auf dem Weg zu einer treibhausgasneutralen chemischen Industrie in Deutschland*, 2019.

[3] Cayuela Valencia, R. *The future of the chemical industry by 2050;* Wiley-VCH: Weinheim, 2013.

[4] Führ, M. *Praxishandbuch REACH;* Heymann: Köln, 2011.

[5] Paris, C. Shipowners' Multibillion-Dollar Quandary: Buy Cleaner Fuel or a Fuel Cleaner? *The Wall Street Journal [Online],* Mar 20, 2018. https://www.wsj.com/articles/ship-owners-multibillion-dollar-quandary-buy-cleaner-fuel-or-a-fuel-cleaner-1521538200 (accessed March 11, 2020).

[6] Rao, D. P. The Story of "HIGEE". *Indian Chemical Engineer* **2015,** *57* (3-4), 282–299.

[7] Neumann, K.; Gladyszewski, K.; Groß, K.; Qammar, H.; Wenzel, D.; Górak, A.; Skiborowski, M. A guide on the industrial application of rotating packed beds. *Chem. Eng. Res. Des.* **2018,** *134*, 443–462.

[8] Reti, L.; Di Giorgio Martini, F. Francesco di Giorgio Martini's Treatise on Engineering and Its Plagiarists. *Technology and Culture* **1963,** *4* (3), 287.

[9] Papin, D. *Recueil de diverses pièces touchant quelques nouvelles machines et autres subjets philosophiques dont on voit la liste dans les pages suivantes;* pour Jacob Estienne marchand libraire de la cour, chez la vesue de Jean George Huter imprimeur de la cour, 1695.

[10] Hobsbawm, E. J. *Europe 1789-1848;* Abacus, 1977.

[11] Inikori, J. E. *Africans and the industrial revolution in England. A study in international trade and development;* Cambridge University Press: Cambridge England, New York, 2002.

[12] Vogel-Prandtl, J. *Ludwig Prandtl - ein Lebensbild ; Erinnerungen, Dokumente;* Universitätsverlag Göttingen: s.l., 2005.

[13] Theisen, E. Process and Apparatus for Absorbing, Extracting, Distilling, or Evaporating Liquids and Gases or Vapours. GBD189725634 18971104, Nov 4, 1897.

[14] Trent, D. L. Chemical Processing in High-Gravity Fields. In *Re-engineering the chemical processing plant: Process intensification*; Stankiewicz, A., Moulijn, J. A., Eds.; Chemical Industries; Taylor & Francis: London, 2004; pp 46–80.

[15] Podbielniak, W. J. Centrifugal counter current contact apparatus. 476,190, Aug 18, 1930.

[16] Podbielniak, W. J. Apparatus for effecting counter current contact between fluids. 87.222, Jun 25, 1936.

[17] Lukin, I.; Pietzka, L.; Groß, K.; Górak, A.; Schembecker, G. Economic evaluation of rotating packed bed use for aroma absorption from bioreactor off-gas. *Chem. Eng. Process.* **2020,** *154*, 108011.

[18] Placek, A. Process and apparatus for treating liquids with a gaseous medium. 128,521, Mar 1, 1937.

[19] Pilo, C. W.; Dahlbeck, S. W. Apparatus for intimate contacting of two fluid media having different specific weight. U.S. Patent 2,941,872, Jun 9, 1959.

[20] Ramshaw, C.; Mallinson, R. H. Mass transfer process. U.S. Patent 4,283,255, Nov 27, 1978.

[21] *Fluidverfahrenstechnik. Grundlagen, Methodik, Technik, Praxis;* Goedecke, R., Ed.; Wiley-VCH: Weinheim, 2006.

[22] Stichlmair, J. Distillation, 2. Equipment. In *Ullmann's encyclopedia of industrial chemistry*; Bohnet, M., Ed.; Wiley Interscience: Hoboken, New Jersey, 1999-; 455-475.

[23] Sholl, D. S.; Lively, R. P. Seven chemical separations to change the world. *Nature* **2016,** *532* (7600), 435–437.

[24] Düssel, R.; Stichlmair, J.; Groebel, M. Rektifikation. In *Fluidverfahrenstechnik*: *Grundlagen, Methodik, Technik, Praxis*; Goedecke, R., Ed.; Wiley-VCH: Weinheim, 2006; pp 689–798.

[25] Hölemann, K.; Górak, A. Absorption. In *Fluidverfahrenstechnik*: *Grundlagen, Methodik, Technik, Praxis*; Goedecke, R., Ed.; Wiley-VCH: Weinheim, 2006; pp 799–905.

[26] Trambouze, P.; Euzen, J.-P. *Chemical reactors. From design to operation / Pierre Trambouze, Jean-Paul Euzen ; translated by Robert Bononno*, [Rev. ed.]; Institut français du pétrole publications; Editions TECHNIP: Paris, 2004.

[27] Gorak, A.; Olujic, Z. *Distillation. Equipment and processes;* Elsevier Science: Burlington, 2014.

[28] Qammar, H.; Gładyszewski, K.; Górak, A.; Skiborowski, M. Towards the Development of Advanced Packing Design for Distillation in Rotating Packed Beds. *Chemie Ing. Techn.* **2019,** *91* (11), 1663–1673.

[29] Rao, D. P.; Bhowal, A.; Goswami, P. S. Process intensification in rotating packed beds (HIGEE): An appraisal. *Ind. Eng. Chem. Res.* **2004,** *43* (4), 1150–1162.

[30] *Principles and Techniques of Biochemistry and Molecular Biology;* Wilson, K., Walker, J., Eds.; Cambridge University Press, 2010.

[31] Gorak, A.; Schoenmakers, H. *Distillation. Operation and applications;* Academic Press: London, 2014.

[32] Yildirim, Ö.; Flechsig, S.; Brinkmann, U.; Kenig, E. Y. Bestimmung der Lastgrenzen konventioneller Strukturpackungen und Anstaupackungen mithilfe des Wallis-Plots. *Chem. Ing. Tech.* **2015,** *87* (10), 1348–1356 (accessed November 12, 2017).

[33] Sherwood, T. K.; Shipley, G. H.; Holloway, F. A. L. Flooding Velocities in Packed Columns. *Ind. Eng. Chem.* **1938,** *30* (7), 765–769.

[34] Maćkowiak, J. *Fluiddynamik von Füllkörpern und Packungen. Grundlagen der Kolonnenauslegung*, 2., wesentlich erw. und aktualisierte Aufl.; Engineering online library; Springer: Berlin, 2003.

[35] Hanley, B. On packed column hydraulics. *AIChE J.* **2012,** *58* (6), 1671–1682.

[36] Neumann, K.; Hunold, S.; Groß, K.; Górak, A. Experimental investigations on the upper operating limit in rotating packed beds. *Chem. Eng. Process.* **2017,** *121*, 240–247.

[37] Rajan, S.; Kumar, M.; Ansari, M. J.; Rao, D. P.; Kaistha, N. Limiting Gas Liquid Flows and Mass Transfer in a Novel Rotating Packed Bed (HiGee). *Ind. Eng. Chem. Res.* **2011,** *50* (2), 986–997.

[38] Singh, S. P.; Wilson, J. H.; Counce, R. M.; Villiersfisher, J. F.; Jennings, H. L.; Lucero, A. J.; Reed, G. D.; Ashworth, R. A.; Elliott, M. G. Removal of Volatile Organic-Compounds from Groundwater Using a Rotary Air Stripper. *Ind. Eng. Chem. Res.* **1992,** *31* (2), 574–580.

[39] Lockett, M. J. "Flooding of Rotating Structured Packing and its Application to Conventional Packed Columns". *Chem. Eng. Res. Des.* **1995,** *73*.

[40] Große, J. Über keramische Schwämme als Kolonneneinbauten : Grundlegende Untersuchungen zu Morphologie, Fluiddynamik und Stoffübergang bei der mehrphasigen Durchströmung im Gegenstrom. Dissertation; Karlsruher Institut für Technologie, Karlsruhe, 2011.

[41] McCabe, W. L.; Smith, J. C.; Harriott, P. *Unit operations of chemical engineering*, 5th ed.; McGraw-Hill chemical engineering series; McGraw-Hill: New York, 1993.

[42] Laso, M.; Brito, M.H. de; Bomio, P.; Stockar, U. von. Liquid-side mass transfer characteristics of a structured packing. *The Chemical Engineering Journal and the Biochemical Engineering Journal* **1995,** *58* (3), 251–258.

[43] Stankiewicz, A.; Van Gerven, T.; Stefanidis, G. *The fundamentals of process intensification;* Wiley-VCH: Weinheim, 2019.

[44] Costello, R. C. Process intensification: think small. *Chem. Eng.* **2004,** *111* (4), 27–31.

[45] Van Gerven, T.; Stankiewicz, A. Structure, Energy, Synergy, Time・The Fundamentals of Process Intensification. *Ind. Eng. Chem. Res.* **2009,** *48* (5), 2465–2474.

[46] Oertel, H. *Prandtl - Führer durch die Strömungslehre;* Springer Fachmedien Wiesbaden: Wiesbaden, 2017.

[47] Zhao, B.; Tao, W.; Zhong, M.; Su, Y.; Cui, G. Process, performance and modeling of CO 2 capture by chemical absorption using high gravity: A review. *Renewable and Sustainable Energy Reviews* **2016,** *65*, 44–56.

[48] Neumann, K.; Hunold, S.; Skiborowski, M.; Górak, A. Dry Pressure Drop in Rotating Packed Beds—Systematic Experimental Studies. *Ind. Eng. Chem. Res.* **2017,** *56* (43), 12395–12405.

[49] Maćkowiak, J. Extended channel model for prediction of the pressure drop in single-phase flow in packed columns. *Chem. Eng. Res. Des.* **2009,** *87* (2), 123–134 (accessed June 13, 2019).

[50] Guo, F.; Zheng, C.; Guo, K.; Feng, Y.; Gardner, N. C. Hydrodynamics and mass transfer in cross-flow rotating packed bed. *Chem. Eng. Sci.* **1997,** *52* (21-22), 3853–3859.

[51] Keyvani, M.; Gardner, N. C. Operating characteristics of rotating beds. *Chem. Eng. Prog.* **1989,** *85* (9), 48–52.

[52] Zheng, C.; Guo, K.; Feng, Y.; Yang, C.; Gardner, N. C. Pressure Drop of Centripetal Gas Flow through Rotating Beds †. *Ind. Eng. Chem. Res.* **2000,** *39* (3), 829–834.

[53] Sandilya, P.; Rao, D. P.; Sharma, A.; Biswas, G. Gas-Phase Mass Transfer in a Centrifugal Contactor. *Ind. Eng. Chem. Res.* **2001,** *40* (1), 384–392.

[54] Hendry, J. R.; Lee, J. G.M.; Attidekou, P. S. Pressure drop and flooding in rotating packed beds. *Chem. Eng. Process.* **2020,** *151*, 107908.

[55] Burns, J. R.; Ramshaw, C. Process intensification: Visual study of liquid maldistribution in rotating packed beds. *Chem. Eng. Sci.* **1996,** *51* (8), 1347–1352.

[56] Basic, A.; Dudukovic, M. P. Liquid Holdup in Rotating Packed-Beds - Examination of the Film Flow Assumption. *AIChE J.* **1995,** *41* (2), 301–316.

[57] Burns, J. R.; Jamil, J. N.; Ramshaw, C. Process intensification: Operating characteristics of rotating packed beds — determination of liquid hold-up for a high-voidage structured packing. *Chem. Eng. Sci.* **2000,** *55* (13), 2401–2415.

[58] Yang, Y.; Xiang, Y.; Chu, G.; Zou, H.; Luo, Y.; Arowo, M.; Chen, J.-F. A noninvasive X-ray technique for determination of liquid holdup in a rotating packed bed. *Chem. Eng. Sci.* **2015,** *138*, 244–255 (accessed September 28, 2017).

[59] Groß, K.; Bieberle, A.; Gladyszewski, K.; Schubert, M.; Hampel, U.; Skiborowski, M.; Górak, A. Analysis of Flow Patterns in High-Gravity Equipment Using Gamma-Ray Computed Tomography. *Chem. Ing. Tech.* **2019,** *91* (7), 1032–1040.

[60] Mersmann, A.; Voit, H.; Zeppenfeld, R. Brauchen wir Stoffaustausch-maschinen? *Chem. Ing. Tech.* **1986,** *58* (2), 87–96.

[61] Beck, H. M. H. Process Intensification: Mass Transfer and Pressure Drop for Countercurrent Rotating Packed Beds. Dissertation; University of Newcastle upon Tyne, Newcastle upon Tyne, England, 1997.

[62] Acharya, A.; Gottzmann, C. F.; Nowobilski, J. J. *AIRBORNE ROTARY AIR SEPARATOR STUDY. Phase II and III Interim Report*: Tonawanda, NY, 1990.

[63] Revie, R. W.; Uhlig, H. H. *Corrosion and corrosion control. An introduction to corrosion science and engineering*, Fourth edition; Wiley-Interscience, a John Wiley & Sons, Inc., Publication: Hoboken, New Jersey, 2008.

[64] Harbold, G.; Park, J. Using the GasTran® Deaeration System to achieve low dissolved oxygen levels for superior line speed and product quality: a case study in carbonated soft drink bottling. https://www.gastransfer.com/water-deaeration.php (accessed April 18, 2020).

[65] Peel, J.; Howarth, C. R.; Ramshaw, C. Process intensification: Higee seawater deaeration. *Chem. Eng. Res. Des.* **1998,** *76* (A5), 585–593.

[66] Zheng, C.; Guo, K.; Song, Y.; Zhou, X.; Al, D.; Xin, Z.; Gardner, N. C. Industrial practice of HIGRAVITEC in water deaeration. In *Process Intensification in Practice*:

Applications and opportunities; Semel, J., Ed.; BHR Group conference series no.28; Mechanical Engineering: Bury St Edmunds, 1997; pp 273–288.

[67] Peel, J. The Mass Transfer and Hydrodynamics of a Gas-Liquid Centrifugal De-oxygenator. Dissertation; University of Newcastle-upon-Tyne, Newcastle-upon-Tyne, 1995.

[68] Guo, F.; Zhao, Y.; Cui, J.; Guo, J.; Chen, J.; Zheng, C. Effect of inner packing support on liquid controlled mass transfer process in rotating packed beds. In *4th International Conference on Process Intensification for the Chemical Industry*; Gough, M., Ed., 2001; pp 107–113.

[69] Chen, Y.-S.; Lin, C.-C.; Liu, H.-S. Mass Transfer in a Rotating Packed Bed with Viscous Newtonian and Non-Newtonian Fluids. *Ind. Eng. Chem. Res.* **2005,** *44* (4), 1043–1051.

[70] Chen, Y. S.; Lin, C. C.; Liu, H. S. Mass Transfer in a Rotating Packed Bed with Various Radii of the Bed. *Ind. Eng. Chem. Res.* **2005,** *44* (20), 7868–7875.

[71] Chen, Y.-S.; Lin, F.-Y.; Lin, C.-C.; Tai, C. Y.-D.; Liu, H.-S. Packing Characteristics for Mass Transfer in a Rotating Packed Bed. *Ind. Eng. Chem. Res.* **2006,** *45* (20), 6846–6853.

[72] Beer, M. M. de; Koolaard, A. M.; Vos, H.; Bargeman, G.; Schmuhl, R. Intensified and Flexible Flash Degassing in a Rotating Packed Bed. *Ind. Eng. Chem. Res.* **2018,** *57* (42), 14261–14272.

[73] Mello, M. V. D.; Huang, H.-M. Systems and methods for deaerating seawater using a rotating packed bed device. 15/211,284, Jun 15, 2016.

[74] Chen, Q.-Y.; Chu, G.-W.; Luo, Y.; Le Sang; Zhang, L.; Zou, H.-K.; Chen, J.-F. Polytetrafluoroethylene Wire Mesh Packing in a Rotating Packed Bed: Mass-Transfer Studies. *Ind. Eng. Chem. Res.* **2016,** *55* (44), 11606–11613.

[75] Shivhare, M. K.; Rao, D. P.; Kaistha, N. Mass transfer studies on split-packing and single-block packing rotating packed beds. *Chem. Eng. Process.* **2013,** *71*, 115–124 (accessed May 16, 2018).

[76] Blass, E. Geometrische und strömungstechnische Untersuchungen an Drahtgeweben. *Chemie Ing. Techn.* **1964,** *36* (7), 747–758.

[77] Neumann, K. *Operating Characteristics of Rotating Packed Beds*; Verfahrenstechnik; Dr. Hut: München, 2018.

[78] Xie, P.; Lu, X.; Ding, H.; Yang, X.; Ingham, D.; Ma, L.; Pourkashanian, M. A mesoscale 3D CFD analysis of the liquid flow in a rotating packed bed. *Chem. Eng. Sci.* **2019,** *199*, 528–545.

[79] Lu, X.; Xie, P.; Ingham, D. B.; Ma, L.; Pourkashanian, M. A porous media model for CFD simulations of gas-liquid two-phase flow in rotating packed beds. *Chem. Eng. Sci.* **2018,** *189*, 123–134.

[80] Hampel, U.; Bieberle, A.; Hoppe, D.; Kronenberg, J.; Schleicher, E.; Sühnel, T.; Zimmermann, F.; Zippe, C. High resolution gamma ray tomography scanner for flow measurement and non-destructive testing applications. *Review of Scientific Instruments* **2007,** *78* (10), 103704.

[81] Bieberle, A.; Schleicher, E.; Hampel, U. Temperature control design for a high-resolution gamma-ray tomography detector. *Review of Scientific Instruments* **2010,** *81* (1), 14702.

[82] Prasser, H.-M.; Baldauf, D.; Fietz, J.; Hampel, U.; Hoppe, D.; Zippe, C.; Zschau, J.; Christen, M.; Will, G. Time resolving gamma-tomography for periodically changing gas fraction fields and its application to an axial pump. *Flow Measurement and Instrumentation* **2003,** *14* (3), 119–125.

[83] Bieberle, A.; Schleicher, E.; Hampel, U. Data acquisition system for angle synchronized γ-ray tomography of rapidly rotating objects. *Meas. Sci. Technol.* **2007,** *18* (11), 3384–3390.

[84] van Aarle, W.; Palenstijn, W. J.; Beenhouwer, J. de; Altantzis, T.; Bals, S.; Batenburg, K. J.; Sijbers, J. The ASTRA Toolbox: A platform for advanced algorithm development in electron tomography. *Ultramicroscopy* **2015,** *157*, 35–47.

[85] Palenstijn, W. J.; Batenburg, K. J.; Sijbers, J. Performance improvements for iterative electron tomography reconstruction using graphics processing units (GPUs). *Journal of structural biology* **2011,** *176* (2), 250–253.

[86] van Aarle, W.; Palenstijn, W. J.; Cant, J.; Janssens, E.; Bleichrodt, F.; Dabravolski, A.; Beenhouwer, J. de; Joost Batenburg, K.; Sijbers, J. Fast and flexible X-ray tomography using the ASTRA toolbox. *Optics express* **2016,** *24* (22), 25129–25147.

[87] Janzen, A.; Schubert, M.; Barthel, F.; Hampel, U.; Kenig, E. Y. Investigation of dynamic liquid distribution and hold-up in structured packings using ultrafast electron beam X-ray tomography. *Chem. Eng. Process.* **2013,** *66*, 20–26 (accessed November 12, 2017).

[88] Chu, G. W.; Gao, X.; Luo, Y.; Zou, H. K.; Shao, L.; Chen, J. Distillation studies in a two-stage counter-current rotating packed bed. *Sep. Purif. Technol.* **2013,** *102*, 62–66.

[89] Neumann, K.; Hunold, S.; Beer, M. de; Skiborowski, M.; Górak, A. Mass Transfer Studies in a Pilot Scale RPB with Different Packing Diameters. *Ind. Eng. Chem. Res.* **2018,** *57* (6), 2258–2266.

[90] MathWorks. Piecewise Cubic Hermite Interpolating Polynomial (PCHIP): Documentation (accessed January 17, 2020).

[91] Singh, S. P. Air Stripping of Volatile Organic Compounds from Groundwater: An Evaluation of a Centrifugal Vapor-Liquid Contactor. PhD Disseratation; University of Tennessee, 1989.

[92] Munjal, S.; Dudukovic, M. P.; Ramachandran, P. A. Mass-transfer in rotating packed beds-II. Experimental results and comparison with theory and gravity flow. *Chem. Eng. Sci.* **1989,** *44* (10), 2257–2268.

[93] Luo, Y.; Chu, G.-W.; Zou, H.-K.; Wang, F.; Xiang, Y.; Shao, L.; Chen, J.-F. Mass Transfer Studies in a Rotating Packed Bed with Novel Rotors: Chemisorption of CO 2. *Ind. Eng. Chem. Res.* **2011,** *51* (26), 9164–9172.

[94] Yang, K.; Chu, G.; Zou, H.; Sun, B.; Shao, L.; Chen, J.-F. Determination of the effective interfacial area in rotating packed bed. *Chem. Eng. J. (Amsterdam, Neth.)* **2011,** *168* (3), 1377–1382 (accessed December 8, 2017).

[95] Baerns, M. *Technische Chemie;* Wiley-VCH: Weinheim, 2006.

[96] Groß, K.; Beer, M. de; Dohrn, S.; Skiborowski, M. Scale-Up of the Radial Packing Length in Rotating Packed Beds for Deaeration Processes. *Ind. Eng. Chem. Res.* **2020**.

[97] Matlab Documentation. bvp5c. https://www.mathworks.com/help/matlab/ref/bvp5c.html (accessed May 6, 2020).

[98] Woods, D. R. *Rules of thumb in engineering practice;* Wiley-VCH; John Wiley [distributor]: Weinheim, Chichester, 2007.

[99] *Perry's chemical engineers' handbook;* Green, D. W., Ed., 8th ed.; McGraw-Hill: New York [etc.], op. 2008.

[100] Seider, W. D.; Seader, J. D. *Product and process design principles. Synthesis, analysis, and evaluation*, 3rd ed. International Student Version; John Wiley: New York, 2010.

[101] Andritz Separation. *Batch-Operated Filtration Centrifuge. Krauss-Maffei Peeler Centrifuge HZ*. Company Brochure.

[102] Andritz Separation. *Minimum footprint meets highest efficiency. Krauss-Maffei Vertical centrifuge VZU*. Company Brochure.

[103] Groß, K.; Neumann, K.; Skiborowski, M.; Górak, A. Analysing the Operating Limits in High Gravity Equipment. *Chem. Eng. Trans.* **2018,** *69*, 661–666. http://doi.org/10.3303/CET1869111 (accessed April 30, 2019).

[104] Sander, R. Compilation of Henry's law constants (version 4.0) for water as solvent. *Atmos. Chem. Phys.* **2015,** *15* (8), 4399–4981.

[105] Han, P.; Bartels, D. M. Temperature Dependence of Oxygen Diffusion inH2O and D2O†. *J. Phys. Chem.* **1996,** *100* (13), 5597–5602.

[106] Kestin, J.; Sokolov, M.; Wakeham, W. A. Viscosity of liquid water in the range −8 °C to 150 °C. *Journal of Physical and Chemical Reference Data* **1978,** *7* (3), 941–948.

10 Appendix

A1: Data literature comparison with flow rates used raw data provided by Neumann: Acharya [*62*], Singh [*38*], Lockett [*39*], Beck [*61*].

Author	di /m	do /m	dc /m	hp /m	Packing type	a_p /$m^2 m^{-3}$	LL /$m^3 m^{-2} h^{-1}$	FG /$Pa^{0.5}$	RCF /-	Entrainment determination method
Acharya	0.152	0.356	NaN	0.059	glass spheres	1181	36	1.1	31	visually
Acharya	0.152	0.356	NaN	0.059	glass spheres	1181	24	1.6	31	visually
Acharya	0.152	0.356	NaN	0.059	glass spheres	1181	76	1.1	86	visually
Acharya	0.152	0.356	NaN	0.059	glass spheres	1181	65	1.6	86	visually
Acharya	0.152	0.356	NaN	0.059	glass spheres	1181	59	1.9	86	visually
Acharya	0.152	0.356	NaN	0.059	glass spheres	1181	48	2.2	86	visually
Acharya	0.152	0.356	NaN	0.059	glass spheres	1181	36	2.5	86	visually
Acharya	0.152	0.356	NaN	0.059	glass spheres	1181	71	2.2	189	visually
Acharya	0.152	0.356	NaN	0.059	glass spheres	1181	65	3.1	189	visually
Acharya	0.152	0.356	NaN	0.059	glass spheres	1181	53	3.7	189	visually
Acharya	0.152	0.356	NaN	0.059	glass spheres	1181	42	4.3	189	visually
Acharya	0.165	0.356	NaN	0.058	Aluminum corrugated foil sheets	2045	66	1.5	9	visually

Author	di /m	do /m	dc /m	hp /m	Packing type	a_p /$m^2 m^{-3}$	LL /$m^3 m^{-2} h^{-1}$	FG /$Pa^{0.5}$	RCF /-	Entrainment determination method
Acharya	0.165	0.356	NaN	0.058	Aluminum corrugated foil sheets	2045	66	2.9	20	visually
Acharya	0.165	0.356	NaN	0.058	Aluminum corrugated foil sheets	2045	45	3.4	20	visually
Acharya	0.165	0.356	NaN	0.058	Aluminum corrugated foil sheets	2045	34	3.8	20	visually
Acharya	0.165	0.356	NaN	0.058	Aluminum corrugated foil sheets	2045	66	2.1	20	visually
Acharya	0.165	0.356	NaN	0.058	Aluminum corrugated foil sheets	2045	45	2.7	20	visually
Acharya	0.165	0.356	NaN	0.058	Aluminum corrugated foil sheets	2045	34	3.2	20	visually
Acharya	0.165	0.356	NaN	0.058	Aluminum corrugated foil sheets	2045	55	3.5	34	visually
Acharya	0.165	0.356	NaN	0.058	Aluminum corrugated foil sheets	2045	45	4.0	34	visually
Acharya	0.165	0.356	NaN	0.058	Aluminum corrugated foil sheets	2045	34	4.5	34	visually

Author	di /m	do /m	dc /m	hp /m	Packing type	a_p /$m^2 m^{-3}$	LL /$m^3 m^{-2} h^{-1}$	FG /$Pa^{0.5}$	RCF /-	Entrainment determination method
Acharya	0.165	0.356	NaN	0.058	Aluminum corrugated foil sheets	2045	61	4.9	48	visually
Acharya	0.165	0.356	NaN	0.058	Aluminum corrugated foil sheets	2045	66	2.3	48	visually
Acharya	0.165	0.356	NaN	0.058	Aluminum corrugated foil sheets	2045	66	4.5	48	visually
Acharya	0.165	0.356	NaN	0.058	Aluminum corrugated foil sheets	2045	66	5.0	104	visually
Acharya	0.165	0.356	NaN	0.058	Aluminum corrugated foil sheets	2045	45	5.1	104	visually
Acharya	0.165	0.356	NaN	0.058	Aluminum corrugated foil sheets	2045	66	2.9	104	visually
Acharya	0.165	0.356	NaN	0.058	Aluminum corrugated foil sheets	2045	45	3.5	104	visually
Singh	0.254	0.762	NaN	0.127	Sumitomo (metal sponge like)	2500	22	0.5	17	pressure drop minimum by Groß
Singh	0.254	0.762	NaN	0.127	Sumitomo (metal sponge like)	2500	22	1.5	51	pressure drop minimum by Groß

Author	di /m	do /m	dc /m	hp /m	Packing type	a_p /$m^2 m^{-3}$	LL /$m^3 m^{-2} h^{-1}$	FG /$Pa^{0.5}$	RCF /-	Entrainment determination method
Singh	0.254	0.762	NaN	0.127	Sumitomo (metal sponge like)	2500	22	2.6	70	pressure drop minimum by Groß
Singh	0.254	0.762	NaN	0.127	Sumitomo (metal sponge like)	2500	22	3.6	60	pressure drop minimum by Groß
Lockett	0.166	0.356	NaN	0.058	unperforated sheets of corrugated aluminum foil thickness 0.15mm	1770	8	3.7	5	pressure drop maximum by author
Lockett	0.166	0.356	NaN	0.058	unperforated sheets of corrugated aluminum foil thickness 0.15mm	1770	8	3.3	9	pressure drop maximum by author
Lockett	0.166	0.356	NaN	0.058	unperforated sheets of corrugated aluminum foil thickness 0.15mm	1770	8	3.3	9	pressure drop maximum by author
Lockett	0.166	0.356	NaN	0.058	unperforated sheets of corrugated aluminum foil thickness 0.15mm	1770	8	3.9	11	pressure drop maximum by author
Lockett	0.166	0.356	NaN	0.058	unperforated sheets of corrugated aluminum foil thickness 0.15mm	1770	8	3.9	11	pressure drop maximum by author

Author	di /m	do /m	dc /m	hp /m	Packing type	a_p /$m^2 m^{-3}$	LL /$m^3 m^{-2} h^{-1}$	FG /$Pa^{0.5}$	RCF /-	Entrainment determination method
Lockett	0.166	0.356	NaN	0.058	unperforated sheets of corrugated aluminum foil thickness 0.15mm	1770	8	3.8	14	pressure drop maximum by author
Lockett	0.166	0.356	NaN	0.058	unperforated sheets of corrugated aluminum foil thickness 0.15mm	1770	8	4.8	16	pressure drop maximum by author
Lockett	0.166	0.356	NaN	0.058	unperforated sheets of corrugated aluminum foil thickness 0.15mm	1770	8	5.2	18	pressure drop maximum by author
Lockett	0.166	0.356	NaN	0.058	unperforated sheets of corrugated aluminum foil thickness 0.15mm	1770	8	5.2	19	pressure drop maximum by author
Lockett	0.166	0.356	NaN	0.058	unperforated sheets of corrugated aluminum foil thickness 0.15mm	1770	8	5.5	22	pressure drop maximum by author
Lockett	0.166	0.356	NaN	0.058	unperforated sheets of corrugated aluminum foil thickness 0.15mm	1770	15	2.7	2	pressure drop maximum by author

Author	di /m	do /m	dc /m	hp /m	Packing type	a_p /$m^2 m^{-3}$	LL /$m^3 m^{-2} h^{-1}$	FG /$Pa^{0.5}$	RCF /-	Entrainment determination method
Lockett	0.166	0.356	NaN	0.058	unperforated sheets of corrugated aluminum foil thickness 0.15mm	1770	15	2.9	3	pressure drop maximum by author
Lockett	0.166	0.356	NaN	0.058	unperforated sheets of corrugated aluminum foil thickness 0.15mm	1770	15	3.4	4	pressure drop maximum by author
Lockett	0.166	0.356	NaN	0.058	unperforated sheets of corrugated aluminum foil thickness 0.15mm	1770	15	3.8	6	pressure drop maximum by author
Lockett	0.166	0.356	NaN	0.058	unperforated sheets of corrugated aluminum foil thickness 0.15mm	1770	15	3.9	7	pressure drop maximum by author
Lockett	0.166	0.356	NaN	0.058	unperforated sheets of corrugated aluminum foil thickness 0.15mm	1770	15	4.8	11	pressure drop maximum by author
Lockett	0.166	0.356	NaN	0.058	unperforated sheets of corrugated aluminum foil thickness 0.15mm	1770	15	5.1	13	pressure drop maximum by author

Author	di /m	do /m	dc /m	hp /m	Packing type	a_p /$m^2 m^{-3}$	LL /$m^3 m^{-2} h^{-1}$	FG /$Pa^{0.5}$	RCF /-	Entrainment determination method
Lockett	0.166	0.356	NaN	0.058	unperforated sheets of corrugated aluminum foil thickness 0.15mm	1770	15	4.8	13	pressure drop maximum by author
Lockett	0.166	0.356	NaN	0.058	unperforated sheets of corrugated aluminum foil thickness 0.15mm	1770	15	6.0	17	pressure drop maximum by author
Lockett	0.166	0.356	NaN	0.058	unperforated sheets of corrugated aluminum foil thickness 0.15mm	1770	15	6.3	22	pressure drop maximum by author
Lockett	0.166	0.356	NaN	0.058	unperforated sheets of corrugated aluminum foil thickness 0.15mm	1770	23	2.1	1	pressure drop maximum by author
Lockett	0.166	0.356	NaN	0.058	unperforated sheets of corrugated aluminum foil thickness 0.15mm	1770	23	2.6	2	pressure drop maximum by author
Lockett	0.166	0.356	NaN	0.058	unperforated sheets of corrugated aluminum foil thickness 0.15mm	1770	23	3.3	3	pressure drop maximum by author

Author	di /m	do /m	dc /m	hp /m	Packing type	a_p /$m^2 m^{-3}$	LL /$m^3 m^{-2} h^{-1}$	FG /$Pa^{0.5}$	RCF /-	Entrainment determination method
Lockett	0.166	0.356	NaN	0.058	unperforated sheets of corrugated aluminum foil thickness 0.15mm	1770	23	3.5	4	pressure drop maximum by author
Lockett	0.166	0.356	NaN	0.058	unperforated sheets of corrugated aluminum foil thickness 0.15mm	1770	23	4.1	6	pressure drop maximum by author
Lockett	0.166	0.356	NaN	0.058	unperforated sheets of corrugated aluminum foil thickness 0.15mm	1770	23	4.7	7	pressure drop maximum by author
Lockett	0.166	0.356	NaN	0.058	unperforated sheets of corrugated aluminum foil thickness 0.15mm	1770	23	5.0	10	pressure drop maximum by author
Lockett	0.166	0.356	NaN	0.058	unperforated sheets of corrugated aluminum foil thickness 0.15mm	1770	23	5.3	12	pressure drop maximum by author
Lockett	0.166	0.356	NaN	0.058	unperforated sheets of corrugated aluminum foil thickness 0.15mm	1770	23	5.6	16	pressure drop maximum by author

Author	di /m	do /m	dc /m	hp /m	Packing type	a_p /$m^2 m^{-3}$	LL /$m^3 m^{-2} h^{-1}$	FG /$Pa^{0.5}$	RCF /-	Entrainment determination method
Lockett	0.166	0.356	NaN	0.058	unperforated sheets of corrugated aluminum foil thickness 0.15mm	1770	23	5.9	19	pressure drop maximum by author
Lockett	0.166	0.356	NaN	0.058	unperforated sheets of corrugated aluminum foil thickness 0.15mm	1770	31	3.6	2	pressure drop maximum by author
Lockett	0.166	0.356	NaN	0.058	unperforated sheets of corrugated aluminum foil thickness 0.15mm	1770	31	3.7	2	pressure drop maximum by author
Lockett	0.166	0.356	NaN	0.058	unperforated sheets of corrugated aluminum foil thickness 0.15mm	1770	31	4.1	4	pressure drop maximum by author
Lockett	0.166	0.356	NaN	0.058	unperforated sheets of corrugated aluminum foil thickness 0.15mm	1770	31	4.7	6	pressure drop maximum by author
Lockett	0.166	0.356	NaN	0.058	unperforated sheets of corrugated aluminum foil thickness 0.15mm	1770	31	5.4	9	pressure drop maximum by author

Author	di /m	do /m	dc /m	hp /m	Packing type	a_p /$m^2 m^{-3}$	LL /$m^3 m^{-2} h^{-1}$	FG /$Pa^{0.5}$	RCF /-	Entrainment determination method
Lockett	0.166	0.356	NaN	0.058	unperforated sheets of corrugated aluminum foil thickness 0.15mm	1770	31	5.7	11	pressure drop maximum by author
Lockett	0.166	0.356	NaN	0.058	unperforated sheets of corrugated aluminum foil thickness 0.15mm	1770	31	6.0	13	pressure drop maximum by author
Lockett	0.166	0.356	NaN	0.058	unperforated sheets of corrugated aluminum foil thickness 0.15mm	1770	31	6.3	18	pressure drop maximum by author
Lockett	0.166	0.356	NaN	0.058	unperforated sheets of corrugated aluminum foil thickness 0.15mm	1770	31	6.6	22	pressure drop maximum by author
Lockett	0.166	0.356	NaN	0.058	unperforated sheets of corrugated aluminum foil thickness 0.15mm	1770	35	3.6	1	pressure drop maximum by author
Lockett	0.166	0.356	NaN	0.058	unperforated sheets of corrugated aluminum foil thickness 0.15mm	1770	35	3.5	2	pressure drop maximum by author

Author	di /m	do /m	dc /m	hp /m	Packing type	a_p $/m^2 m^{-3}$	LL $/m^3 m^{-2} h^{-1}$	FG $/Pa^{0.5}$	RCF /-	Entrainment determination method
Lockett	0.166	0.356	NaN	0.058	unperforated sheets of corrugated aluminum foil thickness 0.15mm	1770	35	4.1	3	pressure drop maximum by author
Lockett	0.166	0.356	NaN	0.058	unperforated sheets of corrugated aluminum foil thickness 0.15mm	1770	35	4.1	4	pressure drop maximum by author
Lockett	0.166	0.356	NaN	0.058	unperforated sheets of corrugated aluminum foil thickness 0.15mm	1770	35	5.1	6	pressure drop maximum by author
Lockett	0.166	0.356	NaN	0.058	unperforated sheets of corrugated aluminum foil thickness 0.15mm	1770	35	5.3	8	pressure drop maximum by author
Lockett	0.166	0.356	NaN	0.058	unperforated sheets of corrugated aluminum foil thickness 0.15mm	1770	35	5.7	11	pressure drop maximum by author
Lockett	0.166	0.356	NaN	0.058	unperforated sheets of corrugated aluminum foil thickness 0.15mm	1770	35	6.0	12	pressure drop maximum by author

Author	di /m	do /m	dc /m	hp /m	Packing type	a_p /$m^2 m^{-3}$	LL /$m^3 m^{-2} h^{-1}$	FG /$Pa^{0.5}$	RCF /-	Entrainment determination method
Lockett	0.166	0.356	NaN	0.058	unperforated sheets of corrugated aluminum foil thickness 0.15mm	1770	35	6.3	14	pressure drop maximum by author
Lockett	0.166	0.356	NaN	0.058	unperforated sheets of corrugated aluminum foil thickness 0.15mm	1770	35	6.3	16	pressure drop maximum by author
Lockett	0.166	0.356	NaN	0.058	unperforated sheets of corrugated aluminum foil thickness 0.15mm	1770	35	6.6	18	pressure drop maximum by author
Lockett	0.166	0.356	NaN	0.058	unperforated sheets of corrugated aluminum foil thickness 0.15mm	1770	35	6.9	21	pressure drop maximum by author
Lockett	0.166	0.356	NaN	0.058	unperforated sheets of corrugated aluminum foil thickness 0.15mm	1770	37	3.8	2	pressure drop maximum by author
Lockett	0.166	0.356	NaN	0.058	unperforated sheets of corrugated aluminum foil thickness 0.15mm	1770	37	4.2	3	pressure drop maximum by author

Author	di /m	do /m	dc /m	hp /m	Packing type	a_p /$m^2 m^{-3}$	LL /$m^3 m^{-2} h^{-1}$	FG /$Pa^{0.5}$	RCF /-	Entrainment determination method
Lockett	0.166	0.356	NaN	0.058	unperforated sheets of corrugated aluminum foil thickness 0.15mm	1770	37	4.5	4	pressure drop maximum by author
Lockett	0.166	0.356	NaN	0.058	unperforated sheets of corrugated aluminum foil thickness 0.15mm	1770	37	4.8	6	pressure drop maximum by author
Lockett	0.166	0.356	NaN	0.058	unperforated sheets of corrugated aluminum foil thickness 0.15mm	1770	37	5.7	10	pressure drop maximum by author
Lockett	0.166	0.356	NaN	0.058	unperforated sheets of corrugated aluminum foil thickness 0.15mm	1770	37	6.0	13	pressure drop maximum by author
Lockett	0.166	0.356	NaN	0.058	unperforated sheets of corrugated aluminum foil thickness 0.15mm	1770	37	6.6	17	pressure drop maximum by author
Lockett	0.166	0.356	NaN	0.058	unperforated sheets of corrugated aluminum foil thickness 0.15mm	1770	37	6.9	19	pressure drop maximum by author

Author	di /m	do /m	dc /m	hp /m	Packing type	a_p /$m^2 m^{-3}$	LL /$m^3 m^{-2} h^{-1}$	FG /$Pa^{0.5}$	RCF /-	Entrainment determination method
Lockett	0.166	0.356	NaN	0.058	unperforated sheets of corrugated aluminum foil thickness 0.15mm	1770	37	7.2	25	pressure drop maximum by author
Beck	0.07	0.21	NaN	0.022	Declon packing (rigidized polyurethane foam	870	131	4.2	8	visually
Beck	0.07	0.21	NaN	0.022	Declon packing (rigidized polyurethane foam	870	131	4.8	12	visually
Beck	0.07	0.21	NaN	0.022	Declon packing (rigidized polyurethane foam	870	131	5.3	15	visually
Beck	0.07	0.21	NaN	0.022	Declon packing (rigidized polyurethane foam	870	131	5.6	20	visually
Beck	0.07	0.21	NaN	0.022	Declon packing (rigidized polyurethane foam	870	131	5.9	24	visually
Beck	0.07	0.21	NaN	0.022	Declon packing (rigidized polyurethane foam	870	220	4.2	8	visually
Beck	0.07	0.21	NaN	0.022	Declon packing (rigidized polyurethane foam	870	220	4.4	12	visually
Beck	0.07	0.21	NaN	0.022	Declon packing (rigidized polyurethane foam	870	220	4.8	15	visually

Author	di /m	do /m	dc /m	hp /m	Packing type	a_p /$m^2 m^{-3}$	LL /$m^3m^{-2}h^{-1}$	FG /$Pa^{0.5}$	RCF /-	Entrainment determination method
Beck	0.07	0.21	NaN	0.022	Declon packing (rigidized polyurethane foam	870	220	5.3	19	visually
Beck	0.07	0.21	NaN	0.022	Declon packing (rigidized polyurethane foam	870	220	5.6	24	visually
Beck	0.07	0.21	NaN	0.022	Declon packing (rigidized polyurethane foam	870	179	3.6	8	visually
Beck	0.07	0.21	NaN	0.022	Declon packing (rigidized polyurethane foam	870	179	4.6	12	visually
Beck	0.07	0.21	NaN	0.022	Declon packing (rigidized polyurethane foam	870	179	4.9	15	visually
Beck	0.07	0.21	NaN	0.022	Declon packing (rigidized polyurethane foam	870	179	5.1	20	visually
Beck	0.07	0.21	NaN	0.022	Declon packing (rigidized polyurethane foam	870	179	5.4	24	visually
Beck	0.07	0.21	NaN	0.022	Declon packing (rigidized polyurethane foam	870	273	2.5	8	visually
Beck	0.07	0.21	NaN	0.022	Declon packing (rigidized polyurethane foam	870	273	3.3	12	visually

Author	di /m	do /m	dc /m	hp /m	Packing type	a_p /$m^2 m^{-3}$	LL /$m^3m^{-2}h^{-1}$	FG /$Pa^{0.5}$	RCF /-	Entrainment determination method
Beck	0.07	0.21	NaN	0.022	Declon packing (rigidized polyurethane foam	870	273	3.7	15	visually
Beck	0.07	0.21	NaN	0.022	Declon packing (rigidized polyurethane foam	870	273	4.1	19	visually
Beck	0.07	0.21	NaN	0.022	Declon packing (rigidized polyurethane foam	870	273	4.5	24	visually
Beck	0.07	0.21	NaN	0.022	Declon packing (rigidized polyurethane foam	870	328	2.0	8	visually
Beck	0.07	0.21	NaN	0.022	Declon packing (rigidized polyurethane foam	870	328	2.1	12	visually
Beck	0.07	0.21	NaN	0.022	Declon packing (rigidized polyurethane foam	870	328	3.0	15	visually
Beck	0.07	0.21	NaN	0.022	Declon packing (rigidized polyurethane foam	870	328	3.6	19	visually
Beck	0.07	0.21	NaN	0.022	Declon packing (rigidized polyurethane foam	870	328	4.1	25	visually

A2: Dry pressure drop comparison

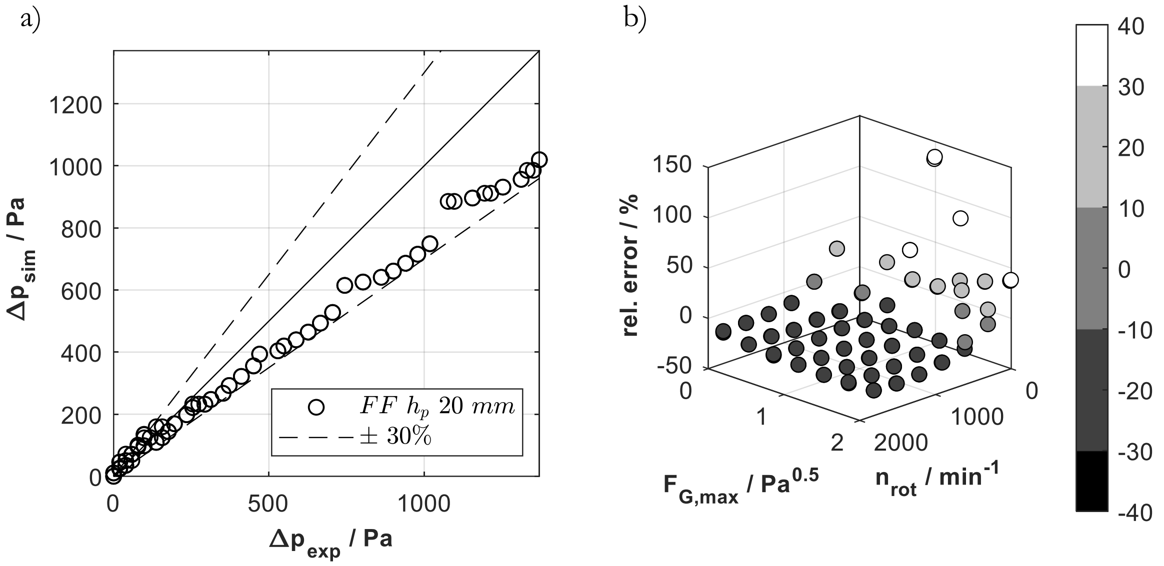

Figure 10.1: a) parity plot for the simulated and the experimental dry pressure drop b) Overview of the full foam (FF) data with $h_p = 20$ mm. ($A_{CH} = 0.88$; φ=0.30).

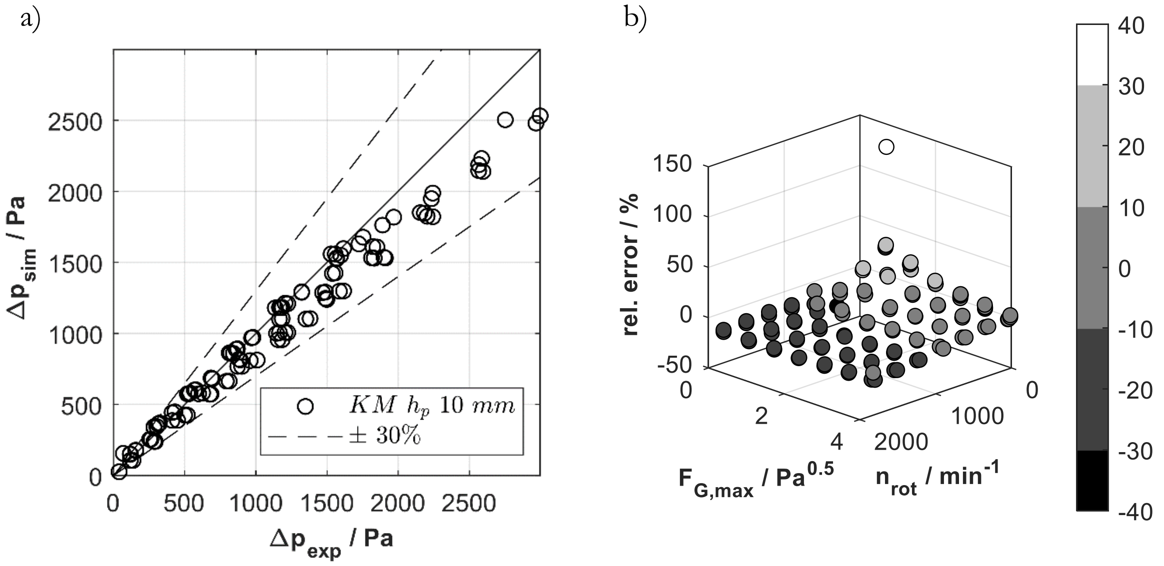

Figure 10.2: a) parity plot for the simulated and the experimental dry pressure drop b) Overview of the knitted mesh data with $h_p = 10$ mm. ($A_{CH} = 0.95$; φ=0.60).

A3: Comparison reference scans

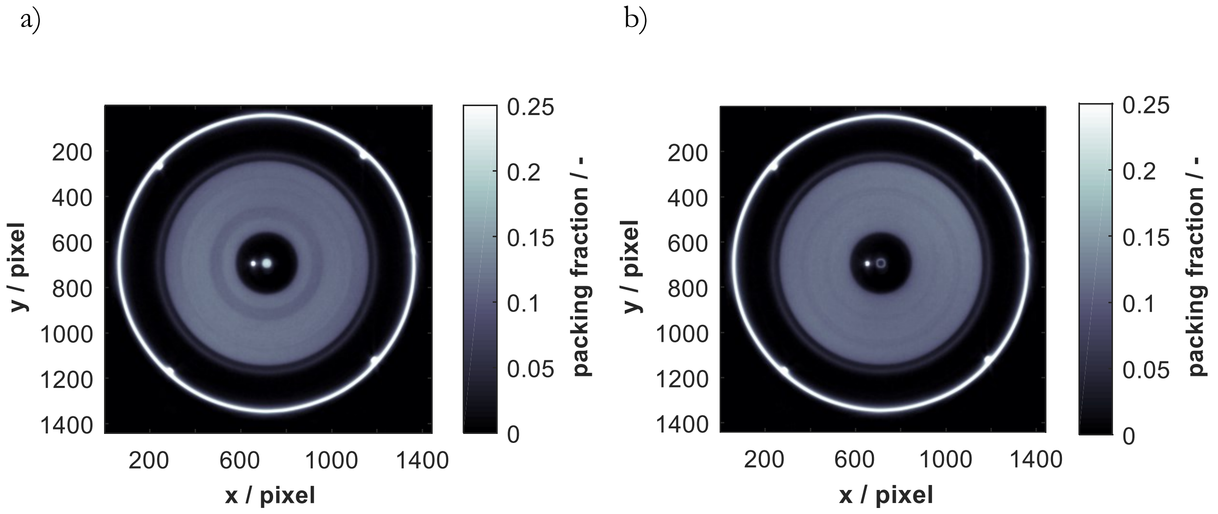

Figure 10.3: Dry reference scan: 1200 min^{-1} *conv*CT a) ring foam b) full foam (FF).

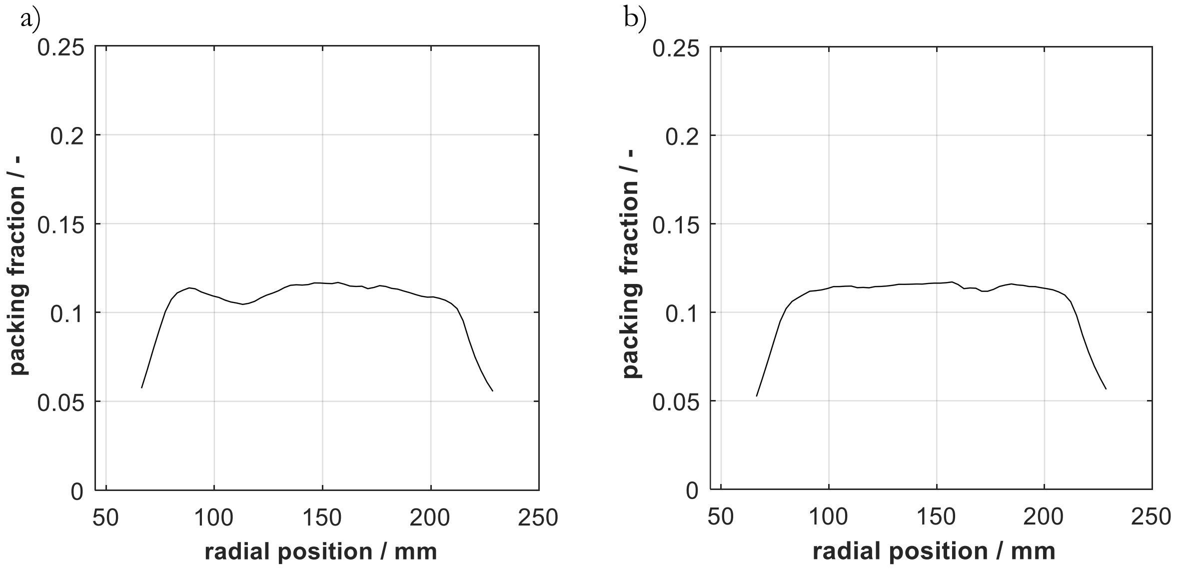

Figure 10.4: Dry reference scan, radial packing fraction: 1200 min^{-1} *conv*CT a) ring foam b) full foam (FF).

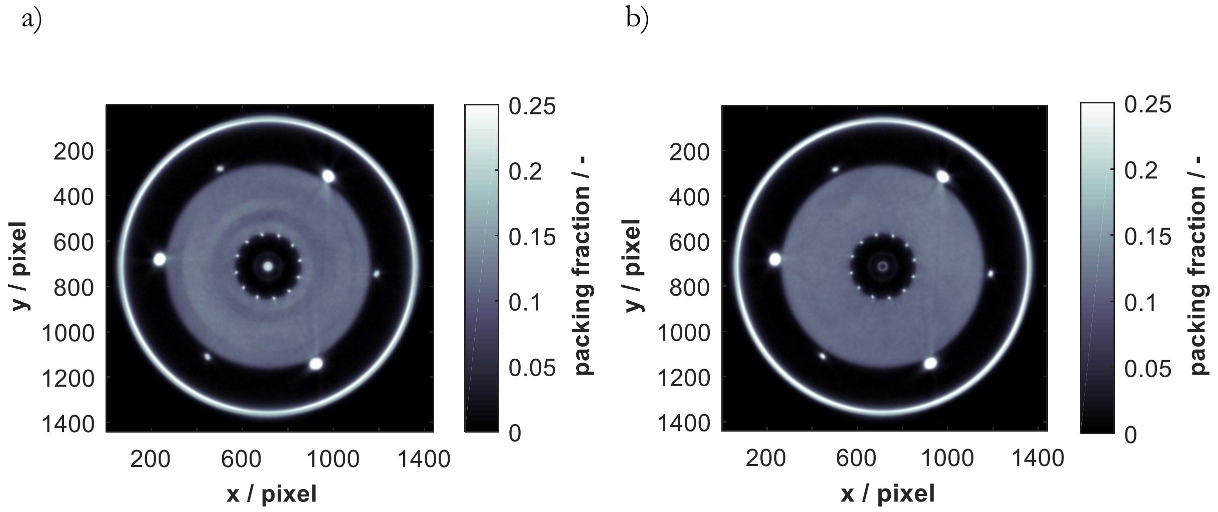

Figure 10.5: Dry reference scan: 1200 min^{-1} *tar*CT a) ring foam b) full foam (FF).

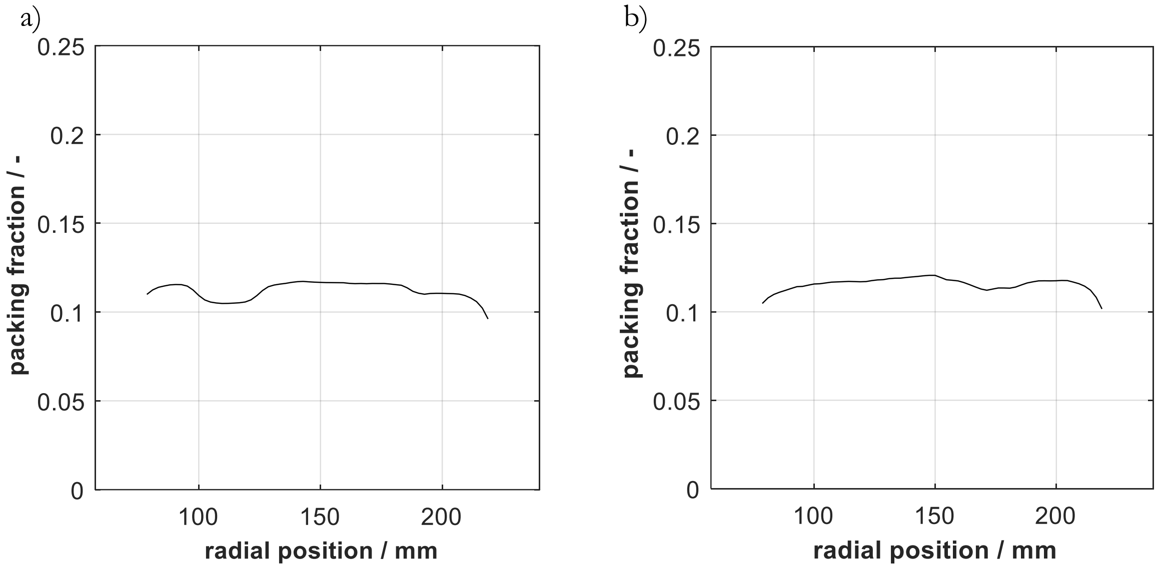

Figure 10.6: Dry reference scan, radial packing fraction: 1200 min^{-1} *tar*CT a) ring foam b) full foam (FF).

A4: Pressure drop curves for the automated entrainment detection (FF packing)

1)

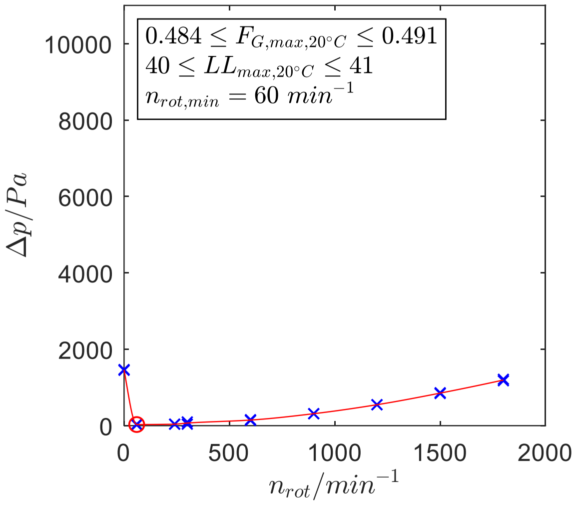

2)

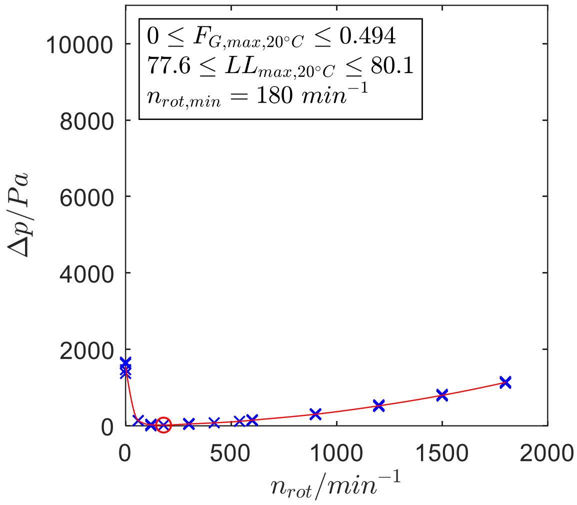

3)

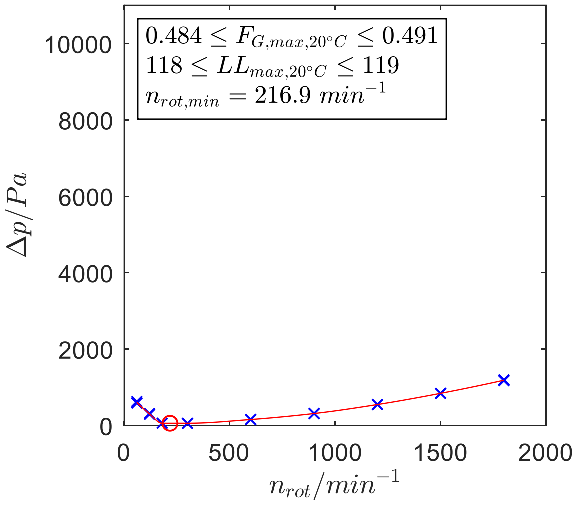

4)

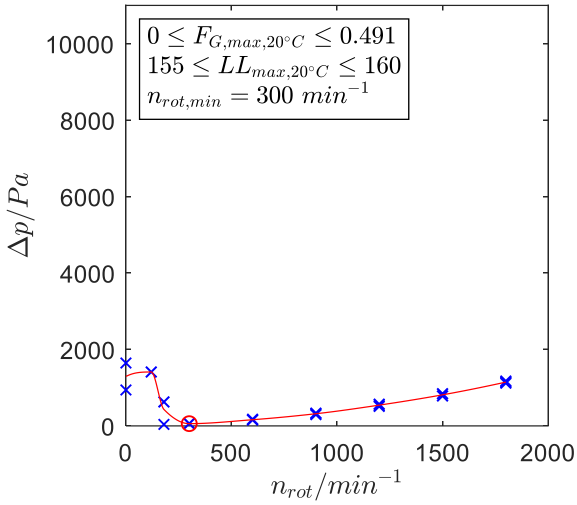

5)

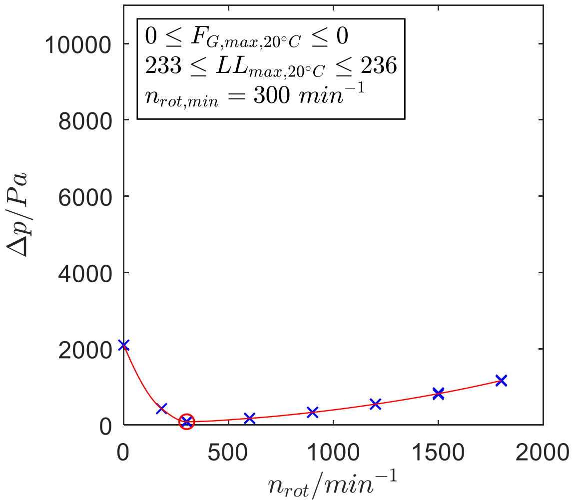

Automated determination of minimal rotational speed for the full foam packing with ($d_i/d_o/h_p$) 0.146/0.450/[0.01,0.02] m in counter-current operation.

Parameter range

0 $\leq F_{G,max,20°C} \leq$ 0.494 / Pa
40 $\leq LL_{max,20°C} \leq$ 236 / $m^3 m^{-2} h^{-1}$

(A4 continuation)

6)

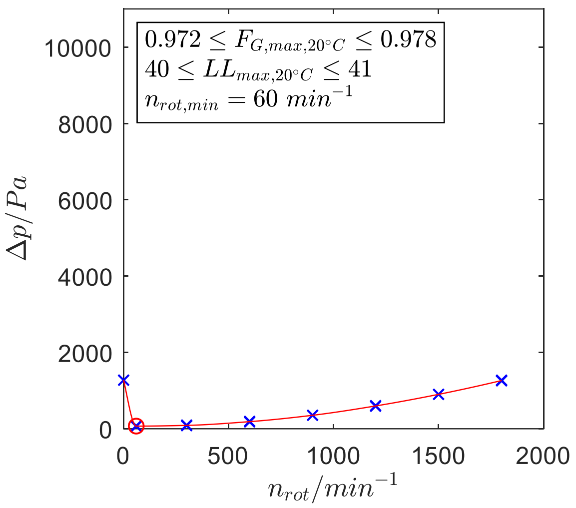

7)

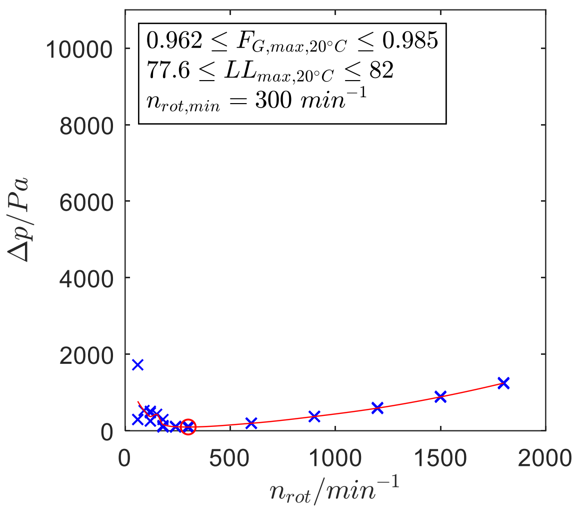

8)

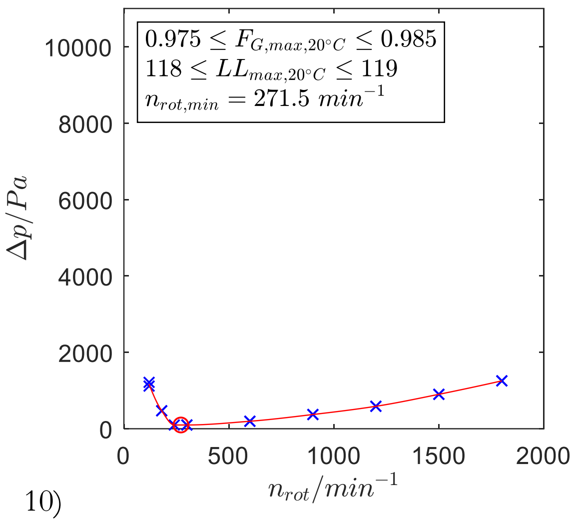

9)

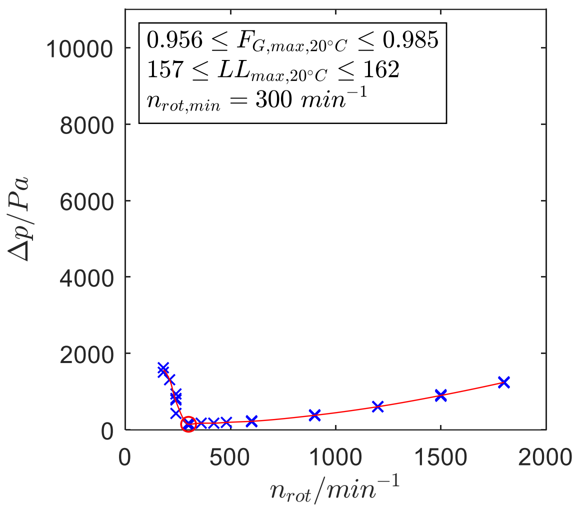

10)

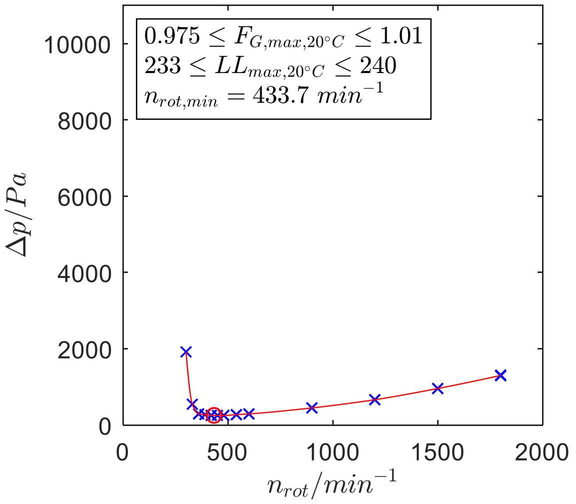

Automated determination of minimal rotational speed for the full foam packing with ($d_i/d_o/h_p$) 0.146/0.450/[0.01,0.02] m in counter-current operation.

Parameter range

0.956	$\leq F_{G,max,20°C} \leq$	1.01	/ Pa
40	$\leq LL_{max,20°C} \leq$	240	/ $m^3 m^{-2} h^{-1}$

(A4 continuation)

11)

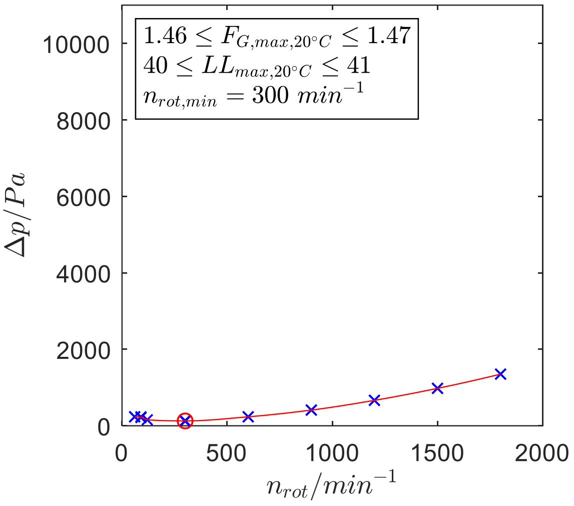

12)

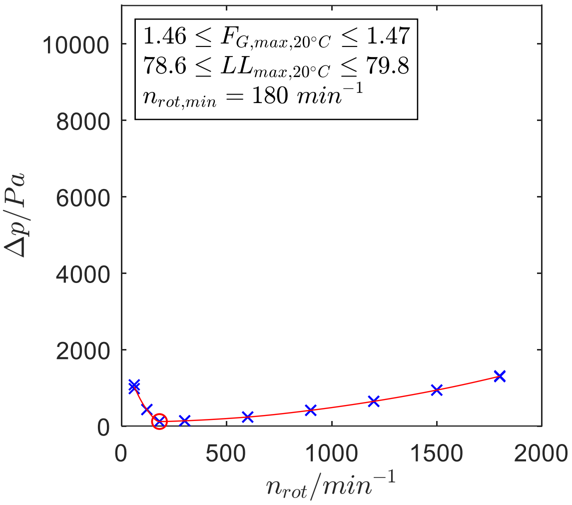

13)

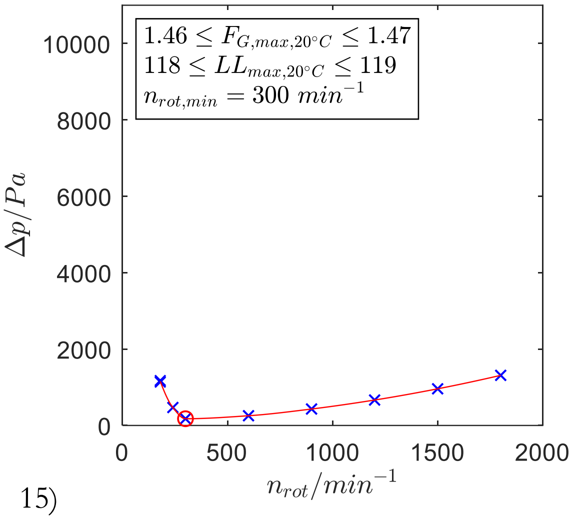

14)

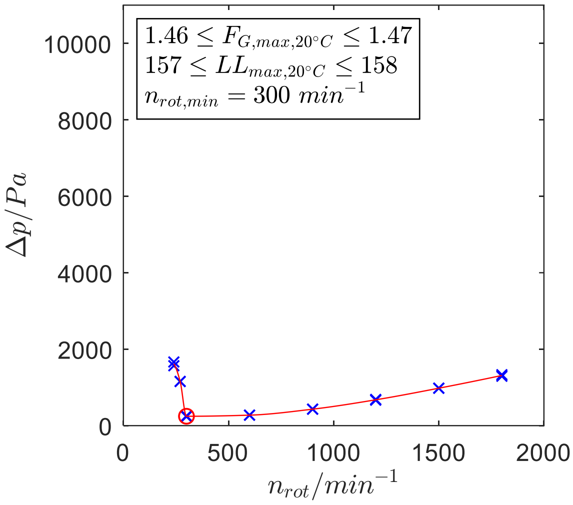

15)

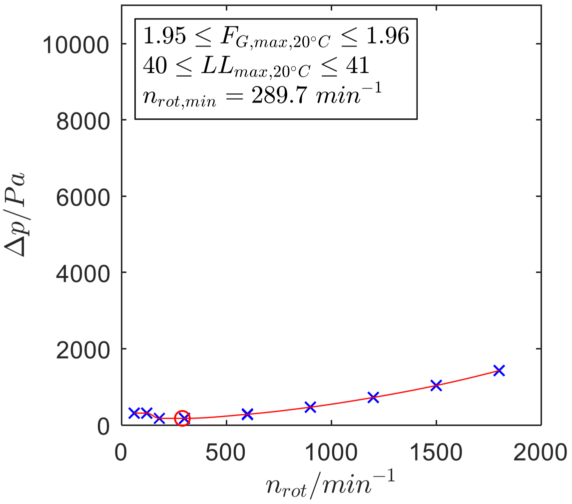

Automated determination of minimal rotational speed for the full foam packing with ($d_i/d_o/h_p$) 0.146/0.450/[0.01,0.02] m in counter-current operation.

Parameter range

1.46	$\leq F_{G,max,20°C} \leq$	1.96	/ Pa
40	$\leq LL_{max,20°C} \leq$	158	/ $m^3 m^{-2} h^{-1}$

(A4 continuation)

16)

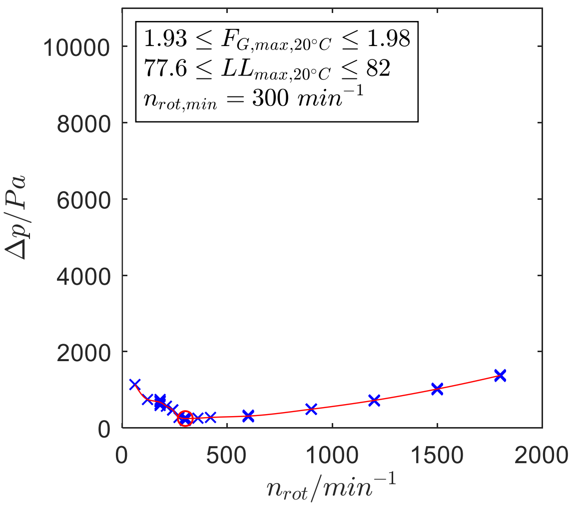

17)

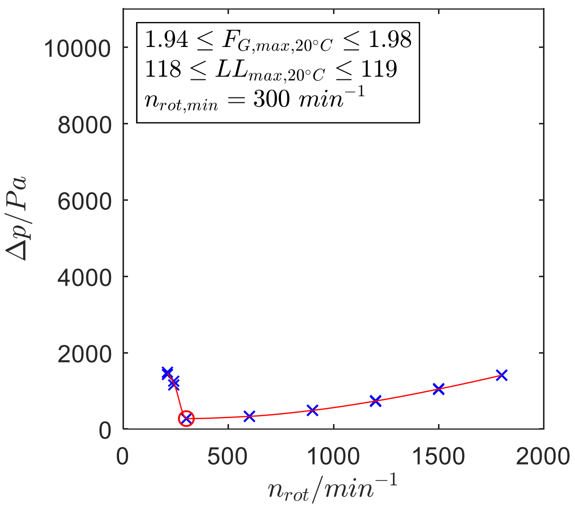

18)

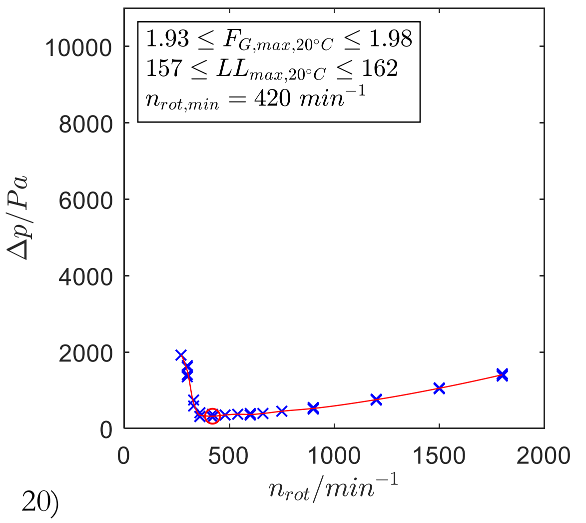

19)

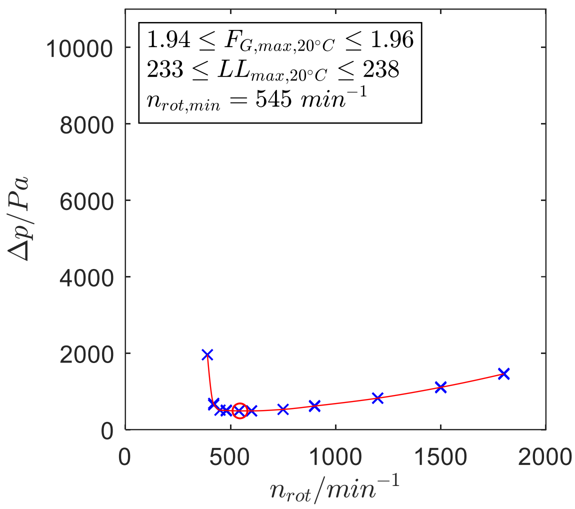

20)

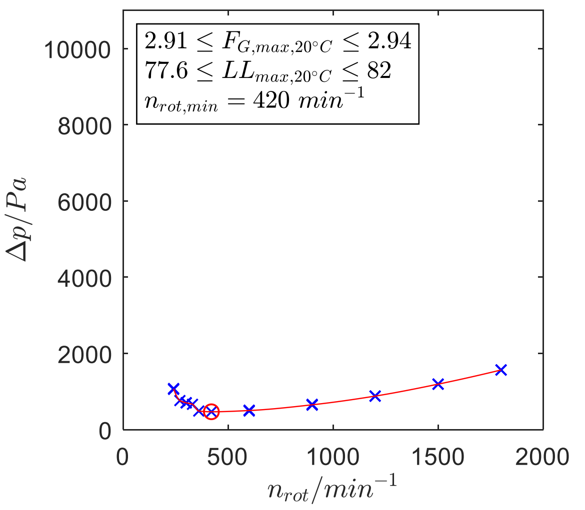

Automated determination of minimal rotational speed for the full foam packing with ($d_i/d_o/h_p$) 0.146/0.450/[0.01,0.02] m in counter-current operation.

Parameter range

$1.93 \leq F_{G,max,20°C} \leq 2.94$ / Pa
$77.6 \leq LL_{max,20°C} \leq 238$ / $m^3 m^{-2} h^{-1}$

(A4 continuation)

21)

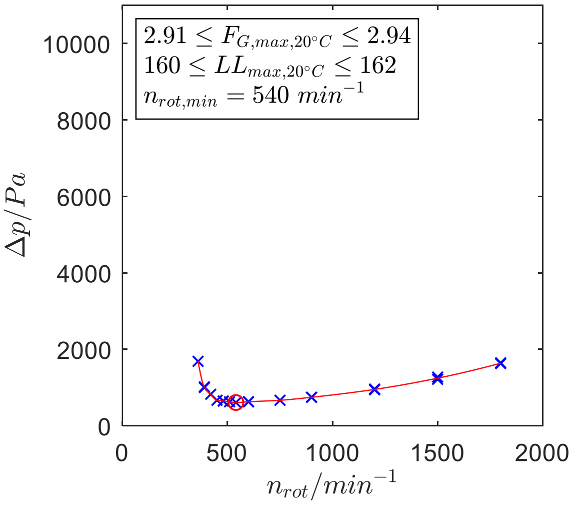

22)

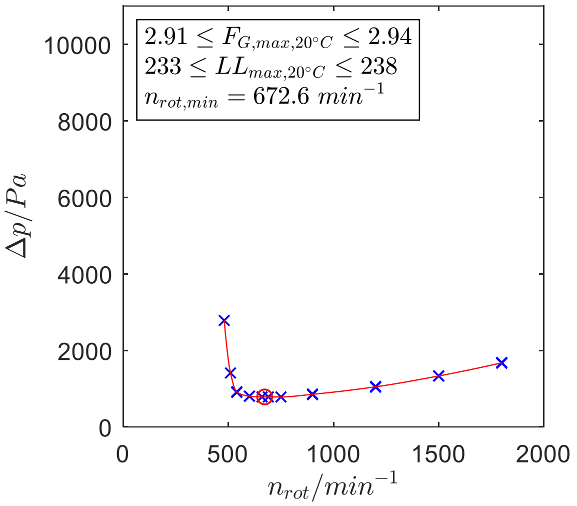

23)

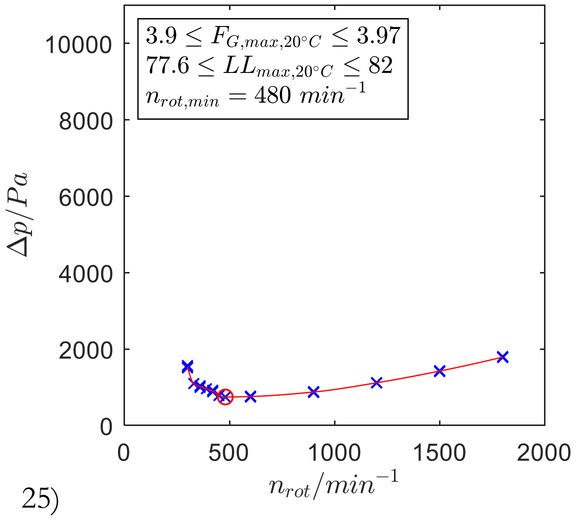

24)

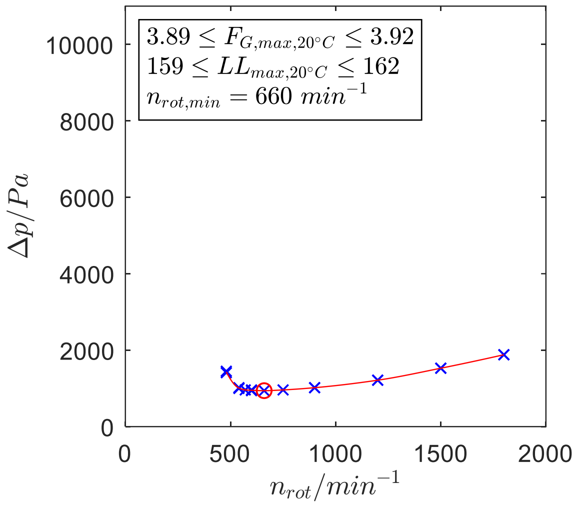

25)

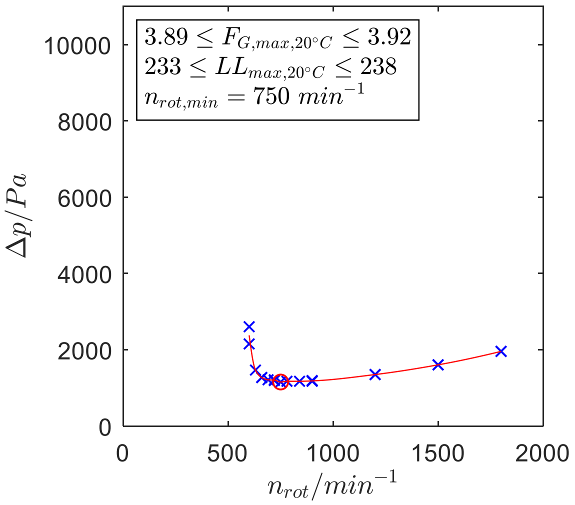

Automated determination of minimal rotational speed for the full foam packing with ($d_i/d_o/h_p$) 0.146/0.450/[0.01,0.02] m in counter-current operation.

Parameter range

2.91	$\leq F_{G,max,20°C} \leq$	3.97	/ Pa
77.6	$\leq LL_{max,20°C} \leq$	238	/ $m^3\,m^{-2}\,h^{-1}$

(A4 continuation)

26)

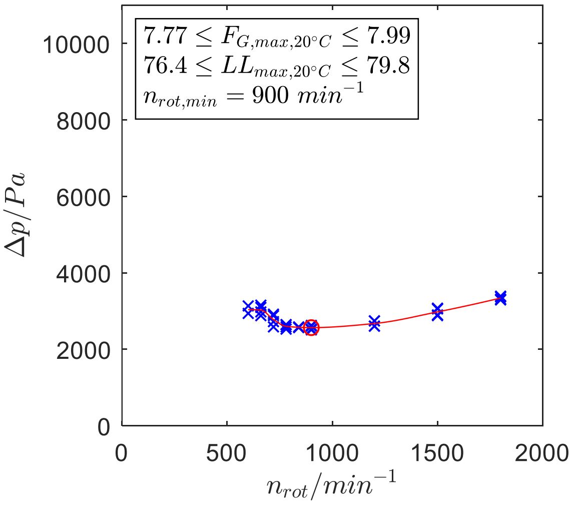

27)

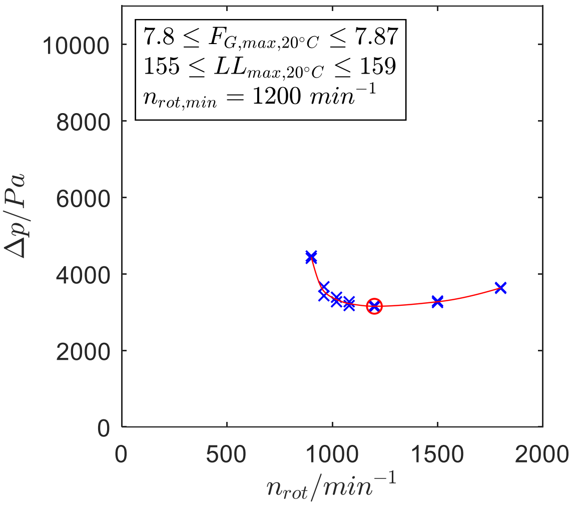

28)

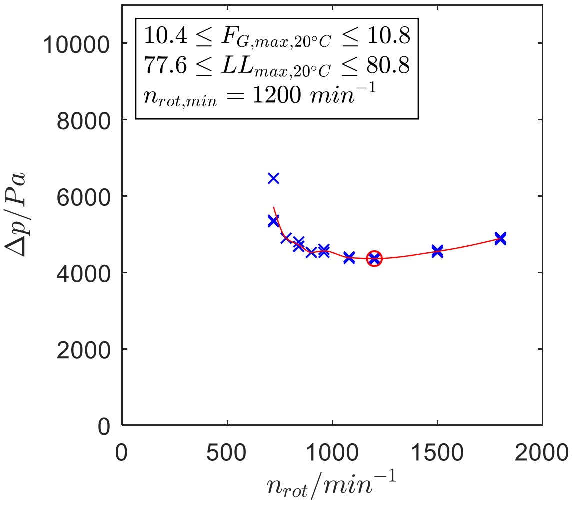

29)

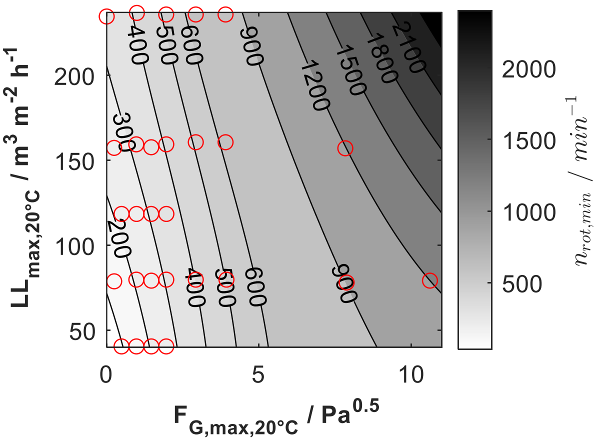

Automated determination of minimal rotational speed for the full foam packing with ($d_i/d_o/h_p$) 0.146/0.450/[0.01,0.02] m in counter-current operation.

Parameter range

$7.77 \leq F_{G,max,20°C} \leq 10.8$ / Pa
$76.4 \leq LL_{max,20°C} \leq 159$ / $m^3\ m^{-2}\ h^{-1}$

A5: Pressure drop curves for the automated entrainment detection (knit mesh packing)

1)

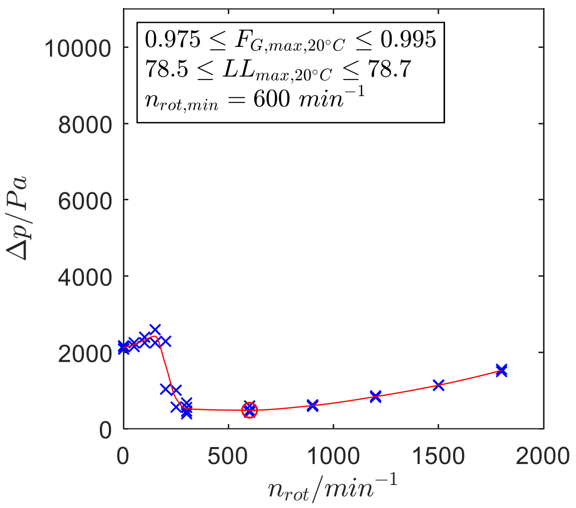

2)

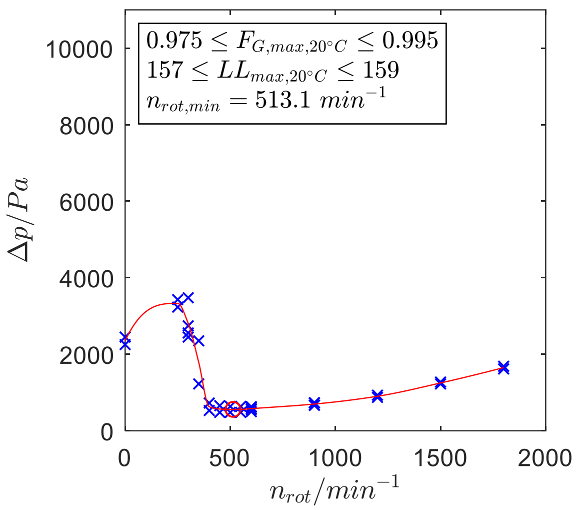

3)

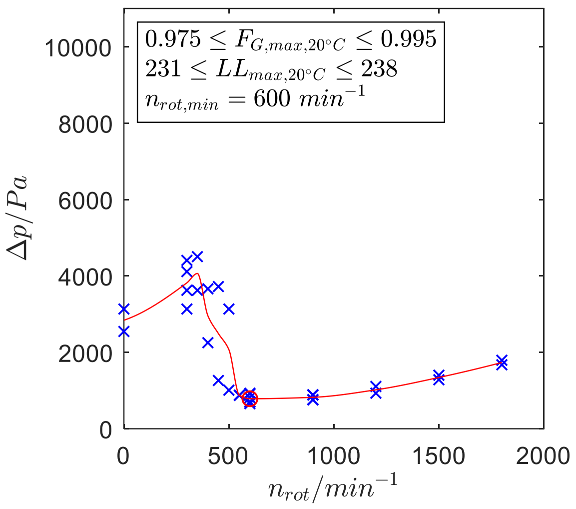

4)

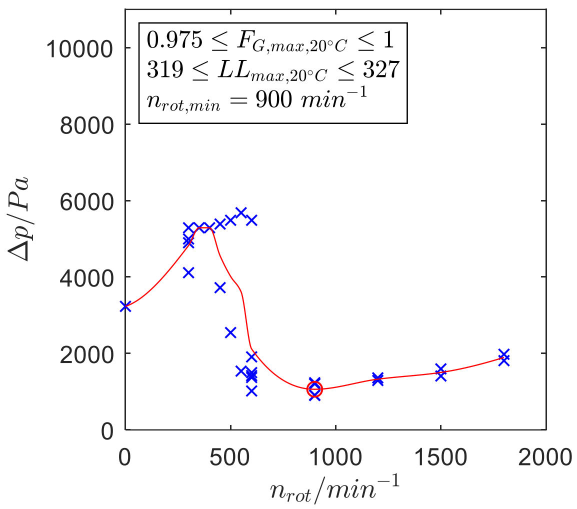

Automated determination of minimal rotational speed for the knitted mesh packing with ($d_i/d_o/h_p$) 0.146/0.450/0.01 m in counter-current operation.

5)

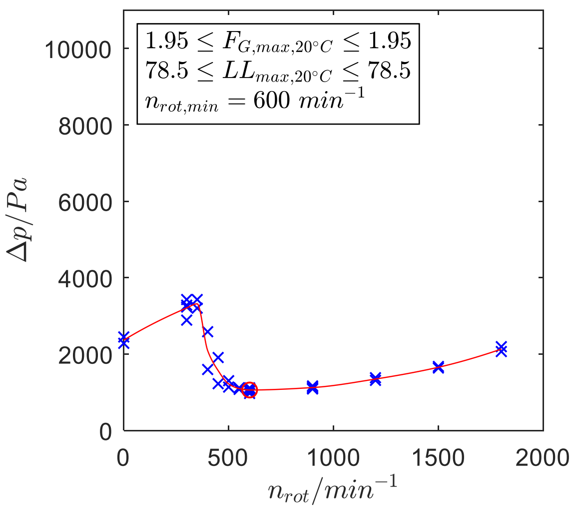

Parameter range

0.975 $\leq F_{G,max,20°C} \leq$ 1.95 / Pa
78.5 $\leq LL_{max,20°C} \leq$ 327 / $m^3 m^2 h^{-1}$

(A5 continuation)

6)

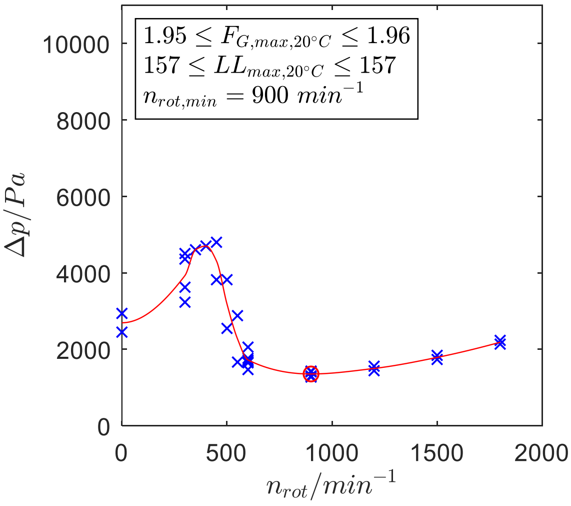

7)

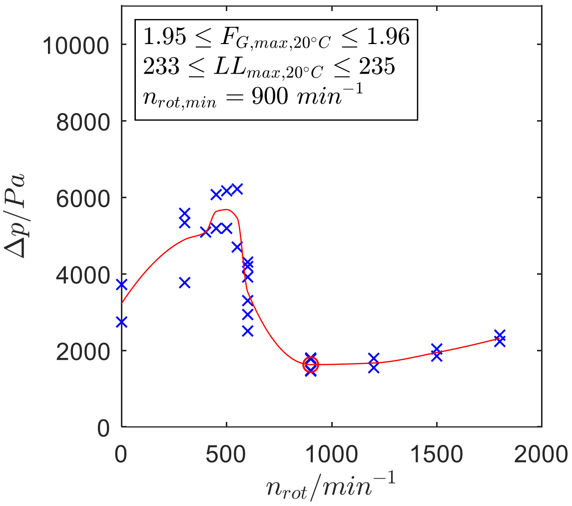

8)

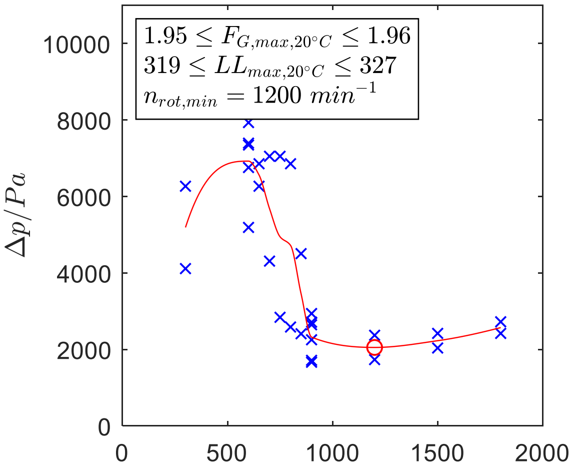

9)

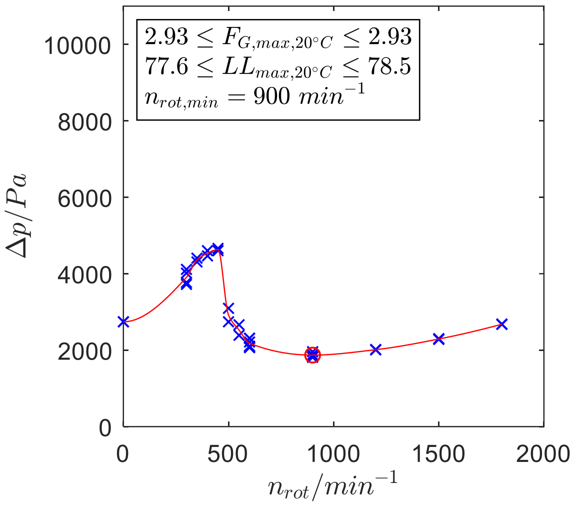

10)

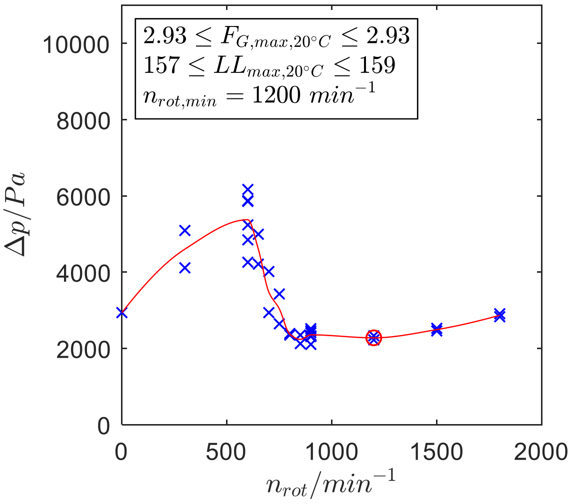

Automated determination of minimal rotational speed for the knitted mesh packing with ($d_i/d_o/h_p$) 0.146/0.450/0.01 m in counter-current operation.

Parameter range

1.95 $\leq F_{G,max,20°C} \leq$ 2.93 / Pa
157 $\leq LL_{max,20°C} \leq$ 327 / $m^3 m^2 h^{-1}$

(A5 continuation)

11)

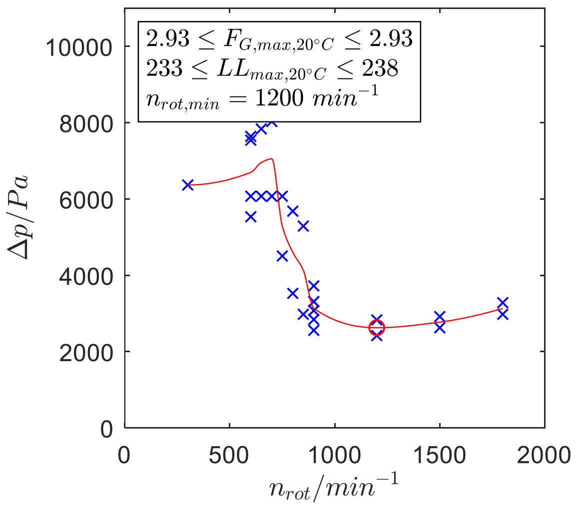

12)

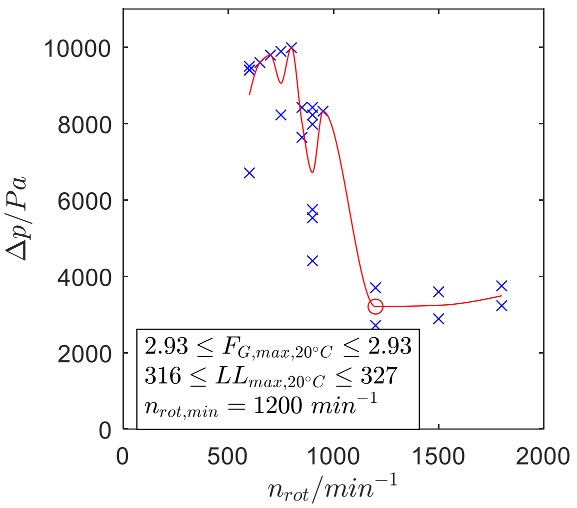

13)

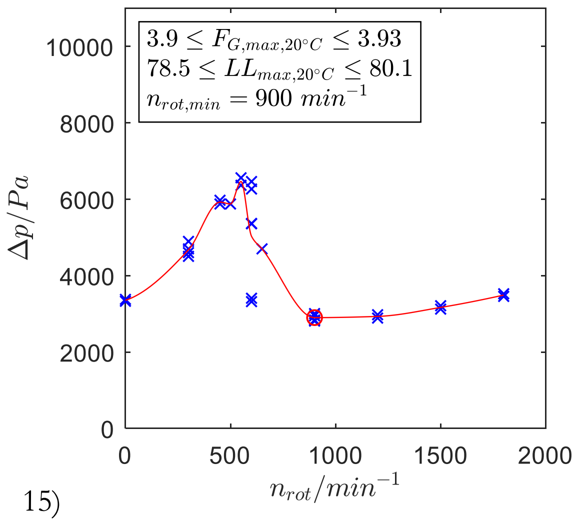

14)

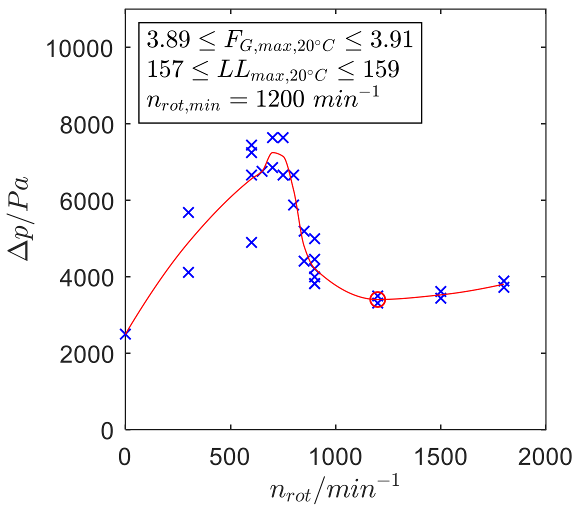

15)

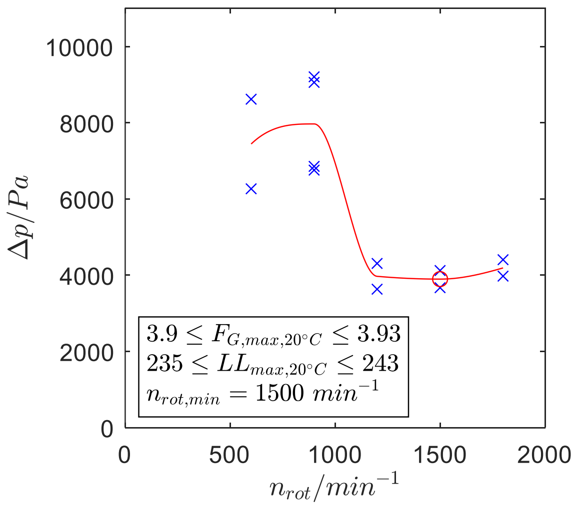

Automated determination of minimal rotational speed for the knitted mesh packing with ($d_i/d_o/h_p$) 0.146/0.450/0.01 m in counter-current operation.

Parameter range

$2.93 \leq F_{G,max,20°C} \leq 3.93$ / Pa
$78.5 \leq LL_{max,20°C} \leq 327$ / $m^3\,m^2\,h^{-1}$

(A5 continuation)

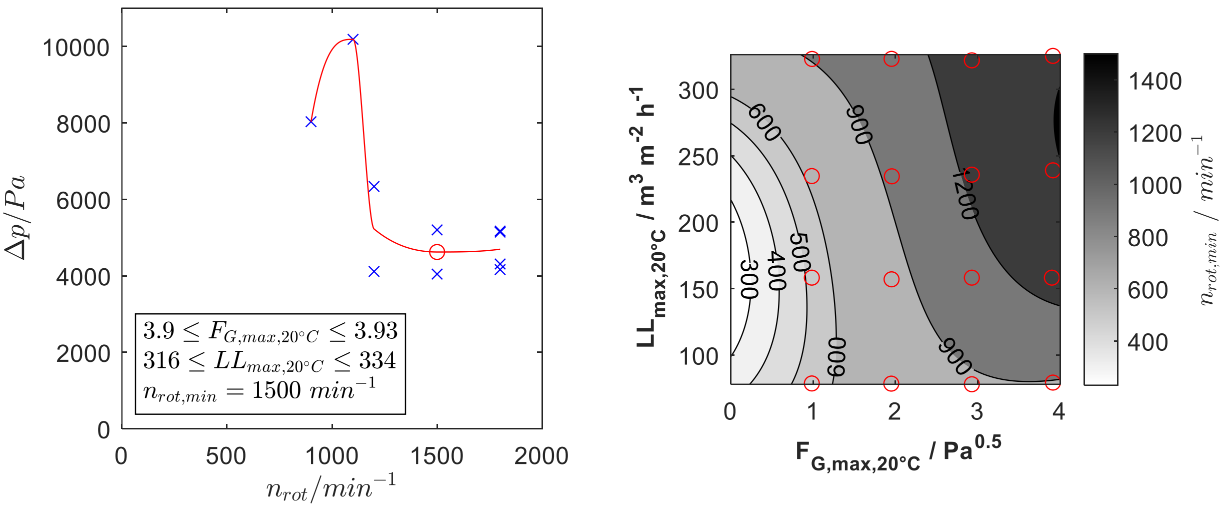

16)

22)

Automated determination of minimal rotational speed for the knitted mesh packing with ($d_i/d_o/h_p$) 0.146/0.450/0.01 m in counter-current operation.

A6: Data for the power consumption calculation of the RPB according to eq. (32),

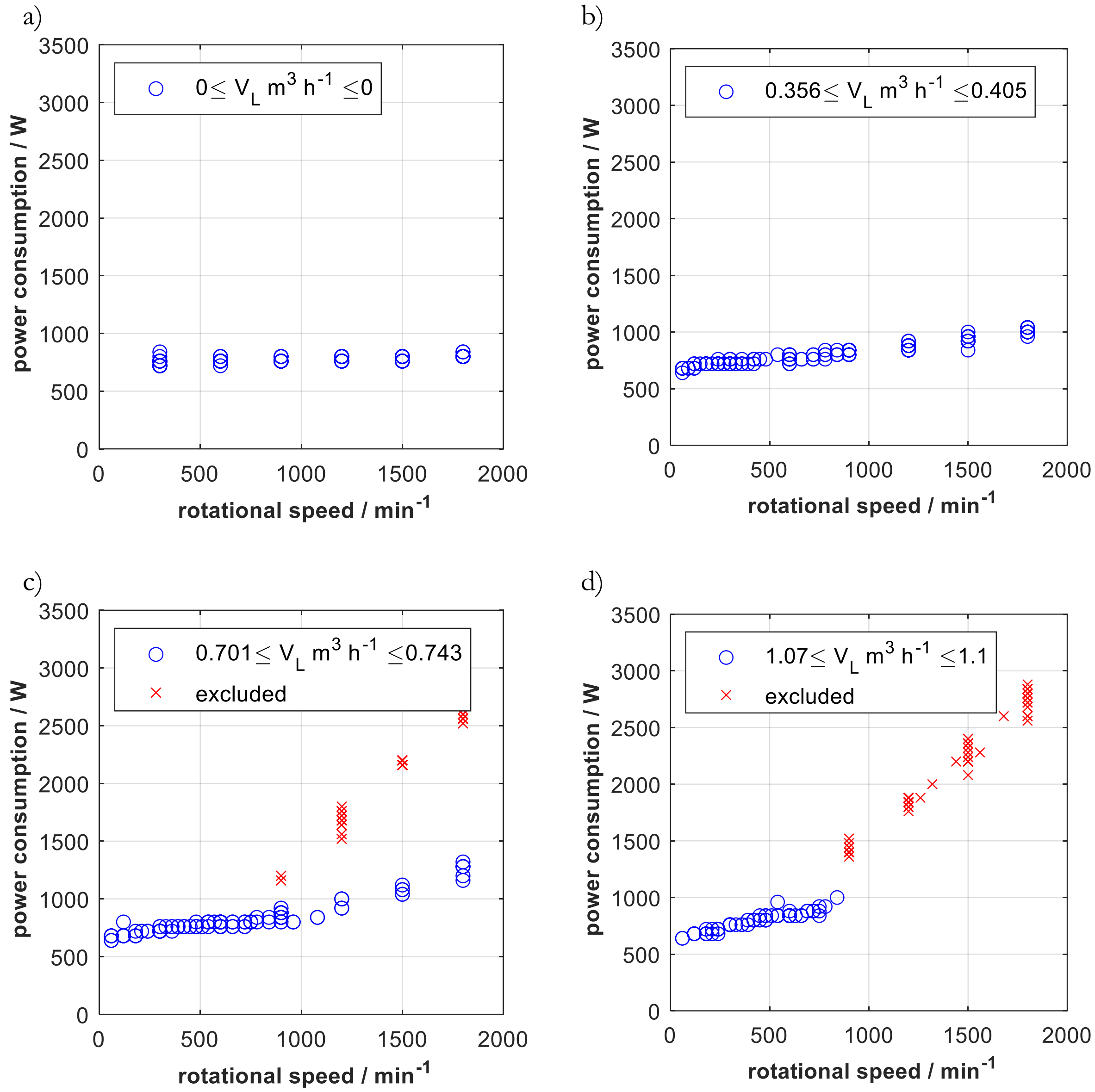

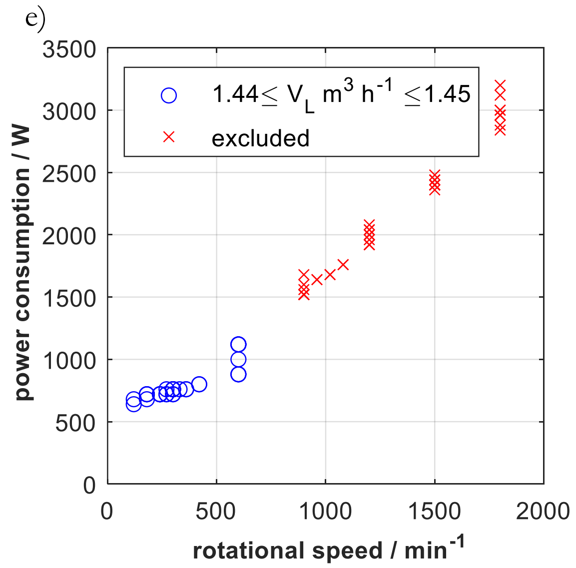

Data for liquid flow rates($\dot{V}_L$) between 0 and 1.45 $m^3 h^{-1}$ and gas flow rates between 0 and 330 $m^3 h^{-1}$ for the full foam packing with ($d_i/d_o/h_p$) 0.146/0.450/[0.01,0.02] m

A7: Data for casing liquid hold-up

Figure 10.7 illustrates the influence of a static liquid hold-up in the casing. In the experimental setup the outlets of the RPB were closed and a constant amount of liquid was added to the casing. Without adding further liquid or gas the rotation was started. When a constant rotational speed was reached the power consumption was noted. It can be seen that the power consumption is strongly connected to the liquid hold-up of the casing.

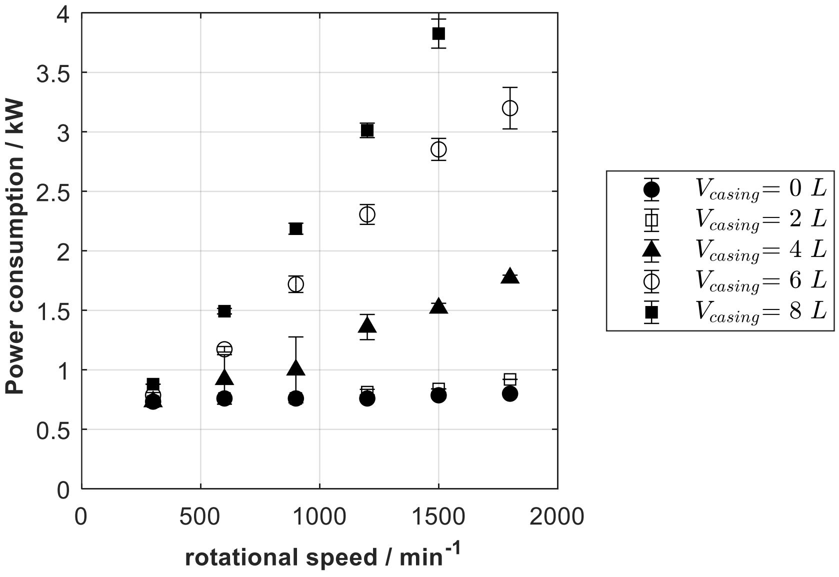

Figure 10.7: Influence of the liquid hold-up on the power consumption, when a static liquid volume is added to the casing and the rotation is started. No additional liquid is fed to the RPB during the experiment. Error bars depict the standard deviation.

A8: Overview of equipment used

e.o.s = end of scale m.v. = measured value

Liquid flow measurement

Type, Manufacturer	Measurement range	Accuracy	Hydraulic study	Mass transfer study
DRS-9159I4L4420, Kobold	2 to 40 L min^{-1}	±1.5 % of e.o.s	x	x
Optiflux 4300C, Krone	< 17 L min^{-1}	±0.5 % of m.v.		x

Gas flow measurement

Type, Manufacturer	Measurement range	Accuracy	Hydraulic study	Mass transfer study
KMT-114R10L1NQ4, Kobold	0.32 to 63 $Nm^3\,h^{-1}$	±1.5 % of m.v. + ±0.5 % of e.o.s	x	x
Orifice flow meter, Envimac	adjustable max 10 mbar orifice Δp	±10 % of m.v.	x	
EL mass flow controller, Bronkhorst	0.12 to 6 m^3h^{-1}	±0.5 % of m.v + ±0.1 % e.o.s		x
UK-040GML0100, Honsberg	0.1-1 NL min^{-1}	±3 % e.o.s		x
UKV-040GML0001, Honsberg	10-100 NL min^{-1}	±3 % e.o.s		x

Packing types

Type	a_p /m^2m^{-3}	ε / -	Dimensions (di / do / hp) mm	Hydraulic study	Mass transfer study
NCX 1116 (FF), Recemat ®	1000	0.92	146 / 450 / 10 146 / 450 / 20 146 / 200 / 10	x x	x x x
Knitted mesh (KM)	2957	0.83	146 / 460 / 10	x	x
Wire mesh	2975	0,915	100 / 152 / 50		x

Oxygen measurements

Type, Manufacturer	Accuracy	Hydraulic study	Mass transfer study
Inpro 6860i, Mettler Toledo	±1 % of m.v + 8 ppb		x
Inpro 6970i, Mettler Toledo	1 % of m.v. + 2ppb		x
Pure Water Optical DO Sensor, Thornton	±1 % of m.v at least 2 ppb		x

B1: Henry coefficient calculation

The calculation of the Henry volatility coefficient ($K_H^{p,x}$) O_2/H_2O is based on the Database APV84 Henry-AP at atmospheric conditions.

$$\ln\left(K_H^{p,x}\right) = \ln\left(\frac{py_i}{x_i}\right) = \left(A + \frac{B}{T_K} + C \cdot \ln(T_K) + D \cdot T_K + E \cdot T_K^2\right) \cdot 10^{-5} \left[\frac{mol \cdot bar}{mol}\right]$$

with

$A = 228.106003$, $B = -9622$, $C = -31.107$, $D = 0.012109$, $E = 0$

Which is converted into the concentration based Henry solubility coefficient (H^{CC}) assuming a dilute, aqueous solution and ideal gas-phase behavior.[*104*]

$$H^{CC} = \frac{1}{K_H^{p,x}} \cdot \frac{\rho_{H_2O}}{M_{H_2O}} \cdot R \cdot (T_C + 273.15) \cdot 10^{-5} \left[\frac{\frac{mol}{m^3}}{\frac{mol}{m^3}}\right]$$

B2: Overview RPB setup

Schematic representation of the experimental setup for the lab- and pilot-RPB. In the lab-setup a) the liquid is preheated and nearly saturated with air in the feed vessel, fed to the RPB at the shaft (controlled by a mass flow controller, MFC), withdrawn from the bottom of the housing and returned to the feed vessel. b) The pilot-RPB uses liquid from the tap water system the flow rates are manually adjusted (monitored by mass flow indicators, MFI). The temperature (T) and oxygen concentration (C_L) is measured at the liquid inlet and outlet of the equipment.

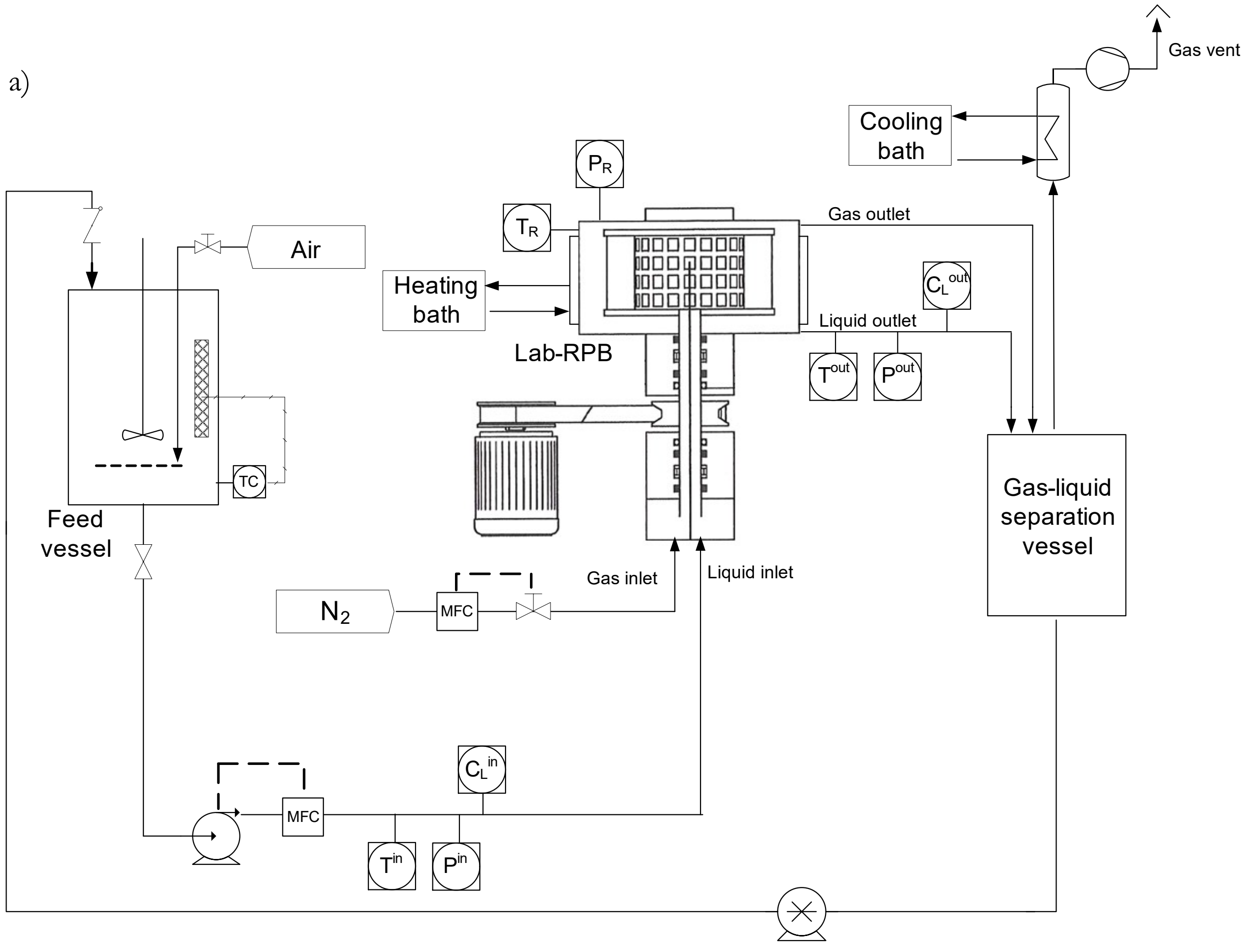

(Reprinted (adapted) with permission from [*96*]. Copyright 2020 American Chemical Society)

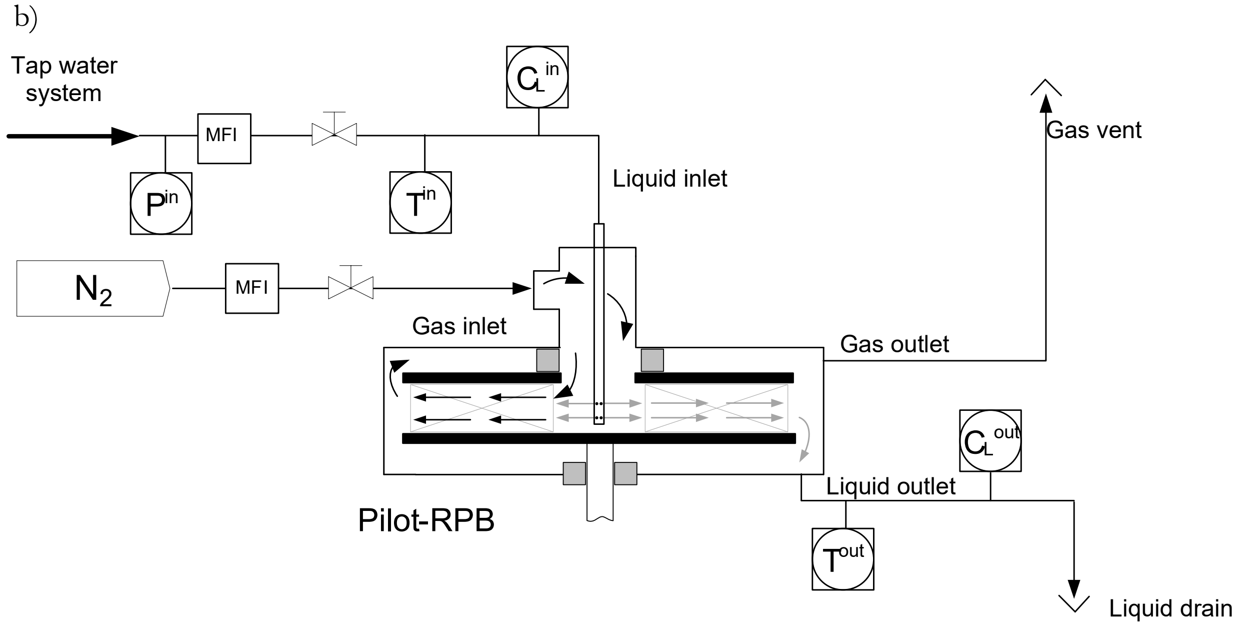

(Reprinted (adapted) with permission from [*96*]. Copyright 2020 American Chemical Society)

B3: RPB model description

This chapter offers a detailed description of the used MATLAB R2020a® program.

Basic equations:

$$\frac{dc_L}{dr} = -\frac{k_L a}{\dot{V}_L} \left(c_L - H_{O_2}^{CC}\, c_G\right) 2\, \pi\, z\, r \tag{58}$$

co-current gas-flow:

$$\frac{dc_G}{dr} = \frac{k_L a}{\dot{V}_G} \left(c_L - H_{O_2}^{CC}\, c_G\right) 2\, \pi\, z\, r \tag{59}$$

counter-current gas-flow:

$$\frac{dc_G}{dr} = -\frac{k_L a}{\dot{V}_G} \left(c_L - H_{O_2}^{CC}\, c_G\right) 2\, \pi\, z\, r \tag{60}$$

Boundary conditions:

co-current gas-flow:

$$c_L(r_i) = c_{L,in} \tag{61}$$

$$c_G(r_i) = c_{G,in} \tag{62}$$

counter-current gas-flow

$$c_L(r_i) = c_{L,in} \tag{63}$$

$$c_G(r_o) = c_{G,in} \tag{64}$$

The boundary value problem was solved with the bvp5c-solver an implicit Runge-Kutta algorithm using the Lobatto IIIa formula [*97*]. Parameters for the solver are given in Tab. 17.

Tab. 17: Parameters for the bvp5c-solver.

Initialization:
Equidistant mesh with 1000 steps between r_i and r_o
$[c_L, c_G]$ initial guess [0,0]
Further options:
Relative tolerance 10^{-10}, Nmax: 1000

The model further can regress the k_La-value based on experimental data when inlet and outlet concentration of the liquid stream are given. Otherwise the liquid phase outlet concentration is estimated based on a given k_La-value. The k_La-value can be a constant or a function. Based on an one stage equilibrium calculation the casing contribution can be subtracted from the overall mass transfer contribution.

The correlation of Chen et al. is implemented in the model as referenced in chapter 2.4.4

$$\frac{k_L a\, d_{spherical}}{D\, a_p}\left(1-0.93\frac{V_o}{V_{total}}-1.13\frac{V_i}{V_{total}}\right) = 0.35\, Sc^{0.5}\, Re^{0.17}\, Gr^{0.3}\, We^{0.3}\left(\frac{a_p}{a_{ref}}\right)^{-0.5}\left(\frac{\sigma_c}{\sigma_w}\right)^{0.14} \tag{65}$$

Where the packings are specified as followed:

Tab. 18: Parameter for EQ (65).

Knitted mesh	
Geometric surface area (a_P) / $m^2\ m^{-3}$	2975
Sphericity of the packing (ψ) / -	0.12
Packing porosity (ε) / -	0.915
Metal foam packing	
Geometric surface area (a_P) / $m^2\ m^{-3}$	1000
Sphericity of the packing (ψ) / -	0.12
Packing porosity (ε) / -	0.90
Correlation reference	
Geometric surface area (a_{ref}) / $m^2\ m^{-3}$	2074
Surface tension (σ_{ref}) / $kg\ s^{-2}$	72·10⁻³

The correlation for the diffusion coefficient from oxygen in water was taken from *Han et al.* [*105*].

$$D_{oxygen,water} = 10^{-4.410+\frac{773.8}{T_K}-\left(\frac{506.4}{T_K}\right)^2}\, 10^{-4} \quad / \quad m^2\, s^{-1} \tag{66}$$

The viscosity was calculated based on the equation of *Kerstin et al.* [*106*].

$$\mu_{water} = 10^{\frac{20-T_C}{T_C+96}\left(1.2364-1.37\ 10^{-3}\ (20-T_C)+5.7*10^{-6}\ (20-T_C)^2\right)}\ 1002\ 10^{-6} \quad / \quad Pa\, s \tag{67}$$

11 Declaration

Contents of this thesis were acquired in cooperation with ISPT (Institute for Sustainable Process Technology) within the scope of the research project ImPaCCt (Improved Process Performance by Process Intensification in Centrifugal Contactors). Parts of this work have been published and have been presented by the author or partly contain measured data or programming components evolved from supervised student theses at the Laboratory of Fluid Separations, Faculty of Biochemical and Chemical Engineering, TU Dortmund University. Detailed information is given below and the chapters 12 Publications, 13 Supervised theses. Subchapter reference always includes lower level subchapters.

Chapter	Subchapter	Content	Scientific work
2	2.2.1	Partially modified from	C
	2.2.2	Partially modified from	C
	2.4.1	Partially modified from	C
	2.4.2	Partially modified from	B,D
	2.4.3	Partially modified from	C
	2.4.4	Partially modified from	A,E
3	3.2	Experimental data from	a-g
	3.3.1-3.3.4	Partially modified from	B
	3.4	Experimental data from	a-e, g
	3.5	Experimental data from	b
4	4.1-4.2	Partially modified from	A
	4.3	Partially modified from	A
		Experimental data from	f
	4.4	Experimental data from	c, d, g
5	5.1.1	Experimental data from	f
	5.1.1	Partially modified from	A
	5.1.2	Experimental data from	c, d, g
	5.2-5.3	Programming partially from	a
	5.2	Partially modified from	G
10	A 1	Partially modified from	F
	A 2	Experimental data from	b,d

	A 3	Experimental data from	B,D
	A 4	Experimental data from	B,D
	A 5	Experimental data from	b
	A 6	Experimental data from	d
	A 7	Experimental data from	b
	A 8	Experimental data from	a
	B 1	Partially modified from	A
	B 2	Partially modified from	A

12 Publications

Journal articles	
A	Groß, K.; Beer, M.; Dohrn, S.; Skiborowski, M.: Scale-Up of the Radial Packing Length in Rotating Packed Beds for Deaeration Processes, Ind. Eng. Chem. Res. 59, (2020), pp. 11042-11053, DOI: 10.1021/acs.iecr.0c00868
B	Groß, K.; Bieberle, A.; Gladyszewski, K.; Schubert, M.; Hampel, U.; Skiborowski, M.; Górak, A.: Analysis of flow patterns in high gravity equipment using gamma-ray computed tomography, Chem. Ing. Tech. 91 (7), (2019), pp. 1032–1040, DOI: 10.1002/cite.201800085
C	Groß, K.; Neumann, K.; Skiborowski, M.; Górak, A.: Analysing the Operating Limits in High Gravity Equipment, Chem. Eng. Trans. 69 (2018), pp. 661–666, DOI: 10.3303/CET1869111
D	Groß, K.; Bieberle, A.; Gladyszewski, K.; Schubert, M.; Skiborowski, M.; Hampel, U.; Górak, A.: Evaluation of Liquid Hold-up in a Rotating Packed Bed for High Gravity Fluid Separation using Process-Synchronized Gamma-Ray Computed Tomography, Proceedings of the 9th World Congress on Industrial Process Tomography (2018), pp. 831–838
E	Neumann, K.; Gladyszewski, K.; Groß, K.; Qammar, H.; Wenzel, D.; Górak, A.; Skiborowski, M.: A guide on the industrial application of rotating packed beds, Chem. Eng. Res. Des. 134 (2018), pp. 443–462, DOI: 10.1016/j.cherd.2018.04.024
F	Neumann, K.; Hunold, S.; Groß, K.; Górak, A.: Experimental investigations on the upper operating limit in rotating packed beds, Chem. Eng. Process. 121 (43), (2017), pp. 240–247 DOI: 10.1016/j.cep.2017.09.003
G	Lukin, I.; Pietzka, L.; Groß, K.; Górak, A.; Schembecker, G.; Economic evaluation of rotating packed bed use for aroma absorption from bioreactor off-gas; Chem. Eng. Process., 2020, 154, 108011, DOI: 10.1016/j.cep.2020.108011

Oral and poster presentations
Groß, K.; Neumann, K.; Skiborowski, M.; Górak, A.: Analyzing the operating limits in High Gravity Equipment, Poster at 11th International Conference on Distillation & Absorption (2018), Florence, Italy
Groß, K.; Bieberle, A.; Gladyszewski, K.; Schubert, M.; Skiborowski, M.; Hampel, U.; Górak, A.: Evaluation of liquid hold-up in a rotating packed bed for high gravity fluid separation using process-synchronized gamma-ray computed tomography, Presentation at 9th World Congress on Industrial Process Tomography (2018), Bath, United Kingdom
Groß, K.; Bieberle, A.; Gladyszweski, K.; Schubert, M.; Skiborowksi, M.; Górak, A.: Analysis of Flow Patterns in High Gravity Equipment Using Gamma-ray Computed Tomography, Presentation at Jahrestreffen der ProcessNet Fachgruppen Fluidverfahrenstechnik und Membrantechnik (2018), Munich, Germany
Groß, K.; Neumann, K.; Qammar, H.; Wenzel, D.: Current Status of Rotating Packed Beds (RPBs): Applications in Chemical Industry, Poster at Jahrestreffen der ProcessNet Fachgruppen Fluidverfahrenstechnik und Membrantechnik (2017), Cologne, Germany
Groß, K.; Wenzel, D.; Neumann, K.; Skiborowski, M.; Górak, A.: Rotating Packed Beds - Vorteile und Herausforderungen, Presentation at Jahrestreffen der ProcessNet-Fachgemeinschaft "Prozess-, Apparate- und Anlagentechnik" (2016), Karlsruhe, Germany
Groß, K.; Neumann, K.; Kupitz, K.; Skiborowski, M.; Górak, A.: HiGee-Technologie – Untersuchung von Hydrodynamik und Stofftransport, Presentation at ProcessNet-Jahrestagung und 32. DECHEMA-Jahrestagung der Biotechnologen (2016), Aachen, Germany.

13 Supervised theses

Bachelor theses	
a	Hubach, Tobias: Development of a cost model for Rotating Packed Beds (2019), TU Dortmund University
b	Schmitt, Marvin: Investigation of hydrodynamic operating limits of metal foam packings in Rotating Packed Beds (2019), TU Dortmund University
c	Kalker, Carola Antonia: Investigation of mass transfer performance for different packing types in Rotating Packed Beds (2018), TU Dortmund University
d	Haas, Christian: Investigation of Initial Liquid Distribution and its Association with Maldistribution in Rotating Packed Beds (2017), TU Dortmund University
e	Niesmann, Marc: Investigation of Initial Liquid Distribution in Rotating Packed Beds (2017), TU Dortmund University

Master theses	
f	Dohrn, Stefanie: Commissioning and Characterization of a Rotating Packed Bed designed for Liquid Distribution Investigations (2017), TU Dortmund University
g	Yalin, Sinan: Characterization and modelling of mass transfer in a Rotating Packed Bed for different rotor internals (2019), TU Dortmund University